DE GRUYTER

Sergey Borisovich Dubovichenko

RADIATIVE NEUTRON CAPTURE

PRIMORDIAL NUCLEOSYNTHESIS OF THE UNIVERSE

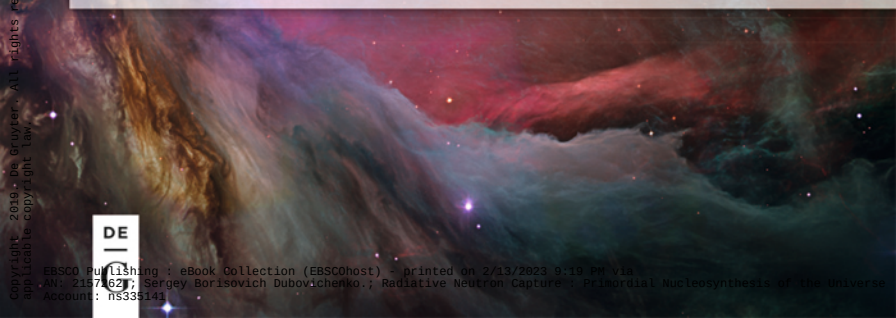

Sergey Borisovich Dubovichenko

Radiative Neutron Capture

Also of interest

Holographic Principle
Universe and Reality
Takeo Oku, 2018
ISBN 978-3-11-054108-3, e-ISBN 978-3-11-054304-9

Isotopic Randomness and Self-Organization
In Physics, Biology, Nanotechnology and Digital Informatics
Alexander Berezin, 2018
ISBN 978-3-11-060505-1, e-ISBN 978-3-11-060649-2

Regularization in Orbital Mechanics
Javier Roa, 2017
ISBN 978-3-11-055855-5, e-ISBN: 978-3-11-055912-5

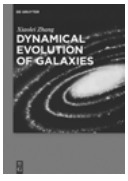

Dynamical Evolution of Galaxies
Xiaolei Zhang 2017
ISBN 978-3-11-052519-9, e-ISBN: 978-3-11-052742-1

Sergey Borisovich Dubovichenko

Radiative Neutron Capture

Primordial Nucleosynthesis of the Universe

DE GRUYTER

Author
Prof. Dr. Sergey Borisovich Dubovichenko
Fesenkov Astrophysical Institute
Laboratory of Nuclear Astrophysics
Kamenskoe plato 23
Almaty
050020 Kazakhstan

ISBN 978-3-11-061784-9
e-ISBN (E-BOOK) 978-3-11-061960-7
e-ISBN (EPUB) 978-3-11-061790-0

Library of Congress Control Number: 2018952442

Bibliographic information published by the Deutsche Nationalbibliothek
The Deutsche Nationalbibliothek lists this publication in the Deutsche Nationalbibliografie; detailed bibliographic data are available on the Internet at http://dnb.dnb.de.

Typesetting: Integra Software Services Pvt. Ltd.
Printing and binding: CPI books GmbH, Leck
Cover image: Science Photo Library - NASA/ESA/STSCI/
M.ROBBERTO,HST ORION TREASURY TEAM / Brand X
Pictures / gettyimages.com

www.degruyter.com

Foreword

Progress in the study of the universe, especially the initial stages of its formation, is closely associated with the development of certain aspects of the atomic nucleus and other elementary particles. This book mainly discusses nuclear physics and the calculation methods of nuclear characteristics of thermonuclear processes. A majority of these thermonuclear processes are involved in primordial nucleosynthesis, which possibly occurred during the initial stages of the development of our universe.

This book presents the calculation methods of thermonuclear reactionse based on numerous scientific articles published in peer-reviewed journals in recent years. In addition to the mathematical calculation methods, computer models and results of some phase-shift analyses of elastic scattering at astrophysical energies are presented in this book. These results were then used for obtaining the binary potentials of interaction of particles during thermonuclear reactions such as radiative capture.

These binary potentials were used for solving some problems of nuclear astrophysics associated with the description of thermonuclear processes involved in primordial nucleosynthesis. All results were obtained within the modified potential cluster model framework, which employs the methods of classification of orbital states according to Young tableaux for determining potentials. Special attention is paid to neutron radiative capture by light atomic nuclei at low and ultralow, that is, astrophysical, energies.

This book is closely associated with a previous book by the author titled "Thermonuclear Processes of the Universe," published in Russian in 2011 in Almaty (the Republic of Kazakhstan, RK), which can be found on the server of Cornell University http://arxiv.org/ftp/arxiv/papers/1012/1012.0877.pdf. The English version of this book was published by the New York publishing house NOVA Scientific Publishers in 2012, and can be found on the official website of the editorial office http://www.novapublishers.org/catalog/product_info.php?products_id=31125.

In 2015, this book was republished in Germany with the title "Thermonuclear Processes in Stars and the Universe," and can be found on the website https://www.morebooks.shop/store/gb/book/Термоядерные-процессы-в-3вездах/isbn/978-3-659-60165-1. The English version of this book published by another German publishing house can be found at https://www.morebooks.shop/store/gb/book/thermonuclear-processes-in-stars/isbn/978-3-639-76478-9. Thus, this book describes the thermonuclear reactions occurring in the sun and stars at different stages of the development of our universe based on the unified principles and within the modified potential cluster model framework.

This book does not attempt to provide an exhaustive explanation of all nuclear astrophysics methods or even all thermonuclear processes. However, it does discuss numerous calculation methods of nuclear characteristics, which have been used in

https://doi.org/10.1515/9783110619607-201

solving the problems of nuclear astrophysics. This book presents new findings that have not been discussed in modern literature yet, and will be useful for both professionals and young researchers in the field of nuclear astrophysics and nuclear physics at low energies.

Igor Strakovsky
Research Professor of Physics
Institute for Nuclear Studies & Department of Physics
The George Washington University, DC, USA
Nov., 30, 2017

Preface

> *Application of modern nuclear physics to the study of universe and thermonuclear reactions occurring in the sun and stars allowed to construct theories that qualitatively agree with the theoretical formation, structure, and evolution of stars, and also explain the prevalence of elements in the universe* [1].

Practically, all nuclear astrophysics problems are associated with nuclear physics problems, usually at ultralow energies and light atomic nuclei participating in the thermonuclear processes occuring during different stages of the formation and development of our universe [1, 2]. For instance, it is impossible to describe astrophysical characteristics of thermonuclear reactions occurring in the sun and stars without accounting for the concepts of nuclear physics at ultralow energies [3]. It is impossible to analyze the processes preceeding the Big Bang [4], which initially began with nuclear reactions at high and ultrahigh energies, without discussing the models and methods of modern physics of elementary particles such as the "Standard Model" [5]. In other words, it is impossible to discuss astronomical phenomena and physical properties of astronomical objects without accounting for the laws of physics, in general, and nuclear physics, in particular!

The development of the "resonating group method" (RGM) [6, 7, 8, 9], a microscopic model, became one of the most successful step in nuclear physics in the last 50–60 years. In addition to RGM, other models have also been described, for instance, the generating coordinate method (GCM) [9] or the algebraic version of RGM (ARGM) [10]. The successful development of these models led physicists to believe that it is possible to obtain new results in the field of nuclear physics at low energies as well as nuclear astrophysics. This led to a widespread, but, apparently, wrong opinion that this was the only way to further research the structure of an atomic nucleus, as well as nuclear and thermonuclear reactions at low, astrophysical, and thermal energies.

Complex RGM calculations are not always required for the explanation of available experimental facts. Possible applications of simple, two-body potential cluster model (PCM) have not been investigated yet, especially, if they use the concept of forbidden states (FS) [11]. Model potentials for a discrete spectrum are constructed to correctly reproduce the main characteristics of the bound states (BS) of light nuclei in cluster channels. In a continuous spectrum, the model takes into account the resonance behavior of the elastic scattering phase shift of the particles interacting at low energies [12].

For many problems in nuclear physics at low energies and even nuclear astrophysics, it is sufficient to use the simple PCM with FS, taking into account the classification of orbital states according to Young tableaux as well as the resonance behavior of elastic scattering phase shifts. This improved model is referred to as the modified potential cluster model (MPCM). As will be shown in this book, this

https://doi.org/10.1515/9783110619607-202

approach aids in the description of many experimental studies involving thermonuclear reactions at low and astrophysical energies [11,12].

Considering the numerous thermonuclear processes that occurred in the universe at different stages of its formation and development [12], this book presents new results in the field of thermonuclear reactions at ultralow, thermal, and astrophysical energies. These processes and reactions have been analyzed and described from the viewpoint of the general laws, approaches, and principles of modern nuclear physics. The two-body MPCM has been used for the analysis, which allows the consideration of thermonuclear processes, namely, reactions of the radiative capture of neutrons and protons based on unified representations, criteria, and methods.

In other words, solutions of certain problems in nuclear astrophysics along with their methods have been discussed, for example, description of thermonuclear processes involved in the primordial nucleosynthesis of the universe at thermal and astrophysical energies within the MPCM framework. In addition, these methods can be used for analyzing thermonuclear reactions occurring in the sun and stars at different thermonuclear cycles. In other words, certain nuclear reactions, such as radiative capture at ultralow energies, have been considered [12].

This book summarizes and discusses the results of several articles and reviews published in the last 5–7 years in Russia, Europe, USA, and some commonwealth countries.

This book consists of three chapters. The first chapter describes the general mathematical methods for calculating the nuclear characteristics of the binding states as well as continuum of nuclear particles, which are used for determining the wave function of these particles by applying known interaction potentials. In addition, we define the general criteria and methods of formation of intercluster potentials in a continuous and discrete spectrum, which are used for further consideration of thermonuclear processes within the MPCM using the FSs, as well as the classification of the orbital states of clusters according to Young tableaux.

Chapter 2 describes the results obtained within the MPCM framework with FS for radiative neutron capture at thermal and astrophysical energies by ten light atomic nuclei with mass ranging 2–16 in a wide power area, usually covering 7–9 orders of energy, beginning with 1–10 meV (1 meV = 10^{-3} eV).

Finally, Chapter 3 discusses new results of radiative neutron capture of some light nuclei, namely, ^{8}Li, ^{10}Be, ^{10,11}B, and the proton capture of ^{16}O at thermal and astrophysical energies (more recent results are presented in the Appendix). In this case, the MPCM model gives adequate results and describes the total cross-sections of these processes.

The most essential stages of construction are considered based on experimental data of two-body potentials which are further employed to calculate the main characteristics of thermonuclear processes involved in radiative capture. This book does not provide an exhaustive description of all the methods used in modern

nuclear astrophysics, including thermonuclear processes. It only attempts to discuss some methods and results of nuclear physics at low energies, which can be applied to some problems of nuclear astrophysics such as the description of thermonuclear reactions occurring on the surface of sun and stars, as well as the derivation, formation, and development of our universe.

It is important to note that this book is significantly altered and is a revised edition of the previous book "Primordial Nucleosynthesis of the Universe" published in Russian in Germany by Lambert Academy Publishing in 2014 (668p). The previous edition included the results of the phase-shift analysis using the three-body model, which were discussed in a separate book titled "The Phase Shift Analysis in Nuclear Astrophysics" published by Lambert Academy Publishing in 2015 (368p). [13]. Some proton reactions are described in the book "Thermonuclear Processes in Stars and the Universe" published by Palmarium Academy Publishing in 2015 (348 p). [14]. New results on the radiative capture of neutrons in the nuclei of ^{8}Li, ^{10}Be, ^{10,11}B and proton capture on ^{16}O are included in this book.

Sergey B. Dubovichenko

Doctor of Phys. and Math. Sci., Professor, Nuclear Astrophysics Laboratory Head, Fesenkov Astrophysical Institute, 050020, Almaty, Kazakhstan, www.dubovichenko.ru, dubovichenko@mail.ru, dubovichenko@gmail.com

P.S. This book is the amended edition of the book with the same title, "Radiative neutron capture and primordial nucleosynthesis of the Universe," published in Germany in 2016 by S.B. Dubovichenko. Fifth Russian revised and corrected edition. Germany, Saarbrucken: Lambert Academy Publ. GmbH&Co. KG. 2016. 496c.; https://www.morebooks.shop/store/gb/book/Радиационный-захват-нейтронов/isbn/978-3-659-82490-6.

Contents

Foreword —— V

Preface —— VII

Introduction —— 1

I Computational methods —— 5
Introduction —— **5**
1.1 Review of the cluster model —— **6**
1.1.1 Basic principles of the model —— **6**
1.1.2 Model development and main results —— **8**
1.1.3 Model representations and the methods —— **10**
1.2 Potentials and wave functions —— **11**
1.3 Methods of the phase-shift analysis —— **14**
1.4 Certain numerical methods —— **16**
1.5 The generalized matrix problem on eigenvalues —— **23**
1.6 Total radiative capture cross-sections —— **29**
1.7 Creation of intercluster potentials —— **31**
1.8 Classification of cluster states —— **33**
Conclusion —— **34**

II Radiative neutron capture on the light nuclei —— 35
Introduction —— **35**
2.1 Neutron radiative capture on ^{2}H in the cluster model —— **40**
2.1.1 Potential description of the elastic n^{2}H scattering —— **40**
2.1.2 The total cross-sections of neutron radiative capture on ^{2}H —— **43**
2.2 Neutron radiative capture on ^{6}Li —— **48**
2.2.1 Potential description of the n^{6}Li scattering —— **48**
2.2.2 Total cross-sections of the neutron radiative capture on ^{6}Li —— **53**
2.3 Cluster n^{7}Li system —— **60**
2.3.1 Classification of cluster states in the n^{7}Li system —— **60**
2.3.2 The potential description of the elastic n^{7}Li scattering —— **62**
2.3.3 Radiative ^{7}Li(n,γ)^{8}Li capture —— **69**
2.4 The astrophysical neutron capture on ^{9}Be —— **74**
2.4.1 Classification of orbital states in the n^{9}Be system —— **74**
2.4.2 Potential description of the n^{9}Be phase shifts —— **77**
2.4.3 Total cross-sections of the neutron capture on ^{9}Be —— **82**
2.5 The radiative capture in the n^{12}C and n^{13}C systems —— **87**
2.5.1 Total cross-sections of the neutron capture on ^{12}C —— **87**
2.5.2 The total cross-sections of the n^{13}C capture —— **97**

2.6 Radiative capture in the $n^{14}C$ and $n^{14}N$ systems — **106**
2.6.1 Classification the $n^{14}C$ and $n^{14}N$ states and $n^{14}N$ scattering potentials — **106**
2.6.2 Total cross sections for the neutron capture on ^{14}C — **109**
2.6.3 The $n^{14}N$ scattering potentials — **112**
2.6.4 Total cross sections of the neutron capture on ^{14}N — **117**
2.7 The radiative neutron capture on ^{15}N — **119**
2.7.1 The potentials of the $n^{15}N$ scattering — **119**
2.7.2 Total cross-sections of the neutron capture on ^{15}N – first variant — **126**
2.7.3 Total cross-sections of the neutron capture on ^{15}N – second variant — **129**
2.8 The radiative capture in the $n^{16}O$ system — **134**
2.8.1 Phase shifts and $n^{16}O$ scattering potentials — **135**
2.8.2 Total cross-sections of the radiative capture — **141**
Conclusion — **148**

III New results for radiative capture — 151
3.1 Neutron radiative capture on ^{10}B — **151**
3.1.1 Structure of cluster states of $n^{10}B$ system — **152**
3.1.2 Intercluster potentials — **157**
3.1.3 Total capture cross-sections — **160**
3.2 Neutron capture on ^{11}B — **169**
3.2.1 Classification of cluster states in the $n^{11}B$ system — **169**
3.2.2 Interaction $n^{11}B$ potentials — **173**
3.2.3 Total cross-sections of the neutron radiative capture on ^{11}B — **177**
3.3 Neutron radiative capture on ^{8}Li — **183**
3.3.1 Astrophysical aspects — **183**
3.3.2 Classification of $n^{8}Li$ states according to Young tableaux — **184**
3.3.3 Structure of the $n^{8}Li$ states — **185**
3.3.4 Interaction $n^{8}Li$ potentials — **186**
3.3.5 Total cross-sections of the neutron radiative capture on ^{8}Li — **190**
3.4 Neutron radiative capture on ^{10}Be — **196**
3.4.1 Structure of the $n^{10}Be$ states — **197**
3.4.2 Interaction $n^{10}Be$ potentials — **199**
3.4.3 Total cross-sections of the neutron radiative capture on ^{10}Be — **203**
Conclusions — **208**

Conclusion — 209

Afterword — 215

Acknowledgments —— 219

Author information —— 221

Appendix —— 223

References —— 277

Index —— 295

Introduction

Experimental data of nuclear reactions and nuclear scattering at low energies are the main sources of information for the structure of nuclei, the properties and mechanisms of interaction between nuclei and their fragments, and the probability of clusterization of such nuclei [19].

One of the main characteristics of thermonuclear processes occuring in natural thermonuclear reactors, such as stars, in controlled thermonuclear fusion is the astrophysical *S*-factor or the total cross-sections of the radiative capture that helps determine the rate of such a reaction. Therefore, one of the main objectives of nuclear astrophysics is to determine the *S*-factor or the total cross-section of the reaction, along with their dependence on energy in the zero energy range – vanishing energies. This problem can be solved in several ways with the help of experimental and theoretical nuclear physics. Experimental measurement of the total cross-section of nuclear reactions at ultralow energies is one such technique. A second theoretical technique is to model nuclear processes at astrophysical energies.

Although, in principle, the astrophysical *S*-factor can be determined experimentallyfor a majority of interacting light nuclei that participate in various thermonuclear processes, it is only possible at energies in the range of 100 keV–1.0 MeV (1 keV – kiloelectronvolt is equal to 10^3 electronvolts of eV, 1 MeV – megaelectronvolt is equal to 10^6 electronvolt of eV). Experimental error of these measurements often reaches 100% [15]. However, for real astrophysical measurements, for example, those involved in the development and evolution of stars [16] and our entire universe at this stage of development [4, 17], its values with minimum possible errors are required at the energies in the range of 0.1–100 keV that corresponds to temperatures at the center of a star, that is, approximately 10^6–10^9 K (K – degree Kelvin).

One of the methods to determine the astrophysical *S*-factor at zero energy, that is, 1 keV and less, is to extrapolate its values from an area where it can be experimentally determined to lower energy areas. This is the most commonly used method after measuring the cross-section of some thermonuclear reactions [18]. However, large experimental errors in the determination of *S*-factor [15, 18] leads to large ambiguities in the extrapolations which significantly reduces the value of such results.

Another method consists of theoretically calculating the astrophysical *S*-factor or the total cross-section of thermonuclear reactions, for example, radiative capture, using a nuclear model [3]. Such a method is based on an obvious assumption that, if a model of nuclear processes describes experimental data in an energy range where they exist, then it can be assumed that it will correctly reproduce *S*-factor at lower energies, about 1 keV and below [14], that is, at an energy range where direct experimental measurements of its values are not yet feasible [15, 18].

The second approach [3, 14, 19] has an advantage over the extrapolation of experimental data to zero energy because any nuclear model is constructed with certain microscopic justifications considering general principles of modern nuclear

https://doi.org/10.1515/9783110619607-001

physics and quantum mechanics. Therefore, there is very definite hope for the existence of some predictive capabilities of this model, especially, if the energy ranges, where there are experimental data and in what region it is required to obtain new, that is, in fact, predictive results, do not differ significantly [12, 14].

For similar calculations, MPCM of light atomic nuclei along with classification of orbital states of clusters according to Young tableaux is commonly used [11, 14, 20, 21, 22]. Such a model performs numerous calculations of astrophysical characteristics, for example, the astrophysical *S*-factor or total cross-sections of radiative capture for electromagnetic transitions from the scattering states of nuclear particles to the BS of light atomic nuclei in such cluster channels [12]. In general, this book demonstrates some opportunities of potential two-body model and intercluster potentials constructed based on elastic scattering phase shifts obtained during phase analysis of experimental cross-sections. For example, 15 light nuclei have been discussed in three chapters.

In Chapter 1, the general calculation methods of nuclear characteristics and thermonuclear processes in MPCM are discussed [19, 23, 24]. In Chapter 2, calculation results of the total cross-sections of ten reactions of neutron radiative capture of some light nuclei at astrophysical energies are presented. Finally, in Chapter 3, the total cross-sections of radiative neutron capture of ^{8}Li, ^{10}Be, and ^{10,11}B are described. Further, in the Appendix, calculation results of the *S*-factor of a proton capture reaction of ^{16}O are presented.

The stated methods of calculation (described in Chapter 1) allows one to avoid ambiguity in the determination of various characteristics of nuclear properties and processes. The algorithms and computer programs used in the calculations of nuclear characteristics, such as total cross-sections of capture reactions, and characteristics of BS of nuclei are also presented in Chapter 1 [24].

Chapters 2 and 3 and the Appendix discuss the results obtained using the MPCM for the processes of radiative neutron and proton capture at thermal and astrophysical energies. These chapters also present the applications obtained as a result of the phase-shift analysis [13] or spectra of levels of final nucleus and characteristics of its BS of intercluster potentials for radiative capture by some light nuclei. A majority of neutron capture reactions are not included in thermonuclear cycles, even though they are believed to participate in the primordial nucleosynthesis involved in the derivation, formation, and development of our universe.

Thus, in all the chapters of this book [13, 14], the essential stages for obtaining the available experimental data (σ_{exp}) of some intermediate parameters – scattering phase shifts (δ_L) and two-body intercluster potentials of interaction (V_0 and γ) – have been considered. This is further required for calculating certain main characteristics, for example, the total cross-sections of thermonuclear processes involved in the radiative capture (σ_c) occuring in the sun and stars, as well as in the primordial nucleosynthesis of our universe.

In general, this book discusses some methods of nuclear physics at low and ultralow energies and describes the results, which can be used for calculating certain

characteristics of thermonuclear reactions at astrophysical energies [12, 14]. The book also describes some methods of determining nuclear characteristics, in particular, the elastic scattering phase shifts of nuclear particles (for more details, see [13]), which are used for determining intercluster potentials which can be applied in performing astrophysical calculations [12, 14]. These potentials are also mentioned [13], which demonstrate a correctness of their construction, and possibility of using similar potentials in calculations of the main characteristics of thermonuclear processes considered here [12, 14] were presented.

I Computational methods

The majority of problems in nuclear physics need the knowledge of wave function of relative movement of particles participating in nuclear collisions or the determination of bound state of nucleus, and are an internal part of the system. Wave functions can be determined from the solutions of Schrödinger equation for specific physical problems in discrete or continuous spectrum, if the potential of interaction of these particles is known [24].

This chapter briefly discusses some mathematical methods and numerical algorithms used in the phase-shift analysis of differential sections of elastic scattering at the solution of the radial Schrödinger equation in problems of discrete and continuous spectrum of system of two particles. Using the methods described here we can solve the generalized matrix problem on own values and functions with use of an alternative way which, especially in the three-body model [13], leads to a stable algorithm for searching eigenvalues.

Introduction

The short review of some main results obtained in the modified potential cluster model (MPCM) with the forbidden states (FSs) and classification of orbital states of clusters according to Young tableaux is presented ahead of calculation methods. Such models are used as there is no concrete theory of light atomic nuclei yet. Therefore, for the analysis of separate nuclear characteristics, various physical models and methods have been used [6, 11, 25–29]. In this regard, the great interest represents studying of resources of the potential cluster model using the intercluster interactions with the FSs. FSs follows from the classification of cluster states according to Young tableaux, and such a model was termed the modified PCM with FS or the MPCM in the Foreword.

MPCM assumes that the nucleus consists of two unstructured and nonpointed fragments, known as clusters. Therefore, it is possible to compare the properties of the corresponding nuclear particles in the free state. And, if required, the charge distribution in such clusters is considered [22]. The potentials used with the FS allows one to effectively consider Pauli's exclusion principle in intercluster interactions and do not demand explicit antisymmetrization of the total wave function of the system that considerably simplifies all computer calculations [12, 22, 24]. The parameters of these potentials are usually coordinated with the phase shifts of the elastic scattering of corresponding free particles [13]. In case of a high probability of clusterization of the considered nuclei, the MPCM allows the correct reproduction of all main characteristics of their bound states in cluster channels [11, 22].

Furthermore, these general representations are used by considering some characteristics of light atomic nuclei in three-cluster configurations [13]. They practically

https://doi.org/10.1515/9783110619607-002

do not differ from the underlying principles in the two-cluster option of the MPCM, which was used by us earlier for consideration of some astrophysical aspects of thermonuclear processes in the sun, and stars [12, 14]. Moreover, some reactions of the primordial nucleosynthesis of our universe at the different stages of derivation, formation, and development have been considered in this book.

1.1 Review of the cluster model

Many properties of light atomic nuclei participating in thermonuclear processes have been well described by cluster models, with the potential cluster model being the most widely used model. In particular, the MPCM is based on a unified pair Hamiltonians of interactions in continuous and discrete spectra at coincidence of all quantum numbers of such states, including Young tableaux. The model assumes that the considered nuclei with a high degree of probability have a certain two-cluster structure [11, 22].

1.1.1 Basic principles of the model

MPCM is efficient because in many light atomic nuclei the probability of formation of nucleon clusters and the extent of their isolation is very high. This has been confirmed by numerous experimental data as well as the results of theoretical calculations obtained in the last 50–60 years [21].

We usually use the results of the phase-shift analysis of experimental data obtained from different cross-sections of the elastic scattering of the corresponding free nuclei [22] to determine the semi-phenomenological potentials of the elastic scattering of cluster pairs. Such potentials are constructed using well-described conditions obtained from the data on cross-sections and phase shifts of elastic scattering of nuclear particles. Potentials of the bound state of clusters are constructed, as a rule, on the basis of the description of some characteristics of the ground state (GS) of a nucleus considered in the cluster channel.

However, phase-shift analysis results in a limited energy range, as a rule, do not allow the reconstruction of the interaction potential. Therefore, an additional condition for intercluster potential is the requirement of agreement with the results of classification according to Young tableaux, that is, except the allowed states (AS) if available, ithas to contain a certain number of FSs, as a rule. For determining the potential of the ground or excited states, as well as the bound state in the considered channel, the additional conditions for correctly reproducing the nuclear binding energy in this cluster channel along with descriptions of other static nuclear characteristics have been laid down.

For instance, these characteristics include the charge radius and asymptotic constant (AC); meanwhile, the characteristics of the clusters bound in the nucleus

are usually identical to the characteristics of the corresponding free nuclei [19]. This additional requirement is idealization as it assumes that the BS of nucleus has a 100% clustering. Therefore, the success of the potential cluster model in describing the system from A nucleons in the bound state is determined by the actual clusterization of the ground state of the nucleus in the two-particle channel [19, 21, 28]. However, some nuclear characteristics of separate, and not even cluster nuclei, can be caused mainly by certain cluster channels with small contributions from other possible cluster configurations. In this case, the used single-channel, two-cluster model allows to identify the dominating cluster channel and to determine the main properties of such a nuclear system [19].

The potential cluster model used here is simple as it solves the two-body problem or its equivalent – one body in the field of the center of force. However, such a model does not correspond to the many-body problem, which is a problem in describing the properties of a system consisting of A nucleons. Therefore, it is necessary to note that one of the most successful models in the theory of an atomic nucleus is the shell model (SM), which mathematically represents the problem of movement of a body in the field of a power center. The physical reasons of the potential cluster model considered here relate to the SM, or to be more exact, to the surprising connection between the SM and cluster model, which is often described in the literature as the model of nucleon associations (MNA) [19, 21].

The wave function of the nucleus in the MNA and the PCM consisting of two clusters with nucleons A_1 and A_2 ($A = A_1 + A_2$) has a form of the antisymmetrized product of completely antisymmetric internal wave functions of clusters $\Psi(R_1)$ and $\Psi(R_2)$, which can be multiplied by the wave function of their relative movement $\mathrm{F}(R = R_1 - R_2)$,

$$\Psi = \hat{A}\{\Psi(R_1)\Psi(R_2)\Phi(R)\}, \tag{1.1.1}$$

where $\hat{A}$ is the operator of antisymmetrization, which acts on the relation to shifts of nucleons from different clusters of a nucleus; R is the intercluster distance; R_1 and R_2 are the radius vectors of the location of cluster mass center.

Usually, the cluster wave functions are chosen such that they correspond to the ground states of the free nuclei consisting of A_1 and A_2 nucleons. These wave functions are characterized by specific quantum numbers, including Young tableaux $\{f\}$, which determine the permutable symmetry of the orbital part of the wave function of the relative cluster movement. Moreover, certain conclusions of the cluster model [19, 21] lead to the concept of FSs as per the Pauli principle. Therefore, only some total wave functions of nucleus $\Psi(\mathrm{R})$ with a certain type of relative motion functions Φ (R) approach zero at antisymmetrization on all A nucleons (1.1.1).

The ground, that is, the existing bound state in this potential of the cluster system, is generally described by the wave function with the nonzero number of

nodes. Thus, the idea of the states forbidden by the Pauli principle allows one to consider many-particle character of the problem in terms of two-body interaction potential between clusters [19, 21]. Meanwhile, in practice, the potential of intercluster interaction is choosing in such a way that it must correctly describe the phase shifts of the elastic scattering of clusters obtained from experimental data in the corresponding partial wave and, preferably, in a state with a definite Young tableaux $\{f\}$ for the spatial part of the wave function A of nucleons of nucleus [28].

1.1.2 Model development and main results

Now, we will discuss some main stages of development of the PCM with FS. In the early 1970s [30–32], it was shown that the phase shifts of the elastic scattering of light cluster systems can be described based on the deep pure attracting potentials of the Woods-Saxon typecontaining the bound states forbidden by the Pauli principle. The behavior of scattering phase shifts at zero energy for such interactions follow the generalized Levinson's theorem [30–34]; however, scattering phase shifts vanish at large energies, remaining positive. The radial wave function of the allowed states of potentials with the FS oscillates at small distances, instead of vanishing, as it was for interactions with the core. Such an approach can be considered to be an alternative of the often used conception of the repulsive core. The core is inserted into the potential of interaction of clusters for the qualitative accounting of Pauli principle without apparent antisymmetrization of the wave function.

Furthermore, for example, in some studies [33, 35–42] intercluster central Gaussian potentials of interaction that correctly reproduced phase shifts of the elastic ^{4}He^{2}H scattering at low energies and contained FSs were parameterized. It is shown that, based on these potentials in the cluster model, it is possible to reproduce the main characteristics of bound states of ^{6}Li, whose probability of clusterization in the considered two-body channel is rather high [28]. All cluster states in such system are pure according to the orbital Young tableaux [30–42], and the potentials obtained from the scattering phase shifts can be applied to the description of characteristics in the ground state of this nucleus.

Success of the single-channel model based on such potentials is not only because of the high degree of clusterization of the discussed nuclei but also because in each state of clusters there is only one allowed orbital Young tableau [11, 22], defining the symmetry of this state. Therefore, a certain "unified" description of the continuous and discrete spectrum, as well as the potentials obtained on the basis of the experimental scattering phase shifts are successfully used for describing various characteristics of the GS of Li nuclei.

For lighter cluster systems of $N^{2}H$, $^{2}H^{2}H$, $N^{3}H$, $N^{3}He$, $^{2}H^{3}He$, in scattering states with minimal spin, mixing according to orbital symmetry is possible, making the

situation more complicated. In states with a minimum spin, in the continuous spectrum, two Young tableaux are allowed, while in the bound ground states, only one from these tableaux corresponds [20–22, 43–54]. Therefore, the potentials directly obtained based on experimental scattering phase shifts depend on the various orbital tableaux and cannot be used for describing the characteristics of the ground state of nuclei. It is necessary to extract a pure component from such interactions, which can be applied for analyzing the characteristics of the BSs.

In heavier nuclear systems, such as N^6Li, N^7Li and $^2H^6Li$ [55–59], for certain cases when various states are mixed according to Young tableaux, a similar situation arises. In works mentioned above, the pure interaction potentials for the above-mentioned heavy nuclear systems were obtained, according to the Young tableaux. In general, they describe the scattering characteristics and the properties of the bound states of the respective nuclei correctly.

Despite progress of such an approach, only pure central intercluster interactions have been considered yet. By considering the $^4He^2H$ system within the potential cluster model, the tensor component is not accounted for, which leads to appearance of the D wave in the wave function of BS and scattering, allowing us to consider the quadrupole moment of ^6Li. Here, the tensor operator refer to the interaction of the operator which depends on the relative orientation of the total spin of the system and intercluster distances. The mathematical form of such an operator coincides with the operator of two-nucleon problem; therefore this potential, by analogy, is called a tensor potential [60–62].

The tensor potentials were used for the description of the $^2H^4He$ interaction in the early eighties of the XX century in work [60], when an attempt to include tensor component into optical potential was made. This allowed us to considerably improve the quality of describing the different cross-sections of the elastic scattering and polarization. In [61], based on a "folding" model, the calculations of cross-sections and polarization were carried out, and accounting for the tensor components of the potential allowed us to improve their description. Such an approach was also used in [62], where by a "convolution" of the nucleon-nucleon potentials the $^2H^4He$ interaction with the tensor components was obtained. In principle, it is possible to describe the main characteristics of the bound state of ^6Li correctly, including the correct sign and the order of magnitude of the quadrupole moment.

However, in [60, 61] only processes of scattering of clusters, and in [62] only characteristics of the BS of ^6Li without analysis of the elastic scattering phase shifts were considered. Nevertheless, the Hamiltonian of interaction needs to be unified for the scattering processes and the BS of clusters as well, as it was made in [30–42] in the case of pure central potentials. The high probability of clustering of ^6Li in the $^2H^4He$ channel allows one to hope for the accuracy of such a task in potential cluster model.

Because the GS of ^6Li [20, 30–42, 63–68] is comparable to the orbital tableau {42}, then in the S state should be the FS with the tableau {6}. Similarly, in the D wave, the FS is absent because the tableau {42} is compatible with the orbital moment $L = 2$.

This means that the wave function of the *S* state will have the node and the WF for *D* wave is nodeless. Such classification of the forbidden and allowed states according to Young tableaux, in general, allows one to define a general form of the wave function of BS cluster $^{2}H^{4}He$ system [20, 33].

In [69], within the potential cluster model, unified Hamiltonian $^{2}H^{4}He$ interactions were obtained, that is, unified potential with tensor potential and forbidden to the S wave state. This satisfies all the above-listed conditions and allow the description of the scattering characteristic, that is, nuclear phase shifts, and properties of the bound states of ^{6}Li, including its quadrupole moment [70].

Furthermore, in [71, 72] the concept of the FSs was extended to the singlet nucleon–nucleon (NN) potential, and then to its triplet counterpart [73]. Subsequently, the NN potential of the Gaussian type with tensor component and one pion exchange potential (OPEP) [74] was reported later, following which [75, 76] managed to obtain the parameters of NN potential with a tensor component and FSs, whose wave functions, as predicted earlier, theoretically contained only the *S* wave in the discrete spectrum and the *D* wave was nodeless [77].

Such a potential approach in the NN system [76] could practically describe all characteristics of the deuteron and NN scattering at low and average energies. In addition, the description of high-energy vector and tensor polarizations in $e^{2}H$ scattering in comparison with the known NN interactions of similar type improved significantly [74].

1.1.3 Model representations and the methods

Before describing the calculations methods of nuclear characteristics, we will discuss some general reasons used usually for the solution of certain problems of nuclear physics and nuclear astrophysics. It is known that the nuclear or NN interaction potential of particles in scattering problems or bound states is unknown, *a fortiori*, and it is not possible to define its form directly in any form. Therefore, a certain form of its dependence on distance can be explained (for example, Gaussian or exponential) and according to some nuclear characteristics (usually nuclear scattering phase shifts) based on certain calculation methods (see, for example [78, 79]) its parameters, are fixed so that it can describe these characteristics. Furthermore such potentials can be applied for calculating other nuclear characteristic such as the binding energy of the nuclei and their properties in the bound states or the cross-sections of various reactions, including thermonuclear processes at ultralow energies [12, 24].

When the nuclear interaction potential of two particles is known, all problems discussed above boil down to the solution of the Schrödinger equation or the coupled system of these equations in case of tensor nuclear forces with certain initial and asymptotic conditions. In principle, it is a purely mathematical task of modeling physical processes and systems. However, available methods [80–87] do not always

give a steady numerical scheme. Many of the frequently used algorithms seldom give accurate results, and generally lead to overflow during computer programs.

Therefore, here, we will define the general direction and designate the main numerical methods that provide steady solution schemes for the considered physical problems. For quantum problems, such decisions are based on the Schrödinger equation which allows one to obtain the wave function of the system of nuclear particles with known interaction potentials. It is possible to solve the Schrödinger equations for the bound states and scattering processes, for instance, by the Runge–Kutt (RK) method [88, 89] or the finite-difference method (FDM) [90].

Such methods allow one to easily obtain eigenwave functions and self-energy of quantum system of particles. As in [24], a combination of numerical and variation methods can be used to control the accuracy of the solution of equation or Schrödinger-coupled equations by means of residuals [91]; this makes the procedure of obtaining the final results considerably simpler. Then, on the basis of the obtained solutions, that is, the wave functions of nucleus which are the solutions of initial equations, numerous nuclear characteristics, including, scattering phase shifts and binding energy of atomic nuclei in various channels, are calculated.

Finally, regarding the mathematical solution methods for certain problems of nuclear physics at low and ultralow astrophysical energies chosen by us, we will notice that all physical problems considered boil down to the problems of variation character. In particular, by considering the three-body model [13], for example, of the nuclei ^{7}Li [22, 24, 92], it is very effective to use an alternative mathematical method for determing the eigenvalues of the generalized variation matrix problem considered based on the Schrödinger equation using nonorthogonal variation basis. This method allows to eliminate instabilities that arise at times during numerical implementation of usual computing schemes of the solution of generalized variation problem [24].

In addition, for the phase-shift analysis of the scattering of nuclear particles [13] the new algorithms, proposed by us in [24] were applied, for realizing numerical methods, which are used for finding particular solutions of the general multiple parameter variation problem for functionality of χ^2 . This value determines the accuracy of the description of experimental data, for example, by differential cross-sections based on the chosen theoretical representation, that is, certain functions of several variables.

1.2 Potentials and wave functions

The intercluster potentials of interaction for each partial wave, that is, for the given orbital moment of L, the total moment J of nucleus with total spin S, and with point-like Coulomb term can be expressed as

$$V(r, JLS) = V_0(JLS)\exp\{-\gamma(JLS)r^2\} + V_1(JLS)\exp\{-\delta(JLS)r^2\} \tag{1.2.1}$$

or

$$V(r, JLS) = V_0(JLS)\exp\{-\gamma(JLS)r^2\}. \tag{1.2.2}$$

Here, V_0 and V_1 and γ and δ are potential parameters that can also depend on the Young tableaux $\{f\}$ and are usually determined, for example, for the scattering processes involved in describing the elastic scattering phase shifts extracted during the phase-shift analysis from experimental data on differential cross-sections, i.e., angular distributions or excitation functions.

Coulomb potential at zero Coulomb radius $R_{\text{coul}} = 0$ is expressed as

$$V_{\text{Coul}}(\text{MeV}) = 1.439975 \cdot \frac{Z_1 Z_2}{r}, \tag{1.2.3}$$

where r is the relative distance between the particles of the initial channel in fm, and Z are the charges of the particles in units of the elementary charge as "e".

In certain cases, the Coulomb radius R_{coul} is introduced to the Coulomb potential, and then the Coulomb part of the potential with the dimension of fm^{-2} [93]

$$V_{\text{Coul}}(r) = 2\mu\frac{m_0}{\hbar^2}\begin{cases} \frac{Z_1 Z_2}{r} & r > R_{\text{Coul}} \\ Z_1 Z_2\left(3 - \frac{r^2}{R_{\text{Coul}}^2}\right)/2R_{\text{Coul}} & r < R_{\text{Coul}} \end{cases} \tag{1.2.4}$$

The behavior of the wave function of bound states, including the ground states of nuclei in the cluster channels at large distances is characterized by the asymptotic constant C_{w} [94], which is determined by Whittaker function

$$\chi_{\text{L}}(r) = \sqrt{2k_0}C_{\text{W}}W_{-\eta\text{L}+1/2}(2k_0 r), \tag{1.2.5}$$

where $\chi_L(r)$ is the numerical wave function of the bound state obtained from the solution of the radial Schrödinger equation normalized to unity, $W_{-\eta L+1/2}$ is the Whittaker function of the bound state defining the asymptotic behavior of the wave function and is the solution of the same equation without nuclear potential, i.e., at large distances of R, k_0 is the wave number due to the channel binding energy, η is the Coulomb parameter determined further, and L is the orbital moment of the bound state. Here, it must be kept in mind that numerical wave functions and AC are functions of all moments of JLS as the nuclear interaction potential depends on them, as shown in (1.2.1) or (1.2.2).

The asymptotic constant (or the asymptotic normalizing coefficient of A_{NC} connected with AC) is an important nuclear characteristic defining behavior of "tail," i.e., an asymptotics of the wave function at long distances. In many cases, its knowledge for A nucleus in the cluster channel $A_1 + A_2$ defines the value of the astrophysical S-factor for the radiative capture of $A_1(A_2, \gamma)A$ [95]. The asymptotic constant is

proportional to a nuclear vertex constant for the virtual process of $A \to A_1 + A_2$, which is a matrix element of this process on a mass surface [96].

The numerical wave $\chi_L(r)$ function of the relative movement of two clusters is the solution of the radial Schrödinger equation in the form

$$\chi''_L(r) + [k^2 - V_n(r) - V_{coul}(r) - L(L+1)/r^2]\chi_L(r) = 0, \tag{1.2.6}$$

where r is the scalar relative distance between particles in fm, $V_{coul}(r) = 2\mu/\hbar^2 Z_1 Z_2/r$ is the Coulomb potential specified to dimension of fm^{-2} , Z_1 and Z_2 are the charges of particles in terms of an elementary charge, $k^2 = 2\mu E/\hbar^2$ is the wave number of the relative movement of particles in fm^{-2}, E is energy of particles, $\mu = m_1 m_2/(m_1+m_2)$ is the reduced mass of two particles, m_i is the mass of each particles, $V_n(r)$ is the nuclear potential which is equal to $2\mu/\hbar^2 V(r,JLS)$, $V(r,JLS)$ is the radial dependence of the potential which is often accepted in the form of (1.2.1) or (1.2.2), a constant $\hbar^2/m_0$ is equal to 41.4686 MeV fm^2, m_0 is the atomic mass unit (amu). Though this value is considered a little outdated today, we continue to use it for simplified comparison of the last and all earlier obtained results (see, e.g., [12, 19, 23] and [22, 24]).

In the phase-shift analysis and three-body calculations [13], the integer values of particle masses were usually specified, and the Coulomb parameter was presented as

$$\eta = 3.44476 \cdot 10^{-2} \frac{\mu Z_1 Z_2}{k},$$

where k is the wave number $k = \sqrt{2\mu E/\hbar^2}$ dimensioned in fm^{-1}, μ is the reduced mass of the nucleus, Z are charges of particles in units of an elementary charge "e".

The asymptotics of the scattering wave function $\chi_L(r)$ at long distances of $R \to \infty$, i.e., at $V_n(r \to R) = 0$ is the solution of equation (1.2.6) and can be presented as follows

$$\chi_{JLS}(r \to R) \to F_L(kr) + \mathrm{tg}(\delta^J_{S,L}) G_L(kr)$$

or

$$\chi_{JLS}(r \to R) \to \cos(\delta^J_{S,L}) F_L(kr) + \sin(\delta^J_{S,L}) G_L(kr),$$

where F_L and G_L are wave Coulomb functions of scattering [97, 98] which are the partial solutions of equation (1.2.6) without nuclear potential, i.e., when $V_n(r) = 0$.

Joining the numerical solution $\chi(r)$ of equation (1.2.6) at large distances (R tending towards 10–20 fm) with this asymptotics, it is possible to calculate the scattering phase shifts of $\delta^J_{S,L}$ for each value of moments J,L,S at the given energy of the interacting particles. Scattering phase shifts in the concrete system of nuclear particles can be determined from the phase-shift analysis of the experimental data using their elastic scattering [13]. Furthermore, the variation of parameters of nuclear potential in advance defined form in the equation (1.2.6) is carried out, and its parameters that the describe results of the phase-shift analysis are determined. Thus, the description of the scattering processes of nuclear particles involves the

search of parameters of nuclear potential, which describe the results of the phase-shift analysis, as well as the experimental data on scattering sections.

It is possible to take into account the spin-orbital interaction in the nuclear potential, and then the potential can be expressed as [90]

$$V_{\mathrm{n}}(r) = 2\mu/\hbar^2[V_{\mathrm{c}}(r) + V_{\mathrm{sl}}(r)],$$

$$V_{\mathrm{sl}}(r) = -(\mathbf{sl})V_{0\mathrm{sl}}\,F(r),$$

where $F(r)$ is the radial dependence of the spin-orbital potential of the relative distance r between particles, which can also be expressed as a Gaussian function (1.2.2), V_{c} is the central part of the nuclear potential, for example, in the form (1.2.2), V_{sl} is its spin-orbital part, and $V_{0\mathrm{sl}}$ is the depth of the spin-orbital part.

The (**sl**) value is a spin-orbit operator and its values can be found from the well-known expression [90]

$$(\mathbf{sl})\chi(r) = 1/2\ [J(J+1) - L(L+1) - S(S+1)]\chi(r),$$

where J is the total moment of the system, L is the orbital moment, and S is the spin of the system of particles. For accounting the spin-orbital interaction, the Schrödinger equation is divided to the system of the unbounded equations, each of which allows one to find the wave function for the given total moment of system of particles at the known moments of JLS.

1.3 Methods of the phase-shift analysis

Knowing the experimental differential sections of the elastic scattering, it is possible to determine a set of parameters called scattering phase shifts $\delta^J{}_{S,L}$, which allow us to describe the behavior of these cross-sections with certain accuracy. Quality of the description of experimental data based on certain theoretical functions (functionality of several variables) can be estimated by the χ^2 method which can be expressed as [93]

$$\chi^2 = \frac{1}{N}\sum_{\mathrm{i}=1}^{\mathrm{N}}\left[\frac{\sigma_{\mathrm{i}}^{\mathrm{t}}(\theta) - \sigma_{\mathrm{i}}^{\mathrm{e}}(\theta)}{\Delta\sigma_{\mathrm{i}}^{\mathrm{e}}(\theta)}\right]^2 = \frac{1}{N}\sum_{\mathrm{i}=1}^{\mathrm{N}}\chi_{\mathrm{i}}^2, \tag{1.3.1}$$

where σ^{e} and σ^{t} are experimental and theoretical, i.e., calculated at certain given values of phase shifts $\delta^J{}_{S,L}$, cross-section of the elastic scattering of nuclear particles for i scattering angle, $\Delta\sigma^{\mathrm{e}}$ is an an error of experimental cross-sections for this angle, and N is the number of experimental measurements.

The expressions describing the differential sections are the expansion of certain functional in a numerical series [13, 93], which makes it necessary to find such a variation of parameters of the expansion which can best describe its behavior. Because expressions for differential cross-sections usually are exact [13, 93], so at

increase in members of the expansion by the orbital moment of L ad infinitum the χ^2 value has to trend to zero. This criterion was used for a choice of the certain set of phase shifts leading to a minimum of χ^2 which could apply for a role of a global minimum of this multivariate variation problem [13, 99]. In detail, the methods and criteria of the phase-shift analysis used in these calculations are given in works [13, 24, 99].

In the simplest case applicable for the phase-shift analysis of the elastic scattering in the ^{4}He^{12}C system which is considered in work [13], expression for differential cross-section has the following form [93]

$$\frac{d\sigma(\theta)}{d\Omega} = \left|f_{\text{coul}}(\theta) + f_{\text{n}}(\theta)\right|^2, \tag{1.3.2}$$

where the cross-section is presented in the form of the sum of Coulomb f_{coul} and nuclear f_{n} of amplitudes, which are expressed through nuclear $\delta_L \to \delta_L + \text{i}\Delta_L$ and Coulomb σ_{L} scattering phase shifts.

$$f_{\text{coul}}(\theta) = -\left(\frac{\eta}{2k \cdot \sin^2(\theta/2)}\right) \exp\left\{i\eta \ln[\sin^{-2}(\theta/2)] + 2i\sigma_0\right\}, \tag{1.3.3}$$

$$f_{\text{n}}(\theta) = \frac{1}{2ik}\sum_{\text{L}}(2L+1)\exp(2i\sigma_{\text{L}})[S_{\text{L}} - 1]P_{\text{L}}(\cos\theta).$$

Here, $S_{\text{L}}(k) = \eta_{\text{L}}(k)\exp[2\text{i}\delta_{\text{L}}(k)]$ is a scattering matrix, and $\eta_{\text{L}}(k) = \exp[-2\Delta_{\text{L}}(\text{k})]$ is the inelasticity parameter depending on imaginary part of the nuclear phase shift $Im\delta_{\text{L}} = \Delta_{\text{L}}(k)$.

Thus, for search of the scattering phase shifts using experimental cross-sections, the minimization procedure of functionality of χ^2 (1.3.1) as functions of a certain number of variables, each of which is a phase shift $\delta^J_{S,L}$ in the partial wave was carried out. For the solution of this task, the χ^2 minimum in certain limited area of values of these variables is searched. However, it is possible to find a set of local minima of χ^2 with the value of the order of unity or less. The choice of the smallest of them allows one to hope that it will correspond to a global minimum which is the solution of such variation task.

The stated criteria and methods were used by us for implementation of the phase shift analysis for n^3He, p^6Li, p^{12}C, n^{12}C, p^{13}C, p^{14}C, n^{16}O, p^{16}O, ^{4}He^{4}He and ^{4}He^{12}C scattering at low energies which are important for the majority of astrophysical problems [13]. All expressions for the calculation of differential cross sections of the elastic scattering of particles with different spin which are required for implementation of the phase analysis in the systems stated above are given in the corresponding paragraphs of work [13]. Furthermore, in this book in Section 2.8 results of the phase shift analysis of the elastic scattering of neutron on ^{16}O at low and astrophysical energies will be considered.

1.4 Certain numerical methods

Finite difference methods which are modification of methods [90], and contain the accounting of Coulomb interactions, variation methods (VM) of solution of the Schrödinger equation and other computing methods used in these calculations of nuclear characteristics, in detail are described in [24]. Therefore, here we will only list in brief the basic moments connected with numerical methods of computer calculations.

In all calculations obtained by finite-difference and variation methods [24], at the end of stabilization range of an asymptotic constant, i.e., approximately on 10–20 fm, numerical or variation wave function was replaced by Whittaker's function (1.2.5), accounting for found earlier asymptotic constant. Numerical integration in any matrix elements was carried out on an interval from 0 to 25–30 fm. Meanwhile, the Simpson method [81] yields good results for smooth and poor oscillating functions at the giving of several hundred steps for the period [24] was used. The wave function at the low and ultralow energies considered here are meet the specified requirements.

For real calculations our computer programs based on a FDM were rewritten and modified [24], for calculating total cross-sections of the radiative capture and characteristics of the bound states of the nucleus from the TurboBasic to the modern version of the Fortran-90, which has much more opportunities. It allowed one to increase the speed and accuracy of all calculations, including binding energy of a nucleus in the two-body channel significantly.

The accuracy of calculation of Coulomb wave functions for scattering processes is controlled by the Wronskian value, as well as the accuracy of searching the root of determinant in the FDM [24]. The accuracy of searching the binding energy of levels is determined as 10^{-15}–10^{-20}. The real absolute accuracy of determining the binding energy in a finite-difference method for different two-body systems is in the range of 10^{-6}~10^{-9} MeV.

For variation calculations, the program was rewritten in Fortran-90 and was slightly modified for determining the variation of the wave function and binding energy of the nucleus in cluster channels. This allowed us to increase the search speed of a minimum of multiple parameters, which significantly determined the binding energy of two-body systems in all considered nuclei [24]. The modified program still uses a multivariable parameter variation method with the expansion of the wave function according to the nonorthogonal variation Gaussian basis with an independent variation of parameters and is presented in the Appendix of this book. The similar variation programs based on multiparameter variation method and for performing phase-shift analysis of different cross-sections for elastic scattering of nuclear particles with different spins [13] are modified and re-written in Fortran-90 language.

For calculating Coulomb scattering functions, the fast converging representation in the form of chain fractions is used [100], allowing to obtain their values with a fine precision for a wide range of variables and using less computing time [101]. Wave

scattering Coulomb functions have two components – regular $F_{\mathrm{L}}(\eta,\rho)$ and irregular $G_{\mathrm{L}}(\eta,\rho)$ – which are linearly independent solutions of the radial Schrödinger equation with the Coulomb potential for scattering processes [102]

$$\chi''_{L}(\rho) + \left(1 - \frac{2\eta}{\rho} - \frac{L(L+1)}{\rho^2}\right)\chi_{\mathrm{L}}(\rho) = 0,$$

where $\chi_{\mathrm{L}} = F_{\mathrm{L}}(\eta,\rho)$ or $G_{\mathrm{L}}(\eta,\rho), \rho = kr$, η is the Coulomb parameter determined above, and k is the wave number determined by energy of particles E. Wronskians of these Coulomb functions can be expressed as [103]

$$\begin{aligned} W_1 &= F'_L G_L - F_L G'_L = 1, \\ W_2 &= F_{L-1} G_L - F_L G_{L-1} = \frac{L}{\sqrt{\eta^2 + L^2}}. \end{aligned} \tag{1.4.1}$$

Recurrence relations between them are represented as

$$L[(L+1)^2 + \eta^2]^{1/2} u_{L+1} = (2L+1)\left[\eta + \frac{L(L+1)}{\rho}\right] u_L - (L+1)[L^2 + \eta^2]^{1/2} u_{L-1}, \tag{1.4.2}$$

$$(L+1)u_{\mathrm{L}}' = \left[\frac{(L+1)^2}{\rho} + \eta\right] u_{\mathrm{L}} - [(L+1)^2 + \eta^2]^{1/2} u_{\mathrm{L}+1},$$

$$L u_{\mathrm{L}}' = [L^2 + \eta^2]^{1/2} u_{\mathrm{L}-1} - \left[\frac{L^2}{\rho} + \eta\right] u_{\mathrm{L}},$$

where $u_{\mathrm{L}} = F_{\mathrm{L}}(\eta,\rho)$ or $G_{\mathrm{L}}(\eta,\rho)$.

The asymptotics of such functions at $\rho \to \infty$ can be represented as [104]

$$\begin{aligned} F_{\mathrm{L}} &= \sin(\rho - \eta \ln 2\rho - \pi L/2 + \sigma_{\mathrm{L}}), \\ G_{\mathrm{L}} &= \cos(\rho - \eta \ln 2\rho - \pi L/2 + \sigma_{\mathrm{L}}). \end{aligned}$$

There are many methods and approximations for calculating Coulomb wave functions of scattering [105–111] that have been used since the 20th century. However, only in the 1970s, rapidly converging performance allowed us to obtain values with high accuracy over a wide range of variables and using less time on computers [100, 101].

Coulomb functions in such methods are presented in the form of continued fractions [112]

$$f_{\mathrm{L}} = F'_{\mathrm{L}}/F_{\mathrm{L}} = b_0 + \frac{a_1}{b_1 + \frac{a_2}{b_2 + \frac{a_3}{b_3 + \ldots}}}, \tag{1.4.3}$$

where

$$b_0 = (L+1)/\rho + \eta/(L+1),$$

$$b_n = [2(L+n)+1][(L+n)(L+n+1)+\eta\rho],$$

$$a_1 = -\rho[(L+1)^2+\eta^2](L+2)/(L+1),$$

$$a_n = -\rho^2[(L+n)^2+\eta^2]\left[(L+n)^2-1\right]$$

and

$$P_L + iQ_L = \frac{G_L^{'} + iF_L^{'}}{G_L + iF_L} = \frac{i}{\rho}\left(b_0 + \frac{a_1}{b_1 + \frac{a_2}{b_2 + \frac{a_3}{b_3 + \ldots.}}}\right),$$

where

$$b_0 = \rho - \eta,\ b_n = 2(b_0 + in),$$

$$a_n = -\eta^2 + n(n-1) - L(L+1) - i\eta(2n-1).$$

Using these expressions, it is possible to determine the relationship between Coulomb functions and their derivatives [113]

$$F_L^{'} = f_L F_L, \quad G_L = (F_L^{'} - P_L F_L)/Q_L = (f_L - P_L)F_L/Q_L, \tag{1.4.4}$$

$$G_L^{'} = P_L G_L - Q_L F_L = [P_L(f_L - P_L)/Q_L - Q_L]F_L.$$

Such a method of calculation can be used in the region

$$\rho \geq \eta + \sqrt{\eta^2 + L(L+1)},$$

i.e., for $L = 0$, we have $\rho > 2\eta$, which allows to obtain high accuracy as a result of fast convergence of continued fractions. As the Coulomb η parameter usually has unit order size, and the orbital moment of L can always be equal to zero, the method yields good results at $\rho > 2$. Values of Coulomb functions for any $L > 0$ can always be obtained using recurrence relations (1.4.2).

Thus, setting an F_L value at ρ point, we can determine all other functions and their derivatives within a constant multiplier defined from Wronskians (1.4.1). Calculations of Coulomb functions using the given formulas and their comparison with the tabular material [103] shows that it is possible to obtain 8–9 correct signs at calculations with a double accuracy easily if ρ meets the condition given above.

The text of the computer program for calculating Coulomb scattering wave functions is given below. The program is written using the algorithmic language Basic for the compiler TurboBasic, Borland [114]. The following notations are accepted:

G – Coulomb parameter η,

L – the orbital angular momentum of the partial wave,

X – distance from the center on which Coulomb functions are calculated,

FF and GG – Coulomb functions,

FP and GP – their derivatives,
W – Wronskian determining the accuracy of calculation of Coulomb functions, the first formula in expression (1.4.1).

```
SUB CULFUN(G,X,L,FF,GG,FP,GP,W)
REM ***** THE PROGRAM FOR CALCULATION OF THE COULOMB FUNCTIONS *****
Q=G: R=X: GK=Q*Q: GR=Q*R: RK=R*R: K=1: F0=1
B01=(L+1)/R+Q/(L+1)
BK=(2*L+3)*((L+1)*(L+2)+GR)
AK=-R*((L+1)^2+GK)/(L+1)*(L+2)
DK=1/BK: DEHK=AK*DK: S=B01+DEHK
1 K=K+1
AK=-RK*((L+K)^2-1)*((L+K)^2+GK)
BK=(2*L+2*K+1)*((L+K)*(L+K+1)+GR)
DK=1/(DK*AK+BK)
IF DK>0 GOTO 3
2 F0=-F0
3 DEHK=(BK*DK-1)*DEHK: S=S+DEHK
IF (ABS(DEHK)-1E-10)>0 GOTO 1
FL=S: K=1: RMG=R-Q
LL=L*(L+1): CK=-GK - LL
DK=Q: GKK=2*RMG
HK=2: AA1=GKK*GKK+HK*HK
PBK=GKK/AA1: RBK=-HK/AA1
OMEK=CK*PBK-DK*RBK
EPSK=CK*RBK+DK*PBK
PB=RMG+OMEK: QB=EPSK
4 K=K+1
CK=-GK-LL+K*(K-1): DK=Q*(2*K-1)
HK=2*K: FI=CK*PBK-DK*RBK+GKK
PSI=PBK*DK+RBK*CK+HK
AA2=FI*FI+PSI*PSI
PBK=FI/AA2: RBK=-PSI/AA2
VK=GKK*PBK-HK*RBK
WK=GKK*RBK+HK*PBK
OM=OMEK: EPK=EPSK
OMEK=VK*OM-WK*EPK-OM
EPSK=VK*EPK+WK*OM-EPK
PB=PB+OMEK: QB=QB+EPSK
IF (ABS(OMEK)+ABS(EPSK)-1E-10)>0 GOTO 4
PL=-QB/R: QL=PB/R: G0=(FL-PL)*F0/QL
G0P=(PL*(FL-PL)/QL-QL)*F0: F0P=FL*F0
ALFA=1/(SQR(ABS(F0P*G0-F0*G0P)))
GG=ALFA*G0: GP=ALFA*G0P: FF=ALFA*F0
FP=ALFA*F0P: W=1-FP*GG+FF*GP
END SUB
```

Results of the control calculation of Coulomb functions for $\eta = 1$ [115, 116] and their comparison with tabular data [103] are given in Table 1.1. One can see that at $\eta = 1$ and $L = 0$ the correct results are already obtained for $\rho = 1$. The value of the Wronskian (1.4.1) presented in the form by W_1–1 at any ρ doesn't exceed 10^{-15}–10^{-16}.

Table 1.1: Coulomb functions.

ρ	F_0 (Our calculation)	F_0 [103]	$F_{0'}$ (Our calculation)	$F_{0'}$ [103]
1	0.22752621	0.22753	0.34873442	0.34873
5	0.68493741	0.68494	−0.72364239	−0.72364
10	0.47756082	0.47756	0.84114311	0.84114
15	−0.97878958	−0.97879	0.31950815	0.31951
20	−0.32922554	−0.32923	−0.92214689	−0.92215

ρ	G_0	G_0 [103]	$G_{0'}$	$G_{0'}$ [103]
1	2.0430972	2.0431	−1.2635981	−1.2636
5	−0.89841436	−0.89841	−0.51080476	−0.51080
10	0.94287424	0.94287	−0.43325965	−0.43326
15	0.34046374	0.34046	0.91053182	0.91053
20	−0.97242840	−0.97243	0.31370038	0.31370

For example, at $L = 2$, it is easy to carry out function's calculations on recurrent formulas (1.4.2). Knowing functions and their derivatives at $L = 0$, we can find functions at $L = 1$ using the second formula, and then using the third formula, we can find their derivatives for $L = 1$. By using this process, it is easy to find all functions and their derivatives at any L [113].

Now we will provide the text of the same computer program used for the calculation of Coulomb scattering wave functions using Fortran-90. Designation of parameters is consistent with the previous program. Here, on the basis of (1.4.3–1.4.4) the functions are defined only at $L = 0$, and for finding functions at all other L, recurrence relations are used. For ensuring the maximum possible accuracy, as in the previous case, double accuracy mode is used. The following designations are considered:

Q – Coulomb parameter η,
LM – the orbital angular momentum of the partial wave,
R – distance from the center on which Coulomb functions are calculated,
F and G – Coulomb functions,
FP and GP – their derivatives for LM = 0,
W – Wronskian determining the accuracy of the calculation of Coulomb functions, i.e., the first formula in expression (1.4.1).

```
SUBROUTINE CULFUN(LM,R,Q,F,G,FP,GP,W)
IMPLICIT REAL(8) (A-Z)
INTEGER L,K,LL,LM
EP=1.0D-015
L=0
F0=1.0D-000
GK=Q*Q
GR=Q*R
RK=R*R
B01=(L+1)/R+Q/(L+1)
K=1
BK=(2*L+3)*((L+1)*(L+2)+GR)
AK=-R*((L+1)**2+GK)/(L+1)*(L+2)
DK=1.0D-000/BK
DEHK=AK*DK
S=B01+DEHK
15 K=K+1
AK=-RK*((L+K)**2-1.D-000)*((L+K)**2+GK)
BK=(2*L+2*K+1)*((L+K)*(L+K+1)+GR)
DK=1.D-000/(DK*AK+BK)
IF (DK>0.0D-000) GOTO 35
25 F0=-F0
35 DEHK=(BK*DK-1.0D-000)*DEHK
S=S+DEHK
IF (ABS(DEHK)>EP) GOTO 15
FL=S
K=1
RMG=R-Q
LL=L*(L+1)
CK=-GK-LL
DK=Q
GKK=2.0D-000*RMG
HK=2.0D-000
AA1=GKK*GKK+HK*HK
PBK=GKK/AA1
RBK=-HK/AA1
AOMEK=CK*PBK-DK*RBK
EPSK=CK*RBK+DK*PBK
PB=RMG+AOMEK
QB=EPSK
52 K=K+1
CK=-GK-LL+K*(K-1.)
DK=Q*(2.*K-1.)
HK=2.*K
FI=CK*PBK-DK*RBK+GKK
PSI=PBK*DK+RBK*CK+HK
AA2=FI*FI+PSI*PSI
PBK=FI/AA2
```

```
RBK=-PSI/AA2
VK=GKK*PBK-HK*RBK
WK=GKK*RBK+HK*PBK
OM=AOMEK
EPK=EPSK
AOMEK=VK*OM-WK*EPK-OM
EPSK=VK*EPK+WK*OM-EPK
PB=PB+AOMEK
QB=QB+EPSK
IF (( ABS(AOMEK)+ABS(EPSK))>EP) GOTO 52
PL=-QB/R
QL=PB/R
G0=(FL-PL)*F0/QL
G0P=(PL*(FL-PL)/QL-QL)*F0
F0P=FL*F0
ALFA=1.0D-000/( (ABS(F0P*G0-F0*G0P))**0.5)
G=ALFA*G0
GP=ALFA*G0P
F=ALFA*F0
FP=ALFA*F0P
W=1.0D-000-FP*G0+F0*GP
IF (LM==0) GOTO 123
AA=(1.0D-000+Q**2)**0.5
BB=1.0D-000/R+Q
F1=(BB*F-FP)/AA
G1=(BB*G-GP)/AA
WW1=F*G1-F1*G-1.0D-000/(Q**2+1.0D-000)**0.5
IF (LM==1) GOTO 234
DO L=1,LM-1
AA=((L+1)**2+Q**2)**0.5
BB=(L+1)**2/R+Q
CC=(2*L+1)*(Q+L*(L+1)/R)
DD=(L+1)*(L**2+Q**2)**0.5
F2=(CC*F1-DD*F)/L/AA
G2=(CC*G1-DD*G)/L/AA
WW2=F1*G2-F2*G1-(L+1)/(Q**2+(L+1)**2)**0.5
F=F1; G=G1; F1=F2; G1=G2
ENDDO
234 F=F1; G=G1
!PRINT *,'F = ',F,G,R,Q,W,WW1,WW2
123 CONTINUE
END
```

This program gives the same results as the control calculation with the same accuracy, as a previous program written in Turbo Basic language.

Other functions used by us, is Whittaker's function, which is the solution of the Schrödinger equation with Coulomb interaction for bound states [103]

$$\frac{d^2W(\mu,\nu,z)}{dz^2} - \left(\frac{1}{4} - \frac{\nu}{z} - \frac{1/4-\mu^2}{z^2}\right)W(\mu,\nu,z) = 0.$$

This equation can be expressed as standard type of the Schrödinger equation

$$\frac{d^2\chi(k,L,r)}{dr^2} - \left(k^2 + \frac{g}{r} + \frac{L(L+1)}{r^2}\right)\chi(k,L,r) = 0,$$

where $g = \frac{2\mu Z_1 Z_2}{\hbar^2} = 2k\eta$, $\eta = \frac{\mu Z_1 Z_2 e^2}{\hbar^2 k}$ is the Coulomb parameter, approximate expression for which is given in §1.2, $z = 2kr$, $\nu = -\frac{g}{2k} = -\eta$ and $\mu = L+1/2$, and k is the wave number of interacting particles.

For determining the numerical values of Whittaker's function, its integrated representation is often used, which has the following form

$$W(\mu,\nu,z) = \frac{z^\nu e^{-z/2}}{\Gamma(1/2-\nu+\mu)}\int t^{\mu-\nu-1/2}(1+t/z)^{\mu+\nu-1/2}e^{-t}dt.$$

This can also be presented as

$$W_{-\eta L+1/2}(z) = W(L+1/2,\,-\eta,z) = \frac{z^{-\eta}e^{-z/2}}{\Gamma(\mathrm{L}+\eta+1)}\int t^{\mathrm{L}+\eta}(1+t/z)^{\mathrm{L}-\eta}e^{-t}dt$$

It is easy to see that at $L = 1$ and $\eta = 1$, the provided integral becomes $\Gamma(3)$, which is reduced with a denominator to a simple expression as

$$W_{-1,1+1/2}(z) = W(1+1/2,\,-1,z) = \frac{e^{-z/2}}{z}.$$

Such a record can be used for controlling the correctness of the Whittaker's function at any value z for $L = 1$, $\eta = 1$, and $z = 2kr$. The questions connected with the calculation of these two functions are detailed in [24] and the Appendix of [12].

1.5 The generalized matrix problem on eigenvalues

For considering the generalized matrix problem on eigenvalues and functions obtained after expanding wave functions on nonorthogonal Gaussian basis, we proceed from the standard Schrödinger equation in a general form [117]

$$H\chi = E\chi,$$

where H is a Hamiltonian of particles system, E is the energy of system, and χ are wave functions.

Separating the wave function on some generally nonorthogonal variation basis [63]

$$\chi = \sum_{\mathrm{i}} C_{\mathrm{i}} \varphi_{\mathrm{i}},$$

and substituting them in the initial system, followed by multiplication on the left by the imaginary conjugated basic function φ_i^* and integrating on all variables, we obtain the known matrix system as [91]

$$(H - EL)C = 0. \tag{1.5.1}$$

This is the generalized matrix problem for finding eigenvalues and eigenfunctions [118–120]. If the expansion of the wave function is carried out on an orthogonal basis, the matrix of overlapping integrals of L turns into a unitary matrix of I, and we have a standard problem on eigenvalues for which several solutions have been proposed [121].

For the solution of the generalized matrix problem, some methods have been described [120]. Let us first consider the standard method for solving the generalized matrix problem for the Schrödinger equation which arises while using non-orthogonal variation in nuclear physics or nuclear astrophysics. Then, we will consider its modification or an alternative method that is convenient to use in numerical calculations on modern computers [24].

Hence, to determine the spectrum of the eigenvalues of energy and eigenwave functions in the variation method while expanding the WF on the nonorthogonal Gaussian basis [63–65], the generalized matrix problem on eigenvalues is solved as [120]

$$\sum_{\mathrm{i}} (H_{\mathrm{ij}} - E\,L_{\mathrm{ij}}) C_{\mathrm{i}} = 0, \tag{1.5.2}$$

where H is a symmetric matrix of a Hamiltonian, L is a matrix of overlapping integrals, E is the eigenvalues of energy, and C is the eigenvectors of the problem.

Representing a matrix of L in the form of multiplication of the low N and the top V triangular matrixes [120], after simple transformation, we come to a usual problem to eigenvalues

$$H'C' = EIC' \tag{1.5.3}$$

or

$$(H' - EI)C' = 0,$$

where

$$H' = N^{-1} H V^{-1}, \qquad C' = VC,$$

and V^{-1} and N^{-1} are inverse matrices with respect to V and N matrices, respectively.

Furthermore, we can find the matrices of N and V by the triangularization of a symmetric matrix of L [121], for example, using the Haletsky method [120]. Subsequently,

we define the inverse matrices of N^{-1} and V^{-1}, for example, by the Gaussian method and calculate matrix elements $H' = N^{-1}HV^{-1}$. Further, we find the full diagonal using the E matrix $(H' - EI)$ and calculate its determinant of det $(H' - EI)$ at some energy of E.

Energy which leads to a zero determinant is the eigenenergy of a problem, and the corresponding vector of C' are the eigenvector of equation (1.5.3). Knowing C', the eigenvector of an initial problem of C can be described (1.5.1), as the matrix of V^{-1} is already known. The described method of generalized matrix problem to a usual matrix problem on eigenvalues and eigenfunctions is the method of orthogonalization, according to Schmidt [122].

However, in some tasks for certain parameter values, the procedure of finding the inverse matrices is unstable and during the work of the computer program overflow is given. For example, in the two-body problems for light nuclei with one variation parameter α_i in the variation wave function such a method is rather steady and gives reliable results. However, in the three-body nuclear system when the variation wave function is presented in the form [63, 65]

$$\Phi_{1,\lambda}(r,R) = Nr^{\lambda}R^{1}\sum_{i} C_i \exp(-\alpha_i r^2 - \beta_i R^2) = N\sum_{i} C_i \Phi_i, \tag{1.5.4}$$

at some values of α_i and β_i parameters, the method of finding the inverse matrices often results in instability and overflow during a computer program [13, 123], representing a certain question for the solution of such problems.

Here, the expression

$$\Phi_i = r^{\lambda}R^{1}\exp(-\alpha_i r^2 - \beta_i R^2)$$

is called a basic function.

Now we consider an alternative method of the numerical solution of the generalized matrix problem on eigenvalues, free from the specified questions and can be run smoothly on a computer program. The initial matrix equation (1.5.1) or (1.5.2) is a homogeneous system of linear equations, that is, it has a nontrivial solution only if its determinant det $(H - EL)$ is zero. For numerical methods realized on a computer, it is not necessary to expand a matrix of L to triangular matrices and find a new matrix of H' and new vectors of C', determining the inverse matrices, as described above using a standard method of orthogonalization proposed by Schmidt.

It is possible to expand nondiagonal but symmetric matrix $(H - EL)$ on the triangular matrices by using numerical methods in a predetermined range to look for energies leading to a zero determinant, that is, eigenenergies. Usually eigenvalues and eigenfunctions are not required in real physical problems. It is necessary to find only 1–2 eigenvalues for a certain energy of a system and, as a rule, it is their lowest values and eigenwave functions corresponding the energy level.

Therefore, for example, using the Haletsky method, the initial matrix $(H - EL)$ expands into two triangular matrices; meanwhile, in the main diagonal of the top triangular matrix of V there are units

$$A = H - EL = NV$$

and its determinant is calculated using the condition $\det(V) = 1$ [120]

$$D(E) = \det(A) = \det(N) \cdot \det(V) = \det(N) = \prod_{i=1}^{m} n_{ii}$$

on zero of which the necessary eigenvalue E, that is, the value of energy of system is looked for. Here m is the dimension of matrices, and a determinant of a triangular matrix N is equal to the multiplication of its diagonal elements [120].

Thus, we have a simple problem of searching zero functional of one variable

$$D(E) = 0,$$

numerical solution of which is not complex and can be determined with sufficient accuracy, for example, using the bisection method [91].

Consequently, we can eliminate the need to look for inverse to V and N matrices, as well as the need to perform matrix multiplications for obtaining new matrix H', and finally, the matrix of eigenvectors of C. Lack of such operations, especially in the search of inverse matrices, considerably increases the computer's computing ability, irrespective of the programming language used [78].

To estimate the accuracy of the solution, that is, the accuracy of the expansion of the initial matrix A into two triangular matrices, the concept of residuals is used [120]. After expanding the matrix A on the triangular matrix, the residual matrix of A_n [120] is calculated as a difference of the initial matrix of A and the matrix

$$S = NV,$$

where N and V are the numerical triangular matrices. Now, the difference on all elements with an initial matrix of A is computed as

$$A_n = S - A.$$

The residual matrix A_n gives a deviation of the approximate value NV, determined by the numerical methods, from the true value of each element of an initial matrix A. It is possible to summate all elements of a matrix A_n and obtain the numerical value of the residual. In all the calculations presented in this book, the method described here was used; the maximum value of any element of a matrix A_n usually does not exceed 10^{-10} at the maximum dimension of an initial matrix of m = 10–12. Such a dimension is usually enough for the accurate search of own binding energy of system of approximately 10^{-6} MeV when using an independent variation of parameters of the expansion of the wave funtion in (1.5.4), both in two- [12, 14] and three-body problems [13].

This method when used for numerical execution allows one to obtain good stability of algorithm of the solution of considered problems and does not lead to overflow during computer programming [124]. Thus, the alternative method of finding eigenvalues of the generalized matrix problem [24] described here, considered on the basis of variation methods of the solution of the Schrödinger equation with the use of nonorthogonal variation basis, relieves us of the instabilities arising together with the application of usual methods of the solution of such mathematical problems, that is, theorthogonalization method.

After determining eigenvalues (as mentioned above this is the first or the second eigenvalue with the minimum value), we solve the known system of the equations for eigenvectors of X, which has the form

$$AX = NVX = (H - EL)X = 0.$$

Such system of linear equations relative to n of unknown variables X can be solved at E, which is equal to the eigenvalue. Equality to zero of its determinant implies linear dependence of one of the equations, that is, its rank R is less than the order of the system n. We assume that the last n-th equation is linearly dependent, and thus we obtain the system of (n – 1) equations with n unknown quantities [125].

$$a_{11}x_1 + a_{12}x_2 + a_{13}x_3 \ldots\ldots + a_{1n}x_n = 0$$

$$a_{21}x_1 + a_{22}x_2 + a_{23}x_3 + \ldots\ldots + a_{2n}x_n = 0$$

$$\ldots\ldots\ldots\ldots\ldots\ldots\ldots\ldots\ldots\ldots\ldots\ldots\ldots\ldots$$

$$a_{n-11}x_1 + a_{n-12}x_2 + a_{n-13}x_3 + \ldots\ldots + a_{n-1n}x_n = 0.$$

Assuming that $X_n = 1$, we obtain the system of $(n - 1)$ equations with $(n - 1)$ unknown quantities and the column of free members from the coefficients at n unknown a_{in} where i changes from 1 to $(n - 1)$.

In a matrix form, it can be expressed as follows

$$A'X' = D, \tag{1.5.5}$$

where A' is a dimension matrix of $n - 1$, X' is the the solution of the system, and D is a matrix of free members a_{in}. We can solve it by expanding expanding on two triangular matrices, that is, X' at the $i = 1 - (n - 1)$.

Now, we know all decisions of the initial system

$$(H - EL)X = 0$$

at the $i = 1 - n$.

Therefore, eigenvectors need to satisfy a normalization condition as

$$N\sum_{i} X_i^2 = 1,$$

It is possible to find this normalization and, finally, to determine the eigenvector.

For estimating the accuracy of the solution of a system, it is possible to use residuals, that is, to calculate a matrix

$$B_{\mathrm{n}} = (H - EL)X,$$

the elements of which have to be close to zero for accurate determination of all X.

As an example, now we will consider the general case of the solution of the matrix equation, and show the application of the Haletsky method for solving similar problems

$$Ax = b,$$

where b and x are the matrices columns of N dimension, and A is a square matrix of $N \times N$ dimension. The matrix of A can be expanded to triangular matrices as

$$A = BC,$$

where B is the lower triangular matrix and C is the top triangular matrix, the main diagonal of which has units. The lower and top triangular matrices are determined according to the following scheme, called the Haletsky method [120]

$$b_{\mathrm{i1}} = a_{\mathrm{i1}},$$

$$b_{\mathrm{ij}} = a_{\mathrm{ij}} - \sum_{\mathrm{k}=1}^{\mathrm{j}-1} b_{\mathrm{ik}} c_{\mathrm{kj}}, \tag{1.5.6}$$

where $i \geq j > 1$ and

$$c_{1\mathrm{j}} = a_{1\mathrm{j}}/\mathrm{b}_{11},$$

$$c_{\mathrm{ij}} = \frac{1}{b_{\mathrm{ii}}}\left(a_{\mathrm{ij}} - \sum_{\mathrm{k}=1}^{\mathrm{i}-1} b_{\mathrm{ik}} c_{\mathrm{kj}}\right),$$

at $1 < i < j$.

Such a method allows one to determine a determinant of an initial matrix A [120]

$$\det(A) = \det(B)\det(C).$$

It is known that the determinant of a triangular matrix is equal to the multiplication of its diagonal elements, and as

$$\det(C) = 1,$$

then

$$\det(A) = \det(B) = (b_{11}b_{12}\ldots.b_{\mathrm{nn}}).$$

After the expansion of a matrix of A to the triangular matrix, as the solution of the matrix system can be expressed as

$$By = b, \quad Cx = y,$$

where solutions are found using the following simple expressions [120]

$$y_1 = a_{1,n+1}/b_{11},$$
$$y_i = \frac{a_{i,n+1} - \sum_{k=1}^{i-1} b_{ik} y_k}{b_{ii}} \tag{1.5.7}$$

at the $i > 1$ and

$$x_n = y_n,$$
$$x_i = y_i - \sum_{k=i+1}^{n} c_{ik} x_k$$

at the $i < n$, where $a_{i,n+1}$ – matrix elements of a column b (here i changes from 1 to N – the dimension of a matrix A).

In such tasks, all triangular matrices and solutions X are determined quite unambiguously.

1.6 Total radiative capture cross-sections

Total radiative capture cross-sections $\sigma(NJ,J_f)$ for EJ and MJ transitions in the potential cluster model are specifiedin [12, 42] or [15] and have the form

$$\sigma_c(NJ,J_f) = \frac{8\pi K e^2}{\hbar^2 q^3} \frac{\mu \cdot A_J^2(NJ,K)}{(2S_1+1)(2S_2+1)} \frac{J+1}{J[(2J+1)!!]^2} \sum_{L_i,J_i} P_J^2(NJ,J_f,J_i) I_J^2(J_f,J_i), \tag{1.6.1}$$

where σ is the total cross-section of the radiative capture process, μ is the reduced mass of particles in the initial channel, q is the wave number of particles in the initial channel, S_1 and S_2 are the spins of particles in the initial channel, K and J are the wave number and the moment of γ-quantum in the final channel, and N is the E or M transitions of J multipolarity from the initial J_i to final J_f state of a nucleus.

For the electric orbital $EJ(L)$ during transition ($S_i = S_f = S$), the P_J value has the following form [12, 19]

$$P_J^2(EJ,J_f,J_i) = \delta_{S_i S_f}[(2J+1)(2L_i+1)(2J_i+1)(2J_f+1)](L_i 0 J 0 | L_f 0)^2 \begin{Bmatrix} L_i & S & J_i \\ J_f & J & L_f \end{Bmatrix}^2 \tag{1.6.2}$$

$$A_J(EJ,K) = K^J \mu^J \left(\frac{Z_1}{m_1^J} + (-1)^J \frac{Z_2}{m_2^J} \right), \quad I_J(J_f,J_i) = \langle \chi_f | r^J | \chi_i \rangle.$$

Here, S_i, S_f, L_f, L_i, J_f, and J_i are the total spins and the moments of particles of the initial *(i)* and final *(f)* channel, m_1, m_2, Z_1, and Z_2 are the masses and charges of particles in the initial channel, I_J is the integral on the wave functions of the initial χ_i

and final χ_f state, as function of the relative movement of clusters with an intercluster distance r.

For the spin part of the magnetic process *M1(S)* ($J = 1$) in the used model, the following expression is obtained: ($S_i = S_f = S$, $L_i = L_f = L$, $J = 1$) [12, 14, 19]:

$$P_1^2(M1, J_f, J_i) = \delta_{S_i S_f}\delta_{L_i L_f}[S(S+1)(2S+1)(2J_i+1)(2J_f+1)]\begin{Bmatrix} S\,L\,J_i \\ J_f\,1\,S \end{Bmatrix}^2, \tag{1.6.3}$$

$$A_1(M1, K) = i\frac{\hbar K}{m_0 c}\sqrt{3}\left[\mu_1\frac{m_2}{m} - \mu_2\frac{m_1}{m}\right], \quad I_J(J_f, J_i) = \langle\chi_f|r^{J-1}|\chi_i\rangle.$$

Here m is the mass of a nucleus, μ_1 and μ_2 are the magnetic moments of clusters. For the magnetic moments of a proton, neutron, and some other nuclei, the following values can be used: $\mu_p = 2.792847356\ \mu_0$, $\mu_n = -1.91304272\ \mu_0$, $\mu(^2\text{H}) = 0.857438231\ \mu_0$ [126], $\mu(^6\text{Li}) = 0.8220467\ \mu_0$, $\mu(^7\text{Li}) = 3.256424\ \mu_0$ and $\mu(^{10}\text{B}) = 1.80065\ \mu_0$ [127]. The validity of this expression for the above transition $M1$ has been checked previously based on proton radiative capture reactions on ^{7}Li and ^{2}H at low energies in our previous works [12, 14, 19, 23].

For finding the cross-section of nuclear photodisintegration by gamma-quantum into two fragments, the detailed balance principle is used [22]

$$\sigma_d(J_0) = \frac{q^2(2S_1+1)(2S_2+1)}{K^2 2(2J_0+1)}\sigma_c(J_0),$$

where J_0 is the total moment of a nucleus, σ_c is the total cross-section of the radiative capture by clusters, σ_d is the cross-section of the photodisintegration of the nucleus into two arbitrary parts.

In calculations of radiative capture, exact values of mass of particles were always set; for instance, $m_p = 1.00727646677$, $m_n = 1.00866491597$, and $m_{2H} = 2.013553212724$ amu. Furthermore, by considering each cluster system, the mass values of clusters were used, for example, from [126] or reviews [127], along with similar reviews for other mass numbers. Radii of clusters were also taken from various reviews, databases, and articles considering each specific system. The same is true for asymptotic constants or spectroscopic factors for the considered cluster systems.

It is necessary to note that in all processes of the radiative capture considered here, the number of nuclei formed as a result of reaction depends on the existence and concentration of dark energy [128]. Perhaps, there is a dependence on the growth rate of perturbations of baryonic matter [129] or from rotation of the early universe [130]. This disturbance in the primary plasma can stimulate nucleosynthesis [131] as well as suppress it, for example, because of the growth of perturbations of nonbaryonic matter in the universe [132] or oscillations of cosmic strings [133].

If the total cross-sections of the reaction are known for the process of radiative capture, it is possible to obtain the reaction rate [15]

$$N_A\langle\sigma v\rangle = 3.7313.10^4\mu^{-1/2}T_9^{-3/2}\int_0^\infty \sigma(E)E\exp(-11.605/T_9)dE, \tag{1.6.4}$$

where E is in MeV, cross-section $\sigma(E)$ is measured in μb, μ is the reduced mass in amu, and T_9 is the temperature in 10^9 K.

1.7 Creation of intercluster potentials

Let us discuss the procedure of constructing intercluster partial potentials at the given orbital angular momentum L along with other quantum numbers, after determining the criteria and sequence of finding the parameters and specifying their errors and ambiguities. First, there are parameters of BS potentials, which at known allowed and FSs in the given partial wave are fixed quite unambiguously on binding energy, nuclear radius, and an asymptotic constant in the considered channel.

Of the accuracy of determining the BS potentials is first connected with the accuracy of the AC, which usually is 10–20% of the accuracy of experimental determination of the charging radius which is usually significantly higher, 3–5%. Such potentials do not contain other ambiguities, for example, the classification of states according to Young tableaux allows one to unambiguously fix the number of the BS, both forbidden or allowed in a given partial wave which completely determines its depth; moreover, the potential width entirely depends on the size of the AC. The principles of determining the number of FS and AS in the set partial wave are presented below.

It is necessary to note here that the calculations of the charging radius are some of the model errors, that is, those caused by the accuracy of the model itself. In any model, the value of the radius depends on the integral of the model wave function, that is, model errors of such functions are simply summarized. At the same time, the AC values are determined by an asymptotics of model wave functions at one point on their asymptotics and contain significantly smaller error. Therefore, the BS potentials constructed in this manner maximally conform to the values of the AC obtained based on independent methods, which allow to extract the AC from the experimental data [95].

Intercluster potential of nonresonant scattering process according to the scattering phase shifts at the given number of the BS, both allowed and forbidden in the considered partial wave, is also constructed unambiguously. Accuracy of determining the parameters of such potential is first connected with the accuracy of extracting the scattering phase shifts from the experimental data, and can reach 20–30%. Such potentials do not contain ambiguities because classification according to Young tableaux allows one to unambiguously fix the number of the BS which determines its depth, and potential width with the known depth is determined by a scattering phase shift form.

For constructing nonresonance scattering potential according to nuclear spectra data in a certain channel, it is difficult to estimate the accuracy of finding its parameters even at the given number of the BS, though it is possible to expect that it does not exceed an error in the previous case. Such potential, as usual, is expected for the energy range up to 1 MeV, and has lead to a scattering phase shift close to zero or gradually drops phase shift because in the nuclear spectra there are no resonance levels.

For analyzing resonance scattering while considering partial wave at energies up to 1 MeV, there is a narrow resonance with a width of approximately 10–50 keV, at the fixed number of the BS, potential is also constructed entirely clear. At known BS, its depth is unambiguously fixed on the resonance energy level, and width is completely determined by the width of such resonance. The error of its parameters usually does not exceed the error in determining the width and approaches approximately 3–5%. This also applies to the construction of partial potentials according to the scattering phase shifts as well as determination of its parameters on the resonance in nuclear spectra.

Consequently, all potentials do not contain ambiguities inherent to the optical model [93], and as discussed below, allows one to describe the total cross-sections of the radiative capture processes correctly. The BS potentials need to correctly describe the known values of the AC, which are connected with the asymptotic normalizing coefficient of A_{NC} which is usually obtained experimentally as follows [95, 96].

$$A_{NC}^2 = S_f \cdot C^2, \tag{1.7.1}$$

where S_{f} is the spectroscopic factor and C is the dimensional asymptotic constant expressed in $\mathrm{fm}^{-1/2}$

$$\chi_{\mathrm{L}}(r) = CW_{-\eta\mathrm{L}+1/2}(2k_0 r), \tag{1.7.2}$$

which is connected with the dimensionless AC C_{w} [94] used in (1.2.5), as $C = \sqrt{2k_0}C_w$, and the dimensionless constant C_{w} is determined by the expression (1.2.5) [94]. All parameters were defined in expressions (1.2.5) and (1.2.6).

In conclusion, for constructing partial interaction potentials, it can considered that they depend not only on the orbital moment L but also on the total spin S and the total moment J of the cluster system. In other words, for different moments of JLS we can have different parameters values. Because usually the transitions $E1$ or $M1$ between the different states $^{(2S+1)}L_{\mathrm{J}}$ in continuous and discrete spectra are considered, the potentials of these states are different. In addition, one of the modifications of the used model lies in the assumption regarding explicit dependence of intercluster potentials from Young tableaux. In other words, if the two tableaux are accepted in states of continuous spectrum, and in discrete only one is considered, such potentials can have different parameters for the same L, that is, for one and the same partial wave.

1.8 Classification of cluster states

States with the minimum spin in the scattering processes of some light atomic nuclei can be mixed according to orbital Young tableaux. For example, the doublet state p^2H or n^2H [20, 21] is mixed according to tableaux {3} and {21}. Similarly, such states in discrete spectrum, for example, the doublet p^2H or n^2H channel of ^3He or ^3H nuclei, is pure according to Young tableau {3} [20, 21]. Here, we present a brief classification of states, for example, N^2 H systems for orbital and spin–isospin Young tableaux, and show how these results are obtained.

In general, the possible orbital Young tableaux $\{f\}$ of some nucleus $A(\{f\})$, consisting of $A_1(\{f_1\}) + A_2(\{f_2\})$ with orbital Young tableaux of $\{f\}_L = \{f_1\}_L \times \{f_2\}_L$ are determined by Littlewood's theorem [20, 21, 28]. Therefore, it is possible that for orbital Young tableaux of the N^2H system, when for ^2H the tableau {2} is used, the symmetries are $\{3\}_L$ and $\{21\}_L$.

Spin–isospin tableaux are direct internal product of the spin and isospin Young tableaux of the nucleus from A nucleons $\{f\}_{ST} = \{f\}_S \otimes \{f\}_T$; a system with number of particles not exceeding eight is described in work [134]. In this case, for the simplest N^2H of cluster system at the isospin $T = ½$, we have $\{21\}_T$; for a spin state with $S = 1/2$, we have $\{21\}_S$; and at S or $T = 3/2$ tableaux, we have the form of $\{3\}_S$ and $\{3\}_T$. In constructing the spin-isospin Young tableaux for the quartet spin state of the N^2H system with $T = ½$, we have $\{3\}_S \otimes \{21\}_T = \{21\}_{ST}$, and for the doublet spin state at $T = 1/2$, we obtain $\{21\}_S \otimes \{21\}_T = \{111\}_{ST} + \{21\}_{ST} + \{3\}_{ST}$ [134].

The total Young tableaux of the nucleus is defined similarly as the direct internal multiplication of the orbital and spin–isospin scheme $\{f\} = \{f\}_L \otimes \{f\}_{ST}$. The total wave function of the system at antisymmetrization does not approach zero if it contains antisymmetric component $\{1^N\}$ due to the multiplication of conjugated $\{f\}_L$ and $\{f\}_{ST}$. Therefore $\{f\}_L$ tableaux conjugated to $\{f\}_{ST}$ are allowed in this channel, and all other orbital symmetries are forbidden because they lead to zero total wave function of the system of particles after its antisymmetrization.

This shows tha,t for the N^2H system in the quartet channel, only the orbital wave function with symmetry $\{21\}_L$ is allowed, and the function with $\{3\}_L$ is forbidden because the multiplication $\{21\}_{ST} \otimes \{3\}_L$ does not lead to antisymmetric component in the wave function. Similarly, in the doublet channel we have $\{111\}_{ST} \otimes \{3\}_L = \{111\}$ and $\{21\}_{ST} \otimes \{21\}_L \sim \{111\}$ [134], and in both cases we obtain the antisymmetric tableau. Thus, we can conclude that the doublet spin state is mixed according to orbital Young tableaux with $\{3\}_L$ and $\{21\}_L$.

In previous works [20, 21], the division of such states according to Young tableaux has been described, showing that the mixed scattering phase shift can be presented in the form of a half-sum of pure phase shifts with $\{f_1\}$ and $\{f_2\}$

$$\delta^{\{f_1\}+\{f_2\}} = 1/2(\delta^{\{f_1\}} + \delta^{\{f_2\}}). \tag{1.8.1}$$

In this case, $\{f_1\} = \{21\}$ and $\{f_2\} = \{3\}$, and the doublet phase shifts taken from the experiment are mixed according to these two tableaux.

Furthermore, it is assumed that the quartet scattering phase shift, which is pure according to the orbital Young tableau {21}, can be identified by the pure doublet scattering phase shift N^2H corresponding to the same Young tableau. Thus, it is possible to find the pure tableau {3} doublet N^2H phase shift, and construct, according to Young tableaux, the pure interaction potential which can be used for determining the characteristics of the bound state [11, 22, 24]. A similar process has been observed for the N^3H, N^3He systems [48].

As mentioned above, we used the MPCM for our calculations. One of the modifications of MPCM lies in the accounting of opportunities of mixing according to Young tableau of scattering states for some cluster systems. Furthermore, mixing according to Young tableaux is present not only for the N^2 H scattering but also for more difficult cluster systems. The accounting of the obvious dependence of interaction potentials from the Young tableaux allows to use different potentials if they depend on different of such tableaux in the scattering states and discrete spectrum.

Conclusion

In conclusion, this chapter described that there are various mathematical methods for determining the solution of second-order differential equations such as the Schrödinger equation. However, in mathematical literature, only abstract methods have been discussed for solving such equations, which can be difficult to apply to particular solutions of the equation, such as the Schrödinger equation, in real physical systems of quantum physics.

Therefore, this chapter described some basic mathematical methods that can be directly applied for finding the wave functions from solutions of the Schrödinger equation for some problems of nuclear physics [24]. Further, the chapters also discussed different methods of obtaining solutions, along with some computer programs that can be applied to problems concerning continuous and discrete spectra of the states of two or three nuclear particles [78, 79].

II Radiative neutron capture on the light nuclei

Interest in neutron radiative capture on atomic nuclei is caused, on the one hand, by in the important role it plays in studying the fundamental properties of nuclear reactions and the nuclei and, on the other hand, the applications of data on capture cross-sections in nuclear physics and nuclear astrophysics, as well as in analyzing the processes of preliminary nucleosynthesis in the universe [135].

This chapter mainly discusses the neutron radiative capture processes at thermal and astrophysical energies on some light atomic nuclei. These processes are described within the modified potential cluster model (MPCM) framework with the forbidden states, the general principles of which were described in chapter 1. Chapter 1 along with the initial chapters of previous book from the author titled "Thermonuclear processes of the Universe," published first in Russian [12] and published on the website http://arxiv.org/abs/1012.0877, describe the calculation methods. The Russian version of the book was republished in English [136] by the American publishing house NOVA Sci. Publ., and is available on the website - http://www.novapublishers.org/catalog/product_info.php?products_id=31125. Subsequently, the book was republished in Germany under the title "Thermonuclear Processes in Stars and the Universe" in 2015, and is available at https://www.morebooks.shop/store/gb/book/Термоядерные-процессы-в-Звездах/isbn/978-3-659-60165-1 [14].

In this chapter, continuing the matter discussed in [12, 14, 136], intercluster potentials obtained from phase-shift analysis [13] for calculating some characteristics, for example, total cross-section for the radiative capture processes on light atomic nuclei are demonstrated. The considered reactions of neutron capture are not directly included into the thermonuclear cycles occurring in the stars. However, many of them take a part in reactions of preliminary nucleosynthesis discussed later. These reactions occurred during the later stages of the formation and development of our universe when the energy of the interacting particles reduced to the keV range.

Introduction

Earlier in this book we showed the possibility of describing the astrophysical S-factors of radiative capture reactions on several light nuclei [1–3] within the MPCM and forbidden states [12, 14, 136]. Such a model takes into account the supermultiplet symmetry of the wave function of the cluster system, with splitting of the orbital states according to Young tableaux [19, 23]. The used classification of the orbital states allows one to analyze the structure of intercluster interactions and to define the presence and quantity of allowed and forbidden states in intercluster potentials, thus allowing to

https://doi.org/10.1515/9783110619607-003

find the number of nodes of radial wave function of the relative movement of clusters [20, 21]. For any cluster system, the many-body character of the problem and the effects of antisymmetrization are qualitatively considered by splitting one-particle bound levels of such a potential into the states allowed and forbidden by Pauli's principle [11, 12, 14, 20, 136].

As discussed earlier, in this approach, the potentials of intercluster interactions for the scattering processes are built on the basis of the description of elastic scattering phase shifts, after accounting for their resonance behavior, which are obtained from the experimental differential cross-sections from the phase-shift analysis [13, 22]. For the bound states of light nuclei in the cluster channels, potentials are not constructed only on the basis of phase shifts, and certain additional requirements are used; for example, reproduction of the binding energy and some other characteristics of the bound state of nuclei is one such requirement, which in certain cases is the most basic [12, 14, 136]. Thus, it is assumed that the BS of the nucleus is generally caused by the cluster channel, consisting of initial particles participating in the capture reaction [137].

The MPCM is chosen for considering similar cluster systems in the nuclei as well as nuclear and thermonuclear processes at astrophysical energies [3, 138] because, in many light nuclei probability of formation of nucleon associations, i.e., clusters and the extent of their isolation from each other, are rather high. This has been confirmed by numerous experimental measurements and theoretical calculations obtained by different authors in the last 50–60 years [11, 12, 14, 22, 136, 139].

Certainly, such an assumption is the specific idealization of the real situation in the nucleus, i.e., assuming that there is 100% clusterization of nucleus for the particles in the initial channel. Therefore, the success of this potential model for the description of the A nucleon system in the bound state is determined by the fact how large is the real clusterization of this nucleus in the channel of $A_1 + A_2$ nucleons.

At the same time, nuclear characteristics of several, even noncluster, nuclei can be predominantly stipulated by a specific cluster channel, i.e., to have certain cluster structures for small contributions from other possible cluster configurations. In this case, the used single channel cluster model allows the identification of the dominant cluster channel, while also emphasizing and describing the characteristics of the nuclear system determined by the channel [19, 136].

Further, while discussing the probability of existence certain cluster channel in the nucleus, we must also keep in mind certain stationary, static states of this nucleus, which do not depend on time. Wave function of this nucleus is presented in the form of the wave function superposition of separate possible channels as

$$\Psi(\rho) = \alpha\Psi_1(\rho_1) + \beta\Psi_2(\rho_2) + \gamma\Psi_3(\rho_3) + \ldots.,$$

where $\alpha\Psi_1(\rho_1)$ is the wave function of possible channels, i.e., first, second, third, etc., with the coefficients near them being the probabilities of such channels. Meanwhile, channels can be either two-body or many-body.

At the same time, certain reactions such as radiative capture, the dynamic, i.e., depending on time reconfiguration are carried out. During this process, pair of clusters from the continuous spectra of the states at positive energy level transfer to the state with negative energy, i.e., discrete spectrum states, and the additional energy radiates in the form of γ quanta.

Thus, it can be assumed that the cross-sectional measurement of such a reaction occurs immediately after its completion, i.e., when the final nucleus formed a moment ago and its initial stationary state coincides with the channel of initial particles. In other words, it can be considered that initially when the measurement of reaction characteristics occurs, the formed nucleus is most likely (with a 100% probability) in the channel consisting of particles in the initial channel. Using this fact it is possible to explain the remarkable success of the the MPCM in describing the total cross-section of radiative capture reactions of over 30, assuming the total clusterization of final nucleus in the initial channel [12, 13, 14, 24, 136, 140].

Furthermore, before considering neutron radiative capture processes, as explained previously [12, 14, 19, 136, 141], on the basis of the potential cluster model with the forbidden states, the astrophysical *S*-factors of 15 proton radiative capture reactions as well as other charged particles on some light atomic nuclei were accounted for. Based on the same model, we will discuss the calculation results of the total cross-sections for some neutron capture processes in this chapter using the same light nuclei.

First, we will consider the possibility of the description of total cross-sections of the neutron capture reaction on ^{2}H based on the potential cluster model, taking into account the supermultiplet symmetry of the wave function and the splitting of orbital states according to Young tableaux. Although the radiative capture reaction of $n^2\mathrm{H} \to {}^3\mathrm{H}y$ at astrophysical energies associated with the formation of an unstable nuclei of tritium at the expense of β disintegration to ^{3}He is not included in the main thermonuclear cycle [1, 3]; however, it can play a role in some models of the Big Bang [142]. In such models, it is assumed that the primordial nucleosynthesis occurred as a chain of reactions of primordial nucleosynthesis in the below form

$$\begin{gathered} {}^1\mathrm{H}(n,\gamma)^2\mathrm{H}(n,\gamma)^3\mathrm{H}({}^2\mathrm{H},n)^4\mathrm{He}({}^3\mathrm{H},\gamma)^7\mathrm{Li}(n,\gamma)^8\mathrm{Li}({}^4\mathrm{He},n)^{11}\mathrm{B}(n,\gamma)^{12}\mathrm{B}(\beta^-) \\ {}^{12}\mathrm{C}(n,\gamma)\cdot{}^{13}\mathrm{C}(n,\gamma)^{14}\mathrm{C}(n,\gamma)^{15}\mathrm{C}(\beta^-)^{15}\mathrm{N}(n,\gamma)^{16}\mathrm{N}(\beta^-)^{16}\mathrm{O}(n,\gamma) \\ {}^{17}\mathrm{O}(n,{}^4\mathrm{He})^{14}\mathrm{C} \end{gathered} \tag{2.0}$$

etc. [142], which also includes the neutron capture on ^{2}H not necessarily at low energies, which will be discussed below. Certain other options of such reactions with some other variants of intermediate processes are known [142].

The neutron capture reaction on ^{2}H is the mirror of the process $p^2\text{H} \rightarrow {}^3\text{He}\gamma$, which was described in our previous works [12, 14, 136, 143]. The proton capture on ^{2}H is directly included in a thermonuclear proton–proton cycle, being the first reaction, proceeding as a result of electromagnetic interactions. This cycle defines the contribution to an energy yield of the nuclear reactions [144], fueling the sun and stars of our universe. Therefore, studies regarding proton and neutron capture reactions on ^{2}H highlight research interest from not only from the viewpoint of nuclear astrophysics problems, but also affects the representations and approaches nuclear physics problems at ultralow energies of light and lightest atomic nuclei, as well as.thermonuclear power.

Regarding neutron capture reaction on ^{6}Li, our previous work [145] demonstrated the phase-shift analysis of the elastic p^6Li scattering in the energy range of 500–1150 keV [146] which is of interest in nuclear astrophysics. The $^2P_{3/2}$ potential of interaction for the ground and $^2P_{1/2}$ potential of the first excited states of ^{7}Be in the p^6Li channel, as well as the potential of the doublet $^2S_{1/2}$ waves of scattering were constructed. The results allowed consideration of astrophysical S-factor of the proton radiative capture on ^{6}Li at low energies [147]. Consequently, it was shown that the approach described the available experimental data for proton radiative capture on ^{6}Li within a wide energy range [148, 149].

In this chapter, drawing on the earlier discussion, we will describe the total-cross sections of neutron radiative capture reaction on ^{6}Li at low energies. This reaction is not of particular interest in nuclear astrophysics [142], and hence, has not been investigated experimentally. This conclusion can be drawn by considering the experimental results of a database of the site of MGU [150] or EXFOR [151]. Using previously published data [150, 151], there are only two types of the measurements conducted at 0.025 eV (25 meV) [152–155] and in the 6.7–7.3 MeV range, wherein there are overloaded resonances at 13.7 and 14.7 MeV relative of the ground state of ^{7}Li with a width of approximately 0.5 MeV, along with some uncertain characteristics such as moment and parity [156].

This, in turn, does not result in their inclusion in the analysis of possible electromagnetic transitions to the ground or first excited state of ^{7}Li, which are formed during the capture reaction of $n^6\text{Li} \rightarrow {}^7\text{Li}\gamma$. Nevertheless, it is interesting to consider the possibility of using the potential cluster model with the forbidden states and classification of states of clusters according to Young tableaux [55] for describing the total cross-sections of this reaction in thermal and astrophysical energy ranging from 0.025 eV to 1–2 MeV, as used earlier for the p^6Li system [12, 14].

Furthermore, the radiative capture $n^7\text{Li} \rightarrow {}^8\text{Li}\gamma$ at astrophysical energies with β formation of an active ^{8}Li will be considered. Such a reaction is not directly included into the basic thermonuclear cycles [3, 12, 14, 136], but can play a role in some models of the Big Bang [142], where it is assumed that primordial nucleosynthesis occurred according to a chain of thermonuclear reactions of the form (2.0) along with other similar reactions. Moreover, the considered reaction is a mirror of $p^7\text{Be} \rightarrow {}^8\text{B}\gamma$ capture

wherein ^{8}B, owing to a weak process, disintegrates into ^{8}Be+e^{+}+ν. Neutrinos of this reaction possess a rather high energy, and remain at terrestrial states for several decades; the unstable ^{8}Be is known to disintegrate further to two α particles. The p^{7}Be → ^{8}Bγ capture reaction is one of the final processes of the thermonuclear proton–proton cycle caused by burning of the sun and majority of the stars in our universe [3, 12, 14, 136].

For calculating the total cross-sections of the neutron radiative capture on ^{7}Li at thermal and astrophysical energies, the potential cluster model [12, 14, 22] was employed, which requires the potentials of n^{7}Li interaction in continuous and discrete ranges. Further, here, we will consider that such potentials need to correspond to the classification of cluster states by orbital symmetry [11] as as discussed previously by us [143] for other cluster nuclei, including the proton radiative capture on ^{7}Li [12, 14, 136, 137, 143].

From the viewpoint of strong interactions, ^{8}Li is stable because it disintegrates along with transition to ^{8}Be only at the expense of weak forces. Therefore, it can be considered as cluster n^{7}Li system, and the MPCM can be employed to describe its characteristics [11, 12, 14, 22]. From the viewpoint of this process and cluster structure of ^{8}Li, two-cluster n^{7}Li system with *LS*-coupling, not when a neutron is situated relatively within ^{7}Li nucleus in the state $p_{3/2}$ with $p_{1/2}$ impurity, as discussed previously [157, 158], for a communication *jj* case is considered here.

Here, we consider the reaction n^{9}Be → ^{10}Bγ and show that in the presence of certain assumptions of the general character concerning the interaction potentials in the n^{9}Be channel of ^{10}Be, it is also possible to describe the available experimental data on capture total cross-sections of neutrons at all considered energies. Because there are no data on the phase-shift analysis of n^{9}Be elastic scattering, the scattering potentials are constructed based on the general information about the structure of the resonances of ^{10}Be and the GS potentials obtained relatively approximately because there is no data on the radius of ^{10}Be.

Further, we will consider neutron capture reactions on ^{12}C and ^{13}C at thermal and astrophysical energies, which are thermonuclear reactions of the primordial nucleosynthesis (2.0) [142]. These reactions (2.0) resulted in the formation of the sun, stars, and our universe [12, 14, 136]. The available experimental data on the total cross-sections such as neutron capture reaction on ^{12}C have been published elsewhere, including [159–165] and [150, 151]. Though they do not cover the entire range, they adumbrate the cross-sections of radiative capture in a wide energy range. Therefore, it is interesting to determine the possibility of describing these cross-sections based on the PCM with FSs, as described us earlier for proton radiative capture on ^{12}C and ^{13}C [141, 166].

Note that the phase-shift analysis [13], including new experimental data on the differential cross-sections of the elastic p^{12}C and p^{13}C scattering at astrophysical energies [166, 167], allowed us to construct the elastic scattering phase shifts of the unambiguous potentials of p^{12}C and p^{13}C interactions. In general, they should not

significantly differ from similar potentials of n^{12}C and n^{13}C of scattering as well as bound states of ^{13}C in n^{12}C and ^{14}C in n^{13}C channels, as is discussed later.

Finally, continuing the study of neutron radiative capture reactions on light atomic nuclei that are part of thermonuclear processes and cycles [3], we will also discuss neutron capture reactions on ^{14}C, ^{14}N, ^{15}N, and ^{16}O at thermal and astrophysical energies. Almost all these processes are included into the main chain of reactions of primary nucleosynthesis (2.0) [1–4], which the development by the universe during its formation and development. In this chapter, we will present the main results of the phase-shift analysis in some partial waves of the n^{16}O elastic scattering at low energies.

Fianlly, we will show that in all the considered systems it is possible to construct the partial interaction potentials corresponding with the classification according to Young tableaux, phase shifts of elastic scattering, and the main characteristics of the BSs of the nuclei; further, we also describe the available experimental data for total cross-sections of neutron radiative capture.

2.1 Neutron radiative capture on ^{2}H in the cluster model

At the beginning of this chapter, we will discuss the the neutron radiative capture on deuteron discussed previously in [168], within the theory of an effective field. In the considered energy range of 40–140 keV, the main influence gives the $M1$ transition, which can be consistent with the calculated total cross-sections after extrapolation from a database [169].

Furthermore, in this chapter, within the modified potential cluster model with the forbidden states and their classification according to orbital Young tableaux, the possibility of describing experimental data of total cross-sections of neutron radiative capture on ^{2}H will be considered at thermal (~1 eV), astrophysical (~1 keV), and low (~1 MeV) energies. It will be shown that the used model and numerical methods of its realization described here can transfer the behavior of experimental cross-sections at energies in the range of 10 meV (10^{-2} eV) to 15 MeV.

2.1.1 Potential description of the elastic n^{2}H scattering

Before progressing to the n^2H system, we will briefly discuss the results of p^2H scattering process, obtained earlier. The potentials of the elastic p^2H scattering for each partial wave were constructed to describe the corresponding partial elastic scattering phase shifts at low energies [170], wherein the doublet channel are mixed according to Young tableaux {3} + {21} [11, 12, 14, 19, 23, 136]. Using the representations described above, we obtained p^2H interaction potentials for

scattering processes in the form of (1.2.1) mixed according to tableaux {3} + {21}. These potentials can be described as

$$V(r) = V_0 \exp(-\gamma r^2) + V_1 \exp(-\delta r) \tag{2.1.1}$$

using the parameters given in the first two rows of the Table 2.1.1 [42, 52, 136]. For $V_1 = 0$ the expression (1.2.1) or (2.1.1) transforms as (1.2.2).

Table 2.1.1: Doublet potentials of interaction p^2H systems [22] mixed according to Young tableaux for the scattering processes. $E_{g.s.}$ – energy of the bound GS of ^3He in the p^2H channel; E_{exp} – experimental value.

$^{(2S+1)}L$ {f}	V_0, MeV	γ, fm^{-2}	V_1, MeV	δ, fm^{-1}	$E_{g.s.}$, MeV	E_{exp}, MeV
^2S {3}+{21}	−55.0	0.2	–	–	–	–
^2P {3}+{21}	−10.0	0.16	+0.6	0.1	–	–
^2S {3}	−41.55562462	0.2	–	–	−5.493423	−5.493423

In the doublet spin channel, pure phase shifts with the tableaux {3} were separated (see, for example, work [13]) and on their basis pure according to Young tableaux potentials of intercluster ^2S interaction for the ground state of ^{3}He in the p^2H channel for which parameters are specified in the third line of Table 2.1.1 are constructed [12, 14, 19, 22, 23, 42, 52, 136]. Parameters of this potential lead to a rather good description of the main characteristics of a nucleus ^{3}He in the p^2H channel (see, for example, [12, 14, 19, 23, 136, 143, 171]). The binding energy, charge radius, and channel AC comprise the main characteristics.

Using these potentials, total cross-sections of the proton radiative capture on ^{2}H and astrophysical *S*-factors at energies at 10 keV [52] were calculated; however, experimental data of *S*-factor were available only at energies higher than 150–200 keV [172]. Subsequently, there were new experimental results at the lowest energies of upto 2.5 keV [173–175]. After the analysis, it was found that the previous calculations based only on *E1* process were consistent with the experimental results at energies ranging from 10 keV to 1.0 MeV [52]. Thus, the used potential cluster model not only described new experimental data but also predicted the behavior of the astrophysical *S*-factor of the proton capture on ^{2}H at energy of 10 keV in advance. The calculations, presented in 1995 in our work [52], were executed before carrying out new experimental measurements [175] in 2002, and some results were even published earlier [173, 174] in 1997.

Here, we will use the obtained in [12, 14, 19, 22, 23, 42, 52] p^2H potentials for neutron radiative capture on ^{2}H at low energies, using the same calculation methods checked for the p^2H system [12, 136]. Parameters $^2S_{1/2}$ of potential of the GS of ^{3}H in the n^2H channel without Coulomb interaction were a little specified for the description of

binding energy of tritium, i.e., 6.257233 MeV [176,177]. Consequently, for the parameters of potential of form (1.2.2) the following expression was obtained [178]

$$V_{\text{g.s.}} = -41.4261655 \quad \text{MeV}, \quad \gamma_{\text{g.s.}} = 0.2\,\text{fm}^{-2}. \tag{2.1.2}$$

Such a potential precisely reproduces the binding energy of ^{3}H, giving a value of –6.257233 MeV using the finite-difference method [24], resulting in charge and mass radii of 2.33 and 2.24 fm, respectively. In these calculations, the charge radius of a neutron was considered to be zero, its mass radius was equal to the radius of a proton of 0.8775 (51) fm [179], and the radius of a deuteron of 2.1424(21) fm was obtained from a database [179]. The asymptotic constant in the form of (1.2.5) was equal to 2.04(1) at an interval of 5–15 fm. The error of the asymptotic constant calculated with such a potential given hereinafter is determined by averaging by the specified interval of distances. Its values obtained in different works are discussed in [94] and are in range of 1.82–2.21. Let us note that the calculated expressions for root-mean-square radii have been presented previously [14, 22].

Binding energy was obtained with accuracy of a finite-difference method of calculation of energy that is equal to 10^{-6} MeV [24], and on increasing the accuracy of calculation to 2.10^{-9} for potential (2.1.2), it is possible to obtain an exact value of energy of –6.257233014 MeV. Further, as the deuteron has a larger radius than tritium 1.755(86) fm [176], it does not exist in the free form, i.e., not in a deformed form and the extent of its deformation, shown previously [50], is approximately 30% (see also [22]).

The same result was obtained previously [180] showing that the deuteron wave function, which exists in tritium, falls down much quicker than that observed for its free state. Thereby, the presence of the third particle, in this case a neutron, leads to deformation, i.e., compression of a deuteron cluster in a tritium nucleus. The same conclusion is seen employing resounding group method (RGM) calculations [7]; the usual estimation of deformation of a deuteron is at the level of 20–40%.

For additionally controlling the calculation of binding energy of ^{3}H in the potential (2.1.2) for the n^2H channel, the two-body variation method with the expansion of the wave function on the Gaussian nonorthogonal basis and an independent variation of all parameters was used [12, 14, 22, 24, 178]

$$\Phi_{\text{L}}(r) = \frac{\chi_{\text{L}}(r)}{r} = N_0 r^L \sum_{\text{i}} C_{\text{i}} \exp(-\alpha_{\text{i}} r^2),$$

where α_{I} are variation parameters, C_{i} are coefficients of expansion, r is intercluster distance, and N_0 is a normalization of the variation wave function.

At Gaussian basis of $N = 10$ and independent variation of all parameters of the variation method gave an energy of –6.2572329999 MeV ≈ –6.257233000 MeV. The asymptotic constant C_{W} of the variation wave function, the parameters of which are specified in Table 2.1.2, at distances of 6–20 fm remains at the level of 2.05(2) that

Table 2.1.2: The variation parameters and coefficients of the expansion of the wave function of bound state in ^{3}H of the n^2H system. Normalization of the wave function at distances of 0–25 fm is equal to N_0 = 9.999999996433182E-001.

i	α_i	C_i
1	3.361218182141637E–001	1.231649877959069E–001
2	2.424705040532388E–002	1.492826524302106E–002
3	1.168704181683766E–002	1.190880013572610E–003
4	9.544908567362362E–002	1.304076551702031E–001
5	4.867951954385213E–002	5.868193953570694E–002
6	9.341901487408062E–001	–2.155090483420204E–002
7	1.756025156195464E–001	1.814952898311890E–001
8	2.396705577261060E–001	6.944804259139825E–002
9	6.503621155681423E–001	1.564362603986158E–002
10	9.684977093058702E–001	1.709621746273126E–002

does not differ from the value of the FDM, and the values of residuals do not exceed 10^{-11} [24].

It is known that variation energy on increasing the dimension of basis increases and gives the top limit of the true binding energy. Simultaneously, finite-difference energy on decreasing the value of a step and increasing the number of steps increases [24]. Therefore, for real binding energy in such potential, it is possible to accept the average value obtained above on the basis of the two used methods which is –6.257233007(7) MeV for the n^2H system. Thereby, the accuracy of the calculation of binding energy of this system in the GS potential (2.1.2) specified by the above-mentioned methods (VM and FDM) based on two various computer programs in Fortran-90 [24] is at the level of ±0.007 eV or ±7 meV [14, 178].

2.1.2 The total cross-sections of neutron radiative capture on ^{2}H

First, we will show the efficiency of the modified potential cluster model used here, potentials obtained based on the p^{2}H elastic scattering phase shifts, and the separation of a pure phase shift as well as the corresponding GS potential of ^{3}H using an example of photodisintegration of ^{3}H in the n^2H channel. This was considered by us earlier in work [52] using a wider energy range but in less details. Furthermore, in Fig. 2.1.1, using the solid curve, calculation results at the energies of γ quanta 6.3–10.5 MeV for the sum of the cross-sections $E1$ and $M1$ of the processes with the p^{2}H scattering potentials specified above are shown (see Table 2.1.1) at the switched-off Coulomb interaction and GS (2.1.2). The experimental data for the total cross-sections of of the photonuclear disintegration of ^{3}H in the n^2H channel for the considered energies are taken from works [181] – black triangles and [182] – open triangles.

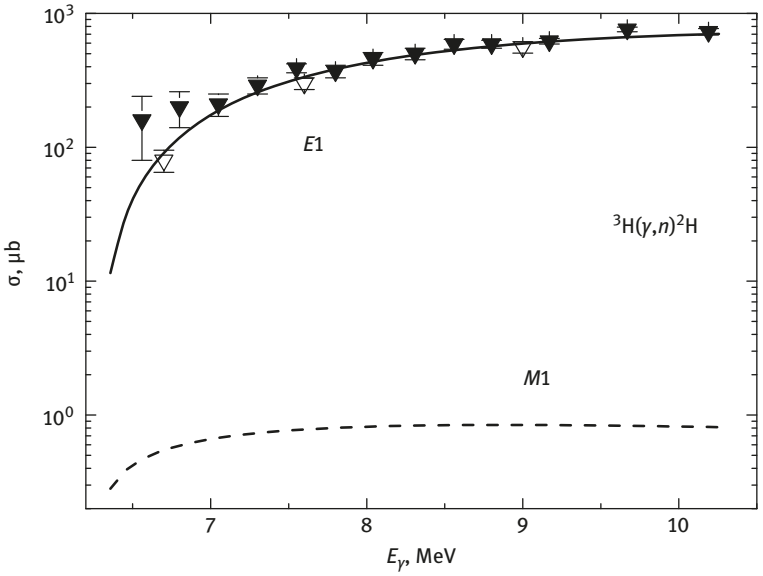

Fig. 2.1.1: Total cross-sections of the photodisintegration of ^{3}H in the n^{2}H channel. Experimental data: ▼ – are taken from works [181] and ▽ – [182]. Curves are explained in the text.

At the bottom of Fig. 2.1.1 using the dotted curves the contribution of the *M1* process to the disintegration of ^{3}H in the general $^2S_{1/2}$ state into a doublet $^2S_{1/2}$ wave of n^2H scattering is shown

1. $$^2S_{1/2} \to {}^2S_{1/2},$$

This practically does not significantly contribute to the total cross-sections of reactions at these energies. Here, we pay attention to the $^2S_{1/2}$ states of the continuous and discrete spectra corresponding to the different Young tableaux, and the different interaction potentials are compared to them. In other words, obvious dependence of parameters of potential from the Young tableaux of the considered states is assumed.

The cross-sections of the considered process of disintegration are caused only by the *E1* transition at the $^2S_{1/2}$ disintegration of the GS ^{3}H in a doublet ^2P scattering wave

2. $$^2S_{1/2} \to {}^2P_{3/2} + {}^2P_{1/2}.$$

Here, in contrast to our previous work [183], we will consider the results of neutron capture on ^{2}H, when the negative sign of the magnetic moment accounts for the neutron [178]. When using the parameters of p^2H nuclear potentials for the ^2S and ^2P scattering waves without Coulomb term and the GS (2.1.2), the total cross-sections of the radiative neutron capture on ^{2}H in the energy range of 10 meV–15 MeV was calculated (Table 2.1.1). The results of such calculations for the sum of

E1 and *M1* transitions at the capture to the GS of ^{3}H are shown in Fig. 2.1.2 denoted by the dashed-dotted curves. It is clear that at energies of 10 meV, the calculated cross-sections have a somewhat higher value than that measured experimentally [187]. The calculated values correspond with data [160] at energy of 25 meV, where the value of 508(15) μb is given. In the latest data at thermal energy [184], the value of 489(6) μb was obtained, which is slightly different from the previous results.

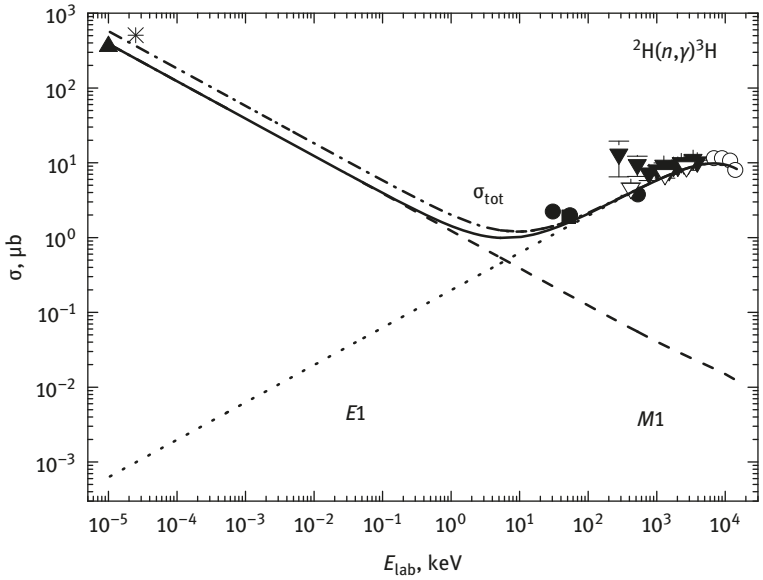

Fig. 2.1.2: The total cross-sections of neutron radiative capture on ^{2}H. Experiment from works: ● – [185], ○ – [186], ▲ – [187], * – [160], ■ – [188], the data obtained for capture: ▼ – from [181] and ∇ – from [182]. Curves are explained in the text.

The experimental data for the total cross-sections of radiative neutron capture on ^{2}H are shown in Fig. 2.1.2, which is obtained from previous works: [185] – at energy of 30, 55, and 530 keV, [186] – circles at 7–14 MeV, [187] –triangle at 0.01 eV, [160] –asterisk at 0.025 eV, [188] –square at 50 keV; and data from [181] was used for capture designated in the figure by 2.1.1 black triangles (▼) and [182] open triangle (∇).

We will emphasize that for calculations of the *M1* capture, contrary to the transition No. 1, the earlier obtained p^2H potential for the ^2S of a scattering wave from Table 2.1.1 without Coulomb interaction was used. However, it should be noted that the difference in results of the various extracts of phase shifts from the experimental data for the elastic p^2H scattering [170], denoted by the black dots in Fig. 2.1.3, approaches 10–20%. Therefore, even the p^2H scattering potential, the phase shift of

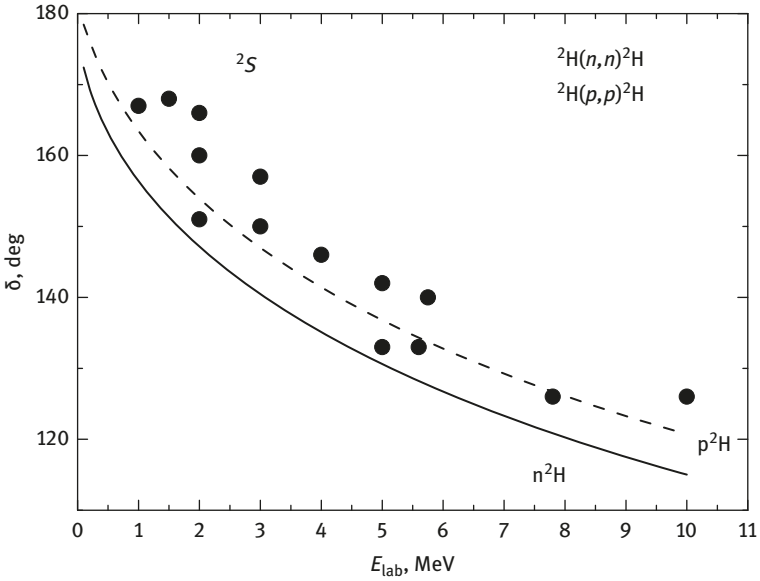

Fig. 2.1.3: ^2S phase shifts of the elastic p^{2}H (dashed curve) and n^{2}H scattering (solid curve). Points: ● – results of extraction of phases from the experimental data obtained in work [170]. Parameters of potentials are given in the text and Table 2.1.1.

which is presented in Fig. 2.1.3 by the dotted curves, is constructed on their basis with sufficiently large ambiguities. Here, we consider the n^2H system for which the results of the phase-shift analysis were not successfully obtained in the considered energy range.

Therefore, we will consider the necessary changes required for the n^2H potential in the ^2S scattering wave, such that the results are consistent with experimental data [187]. Finally, results for the total *E1* were obtained as

3. $$^2P_{3/2} + {}^2P_{1/2} \rightarrow {}^2S_{1/2}$$

and *M1* (the reverse for No. 1) transitions, the total cross-section of the radiative capture, which is presented in Fig. 2.1.2 denoted by the solid curve.

The depth of the ^2S potential in the n^2H elastic scattering was not significantly less than that for the p^2H system from the Table 2.1.1 [178]

$$V\mathrm{s} = -52.0\,\mathrm{MeV}, \quad \gamma_S = 0.2\,\mathrm{fm}^{-2}.$$

The phase shift of the elastic scattering obtained for such potential is presented in Fig. 2.1.3 denoted by the solid curve. It is clear that the ^2S phase shift of the changed n^2H potential at low energies reduces rapidly compared to a similar phase shift for the p^2H potential from the Table 2.1.1. This, in turn affects the calculation of the total cross-sections for *M1* process, as shown in Fig. 2.1.2, use of this potential allows to

describe the available data for the total cross-sections at the lowest energies of 10 meV [187].

The results shown in Fig. 2.1.2 show the prevalence of the *M1* process at energies lower than 1 keV, the cross-section of which is denoted by the dashed curve, and the dotted curve in Fig. 2.1.2 shows the contribution of the *E1* transition. As can be seen from Fig. 2.1.2, the cross-section of the *E1* transition reduces sharply and at 0.1 keV can be neglected. Simultaneously, at energy higher than 10 keV, this process prevails and completely defines the behavior of the total cross-sections, describing the available experimental data at energies ranging from 50–100 keV to 15 MeV reasonably.

Thereby, the change of the parameters of n^2H potential in the ^2S scattering wave by approximately 5% (results presented in Table 2.1.1) allows to describe the available experimental data at low energies quite reasonably. Such change in parameters can be explained by the uncertainty of the p^{2}H phase shifts, which are extracted from the experimental data, as well as their absence for the n^2H elastic scattering.

Consequently, the used modified potential cluster model correctly reproduces the experimental data for total cross-sections of the neutron radiative capture on ^{2}H in energy range when energy at edges of this range differs more than nine orders, i.e., from 10^{-5} keV to 1.5×10^4 keV [14, 178]. The assumption of obvious dependence of potentials of discrete and continuous spectra from the Young tableaux affords the model more flexibility and allows one to describe the available experimental data correctly. Expansion or modification of the usual potential cluster model is also possible, giving us the MPCM.

Furthermore, we will notice that at energies ranging from 10^{-5} to 0.1 keV, the calculated cross-section (shown in Fig. 2.1.2 by the solid curves) practically forms a straight line, and can be approximated by the simple function from energy

$$\sigma_{\text{ap}}(\mu\text{b}) = \frac{A}{\sqrt{E(\text{keV})}}. \tag{2.13}$$

The value of the constant $A = 1.2314\ \mu\text{b} \cdot \text{keV}^{1/2}$ was determined by a single point in cross-sections at the minimum energy of 10^{-5} keV (l.s.). Furthermore, it is possible to consider the module $M(E)$ of a relative deviation of the settlement theoretical cross-section (σ_{theor}) and approximation of this cross-section (σ_{ap}) function (2.1.3) at energies ranging from 10^{-5} to 0.1 keV

$$M(E) = \left|\left[\sigma_{\text{ap}}(E) - \sigma_{\text{theor}}(E)\right]/\sigma_{\text{theor}}(E)\right|. \tag{2.1.4}$$

Hence, at energies lower than 100 eV, the deviation does not exceed 1.0%. It can be assumed that the form of dependence of the total cross-section on energy (2.1.3) will remain at lower energies. In this case, the performance evaluation of the cross-section, for example, at an energy of 1 μeV (1 μeV = 10^{-6} eV) gives a value of 38.9 mb [14, 178].

The similar coefficient for the dashed-dotted curve in Fig. 2.1.2 is $A = 1.8205$ μb keV$^{1/2}$, deviation (2.1.4) of our calculations and approximations (2.1.3) at 100 eV is approximately 1%, and the value of cross-section at 1 μeV is approximately 57.6 mb [14, 178].

2.2 Neutron radiative capture on ^{6}Li

As far as we know, the total cross-sections of the neutron radiative capture on ^{6}Li were previously considered in the folding model [189], where an acceptable consent with the experimental data given in work [190] for the energy range of 20–60 keV was obtained. Subsequently, the data [190] were considered by the method of the distorted waves in [191], with a good description. However, in both cases, only the energy range of 20–60 keV was considered, i.e., the behavior of total cross-sections at the lowest energies was not analyzed [152–155].

Here, using the MPCM with the forbidden states and classification of cluster states according to Young tableaux, we will show the possibility of describing experimental data for total cross-sections of neutron radiative capture on ^{6}Li at energy ranging from 25 meV (25×10^{-3} eV) to 1.0–2.0 MeV. For an acceptable description of the available experimental data, it was enough to consider only the *E1* transitions from the doublet $^2S_{1/2}$ states of a continuous spectrum of the n^6Li system to the doublet ground $^2P_{3/2}$ and doublet first excited $^2P_{1/2}$ bound states of ^{7}Li in the final channel, i.e.,

1. $$^2S_{1/2} \to {}^2P_{3/2}$$

and

2. $$^2S_{1/2} \to {}^2P_{1/2}.$$

The potentials of these scattering states and discrete spectrum will be constructed based on the known p^6Li scattering phase shifts and description of the main characteristics of the BS of ^{7}Li.

2.2.1 Potential description of the n^{6}Li scattering

Moving on to the direct consideration of the $n^6\text{Li} \to {}^7\text{Li}\gamma$ capture reaction, we will notice that the initial phase-shift analysis of the elastic p^6Li scattering was conducted at energy ranging from 0.5 to 5.6 MeV taking into account the spin-orbit splitting phase shifts [192]. Subsequently, these results for the *S*-phase shifts of scattering were somewhat clarified [145] and used for constructing intercluster potentials, with which the calculation of an astrophysical *S*-factor of the proton radiative capture

on ^{6}Li is carried out [147]. Consequently, it was shown that the employed approach allows one to describe the available experimental data for the proton radiative capture on ^{6}Li in a wide energy range [12, 14, 136, 193].

Here, we use the interaction p^6Li potentials obtained earlier, but without a Coulomb term [19, 23, 145], and we will consider, on the basis of the MPCM, the total cross-sections of the neutron radiative capture reaction on ^{6}Li at astrophysical energies. Initially, we will note that for describing our results according to the phase shifts of the elastic p^6Li scattering, as shown previously [145, 147, 193], the doublet $^2S_{1/2}$ potential of the form (1.2.2) with parameters is preferable

$$V_s = -124.0\,\text{MeV}, \quad \gamma_S = 0.15\,\text{fm}^{-2}, \tag{2.2.1}$$

which contains two forbidden bound states, corresponding to orbital Young tableaux {52} and {7} [19, 23, 147]. The phase shifts of this potential for the elastic p^6Li and n^6Li scattering are shown in Fig. 2.2.1 using the dashed and solid curves, respectively.

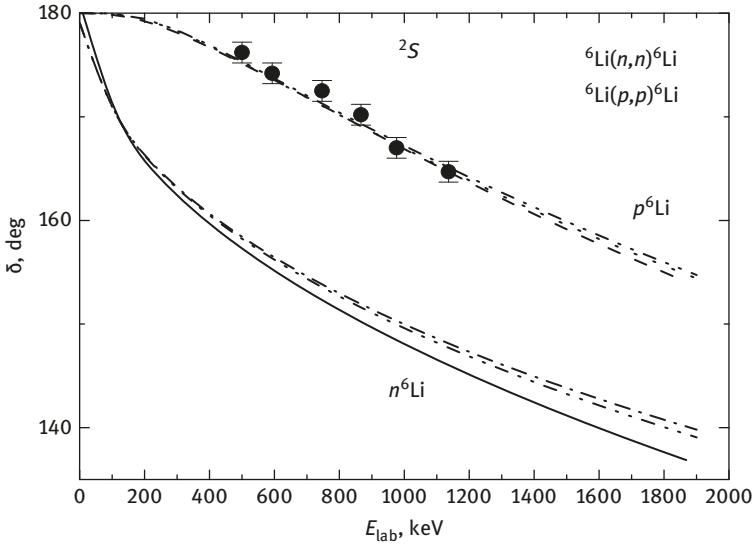

Fig. 2.2.1: The ^2S phase shifts of the elastic n^6Li and p^6Li scattering. Points: ● – extraction of p^6Li phases [145] from the experimental data [146]. Curves – phase shifts of the elastic scattering with the potentials explained in the text.

However, in works [19, 23, 147, 193] it was noticed that, for the ^2S and ^2P waves in the N^{6}Li system, there can be two variants of potentials. In the above case, the S and P partial waves contain two BSs, and only one of them in the ^2P waves is allowed corresponding to the BS of nuclei with A = 7, while all others are forbidden. These

partial waves contain in the second case only one BS – it is forbidden in the ^2S wave, and in ^2P waves they correspond to the allowed BSs $^2P_{3/2}$ and $^2P_{1/2}$.

Furthermore, we will consider both the variants of potentials for the ^2S scattering state and ^2P BS of ^{7}Li in the n^6Li channel. Meanwhile, only variants of potentials capable of describing the total cross-sections of the neutron radiative capture on ^{6}Li, phase shifts of elastic scattering and the main characteristics of the GS of ^{7}Li, including its channel asymptotic constant, will be considered.

The phase shifts of the other variant of shallow ^2S scattering potential which contains only one bound FS at {52} and has the following parameters

$$V_S = -34.0\,\text{MeV}, \quad \gamma_S = 0.15\,\text{fm}^{-2}, \tag{2.2.2}$$

are shown in Fig. 2.2.1 by the dotted curves for p^{6}Li and the dashed-dotted for n^6Li scattering. Our extraction of the p^{6}Li elastic scattering phase shifts [145] from new experimental data [146] are denoted by points in Fig. 2.2.1. From Fig. 2.2.1, it is clear that both scattering potentials lead to the identical description of p^{6}Li scattering phase shifts at energies of 1 MeV, while n^6Li phase shifts slightly differ at these the energies. It appears impossible to find the ^2S variant of potential for p^6Li scattering without FS capable of describing the doublet scattering phase shifts given in Fig. 2.2.1. In other words, for describing scattering phase shifts and the considered processes of the radiative capture requires the existence of the bound FS with the tableaux {52} in this partial wave.

In the considered N^{6}Li system, similar to N^{2}H, mixing occurs as per the Young tableaux. As it will be shown further, the doublet state is mixed according to tableaux {43} and {421}; therefore, it is considered that the GS has the tableau {43}, and the states of a continuous spectrum correspond to both the tableaux. Therefore, the pure orbital symmetry with the Young tableaux {43} $^2P_{3/2}$ wave potential of the GS of ^{7}Be [147] was constructed to describe the channel binding energy of the ground state of a nucleus as the p^6Li system, its root-mean square radius, and the AC.

Here, we slightly change the depth of the p^6Li potential [147] transferred to the binding energy of ^{7}Li in the n^6Li channel. In this case, the parameters of pure $^2P^{\{43\}}$ potential [194] (1.2.2) of n^6Li interaction for the nucleus of the GS of a nucleus ^{7}Li c $J^\pi = 3/2^-$ can be presented as

$$V_{g.s.} = -250.968085\,\text{MeV}, \quad \gamma_{g.s.} = 0.25\,\text{fm}^{-2}. \tag{2.2.3}$$

This potential leads to a binding energy of –7.249900 MeV at an experimental value of –7.2499 MeV [127], and has one forbidden state corresponding to the Young tableaux {61} [19]. The average square charge radius is 2.55 fm and mass is 2.58 fm, which generally corresponds with the experimental data [127], which is 2.39(3) fm for a charging radius. For an asymptotic constant at an interval of 5–15 fm, a value of 2.45 (1) is obtained. For these calculations, the charge radius of neutron is zero and the

mass radius is equal to the radius of proton and ^{6}Li nucleus, which is slightly more than ^{7}Li radius, and is equal to 2.51(10) fm [127].

According to the results of [195] wherein various experimental data and theoretical results were collected, AC is 1.76(14) fm$^{-1/2}$. After recalculation to a dimensionless value we get a value of 1.68(13). In work [196], a value of 1.890(13) fm$^{-1/2}$ was given or in a dimensionless look 1.800(12). Such recalculation is required because in these works some other determination of the AC C, given earlier in (1.7.2) which differs from our C_w (1.2.5) with a factor $\sqrt{2k_0}$ was used.

For the potential (1.2.2) of the first excited state of ^{7}Li with $J^\pi = 1/2^-$ parameters are found

$$V_{e.s.} = -248.935336\,\text{MeV}, \quad \gamma_{e.s.} = 0.25 \quad fm^{-2}. \tag{2.2.4}$$

The potential allows one to obtain a binding energy of –6.772300 MeV at a experimental value of –6.7723 MeV [127], the charge radius remains unchanged from previous results, and the AC at an interval of 5–15 fm is 2.33(1). Such potential also contains the forbidden bound state with the Young tableaux {61}. In work [196], an AC value of 1.652(12) fm$^{-1/2}$ was obtained, which after recalculation with $\sqrt{2k_0} = 1.03$ gives 1.60(1).

These AC results from [195,196] were recalculated without a spectroscopic factor S_f, which for the considered channel is discussed in [191]. Table 2.2.1 from this work without indication of links to concrete publications in which these results were obtained.

Table 2.2.1: Theoretical and experimental values of the neutron spectroscopic factor S_f of the ground and the first excited states of ^{7}Li [191]. In the tenth line, results of described in [191] are shown.

No.	^{7}Li (GS)	^{7}Li (first ES)	Experimental or theoretical
1	0.72	0.89	Theoretical
2	0.80	0.98	Theoretical
3	0.79	0.97	Theoretical
4	0.77	1.07	Theoretical
	Average theoretical = 0.77	*Average theoretical = 0.98*	–
5	0.90	1.15	^{6}Li(d,*p*)
6	0.71	—	^{7}Li(*p*,d)
7	0.72(1)	—	^{7}Li(*p*,d)
8	0.87	—	^{7}Li(*p*,d)
9	1.85(37)	—	^{6}Li(d,*p*)
10	0.73(5)	0.90(9)	^{7}Li(^{6}Li, ^{7}Li) – results of work [191].
	Average experimental = 0.96 *Average = 0.87*	*Average experimental = 1.03* *Average = 1.00*	– –

It is clear from Table 2.2.1 that the S_f of the first ES is equal to unity, and S_f of the GS can range from 0.71 to 1.85, with an average of 0.87. According to expression (1.7.1)

$$A_{NC}^2 = S_f \cdot C^2,$$

if for the A_{NC} GS, the value 1.890(13) $fm^{-1/2}$ is used [196], then at the average spectrofactor for which we use a value of 0.87, for dimensionless C_w we will obtain 1.92. If the interval of S_f values given above is used, for this A_{NC} value we will obtain C_w interval of 1.32–2.14. If we were to consider an error of the AC [196], in the range of 1.76–2.02, for an interval of C_w we will obtain 1.23–2.28.

The values of the neutron spectrofactor ranging from 0.435 to 0.87 were given in [197]. For the experimental A_{NC} value the size of 1.78(14) $fm^{-1/2}$ is given. These data allow to determine C_w interval of 1.82–2.57, and taking into account the errors of the AC, this interval extends to 1.67–2.77. The value of the AC obtained above for the potential (2.2.3) of 2.45, agrees with such a range of values. S_f values ranging from 0.59 to.1.21 at A_{NC} of 1.83 $fm^{-1/2}$ are given in the same work [197] for the first ES. Then, for the C_w values we find the range of 1.62–2.31 which is well coordinated with the value of the AC given above for the potential (2.2.4).

Another variant of the pure according to Young tableau $^2P_{3/2}$ potential with the {43} of n^6Li interaction for the GS of ^{7}Li without the bound FS can be presented in the form

$$V_{g.s.} = -75.190114 \quad \text{MeV}, \qquad \gamma_{g.s.} = 0.175 \quad \text{fm}^{-2}. \tag{2.2.5}$$

It leads to a binding energy of –7.249900 MeV and has only one bound allowed state corresponding to the Young tableau {43}. The root-mean square charge and mass radii are congruent with 2.54 fm, and the AC is 2.03(1) at an interval of 5–16 fm, which is consistent with previously published results [196, 197].

For additionally controlling the accuracy of calculation of binding energy ^{7}Li in the potential of the GS (2.2.3), the two-body variation method with an independent variation of parameters and the expansion of the wave function on a non-orthogonal Gaussian basis was used [24] (see the Appendix). On the basis of this method at a dimension of basis *N = 10* and an independent variation of parameters, the binding energy of –7.249898 MeV is obtained. The asymptotic constant C_w of the variation wave function, parameters of which are specified in Table 2.2.2, at distances of 5–15 fm remains at the level of 2.45 (5), and the residual value does not exceed 10–11 [24].

Let us remember [12,24] that as the variation energy with increase in the dimension of basis decreases and approached the top limit of the true binding energy, and the finite-difference energy with reduction of the value of a step and increasing a number of steps increases, for real two-body binding energy of the n^6Li system in such potential it is possible to accept the average value of –7.249899(1) MeV. Therefore, the accuracy of determining the binding energy of this two-cluster system in the GS potential of ^{7}Li specified above for the n^6Li channel (2.2.3), obtained using

Table 2.2.2: The variation α_i parameters and expansion coefficients C_i of wave function of the GS (2.2.3) n^6Li system for ^{7}Li. The WF normalization at distances of 0–25 fm is equal to N_0 = 0.9999999999999947.

i	α_i	C_i
1	2.468292899352664E–002	–8.443780272416886E–004
2	5.659824615487678E–002	–1.494186015886072E–002
3	1.229406461038807E–001	–9.267494206256470E–002
4	2.513715488575826E–001	–3.217760480847366E–001
5	7.328392817240388E–001	1.463594686074960
6	1.394554324801138	8.744682134317008E–001
7	1.968191404804425	–2.564925474852117
8	2.224827222346167	3.963681316635119
9	2.494348228525606	–2.317285290938208
10	2.835387525435829	4.485636531606636E–001

two different numerical methods (VM and FDM) calculated using various computer programs [24] written on Fortran-90 [12,14] is at the level of ±1 eV.

Similar results with the energy value of –7.249900 MeV using residuals no more than 10^{-10}, i.e., determined with an accuracy of <±0.5 eV, and other characteristics of the GS of ^{7}Li in the n^6Li channel were obtained for potential (2.2.5), and the parameters of its wave function are specified in Table 2.2.3.

Table 2.2.3: The variation parameters and expansion coefficients of the GS wave function of the n^6Li system for potential (2.2.5.). The wave function normalization at distances of 0–25 fm is N_0 = 0.9999999999999968.

i	α_i	C_i
1	2.653995234178599E–002	–9.552868397144253E–004
2	5.916693410819475E–002	–1.325632996745183E–002
3	1.214005238211452E–001	–6.817793605505393E–002
4	2.312872693555081E–001	–1.994404481758770E–001
5	4.977633546319589E–001	–1.420218482450155
6	5.485119023279393E–001	2.461491882301208
7	6.173563857857660E–001	–1.533948700508486
8	7.395207514049224E–001	3.547232132753293E–001
9	1.003543127851490	–3.452745893002195E–002
10	1.509188370554815	2.278247300258973E–003

2.2.2 Total cross-sections of the neutron radiative capture on ^{6}Li

By consideration of the total cross-sections of the radiative capture within the MPCM framework with the FSs, we took into account the *E1* transitions from nonresonant ^2S

and ^2D scattering states to the ground $^2P_{3/2}$ (transition No. 1) and the first excited $^2P_{1/2}$ bound states (transition No. 2) of ^{7}Li in the n^6Li channel. The calculation of the ^2D wave function without spin-orbit splitting was carried using ^2S potential (2.2.1) or (2.2.2) at $L = 2$, however, in expressions for the capture cross-sections, the exact coefficients for *E1* transitions from $^2D_{3/2}$ and $^2D_{5/2}$ scattering waves were considered [147, 178, 194]. Because the wave function of the ground and first excited states of ^{7}Li do not differ, including the binding energy, radiii, etc., in real calculations for determining both levels only the potential of the ground state (2.2.3) or (2.2.5) was used.

Such an assumption is represented as we consider only the general form of the total radiative capture cross-sections for energy range, the limits of which differ by eight orders of magnitude. We would not consider the details of this process as it has been discussed previously [198]. The possibility of describing the total cross-section of the photodisintegration process of ^{7}Li in the n^6Li channel has been considered in detail at energies of 7.3–8.8 MeV.

Furthermore, by considering the neutron capture on ^{6}Li, we used the potentials obtained from the p^{6}Li scattering and checked the p^{6}Li system of ^{7}Be (2.2.1) and (2.2.3) [147, 194], however, without the Coulomb interaction and new variants of interactions with one BS (2.2.2) and (2.2.5). The structure of resonances in the n^6Li system differs slightly, than that in p^6Li, implying that the scattering phase shifts will be others. Therefore, the intercluster potentials of the n^6Li interaction can slightly differ from the potentials obtained earlier for the p^6Li system. Simultaneously, for the real calculations of *E1* transition, only the ^2S scattering potential is used, for which both p^6Li and n^6Li systems have no resonances at energies ranging up to 3.0 MeV [127]. Energy ^2S phase shift behavior of the elastic scattering for these p^6Li and n^6Li potentials has been shown in Fig. 2.2.1; potentials differ only by the Coulomb interaction and give a few different scattering phase shifts.

Note that the experimental data from previous works [150, 151] regarding capture cross-sections refer only to energies of 25 meV and three keV-energies described previously [190]. The results of measurements of the capture cross-sections at energies, for example, in the range of 0.1–1.5 MeV are absent. However, in [150, 151] and [199–201], data have been presented for the total cross-sections of photodisintegration of the GS of ^{7}Li in the n^6Li channel at the energies of γ quantum, i.e., from 7.25 to 8.75 MeV, i.e., to a resonance with $J^\pi, T = 3/2^-, 1/2$ at 8.75 MeV concerning the GS of the ^{7}Li [127]. Therefore, previously published data [199–201] for ^{7}Li photodisintegration in the n^6Li channel were recalculated in capture cross-sections, and are shown in Fig. 2.2.2 and 2.2.3 using circles, open and black squares at energies of 1.5 MeV.

As we have the disintegration cross-sections of σ_d only with the GS of ^{7}Li, for the capture total cross-section of σ_c on the ground and the first excited state, the detailed balance principle at identical cross-sections of the disintegration was used

$$\sigma_c(3/2+1/2) = \sigma_c(3/2) + \sigma_c(1/2) = [4\sigma_d(3/2) + 2\sigma_d(1/2)]A(q,K),$$

where

$$\sigma_c(J_0) = (2J_0+1)\frac{2K^2}{q^2(2S_1+1)(2S_2+1)}\sigma_d(J_0) = (2J_0+1)A(q,K)\sigma_d(J_0).$$

The calculation results of the total cross-sections of neutron capture on ^{6}Li for (2.2.1) and (2.2.3) potentials at energies from 10^{-5} to 2×10^3 keV are presented in Fig. 2.2.2 denoted by the solid curve – transition No. 1 and No. 2. Using the dotted curve in Fig. 2.2.2, the calculation results of cross-sections of $E1$ transitions No. 1 and No. 2 with the (2.2.2) and (2.2.5) potentials are given.

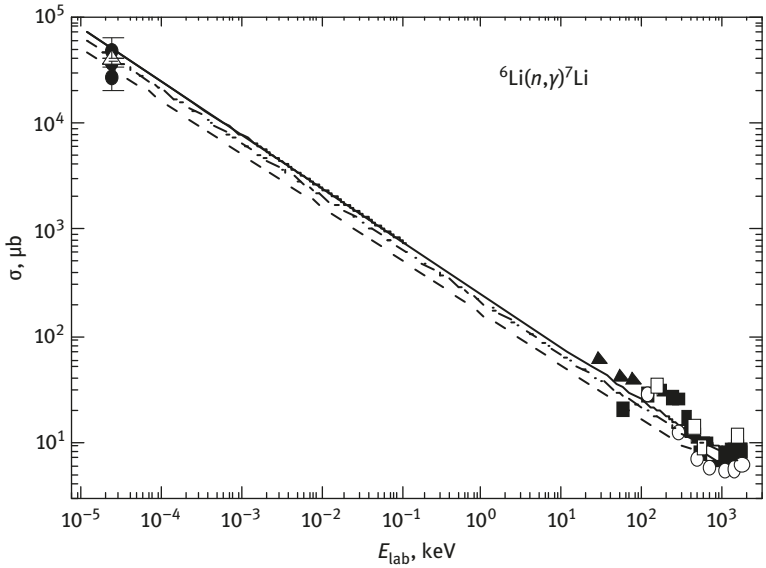

Fig. 2.2.2: The total cross-sections of the neutron radiative capture on ^{6}Li at low energies. Experimental results: ● – [152–155] and Δ – [184] at 25 meV and ▲ – [190], ■ – [199], ○ – [200], □ – [201]. Curves – the calculation of total cross sections with potentials explained in the text.

The corresponding calculation results of the photodisintegration cross-sections of the GS of ^{7}Li in the n^6Li channel with (2.2.1) and (2.2.3) potentials are shown in Fig. 2.2.3 denoted by the solid curve and for variants of (2.2.2) and (2.2.5) potentials denoted by the dotted line. From these figures, it can be seen that in both cases it is possible to obtain the potentials which generally describe the energy behavior of the capture and photodisintegration total cross-sections of at energies from 25 meV [152–155, 184] to 1.5 MeV [199]. Meanwhile, new data from [184] generally coincide with more early measurements [152–155].

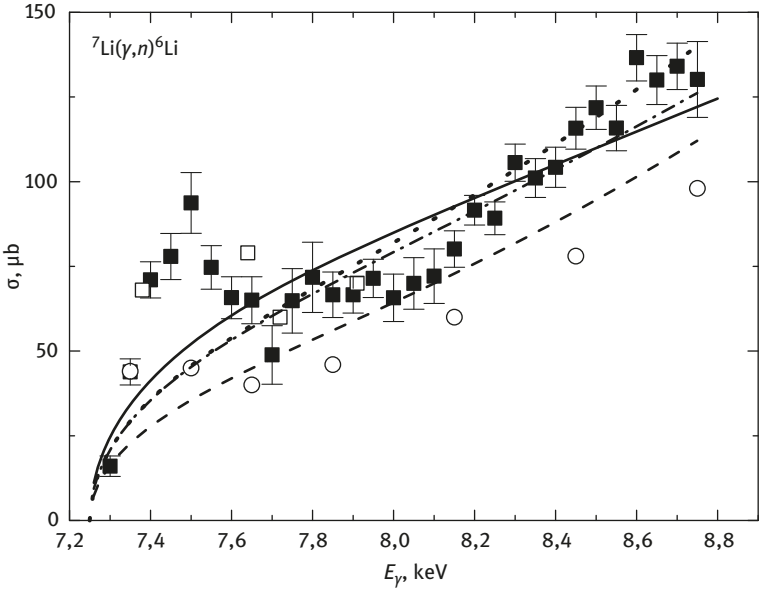

Fig. 2.2.3: Total cross-sections of the ^{7}Li(γ, n)^{6}Li reaction at low energies. The experimental results of works: ■ – [199], ○ – [200] and □ – [201]. Curve – calculation with the potentials explained in the text.

Such interactions correspond with the phase shifts of the elastic scattering and generally describe some main characteristics of the GS of ^{7}Li in the n^6Li channel correctly, which could be as considered the potential variant without the FS (2.2.5) describing the value of an asymptotic constant, which lies approximately in the middle range of possible values stated above.

Furthermore, instead of (2.2.5) it is possible to use the potential of the GS of ^{7}Li without FS which gives a smaller value of the AC, which is closer to the lower limit of the determined above range of the AC values, for example, with the parameters

$$V_{g.s.} = -83.161074 \quad \text{MeV}, \quad \gamma_{g.s.} = 0.2\,\text{fm}^{-2}. \tag{2.2.6}$$

In this case, when using the ^2S scattering potential with one FS (2.2.2), we obtain the result presented in Fig. 2.2.2 and Fig. 2.2.3 by the dashed curves. Such potential leads to the binding energy of –7.249900 MeV, AC of 1.85(1) at an interval of 5–13 fm, charge of 2.54 fm, and mass radii of 2.53 fm.

The calculation results of variation binding energy give a value of –7.249899 MeV. When comparing it with the FDM results, an accuracy of ±0.5 eV is obtained for determining this energy using two methods in the given potential. Other GS characteristics of ^{7}Li in the n^6Li channel for (2.2.6) potential are similar to the results obtained above using the FDM. The residuals have an order of 10^{-10}, and the parameters of wave function are listed in Table 2.2.4.

Table 2.2.4: The variation parameters and expansion coefficients of the wave function of GS of the n^6Li system for the (2.2.6) potential. Wave function normalization at distances of 0–25 fm is $N_0 = 0.9999999999999987$.

i	α_i	C_i
1	2.665347013743804E–002	–8.871735330500928E–004
2	5.940895728884596E–002	–1.221361696531949E–002
3	1.219273413814190E–001	–6.284879952239499E–002
4	2.340611751544998E–001	–1.968287096274776E–001
5	4.751229388850844E–001	–8.572931845080505E–001
6	5.485119023279393E–001	1.556074541398506
7	6.173563857857660E–001	–1.203431194740232
8	7.395207514049224E–001	2.934610010474853E–001
9	1.003543127851490	–3.090692233217297E–002
10	1.509188370554815	2.059998226181524E–003

The calculation results of the total cross-sections for this potential are still consistent with the data published in [152–155] at 25 meV due to large experimental errors, but are slightly below than the available data at energies in the range of 100 keV–1 MeV. From Fig. 2.2.3, it can be seen that they settle down between the data [199] and [200], shown in figures by black squares and open circles, respectively.

However, if we accept the following parameters for the ^2S scattering potential with one FS

$$V_S = -45.0 \text{ MeV}, \quad \gamma_S = 0.25 \text{ fm}^{-2}. \tag{2.2.7}$$

Then the results of the calculation of the capture and disintegration total cross-sections for the (2.2.6) potential are shown in Fig. 2.2.2 and Fig. 2.2.3 by the dashed-dotted curves. It does not differ from the variant given by the dotted line and well describes the experimental data in the entire energy range. The phase shifts of potential (2.2.7) for both processes of p^6Li and n^6Li scattering are shown in Fig. 2.2.1 by the dashed-dotted-dotted curves. This helps describe the N^{6}Li scattering phase shifts, which are almost similar to the results for (2.2.2) potential.

Thus, it is quite possible to describe the capture and disintegration total cross-sections, elastic phase shifts scattering, and the main characteristics of the BS of ^{7}Li in the n^6Li channel, including the radii and AC, for the GS potentials without the bound FS and the ^2S scattering with one bound FS. Here, it is important that the potential of the GS leads to the AC in the value interval determined above, and the scattering potential correctly describes the elastic p^6Li phase shifts. Meanwhile, the potential of n^6Li scattering differs from it only by the Coulomb member. All these potentials well agree with one of the variants of classification of FSs and ASs according to Young tableaux, presented in detail in Table 2.2.5.

Table 2.2.5: Classification of states according to Young tableaux in the N[6]Li system.

System	T	S	$\{f\}_T$	$\{f\}_S$	$\{f\}_{ST} = \{f\}_S \ \{f\}_T$	$\{f\}_L$	L	$\{f\}_{AS}$	$\{f\}_{FS}$
n^6Lip^6Li	1/2	1/2	{43}	{43}	{7}+{61}+{52}+	{52}	0,2	–	{52}
					+{511}+{43}+	***{43}***	1,3	{43}	–
					+{421}+{4111}+	***{421}***	1,2	{421}	–
					+{322}+***{3211}+***				
					+{2221}+{331}				
		3/2	{43}	{52}	{61}+{52}++{511}	{52}	0,2	–	{52}
					+{43}++2{421}	{43}	1,3	–	{43}
					+{331}++ {322}+	***{421}***	1,2	{421}	–
					+{3211}				

Here, the following notations are accepted: *T, S*, and *L* – an isospin, spin, and the orbital moment of system of particles N[6]Li, respectively; $\{f\}_S$, $\{f\}_T$, $\{f\}_{ST}$ and $\{f\}$ – spin, isospin, spin-isospin, and possible orbital Young tableaux, respectively; $\{f\}_{AS}$, $\{f\}_{FS}$ – Young tableaux of the allowed and forbidden orbital states, respectively [42]. Bold italics mark the conjectured to each other $\{f\}_{ST}$ and $\{f\}_L$ Young tableaux. For an explanation of work with the Young tableaux see §1.8.

For describing some resonance states, we notice that the resonance at 7.45 MeV [127] with the moment of *5/2*-lying above of the n^6Li channel threshold only on 0.2 MeV (cm) with width of 80 keV (c.m.) belongs to the $^4P_{5/2}$ wave. The possibility of *M1* transition at photodisintegration of ^{7}Li in the n^6Li channel taking into account this state was recently considered in a review [198]. The resonance at energy 8.75 MeV concerning the GS which lies above the threshold of the n^6Li channel at 1.5 MeV with a width of 4.7 MeV and the moment $3/2^-$ can belong to $^2P_{3/2}$ or $^4P_{3/2}$ partial waves [127]. However, its influence on the total cross-sections of the radiative capture has not been considered here because there are no results of the phase shifts n^6Li analysis in this energy range. In this case, constructing a potential which would lead to wide resonance for any ^2P phase shift only using spectra data, as was done by us for other cluster systems [12,19,23,136], is hardly possible. Relationship of the resonances considered above to concrete partial waves can be definitively established based on the results of the detailed phase-shift analysis of the elastic n^6Li scattering at energies ranging up to 1.5–2.0 MeV; however, we did not find such an analysis in the literature.

Thus, the used MPCM and the given intercluster potentials, as well as in the case of other light nuclei [12,42], give acceptable results of the description of the neutron radiative capture on ^{6}Li at the astrophysical energy range. The calculation results of the total cross-sections of the neutron capture on ^{6}Li obtained only on the basis of the *E1* transitions at energies ranging from 25 meV to 1.5 MeV are generally consistent with the known experimental data, as well as for the capture process and the recalculated measurements of the total cross-sections of the two-body photodisintegration of ^{7}Li in the n^6Li channel.

The preference between two variants of intercluster potentials should be given to variant with one BS, i.e., the FS is available only in ^2S scattering wave; ^2P bound levels

do not contain FSs. This conclusion differs from our previous works [22, 42, 55, 145] where N^{6}Li options of potentials with two BS, i.e., two FS in ^2S waves and FS and AS in 2P waves were considered. The results show that, for accurate description of the experimental data, it is enough to have only one BS in each partial wave. Such state with the {52} tableaux is forbidden for the S scattering waves and is allowed for {43} in doublet bound ^2P levels of ^{7}Li.

In this case for classification of cluster states according to Young tableaux for the system of particles with $A = 7$ in the 6+1, channel it is necessary to consider the only tableaux for ^{6}Li {42}, without the forbidden states in ^{6}Li orbital {6} configuration. It leads to possible orbital states of the N^{6}Li system with {52}, {43}, and {421} tableaux corresponding to the FS only in ^2S wave, and two other tableaux are compatible with the allowed ^2P states [42], as shown in Table 2.2.5. Meanwhile, it is clear from Table 2.2.5, that in the quartet channel there is no AS with tableaux {43}. Nevertheless, it is possible to consider a variant of the GS as a mixture of $^2P_{3/2}$ and $^4P_{3/2}$ waves, as it was done in the n^7Li system. This allows one to calculate the resonance cross-section at 0.2 MeV (cm), as shown in Fig. 2.2.3.

The intercluster potentials coordinated with such classification of orbital states allow to describe the characteristics of the all BS of the ^{7}Li nucleus considered above in the n^6Li channel, elastic n^6Li scattering, and neutron radiative capture on ^{6}Li. The presence of FS in ^{6}Li channel with the orbital {6} tableaux, as was done [22, 42, 55, 145], is not required – it does not improve the quality of the description of the considered experimental data or an explanation of any additional effects or even obtaining new results.

Further, it follows from Table 2.2.5 that the doublet state, as mentioned above, is mixed according to tableaux {43} and {421}, and can be presented in the form of a half-sum of pure phase shifts, as discussed in §1.8 [42]. Meanwhile, usually it is considered that the BS corresponds the pure state with the tableaux {43}, and the ^2P scattering phase shifts taken from the experimental data are mixed according to these tableaux [20, 42]. Therefore, all doublet scattering potentials specified above correspond to two of these tableaux, and the GS potentials correspond to only one of them {43}.

For the energies ranging from 10^{-5} to approximately 100 keV, the calculated cross-section is almost a straight line (see Fig. 2.2.2 the solid curve), it can be approximated by a simple function of the form (2.1.3) with a constant $A = 246.6118$ μb keV$^{1/2}$ determined by one point in cross-sections at a minimum energy of 10^{-5} keV (ls). The module of a relative deviation (2.1.4) of the calculated theoretical cross-section and the approximation of this cross-section of the used function (2.1.3) in the range from 10^{-5} to 100 keV appears less than 0.3%.

It is possible to assume that this form of dependence of the total cross-section of the energy will be saved at lower energies. Therefore, we will estimate the value of the total cross section, for example, at energy of 1 μeV (10^{-6} eV = 10^{-9} keV), which gives 7.8 b [178, 194].

For the dotted curve in Fig. 2.2.2, the coefficient in approximation of the cross-section is A = 208.7136 μb keV$^{1/2}$, the deviation of such approximation from calculation at the energies up to 100 keV does not exceed 0.9%, and the value of the cross-section at 1 μeV is 6.6 b. For the dashed-dotted curve in Fig. 2.2.2, the coefficient value for expression (2.1.3) is equal to A = 207.7438 μb keV$^{1/2}$ with approximately the same cross-section at an energy of 1 μeV.

2.3 Cluster n^{7}Li system

At the outset notice that for the first time *E1* transition in the n^7Li system at the radiative capture was considered in [202] where accurate description of the total cross-sections in the nonresonance energy range based on one-body model and the Woods-Saxon potential corresponding with energies of ^{8}Li levels has been shown. Furthermore, such process based on the model of direct capture has also been considered [157].

Such results have been discussed in recent studies also [142], wherein capture total cross-sections were described based on the *E1* process without their resonance behavior. Considering resonance in the total cross-sections at 0.25 MeV, as far as we know, the first attempt to describe this [203] on the basis of generator coordinate method. Furthermore, recently, based on the model independent methods, the results with the acceptable description of these sections of radiative capture in resonance energy range [204] have been obtained.

Furthermore, we will show that similar results can be obtained in the MPCM for describing this resonance on the basis of the *M1* transition from the $^5P_3$ scattering wave having a resonance at this energy to the $^5P_2$ component to the wave function of the GS of ^{8}Li in the n^7Li channel. Here, within the MPCM, the neutron radiative capture on ^{7}Li will be considered at energies ranging from 5 meV to 1.0 MeV where there are experimental data lie. This reaction is included in the main chain of the primordial nucleosynthesis (2.0), playing a role in the evolution of the universe.

2.3.1 Classification of cluster states in the n^{7}Li system

First, we will note that the n^7Li system has the isospin projection T_z = –1 possible only at a value of total isospin of T = *1* [205]. Therefore, such a cluster system, unlike p^7Li mixed on an isospin with T = 0 and 1 [205] and p^7Be at T_z = +1 and T = 1, is pure on an isospin. At the same time, the spin, as for p^7Li or p^7Be systems, can accept two values S = 1 and 2, and some states of the n^7Li system can also be mixed according to spin [12, 14, 136, 178].

Furthermore, we will briefly discuss the classification of orbital states of clusters of the system considered here. In our previous works [12, 14, 137], it was

shown that, if for ^{7}Li the {7} tableaux is used, the resulting symmetries {8} and {71} of eight particles in the channel 1 + 7 are forbidden because there cannot be more than four cells in one line [28,29]. They correspond to the forbidden states with the moment concerning the movement L = 0 and 1, which is determined by the Eliot's rule [11, 28].

In the second case when for ^{7}Li the {43} tableaux is accepted, n^7Li, p^7Be (at T = 1) or p^7Li, n^7Be (at T = 0,1) systems containing the triplet spin channel the levels forbidden in the ^3P waves with the {53} Young tableaux and in the $^3S_1$ wave the FS at symmetry of the wave function {44}, and have the ^3P allowed state with the spatial tableaux {431}. Thus, the n^7Li potentials in the triplet spin state for the scattering processes discussed later, must have the forbidden bound $^3S_1$ state with the {44} tableau. In the ^3P waves, the forbidden and allowed bound levels with Young tableaux {53} and {431} are contained, the last of which corresponds to the $^3P_2$ ground bound ^{8}Li state in the n^7Li channel. At the same time, for the scattering processes in all ^3P waves, the allowed state will be considered as the nonbound state; only FS remains bound.

At the spin S = 2, the allowed symmetries and the bound allowed levels in the n^7Li system are completely absent at any values of the orbital moment of L [137]. Thereby, the potential of the $^5S_2$ scattering wave also has the bound FS with the {44} tableaux, and in the ^5P wave of the scattering process, the potential contains the FS with the {53} and {431} tableaux. Moreover, the last of them can remain in a continuous spectrum and the potential has only one bounded FS with the {53} tableaux. Such a conclusion for the ^5P scattering waves is not unique, and the variant of ^5P potentials with two bound FSs for the {53} and {431} tableaux is possible.

As the third variant, it is possible to consider both Young tableaux {7} and {43} for the ground state of ^{7}Li as both of them are present among the FS and AS of this nucleus in ^{3}H+^{4}He configuration [22, 137]. Hence, the classification of levels differs slightly, the number of the forbidden states increases, and in each partial wave with L = 0 and 1, the forbidden bound level is added.

A complete classification of the orbital states was described by us earlier [12, 23], and is further presented in Table 2.3.1. Meanwhile, the results for the first of these variants in the last four columns of the table are marked by italic and separated by a solid line from the results for the second option of classification of states.

Because in the n^6Li system for ^{6}Li, it is possible to use only the allowed {42} tableaux without its forbidden configuration {6}, we will consider the second variant of the structure of FSs and potentials with the tableaux {43} allowed in ^{7}Li as the basic variant of the classification of FSs and ASs in such a system. The $^{3,5}S$ potentials of the scattering wave are considered which are necessary for the consideration of the electromagnetic *E1* transitions to the GS of ^{8}Li at the neutron capture on ^{7}Li, having only the bound forbidden states with the {44} tableaux.

Table 2.3.1: Classification of states according to Young tableaux [22] in the N^7Li and N^7Be systems.

Systems	T	S	$\{f\}_T$	$\{f\}_S$	$\{f\}_{ST} = \{f\}_S \{f\}_T$	$\{f\}_L$	L	$\{f\}_{PC}$	$\{f\}_{3C}$
p^7Li	0	1	{44}	{53}	{71}+{611}++{53}+{521}	*{8}*	*0*	–	*{8}*
n^7Be					++{431}+{4211}++{332}	*{71}*	*1*	–	*{71}*
					+{3221}	{53}	1,3	–	{53}
						{44}	0,2,4	–	{44}
						{431}	1,2,3	{431}	–
		2	{44}	{62}	{62}+{521}+{44}++{431}	*{8}*	*0*	–	*{8}*
					+{422}++{3311}	*{71}*	*1*	–	*{71}*
						{53}	1,3	–	{53}
						{44}	0,2,4	–	{44}
						{431}	1,2,3	–	{431}
p^7Be	1	1	{53}	{53}	{8}+2{62}+{71}++{611}	*{8}*	*0*	–	*{8}*
n^7Li					+{ 53}++{44}+2{521}+	*{71}*	*1*	–	*{71}*
p^7Li					+{5111}+{44}++{332}	{53}	1,3	–	{53}
n^7Be					+2{431}++2{422}	{44}	0,2,4	–	{44}
					+{4211} ++{3311}	***{431}***	1,2,3	{431}	–
					+{3221}				
		2	{53}	{62}	{71}+{62}++{611}+2{53}	*{8}*	*0*	–	*{8}*
					++2{521}+2{431}+	*{71}*	*1*	–	*{71}*
					+{422}+{4211}++{332}	{53}	1,3	–	{53}
						{44}	0,2,4	–	{44}
						{431}	1,2,3	–	{431}

The following notations are accepted: *T, S* and *L* – isospin, spin, and the orbital moment of a system of particles of N^7Li, respectively; $\{f\}_S$, $\{f\}_T$, $\{f\}_{ST}$ and $\{f\}_L$ – spin, isospin, spin-isospin, and possible orbital Young tableaux, respectively; $\{f\}_{AS}$, $\{f\}_{FS}$ – Young tableaux of the allowed and forbidden orbital states, respectively [42]. The bold italics interfaced to each other by $\{f\}_{ST}$ and $\{f\}_L$ of the Young tableaux.

The potential of the resonance $^5P_3$ scattering wave at 0.25 MeV, allowing to consider the *M1* transition to the GS of ^8Li can has one with the {53} tableaux or two bound forbidden states at {53} and {431}. The potential of the BS of ^8Li in the n^7Li channel, which is mixed with two $^3P_2$ and $^5P_2$ states, has one forbidden bound state with {53} and allowed bound state with {431}, corresponding to the ground state at a binding energy of –2.03239 MeV [205].

2.3.2 The potential description of the elastic n^7Li scattering

We did not manage to find data on phase shifts of the elastic n^7Li or p^7Be scattering at astrophysical energies [150]. Therefore, here, the potentials of scattering processes in the n^7Li system will be constructed using the analogy with the p^7Li scattering [137] employing data on the spectra of levels of ^8Li [205], which are shown in Fig. 2.3.1, along

with similar spectra data of ^{8}Be and ^{8}B nuclei. Spectra are given so as to combine the levels 2^+1, which in ^{8}Li and ^{8}B are the ground states and stable from the viewpoint of nuclear interactions, breaking up only at the expense of the β-process.

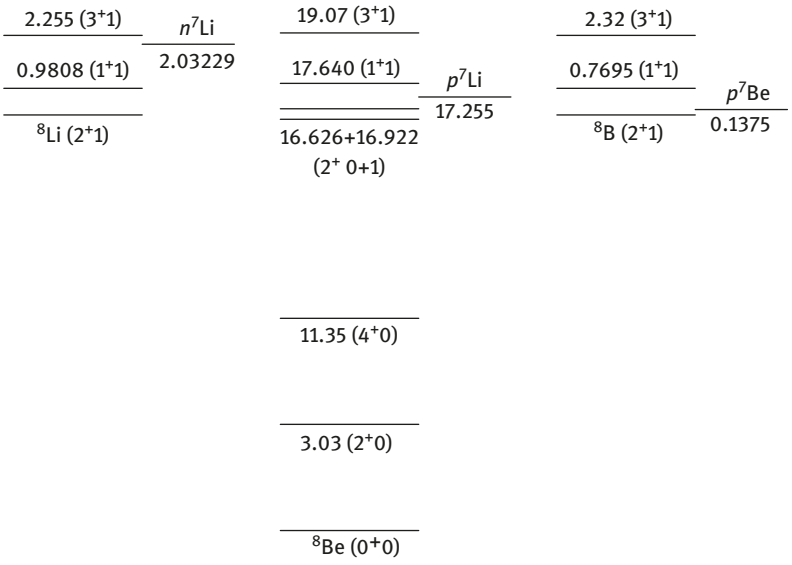

Fig. 2.3.1: Spectrum of levels in MeV (cm) of ^{8}Li, ^{8}Be and ^{8}B nuclei [205].

The bound state of the p^7Li system considered by us earlier with $J^\pi, T = 0^+,0$ [205], corresponding to the ground ^{8}Be state, because of the rules of addition of the moments can be formed only in the triplet spin channel with $L = 1$ which is found to be pure up to a $^3P_0$ spin state with $T = 0$ [205]. Therefore, for describing electromagnetic transitions, all the potentials obtained previously for this system [12, 23, 137] corresponding to the triplet spin state with a certain number of AS and FS defined above. All electromagnetic transitions occur between different levels in the triplet spin state, which has an allowed Young tableaux, and consequently, the allowed bound state corresponds to the ground state of ^{8}Be in the p^{7}Li channel.

In particular, the *E1* transition between the $^3S_1$ scattering state (mixed by isospin with $T = 0$ and 1) and the $^3P_0$ ground bound state with $T = 0$, as well as the *M1* transition between the resonance $^3S_1$ wave ($T = 1$) and the GS of ^{8}Be were considered. We will notice that some scattering states, for example, $^3S_1$ wave as in the p^{7}Li system $T_z = 0$, are mixed on an isospin with $T = 0,1$. Therefore, for the $^3S_1$ wave, only a part of potential which has $T = 1$ [12,23,137] was obtained. The $^3P_1$ scattering wave and its potential have a phase shift resonance, i.e., the resonance level of ^{8}Be for which $T = 1$ was experimentally defined, and such a state is pure on an isospin. These two processes allowed almost accurate description of the experimental data on an astrophysical *S*-factor of the proton radiative capture on ^{7}Li. For all these transitions, it

was possible to consider that there is a change of an isospin, i.e., the constraint $\Delta T = 1$ [12, 23, 137] was satisfied.

In this case, the bound state of the n^7Li system with $J^\pi, T = 2, ^+1$, corresponding to the GS of ^{8}Li, can be formed at $S = 1$ and 2 with the orbital moment of $L = 1$ and is a mix of $^3P_2$ and $^5P_2$ states. Despite lack of AS in the channel with $S = 2$ as it follows from the results of works [12,23,137], and the classification given above, it is necessary to consider the presence of the wave function of GS and the admixture of the $^5P_2$ wave. It is necessary to consider the *M1* transition from the $^5P_3$ resonance in the n^7Li scattering at 0.22 MeV (c.m.) with $J^\pi, T = 3^+, 1$ to the $^5P_2$ component of the wave function of GS of ^{8}Li.

The resonance with $J^\pi, T = 3^+, 1$ in the spectrum of ^{8}Li (Fig. 2.3.1) corresponds to the resonance of the $^5P_3$ phase shift of the elastic n^7Li scattering at energy of 0.22 MeV (cm) or 0.25 MeV (ls), which is higher than the n^7Li threshold [205]. Such resonance $^5P_3$ state of ^{8}Li can be formed only at total spin $S = 2$ of the n^7Li system. Furthermore, for creating the potential corresponding to such resonance of the phase shift of the elastic n^7Li scattering, we will use the data on spectra of levels of ^{8}Li and for widths of these states [205]. Of course, the state with $J^\pi, T = 3^+, 1$ can also be formed by the triplet $^3F_3$ configuration of the n^7Li system, and the resonance will be present in the $^3F_3$ phase of the elastic n^7Li scattering. In such cases, it is not necessary to assume the presence of admixtures of the $^5P_2$ state in the GS of ^{8}Li in the n^7Li channel, and it will be enough to consider only the $^3P_2$ configuration. However, based on all results of the phase-shift analysis [13] and similar results reported by us previously for similar cluster systems [12, 14], it is possible to conclude that the existence of resonance for the $^3F_3$ phase at such low scattering energy in the n^7Li system is very doubtful.

The state with $J^\pi, T = 1^+, 1$ is caused by $S = 1$ and 2, and $L = 1$ is the $^{3+5}P_1$ level in the n^{7}Li channel, which appears to be bound at a energy of 0.9808 MeV concerning the GS of ^{8}Li or –1.05149 MeV, relative to the threshold of the n^{7}Li channel [205]. Furthermore, we will consider the *E1* transitions to this level from the triplet and quintet *S* scattering wave. Therefore, all results will relate to ^{7}Li$(n,\gamma_0)^8$Li and ^{7}Li$(n,\gamma_1)^8$Li reactions and to the sum of their cross-sections. Furthermore, by the analogy with p^{7}Li scattering and based on data from [205], we will consider that $^3S_1$ and $^5S_2$ phase shifts in the range to 1.0 MeV are almost zero. This is confirmed by the absence the resonance levels of negative parity at such energies in the spectra of ^{8}Li.

Because previously in the p^{7}Li system [23, 137], we considered the variants of potentials with two FSs, for comparison we will also use the potentials for all further calculation of the radiative capture in the partial scattering waves with different number of the FSs. First, we will obtain *S* and *P* potentials with two FSs as it follows from the results given above as the third option of the classification of AS and FS (Table 2.3.1), and then we will consider the variants with one (the second variant of classification) and with zero FS, i.e., their complete absence in each partial wave.

Practically zero phase shift for the $^3S_1$ and $^5S_2$ scattering wave at low energies can be obtained with the following parameters

$$V_S = -145.5 \text{ MeV}, \quad \gamma_S = 0.15 \text{ fm}^{-2}. \tag{2.3.1}$$

Similar potential was used by us for considering the p^7Li scattering in the $^3S_1$ state [23,137], which contains two bound FSs with {8} and {44} as it follows from the third option of the classification of states given above as well as in [12,23].

The zero phase shift can be obtained with a potential

$$V_S = -50.5 \text{ MeV}, \quad \gamma_S = 0.15 \text{ fm}^{-2}, \tag{2.3.2}$$

which has only one FS for the second variant of the classification with {44} tableaux, and also without the FS at zero value of the depth of potential of Gaussian form (1.2.2), i.e., at $V_S = 0$ for both S-scattering waves.

Of course, S phase shifts close to zero in the both spin channels is possible by other variants of parameters of potential of the form (1.2.2). Thus, it is not possible to unambiguously fix the parameters of such an interaction and for parameters (2.3.1) and (2.3.2) with different number of FSs other combinations of V and γ are possible. However, as discussed further, for describing the total cross-sections of radiative capture, the greatest role is not played by different combinations of parameters V and γ or the quantity of FSs, but by closeness to zero scattering phase shifts obtained with such interactions.

The resonance $^5P_3$ phase shift of the elastic n^7Li scattering can be described by the deep Gaussian potential of the form (1.2.2), for example, with parameters

$$V_P = -4967.45 \text{ MeV}, \quad \gamma_P = 3.0 \text{ fm}^{-2}. \tag{2.3.3}$$

Such potential has two bound forbidden states which can be compared to {53} and {431} tableaux for the second variant of classification of the FSs if we were to consider that the FS with the {431} tableaux is bound. The calculation results of the $^5P_3$ scattering phase shift are shown in Fig. 2.3.2 by dotted curves. The resonance is at the energy of 254 keV (ls) with a width of 37 keV (cm) which completely coincides with the experimental value of 254(3) keV [205]. The experimental width $^5P_3$ of resonance is equal to 35(5) keV (ls) or 33(6) keV (cm) as per data presented in [205].

Potential parameters with one bound FS at {53}, which also corresponds to the second variant of the classification provided that FS with {431} is in a continuous spectrum, have the following form

$$V_P = -2059.75 \text{ MeV}, \quad \gamma_P = 2.5 \text{ fm}^{-2}. \tag{2.3.4}$$

The calculation results of scattering phase shift are shown in Fig. 2.3.2 by the dashed curve. Resonance is reached at the energy of 254 keV, and the width of the $^5P_3$ resonance is 35 keV (cm).

The potential parameters without the bound FSs which will be considered additionally are represented in the form

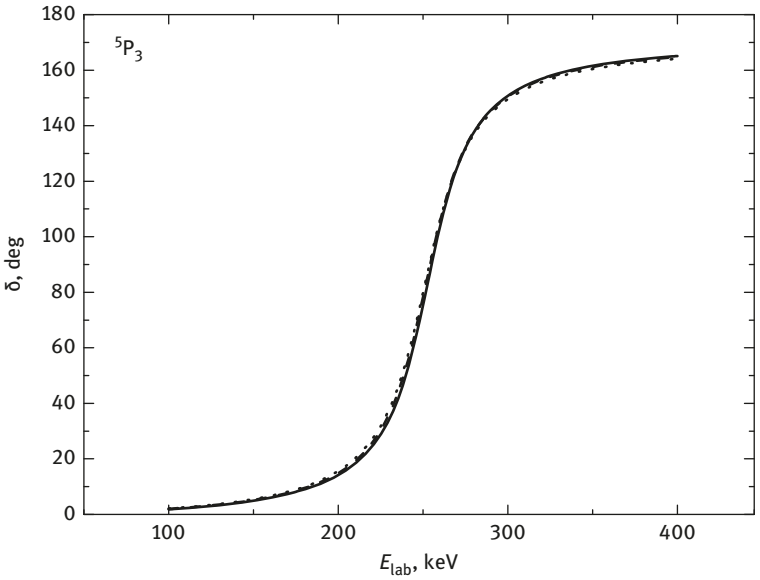

Fig. 2.3.2: Resonance $^5P_3$ phase shift of the elastic n^7Li scattering at low energies.

$$V_P = -425.15 \quad \text{MeV}, \quad \gamma_P = 1.5\,\text{fm}^{-2}. \tag{2.3.5}$$

The calculation results of the $^5P_3$ phase shift with such parameters are shown in Fig. 2.3.2 by the solid curve. The resonance is at the energy of 255 keV, and its width is equal to 34 keV (cm). Here, it is necessary to emphasize that the potential parameters at the given number of the bound FSs are determined completely unambiguously by the energy of the resonance and its width. The width of the $^5P_3$ resonance is determined according to the expression

$$\Gamma_{cm} = 2(d\delta/dE_{\text{cm}})^{-1}. \tag{2.3.6}$$

We generally consider the second variant of classification of cluster states of ^{8}Li according to Young tableaux for the potential of the bound $^{3+5}P_2$ state of the n^7Li system, therefore, it is possible to use the parameters

$$V_{\text{g.s.}} = -429.383779 \quad \text{MeV}, \quad \gamma_{\text{g.s.}} = 0.5\,\text{fm}^{-2}. \tag{2.3.7}$$

Except for the allowed BS, corresponding to the GS of ^{8}Li with {431}, such $^{3+5}P_2$ potential has the bound FS with {53} in full compliance with the second variant of

the classification of orbital states given above and in works [12,23,137]. With such potential, the binding energy reaches –2.032290 MeV, which is consistent with the experimental value [205], charge radius is 2.38 fm, and mass radius is 2.45 fm.

The root-mean square charge radius of ^{8}Li should not considerably exceed the ^{7}Li radius, which is 2.35(10) fm [205]. Therefore, the value of root-mean square radius obtained above for the n^7Li channel of the GS of ^{8}Li has a reasonable value. For the charge radius of neutron, zero value was used, and its mass radius, as usual, was considered to be 0.8775(51) fm [126], which is equal to the corresponding radius of proton.

The asymptotic constant in a dimensionless form (1.2.5) for such GS potential was equal to $C_w = 0.78(1)$. The error of an asymptotic constant is determined by averaging on an interval of 5–30 fm where its value was rather stable. The width of such potential of the GS (2.3.7) is selected based on the description of the charge radius of the nucleus and the AC, and the depth from a condition of reproduction of the channel binding energy at known FSs and ASs; consequently, all the parameters are fixed quite unambiguously.

For comparison consider the value of the AC of the n^7Li system $C(p_{3/2}) = 0.62$ fm$^{-1/2}$, obtained from experimental data analysis [158] which, after recalculation to the dimensionless value at $\sqrt{2k_0}$= 0.767, was 0.81. This value corresponds to the result obtained for the potential variant (2.3.7) of the GS of ^{8}Li in the n^7Li channel. In [206], the value 0.78 fm$^{-1/2}$ was obtained, which for the dimensionless value is 1.02. In work [195], the value 0.74 fm$^{-1/2}$ was obtained, giving a value of 0.96. In [196], for $C(^5P_2)$ the 0.59 fm$^{-1/2}$ is obtained and $C(^3P_2)$ = 0.28 fm$^{-1/2}$ which in a dimensionless form gives 0.77 and 0.36. All results are given in the assumption that S_f spectrofactor from (1.7.1) for the GS of ^{8}Li is equal to the unity.

However, values ranging from 0.66 to 1.143 with an average of 0.90 for a spectrofactor of the GS at an ANC of 0.657(3) fm$^{-1/2}$ have been reported previously [197]. This value of an average S_f is close but is not equal to unity. Therefore, based on (1.7.1), for average dimensionless C_w 0.90 is obtained. The range of possible values of the AC at this dispersion of S_f is 0.80–1.05, which is consistent with the obtained value for potential (2.3.7).

For the potential of the first excited state the following parameters are obtained

$$V_{e.s.} = -422.126824 \quad \text{MeV}, \quad \gamma_{e.s.} = 0.5\,\text{fm}^{-2}. \tag{2.3.8}$$

Here, allowed BS with {431} corresponds to the first excited state of ^{8}Li at an energy of 0.9808 MeV above the GS. In addition, this $^{3+5}P_1$ potential has the FS with {53} in full compliance with the second variant of classification of orbital states. With such potential based on the FDM [24] with an accuracy of 10^{-6} MeV the binding energy of –1.051490 MeV, which is consistent with the experimental value [205]; a charging radius of 2.39 fm and mass radius of 2.52 fm was also obtained. The asymptotic constant (1.2.5) of this potential is equal to $C_w = 0.59(1)$. The error in AC is defined by

its averaging on an interval of 4–25 fm where the asymptotic constant remains rather stable.

In [197], for the spectrofactor of the first ES, the values range from 0.322 to 0.517 with an average of 0.42 at an ANC of 0.288(3) $fm^{-1/2}$. Hence, based on (1.7.1) for the average dimensionless C_w at $\sqrt{2k_0}$= 0.65, we obtain a value of 0.68. The range of the possible values of the AC at a interval of S_f is 0.62–0.78, which is consistent with the obtained value for potential (2.3.8).

For the additional control of calculation of binding energy, the two-body VM with the expansion of the cluster wave function of the relative movement of the n^7Li system on nonorthogonal Gaussian basis at an independent variation of parameters [22,24] was used. At the dimension of N = 10 for the variant of GS potential (2.3.7), the energy of –2.0322896 MeV is obtained. For residuals of the order of 10^{-14} [24], an asymptotic constant, at the interval of 5–20 fm, was equal to 0.78(1), and the charge radius does not differ from the previous FDM results. The parameters of the expansion of the GS radial wave function of ^{8}Li in the cluster n^7Li channel are presented in Table 2.3.2.

Thus, for the real two-body binding energy in such a potential, it is possible to accept an average value of –2.0322898(2) MeV. In other words, the real accuracy of the determination of binding energy of ^{8}Li in the cluster n^7Li channel for the GS potential for determining this energy by two various numerical methods (FDM and VM) and using two various computer programs, is at the level of ±0.2 eV.

Table 2.3.2: The coefficients and parameters of the expansion of the radial variation wave function of the GS of ^{8}Li in the n^7Li channel [22]. The normalization factor of the wave function obtained in the range of 0–25 fm is N_0 = 9.999998392172028E–001.

i	α_i	C_i
1	2.111922863906128E–001	–1.327201117117602E–001
2	1.054889049037163E–001	–4.625421860118692E–002
3	9.251179926861837E–003	–1.875176301729967E–004
4	2.236449875501786E–002	–2.434284188136483E–003
5	4.990617934603718E–002	–1.282820835431680E–002
6	3.849142988488459E–001	–2.613687472261875E–001
7	5.453825421384008E–001	–2.108830320871615E–001
8	1.163891769476509	1.438162032150163
9	1.716851806191120	1.426517649534997
10	2.495389760080367	1.792643814712334E–001

For the first excited state of the VM, the obtained energy is –1.051488 MeV at the residuals 10^{-14} [24] – all other characteristics do not differ from the above values obtained using FDM. The expansion parameters of the wave function are given in Table 2.3.3, and the average energy can –1.051489(1) MeV, i.e., the error of its

calculation for such potential is 1 eV and coincides with the set accuracy of FDM of 10^{-6} MeV.

Table 2.3.3: The coefficients and parameters of the expansion of the radial wave function of the first excited state of ^{8}Li in the n^7Li channel [22]. The normalizing coefficient of the wave function obtained on an interval of 0–25 fm is N_0 = 9.999907842436313E-001.

i	α_i	C_i
1	2.034869839899546E–001	–1.268995424220545E–001
2	9.605255016688968E–002	–4.250984818616291E–002
3	6.473027608029138E–003	–2.029700124120304E–004
4	1.743880699865412E–002	–2.308434897721290E–003
5	4.241481028548091E–002	–1.167539819061673E–002
6	3.943411589808715E–001	–2.876208138367455E–001
7	5.758070107927670E–001	–1.307197681388061E–001
8	1.148526246366072	1.335023264621784
9	1.706295940575450	1.303208908841006
10	2.491484117851039	1.558051077479201E–001

For the considered system, it is visually shown in the approach used by us how the potentials of intercluster interactions for the scattering processes are constructed. They have to correctly reproduce the phase shifts of the elastic scattering of the considered particles accounting for their resonance behavior or spectrum of resonance levels of a final nucleus.

For the bound states as well as the excited or ground states of nuclei, which are formed as a result of reaction in the cluster channel coinciding with initial particles, intercluster potentials are constructed under the assumption of the description of binding energy of these particles in the final nucleus and certain main characteristics of such states [22, 24]. For example, the root-mean square charge or mass radius of the final nucleus and its asymptotic constant in the considered cluster channel are considered.

2.3.3 Radiative ^{7}Li(n,γ)^{8}Li capture

Here, in contrast to our previous work [207], we consider a variant of calculations when for a neutron the negative sign of the magnetic moment is considered which affects the resonance value at 0.22 MeV without affecting the cross-sections at other energies considerably. By considering electromagnetic processes in reaction ^{7}Li(n,γ)^{8}Li, as before for the proton capture on ^{7}Li [137], we will consider the *E1* transition from nonresonance$^3S_1$ scattering wave to the triplet $^3P_2$ part of wave function of the GS

1. $$^3S_1 \rightarrow {}^3P_2.$$

Besides, unlike the p^7Li system, the transition from the quintet $^5S_2$ scattering wave to a quintet $^5P_2$ part of the GS wave function of ^{8}Li will be added

2. $$^5S_2 \rightarrow {}^5P_2.$$

As already above, we take into account the *M1* transition from the resonance $^5P_3$ scattering wave with level at $J^\pi, T = 3^+, 1$ (Fig. 2.3.2) as the quintet $^5P_2$ part of the wave function of the ground state

3. $$^5P_3 \rightarrow {}^5P_2.$$

Within the considered model, because there is no opportunity to allocate in the wave function GS $^5P_2$ and $^3P_2$, we will use the P_2 function of a state mixed according to spins, which turns out at the solution of the Schrödinger equation with a potential of the BS for the parameters (2.3.7) for the calculations.

For transition to the first excited $^{3+5}P_1$ state the *E1* process from both ^{3+5}S scattering waves was considered

4. $$^3S_1 \rightarrow {}^3P_1$$

and

5. $$^5S_2 \rightarrow {}^5P_1.$$

Then, the total capture cross-section with all electromagnetic transitions considered here for the n^7Li capture can be presented as follows

$$\sigma_0(E1 + M1) = \sigma(E1,\ {}^3S_1 \rightarrow {}^3P_2) + \sigma(\mathrm{E1}, {}^5S_2 \rightarrow {}^5P_2) + \sigma(M1, {}^5P_3 \rightarrow {}^5P_2)$$

and

$$\sigma_1(E1) = \sigma(E1, {}^3S_1 \rightarrow {}^3P_1) + \sigma(E1, {}^5S_2 \rightarrow {}^5P_1).$$

The results of the calculations were compared with the experimental measurements of the total capture cross-sections at energies ranging from 5 meV to 1.0 MeV [165, 208–212].

As for each partial scattering wave three potential variants were obtained, we will discuss the results for each of these combinations in detail. We will give the final and the best calculation result for all the transitions of the total cross-section of neutron radiative capture on ^{7}Li to the GS of ^{8}Li at an energy up to 1.0 MeV (ls), which is shown in Fig. 2.3.3 by the dashed-dotted curve; at resonance, the cross-section has a value of approximately 59 μb. These results were obtained for the GS potential (2.3.7), the S scattering wave in the triplet and quintet states with parameters (2.3.2) and potential of the resonance $^5P_3$ scattering wave with parameters (2.3.4).

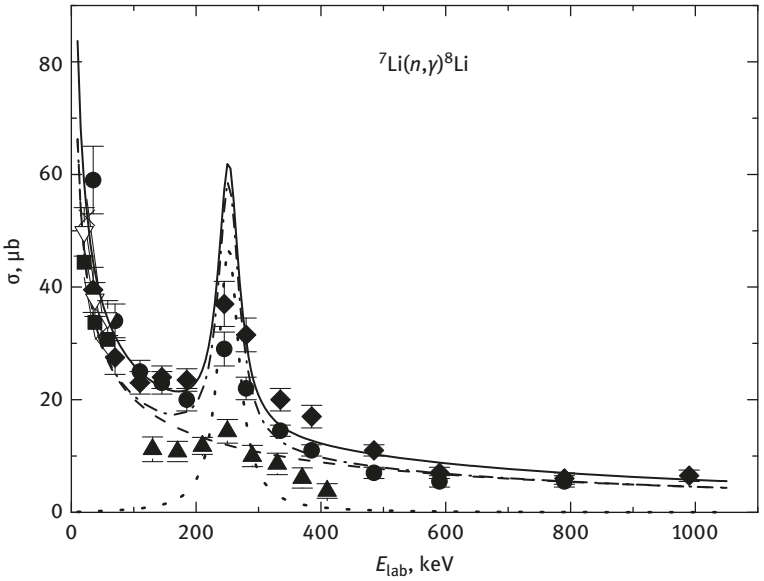

Fig. 2.3.3a: The total cross-section of the neutron radiative capture on ^{7}Li at low energies. Experimental data: ● and ◆ – from work [208], ■ – [209] for capture on the GS and ∇ - total cross-section for the capture on the GS and the FES, ▲ – [210], x – [165]. Curves – results of calculation for different electromagnetic transitions with the potentials are explained in the text.

Using a dashed curve the cross-section, corresponding to the sum of the $E1$ transitions from the $^3S_1$ and $^5S_2$ waves to the GS is shown, by a dotted curve – the $M1$ cross-section transition between the $^5P_3$ scattering state and the GS of ^{8}Li in the n^7Li channel with the resonance value of the cross-section of approximately 47 μb is shown. The solid curve denotes the results for the total cross-sections with all capture processes to the GS and FES approaching 62 μb are given. For the FES the potential (2.3.8) and the same potentials were used for the ^{3+5}S scattering wave. The contribution to the total cross-section of the transition at the resonance energy gives a value of approximately 3 μb.

In Fig. 2.3.3b, the form and value of the estimated total capture cross-sections for these potential variants at energies from 1 meV to 150 keV is shown in more detail

(the notations are the same as the previous figure). It is clear from these results that using potentials with one bound FS in the S and P waves in the framework of the potential cluster model, it is possible to describe available experimental data at the most wide energy range from 5 meV to 1.0 MeV [178,207].

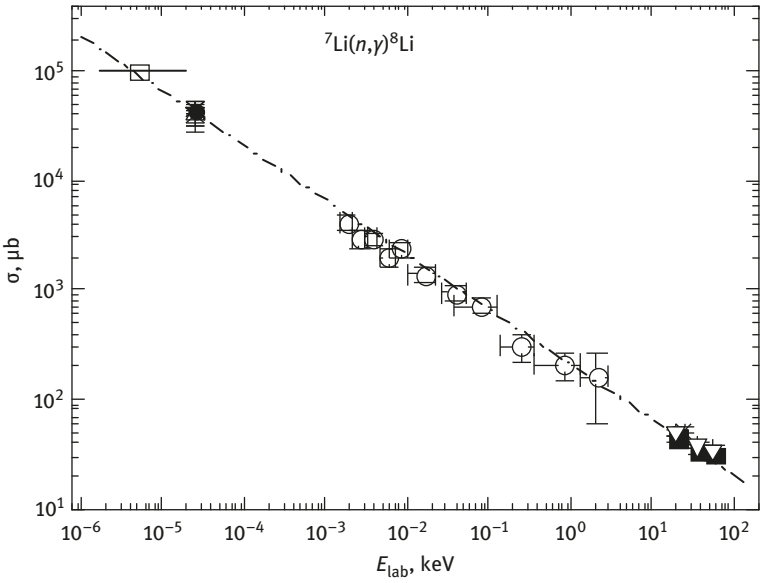

Fig. 2.3.3b: The total cross-section of the neutron radiative capture on ^{7}Li at very low energies. Experimental data: ■ – [209] for the capture to the GS and ∇ - the total cross-section for the capture of the GS and FES, ○ – [211] capture to the GS, □ – [142], Δ – [208], * – [212], x – [165], ● – [184]. Designations of the curves are as in Fig. 2.3.3a.

Here, it is necessary to note that in [211], the results of which are shown in Fig. 2.3.3b by open circles, the total capture cross-sections were measured only to the ground state of ^{8}Li; the calculated cross-section of this transition is shown by the dashed-dotted curve. In [209], the measurements for the capture as to the GS (black squares), and the total sum cross-sections taking into account the transitions to the GS and FES were carried out (the turned open triangles in fig. 2.3.3a, b), and the calculation of the total cross-sections are presented in this figure by the solid curve.

Using the variant of the scattering potential in the $^5P_3$ wave with two bound FSs (2.3.3) increases the cross-sections in the resonance at 0.25 keV approximately by 5%. Thereby, the ambiguity of FS number, noted above, in such a potential practically does not affect the results of the calculation. Using the variants of the scattering potential in the S waves with two FSs or without FS does not practically change the results of the calculation of the cross-sections.

Moreover, the use of ^3S and ^5S parameters of the potentials with depth of 100 MeV with a width of 0.3 fm^{-2}, i.e., twice differing from the initial (2.3.2), which also lead to zero scattering phase shifts, and influences the final results [178,207] a little.

However, the calculation of the cross-sections for the scattering potential in $^5P_3$ wave without the FS results in a decrease in the value of the total cross-section for the transition to the GS and the FES at a resonance energy of approximately 48 μb with the cross-section of the *M1* transition of 33 μb. This result improves the description quality of the available data in Fig. 2.3.3a for the total experimental cross-sections [208] within this energy range. However, the data [208] becomes maximum at 245 keV with the value of 37 μb, and the resonance is at energy of 255 keV; no data has been reported yet though. Therefore, it is impossible to estimate the value of the experimental cross-sections for the resonance energy, and some variants of potential would better describe the results.

Thereby, it cabe considered that the use of the potentials of the GS of ^{8}Li in the n^7Li channel with one FS (2.3.7) and the corresponding potentials of the scattering (2.3.2) and (2.3.4) reasonably describe the available experimental data regarding the total cross-sections of radiative capture in all considered energy ranges, which are distinguished by almost nine orders of magnitude. The presence or absence of forbidden states in the potentials of *S*-scattering waves does not play any role, and only the zero (0°±2°) values of the phase shifts are important.

Small changes in the estimated value of the total capture cross-sections do not allow unambiguous conclusions concerning the number of the bound FSs (1 or 2) for the $^5P_3$ scattering potential in the resonance energy region. Moreover, lack of experimental data at the resonance energy does not allow one to conclude the number of bound FSs (0 or 1, 2) for this $^5P_3$ potential [178,207].

Furthermore, similar to the previous systems, because for energies ranging from 1 meV to 100 keV the calculated cross-section is practically a straight line (see Fig. 2.3.3b a solid curve), it can be approximated by function of the form (2.1.3). The value of the constant A = 265.7381 μb keV$^{1/2}$ was determined by a single point in cross-sections with a minimum energy of 1 meV (l.s.). Similar to the previous cases, it is possible to consider the module of a relative deviation (2.1.4) the calculated theoretical cross-sections and approximations of this cross-section using the expression given above (2.1.3) as function of energy ranging from 10^{-6} to 100 keV (ls). Thus, we find that at the energies below 100 keV, this value does not exceed 1.0%.

If we were to assume that this form of dependence of the total cross-section from the energy (2.1.3) will remain at lower energies, it is possible estimate the value of the cross-section at energies of 1 μeV (1 μeV = 10^{-6} eV = 10^{-9} keV) giving a value of 8.4 b. For the dashed-dotted curve in Fig. 2.3.3b, the coefficient in the approximation of the cross-section is A = 210.538 μb keV$^{1/2}$, the deviation of approximation and calculation is lower than 100 keV and no more than 1.0%, and cross-section value at 1 μeV is approximately equal to 6.7 b [178,207].

2.4 The astrophysical neutron capture on ^{9}Be

Continuing the study of neutron capture reactions on light nuclei in the potential cluster model with a classification cluster states of Young tableaux and forbidden states, in some cases, [11, 22], we consider the $n^{9}\mathrm{Be} \to {}^{10}\mathrm{Be}\gamma$ reaction at thermal and astrophysical energies. For calculating total cross-sections of this reaction within the MPCM framework [12, 14], the knowledge of the potentials of the n^{9}Be interaction in a continuous and discrete spectrum is required [24]. Still, we will consider that such potentials correspond to the classification of cluster states by orbital symmetry [12, 14], as it was discussed earlier for other nuclear systems participating in the various thermonuclear processes or reactions of the primordial nucleosynthesis of the universe [3].

2.4.1 Classification of orbital states in the n^{9}Be system

Let us first consider the classification of the orbital states of clusters based on Young tableaux for ^{9}Be. If we assume that in the 8 + 1 particle system the {44} and {1} tableaux can be used, then for the ^{9}Be we will obtain two possible orbital symmetries {54} + {441}. The first of them is forbidden as it contains five cells in the same row, and the second relates to the allowed tableaux and corresponds to the allowed state in the relative motion of the N^{8}Be clusters (in this case, the neutron and ^{9}Be) [20].

At once we will note that the classification of the orbital states according to Young tableaux given here has only the qualitative character as the system of the A = 9, 10 particles, we could not successfully find the tables of internal multiplication of the Young tableaux, which define the spin-isospin symmetry of wave function of cluster system. Such data were available earlier for all A < 9 [134] and were used in the previous sections for analyzing the number of AS and FS in the wave functions of various cluster systems [12, 14, 19, 42, 136].

Furthermore, for the ground state of ^{9}Be, we accept the {441} tableaux, therefore, for the N^{9}Be system we have: {441} + {1} = {541} + {442} + {4411}. At this set there is the FS with the {541} tableaux for L = 1, 2, 3, etc., and the AS with a configuration {4411} at L = 1, 3. The orbital moment is determined using the Eliot's rule [28]. Furthermore, there is the allowed tableaux {442} with L = 0, 2, etc., which can lead to the allowed bound states in the S and D waves. Here, we are limited to the minimum values of the orbital angular momentum L, which will be required in future calculations of the total capture cross-sections.

We will remind that the possible orbital Young tableaux $\{f\}$ of the $A(\{f\})$ nucleus, consisting of two parts $A_1(\{f_1\}) + A_2(\{f_2\})$ is the direct external multiplication of the orbital Young tableaux of these parts $\{f\}_L = \{f_1\}_L \times \{f_2\}_L$ and are determined by the Littlewood theorem described previously [20, 21, 28]. Therefore, it is possible by the orbital Young tableaux of the N^{9}Be system, when for ^{9}Be the {441} tableau is used,

$\{541\}_L$, $\{442\}_L$ and $\{4411\}_L$ are the symmetries. The spin-isospin tableaux of the wave function BS are the direct internal multiplication of the spin and isospin Young tableaux the nucleus from the A nucleons $\{\{f\}_{ST} = \{f\}_S \otimes \{f\}_T$ and for the system, with not more than eight number of particles, which is given in [134].

In this case, for the n^{9}Be cluster system at the isospin $T = 1$ we have $\{64\}_T$ and for a spin state with $S = 1$, we also obtain $\{64\}_S$. Because the GS of ^{10}Be with the total moment of $J^\pi = 0^+$ can be formed only in a triplet spin $^3P_0$ state with the {4411} tableaux, for all other states in the n^9Be channel we will consider only $S = 1$. Therefore, for the spin-isospin Young tableau for triplet spin n^{9}Be state of the system we have $\{64\}_S \otimes \{64\}_T$.

The total wave function of the system at antisymmetrization does not become zero, only if ut contains the antisymmetric component $\{1^N\}$ realized at the multiplication of conjugated $\{f\}_L$ and $\{f\}_{ST}$. Therefore, $\{f\}_L$ tableaux conjugated to $\{f\}_{ST}$ are allowed in this channel, and all other orbital symmetries are forbidden as it leads to a zero total wave function of the particle after its antisymmetrization.

However, as we have no multiplication tables of the form [134], it is impossible to define the result $\{f\}_{ST} = \{64\}_S \otimes \{64\}_T$ of such a multiplication. Therefore, there is no opportunity to determine unambiguously which of the possible orbital tableaux will be allowed and what will be forbidden [12,19,42,136]. However, for the sake of definiteness, it is possible to consider that there is the bound AS in the ^3S wave at {442}, and in the ^3D wave, which contains the bound FS for {541} tableaux, the state with {442} is not bound. Certainly, such an assumption is not unambiguous and it is a possible variant of the ^3D potential with two BSs, the second of which can be allowed

Thus, the n^{9}Be potential of the $^3P_0$ wave should have the bound states with the {541} and {4411} Young tableaux, first of which is forbidden and the second is allowed, which corresponds to the GS of ^{10}Be in the n^9Be channel. In other ^3P waves by the consideration of the excited states of the AS for the {4411} corresponds to this excited state. In the scattering processes for the ^3P waves, we will consider the unbound AS, i.e., their potentials will contain only one bound FS with the {541} tableaux. Spectrum of ^{10}Be levels is shown in Fig. 2.4.1a.

For the $^3S_1$ scattering wave with one bound AS for the {422} tableaux, we will consider the variant of the potential wherein we will compare it to the excited state of the nucleus at an energy of 5.9599 MeV for $J^\pi = 1^-$ concerning the GS of ^{10}Be, bound in the n^9Be channel. Thereby, we unambiguously fix the structure of the FS and AS in each partial potential for $L = 0,1,2$, which will be considered below. We will notice that the number of the BS, forbidden or allowed in any partial potential, defines the number of nodes of the wave function at short distances – typically less than 1 fm [11,12,136]. Remember that the wave function of the bound state with the minimum energy has no nodes, the energy of the BS has one node, and so on.

In [213], based on the consideration of transitions only to the GS of ^{10}Be from the ^3S scattering wave with the zero phase shift, it was shown that ambiguity of forbidden or allowed BS to the $^3S_1$ scattering wave and the $^3P_0$

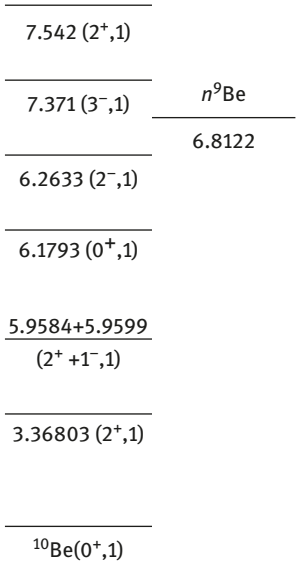

Fig. 2.4.1a: Spectrum of ^{10}Be levels in MeV (cm) of [205].

potential of the GS ^{10}Be has practically no effect on the calculations in case these potentials contain 1–2 BS in the first case and 2–3 BS in the second. Consequently, the ^3S and $^3P_0$ potentials of waves will be consistent with the above classification of the FS and AS according to Young tableaux considered above and in [213] as the second classification variant.

Furthermore, we will consider the transitions from the ^3D scattering wave, and as the basic version, we accept the variant of the potential with one FS at {541}, considering the unbound state for the {442} tableaux. The calculation result with such potential is compared with two of its other variants. The first variant of potential is considered without any BS, which is not consistent with the above classifications. As the second variant of the potential with two BS is used, first of which is forbidden for the {541} tableaux and the second is allowed and bound at {442}. Such a variant will also be consistent with the classification mentioned above as it does not give the chance to define whether there will be bound AS.

Here, it must be kept in mind that for the ^3S wave the internal part of a nucleus is "transparent" due to the lack of a Coulomb and centrifugal barrier for the capture of neutrons and the number of nodes of the wave function at small distances plays an important role. Therefore, the wave function results at zero nodes and one-two nodes differ considerably [213]. In case of the ^3D wave, there is a centrifugal barrier; therefore, the dependence of results from the structure of the ^3D wave in the internal area, i.e., the number of nodes at short distances, are significantly weaker than that in the previous case.

2.4.2 Potential description of the n^{9}Be phase shifts

Because we did not manage to find any data on the phase shifts of the elastic n^9Be scattering at astrophysical energies [150,151], the potential of the $^3S_1$ scattering process leading to to phase shifts appraching zero or smoothly falling down at energies to 1.0 MeV are considered. It follows from the data on the spectra ^{10}Be levels which do not contain the ^3S resonances $J^\pi = 1^-$ at this energy region [205]. The potential will be constructed to correspond to the third ^{10}Be excited state, which is bound in the n^9Be channel. This potential will be used for calculating the total cross-sections of the *E1* transition from the $^3S_1$ scattering wave on some bound states of ^{10}Be in the n^9Be channel from the ^3P scattering waves to the $^3S_1$ third excited, but the bound state of ^{10}Be.

Potential of the bound allowed $^3P_0^1$ state (hereinafter on the right above from L, the number of level is specified) is constructed using the description of the main characteristics of ^{10}Be in the n^9Be system, i.e., the binding energy, the charge radius, and the asymptotic constant [205]. For this potential corresponding to the ground state of ^{10}Be in the considered cluster channel, the following parameters are found

$$V_{\text{g.s.}} = -363.351572\,\text{MeV}, \quad \gamma_{\text{g.s.}} = 0.4\text{fm}^{-2}. \tag{2.4.1}$$

With such a potential, the binding energy of −6.812200 MeV at an FDM accuracy of 10^{-6} MeV [24] is obtained, the root-mean square charge radius of 2.53 fm, and mass radius of 2.54 fm. The experimental value for the charge radius of ^{10}Be [205,214] is absent, and for ^{9}Be is 2.518(12) fm [214]. We will further consider that ^{10}Be radius should not considerably exceed the ^{9}Be radius. For the charge radius of a neutron, as usual, the zero value is used, and its mass radius was accepted to be equal to the radius of a proton specified in a database as −0.8775(51) fm [126].

The asymptotic constant (1.2.5) of such a potential calculated using the Whittaker's function (1.2.5) [94] at distances of 4–16 fm was C_w = 1.73(1). The AC error is determined by its averaging by the specified interval where the asymptotic constant remains almost stable. Except the allowed BS, corresponding to the ground state of ^{10}Be with the {4411} tableaux, such $^3P_0$ potential has the bound FS for the {541} tableaux, which is in full compliance with the classification of orbital states of clusters discussed above (in this case it is a neutron and ^{9}Be) in system of 10 nucleons for the channel 9 + 1.

For comparing the asymptotic constants, we will give the results of work [215] where C^2 = 1.69(15) fm^{-1} was reported. This result is obtained for the spectroscopic factor S_f which is not equal to unity (1.7.1). Therefore, the initial C^2 value should be divided into S_f value in this channel [215], which according to the results of theoretical work [216] is 0.2. However, in [205] using the analysis of the experimental data on the ^{9}Be(^{2}H,p_0)^{10}Be reaction for S_f of ^{10}Be in the n^9Be channel gives a value of approximately 0.9. As at the time of writing of this material in the initial articles

[178, 217], we did not manage to find the other results as average S_f value was 0.55. Then, for the AC in a dimensionless look (1.2.5) $\sqrt{2k_0}$= 1.045 from (1.2.5) and (1.7.2) we will obtain C_w = 1.68(7). Such value corresponds with the results of the AC of the potential of the GS (2.4.1) specified above.

At the same time, in the later review [197], which was released in parallel to our main article [217], shows completely different values obtained based on various theoretical calculations. For a spectrofactor, the interval from 1.515 to 2.672 with an average value of 2.09 was given at the theoretical ANC (1.7.1), which is 3.02 $fm^{-1/2}$. In that case, using the average value of spextrofactor, the AC value of C_w = 2.00 is obtained, which is defined in (1.2.5). If we were to consider the whole range of spectrofactor values, we will obtain that the value of C_w is in the range of 1.77–2.35. This interval corresponds with the previous results [205,216] and the calculations for the potential (2.4.1).

For the additional control of the accuracy of calculation of the binding energy of the GS, the variation method with the expansion of the wave function of the n^9Be cluster system on nonorthogonal Gaussian basis was used [24]. At the dimension of basis N = 10, for the potential of the GS (2.4.1) the energy of –6.812193 MeV which only on 7.0 eV differs, from the given above, finite-difference value [24] is obtained. The residuals of the order of 10^{-10}, asymptotic constant in the interval of 5–12 fm is 1.73(2), and the charge radius does not differ from the previous FDM results. The parameters of expansion of the obtained variation radial wave function of the GS ^{10}Be in the cluster n^9Be channel are specified in Table 2.4.1.

Table 2.4.1: Coefficients and parameters of the expansion of the radial variation wave function of the ground state of ^{10}Be in the n^9Be channel (2.4.1) on the non-orthogonal Gaussian basis [24]. The normalizing coefficient of the wave function is N_0 = 1.000000000000000.

i	α_i	C_i
1	3.243377804018342E–002	–2.109602538815203E–003
2	7.917555096623996E–002	–2.750811638982709E–002
3	1.784595811352628E–001	–1.453439750665609E–001
4	3.746612146329068E–001	–4.789696250511998E–001
5	1.126366082891110	2.312966715268185
6	2.331534330644200	3.209514146107344
7	2.741502097647982	–5.201076539985449
8	3.216691148332270	3.694013806676463
9	3.852002896536004	–1.161048304949317
10	4.956980070114872	1.186950441156130E–001

As the variation of energy increases an the dimension of the basis decreases and gives the top limit of the true binding energy, and the finite-difference energy reduces at the value of step and increases the number of steps [24], then for the real binding energy in such potential it is possible to accept the average value –6.8121965(35) MeV. Thus, the accuracy of determining two-body binding energy of ^{10}Be in the cluster

n^9Be channel by two various methods (FDM and VM) according to two different computer programs for potential (2.4.1) is in the level of ±3.5 eV.

For the potential of the first excited $^3P_2^1$ state of ^{10}Be at energy of −3.44417 MeV relatively to the n^9Be channel threshold with $J^\pi = 2^+$ parameters were obtained

$$V_{P2} = -345.676472 \quad \text{MeV}, \quad \gamma_{P2} = 0.4 \quad \text{fm}^{-2}. \tag{2.4.2}$$

Such potential leads to the energy of −3.444170 MeV, charge 2.54 fm and mass radii of 2.57 fm, the AC is equal to 1.15(1) at the interval of 4–18 fm and has one bound FS at {541}, i.e., corresponding to the classification of cluster orbital states according to Young tableaux given above. As we have no data on the AC of this ES, for creating such potential the γ width, as for the potential of GS which provided the correct value of its AC is used.

For the potential of the second excited state $^3P_2^2$ of ^{10}Be at energy of −0.85381 MeV in the n^9Be channel with $J^\pi = 2^+$ which also has one FS, the following parameters were obtained

$$V_{P2} = -328.584413 \quad \text{MeV}, \quad \gamma_{P2} = 0.4 \quad \text{fm}^{-2}, \tag{2.4.3}$$

This potential allows to obtain the binding energy of −0.853810 MeV, charge radius of 2.55 fm, mass radius of 2.69 fm, and AC of 0.60(1) at an interval of 4–26 fm.

At the energy of 5.95990 (6) MeV or −0.8523 MeV concerning the threshold of the n^9Be channel the third ES with $J^\pi, T = 1^-, 1$ [205] is observed. Such ES of ^{10}Be can be considered as the bound AS in the $^3S_1$ wave with Young tableau {422}. Therefore, we use the potential of the form

$$V_{S1} = -33.768511 \quad \text{MeV}, \quad \gamma_{S1} = 0.4\ \text{fm}^{-2}, \tag{2.4.4}$$

This leads to the binding energy of −0.852300 MeV [205], to the charge and mass radii of 2.57 fm and 2.76 fm, and the AC of 1.24(1) at an interval of 4–30 fm. The phase shift of such potential is shown in Fig. 2.4.1b by the dashed curve and smoothly reduces to 121° at 1.0 MeV.

It would be possible to consider $M1$ transition from the nonresonance $^3S_1$ scattering wave to the same $^3S_1$ bound state of ^{10}Be. However, usually it is considered that the cross-sections of such ^{9}Be$(n,\gamma_3)^{10}$Be process will be by 1 or 2 orders smaller than that obtained in the *E1* capture. If were to use the $^3S_1$ wave in the continuous and discrete spectrum the same potential of the third ES (2.4.4), such cross-section will aspire in general to zero because of orthogonality of wave function. Therefore, the potential (2.4.4) without the FS will be used further for the calculation the total cross-sections of the *E1* transition from the $^3S_1$ scattering wave $^3P_0^1$ to the bound GS of ^{10}Be in the n^9Be channel of the form

1. $$^3S_1 \rightarrow {}^3P_0^1$$

and the fourth excited $^3P_0^2$ state at 6.1793 MeV with $J^\pi = 0^+$, considered further, i.e. for

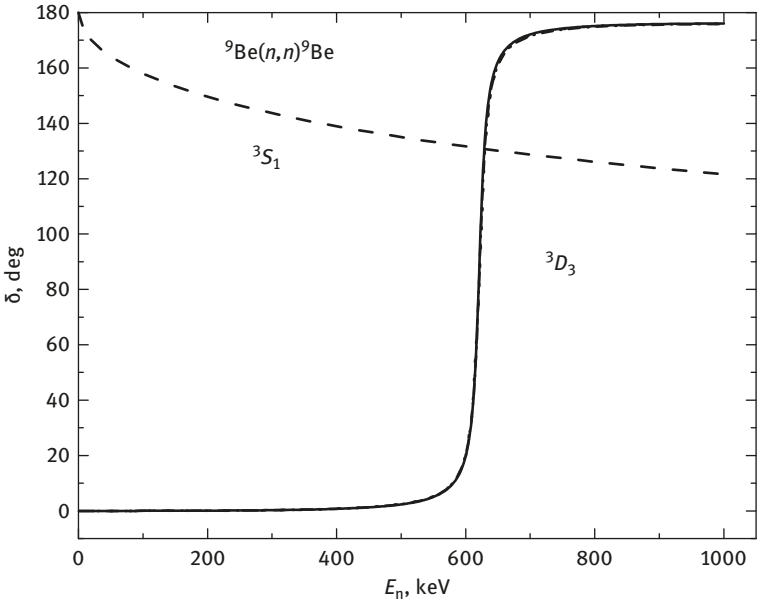

Fig. 2.4.1b: $^3S_1$ and $^3D_3$ phase shifts of the elastic n^9Be scattering at low energies. The lines - calculations with Gaussian potentials the parameters of which are given in the text.

2. $$^3S_1 \rightarrow {}^3P_0^2$$

transitions.

Moreover, the $E1$ transition is possible to the first $^3P_2^1$ ES at energy of 3.36803 MeV and to the second $^3P_2^2$ ES at 5.95839 MeV with $J^\pi = 2^+$, i.e.

3. $$^3S_1 \rightarrow {}^3P_2^1 + {}^3P_2^2.$$

The fourth ES $^3P_0^2$ at energy of 6.17930(7) MeV relative to the GS or −0.6329 MeV relative to the threshold of the n^9Be channel of ^{10}Be [205] for their quantum numbers J^π,T = 0^+,1 which coincides with the GS. Therefore, it is possible to consider $E1$ transition to this BS from the scattering wave $^3S_1$ with the potential (2.4.4). We will use the potential of the fourth ES with the next parameters

$$V_{P0} = -326.802239\,\text{MeV}, \quad \gamma_{P0} = 0.4 \quad \text{fm}^{-2}, \tag{2.4.5}$$

This leads to the binding energy in this channel of −0.632900 MeV, to the charge and mass radii of 2.56 fm and 2.72 fm, respectively, and the AC is equal to 0.53(1) at an interval of 4–28 fm.

We will further consider the resonance states of the n^9Be scattering at energies less than 1.0 MeV. It is known that in the spectra of ^{10}Be in the n^9Be channel there is a superthreshold level with $J^\pi = 3^-$ at the energy 0.6220(8) MeV (ls) and a width of 15.7 keV (cm) [205], which can be compared to the $^3P_2$ resonance in the elastic n^9Be scattering. In addition, the level with $J^\pi = 2^+$ is observed at the energy of 0.8118(7) MeV (ls) and the width of 6.3 keV, which can correspond $^3P_2$ to the resonance in the n^9Be scattering [205]. In the first case, it would be possible to consider the $E3$ transition, and in the second case, the $M2$ process on the GS of ^{10}Be. However, the cross-sections of such transitions much less than the $E1$ process and will not be considered.

Therefore, furthermore it is possible to consider the $E1$ transition, for example, from the resonance $^3D_3$ scattering wave on the first and the second $^3P_2$ excited states of ^{10}Be with $J^\pi = 2^+$ at the energies of 3.36803 MeV and 5.95839 MeV relative to the GS which are bound at −3.44417 MeV and −0.85381 MeV relative to the threshold of the n^9Be channel [205]

4. $$^3D_3 \rightarrow {}^3P_2^1 + {}^3P_2^2,$$

owing to which all the calculated cross-sections ^{9}Be$(n,\gamma)^{10}$Be will have the smooth character only in the range of small energy, i.e., approximately to 0.1–0.2 MeV.

For the potential of the resonance $^3D_3$ scattering wave the following parameters are found

$$V_{D3} = -457.877 \quad \text{MeV}, \quad \gamma_{D3} = 0.35 \quad \text{fm}^{-2}. \tag{2.4.6}$$

The phase shift of the elastic scattering for this potential is shown in Fig. 2.4.1b by the solid line, which has a resonance character. The potential contains the bound FS with {541} according to the classification given above, and the state for {422} is unbound. If for the calculation of width of the level according to the scattering phase shift δ to use the expression (2.3.6), the width of such resonance is equal to 15.0 keV (cm) that quite corresponds to the results given in the review [205].

This variant of the potential, with such structure of FSs, we will consider as basic, however, for the comparison we will consider further two more other variants of the $^3D_3$ potentials. The second variant of the $^3D_3$ potential has the following parameters

$$V_{D3} = -132.903 \quad \text{MeV}, \quad \gamma_{D3} = 0.22 \quad \text{fm}^{-2}. \tag{2.4.7}$$

The phase shift of the elastic scattering is shown in Fig. 2.4.1b by the dashed-dotted curve, the resonance is also at 622 keV with a width of 15.7 keV, and the potential itself does not contain any forbidden bound or allowed states, i.e., this potential corresponds to the case where the FS for the {541} is absent and the state with {422} remains unbound.

Now, we consider the variant of the potential of the $^3D_3$ scattering wave with parameters

$$V_{D3} = -985.183 \quad \text{MeV}, \quad \gamma_{D3} = 0.43 \quad \text{fm}^{-2}, \tag{2.4.8}$$

that at a resonance in 622 keV leads to the width of 15.5 keV and has two bound states. The first corresponds to the bound FS with {541}, and the second to the bound state at {422}. The phase shift is shown in Fig. 2.4.1b by the dotted curve. This differs from the solid line only at the lowest energies, namely, lower than 400 keV.

For potentials of the nonresonance $^3D_2$ and $^3D_1$ scattering wave were used the values of parameters

$$V_D = -300.0 \quad \text{MeV}, \quad \gamma_D = 0.35 \quad \text{fm}^{-2}. \tag{2.4.9}$$

which lead to the zero phase shifts because in these waves the resonances are not observed. Such potentials, similar to the variant of the potential (2.4.6), contain the bound FS with {541} according to the classification given above, and the state for {422} is not bound.

As mentioned earlier, in the elastic n^9Be scattering the resonance level with $J^\pi = 2^+$ at energy of 0.8118(7) MeV (ls) is higher than the n^9Be threshold and with the width of 6.3 keV, which can be compared to the $^3P_2$ resonance [205]. In other partial $^3P_0$ and $^3P_1$ waves of resonances, the potentials containing one bound FS for the {541} tableaux has not not been observed, have to lead to the phase shifts close to zero. The parameters of potentials with one BS which is forbidden are obtained for them

$$V_P = -206.0 \quad \text{MeV}, \quad \gamma_P = 0.4 \quad \text{fm}^{-2}. \tag{2.4.10}$$

We did not manage to obtain the potential for the resonance $^3P_2$ wave which can describe its small width of 6.3 keV [205], therefore, for calculating *E1* transitions

5. $$^3P_0 + {}^3P_1 + {}^3P_2 \rightarrow {}^3S_1$$

on the third ES for all ^3P scattering waves the identical, specified above potential (2.4.10), was used, i.e. in the carried out calculations the influence of the $^3P_2$ resonance was not considered. In all carried out calculations the mass of ^{9}Be equals m (^{9}Be) = 9.0121829 amu was used [214].

2.4.3 Total cross-sections of the neutron capture on ^{9}Be

By considering the electromagnetic transitions for radiative capture first of all the *E1* transition from the nonresonance $^3S_1$ scattering wave with potential (2.4.4) to the

bound in the cluster n^9Be channel the $^3P_0^1$ ground state of ^{10}Be at $J^\pi,T = 0^+,1$ with potential (2.4.1). For these potentials, the results of the total capture cross-sections are shown in Fig. 2.4.2 by the double dotted-dashed line.

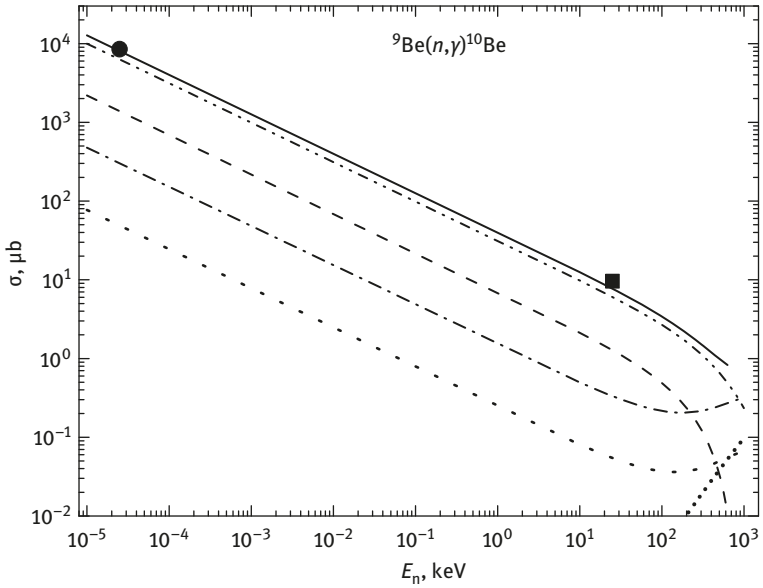

Fig. 2.4.2.: The total cross-section of the radiative neutron capture on ^{9}Be. Points (●) – the experimental data from work [184,218] at 25 meV and squares (■) – from [219] at 25 keV. Curves – the results of the calculation of the total cross-sections.

The experimental data for the total cross-sections at energies ranging from 25 meV to 25 keV (ls) from previous studies [184, 218, 219]. In [219], the results of the different extrapolations of total cross-sections for the radiative neutron capture on ^{9}Be at energies of 10 meV–20 MeV are also given. Data for the cross-section at thermal energy of 8270(130) μb is given in the new experimental work [184], which is slightly different from the results of [218], where the value of 8490(340) μb is given.

The results for the total cross-sections of the $^3S_1 \to {}^3P_2^1$ transition with the potential combinations of the first ES in the $^3P_2$ wave (2.4.2) and the $^3S_1$ scattering wave (2.4.4) are shown by the dashed curve in Fig. 2.4.2. The results for the $^3S_1 \to {}^3P_2^2$ transition with a potential of the second ES (2.4.3) and a potential of the ^3S wave (2.4.4) are shown by the dashed-dotted curve. The results for transition from the ^3S scattering wave (2.4.4) to the fourth $^3P_0^2$ ES with $J^\pi = 0^+$ and potential (2.4.5) are denoted by the dotted curve.

The solid curve is the sum of all these transitions. As can be seen from these results, the estimated value of the total cross-section in the range of 25 meV to 25 keV gradually increases with decreasing energy, and the used transitions allow one to

describe the total cross-sections in the resonance energy region. All used potentials satisfy the classifications according to Young tableaux and have the FSs in the ^3P waves.

Now, let us consider the *E1* transitions from the $^3D_3$ resonance scattering wave with $J^\pi, T = 3^-, 1$ and the energy of 0.6220(8) MeV (ls) and a width of 15.7 keV [205] for the first and the second excited states of ^{10}Be with $J^\pi, T = 2^+, 1$ which can be compared the $^3P_2$ bound states of the n^9Be system relatively to its threshold. The calculation results of the total cross-section of the *E*1 transition to the second excited state with the (2.4.3) and (2.4.6) potentials are presented in Fig. 2.4.3a denoted by the dotted curve and the dashed curve represents the transition to the first excited state with (2.4.2) and (2.4.6) potentials. The dashed-dotted line shows the sum of all cross-sections for the *E1* transitions, as shown in Fig. 2.4.2 by the solid curve. The solid curve in Fig. 2.4.3a is the sum of all cross-sections of the above-mentioned transitions in the ^{9}Be(n,γ)^{10}Be reaction.

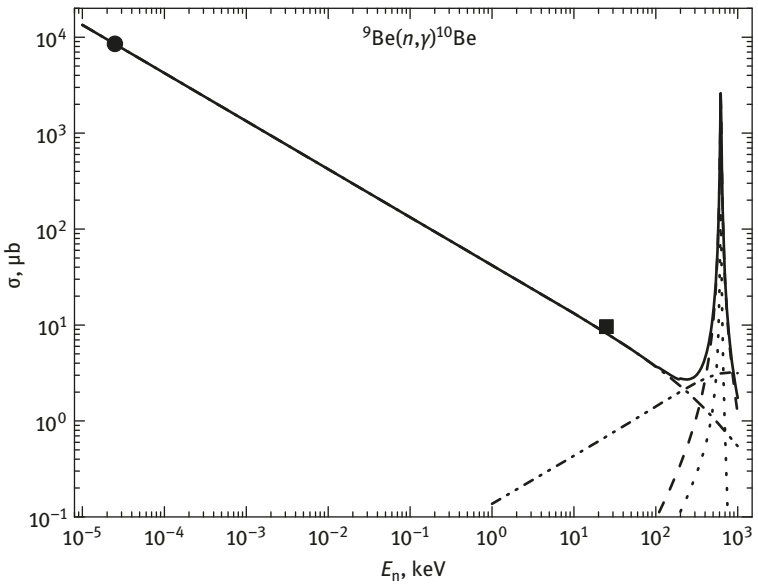

Fig. 2.4.3a: The total cross-section of the radiative neutron capture on ^{9}Be taking into account the resonance at 622 keV. Points (●) – experimental data from work [184,218] at 25 meV and squares (■) from [219] at 25 keV. Curves – the results of the calculation of the total cross-sections.

It can be seen that the magnitude of the cross-sections for the *E1* transitions in the resonance region of 622 keV (dashed-dotted line in Fig. 2.4.3a) is three orders of magnitude less than the cross-section of the transition to the first and second excited states of the resonance $^3D_3$ wave and does not have a noticeable contribution in the total cross-section. At the resonance energy of 622 keV, the total cross-section of the

transition from the $^3D_3$ scattering wave on the first excited state at −3.44417 MeV reaches 2.45 mb, and the second with the energy of −0.853810 MeV is approximately 0.16 mb.

The resonance range at 622 keV in more details is shown in Fig. 2.4.3b – the solid curve also shows the total cross-section for the capture process, and the width of the resonance, which is extracted from the total capture cross-sections is approximately 16–17 keV. The dashed and dotted curves coincide with the results shown in Fig. 2.4.3a for the transitions to the first and second ESs.

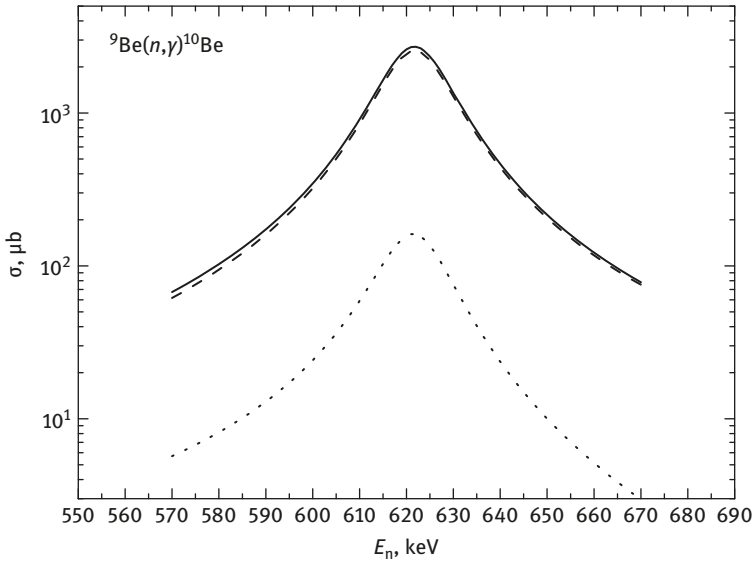

Fig. 2.4.3b: The total cross-sections of the radiative neutron capture on ^{9}Be taking into account the resonance at 622 keV.

We considered the nonresonance transitions from the $^3D_2$ or $^3D_1$ scattering states with the (2.4.9) potentials to the first ES for the (2.4.2) potential

6. $$^3D_1 + {}^3D_2 \to {}^3P_2$$

and the transition from the $^3D_1$ scattering wave to the GS (2.4.1) of ^{10}Be, i.e.,

7. $$^3D_1 \to {}^3P_0^1.$$

In the first case, the capture cross-section is shown by a portion of dots at the bottom right in Fig. 2.4.2. It practically does not differ from the results of the second case with

transition to the GS. Thus, it is clear that such transitions start playing a significant role only at energies higher than 1.0 MeV.

Furthermore, the results of the ^{9}Be(n,γ_3)^{10}Be calculation for the sum of all three *E1* transitions $^3P_0 + {}^3P_1 + {}^3P_2 \rightarrow {}^3S_1$ with potentials of all ^3P waves in the form of (2.4.10) and the bound ^3S state (2.4.4) are shown in Fig. 2.4.3a by the double dotted-dashed line. It is clear that the cross-sections obtained as a result of such transitions make a slight contribution to the total cross-sections only at energy higher than 10 keV, and from area higher than 150 keV their value exceeds the cross-sections for the ${}^3S_1 \rightarrow {}^3P_0^1$ transition, shown in Fig. 2.4.3a by the dashed-dotted curve.

Use of potentials for the resonance $^3D_3$ phase shift with the different number of FSs practically does not affect the resonance value which influence is observed in sections at the energies higher than 0.2 MeV. Therefore, it is always possible to consider that the ^3D scattering wave can contain one bound FS for the {541} tableaux and the state with {422} is not bound.

Simultaneously, the $^3S_1$ wave contains in a continuous and discrete spectrum allowed BS with the {422} tableaux, and FSs are absent. All the ^3P potentials of the discrete spectrum contains a single bound FS for the {541} tableau and one bound AS for {4411}. The bound allowed state in the $^3P_0$ wave corresponds to the GS of ^{10}Be for the n^9Be channel. The ^3P scattering potentials have the bound FS, and the bound AS is absent. Thereby, all considered potentials correspond to the classification of the FSs and ASs according to Young tableaux and using the consideration of several possible *E1* transitions between different states of ^{10}Be and scattering processes allow one to describe the available experimental data on the capture cross-sections.

Thus, within certain assumptions of the general character concerning the potentials of interaction of the n^9Be channel in a continuous and discrete spectrum, it is possible to describe the available experimental data on the total cross-sections for the neutron capture at energies of 25 meV and 25 keV. However, it should be noted that the experimental data which are available at our disposal on sections of the considered reaction of capture it is obviously are not enough. Furthermore, more careful research of the radiative $n^9\text{Be} \rightarrow {}^{10}\text{Be}\gamma$ capture at thermal and astrophysical energies is required, especially in the field of a resonance for $J^\pi = 3^-$ at 0.622 MeV.

Because at the energies from 10^{-5} to 10 keV the calculated cross-section presented in Fig. 2.4.2 by the solid curve is practically a straight line, it can be approximated by a simple function from energy of a look (2.1.3). The value of a constant A = 42.4335 μb keV$^{1/2}$ was determined by one point in the total cross-sections with a minimum of energy of 10^{-5} keV (l.s.).

Furthermore, it is possible to consider the module of the relative deviation (2.1.4) from the calculated theoretical cross-section and approximations of this cross-section by such function in the energy range from 10^{-5} to 10 keV. It appeared that at energies lower than 10 keV, this deviation does not exceed 0.7%, which allows one to use the approximation of the cross-section given above in the most problems.

It is possible to suggest that this form of dependence of the total cross-section by energy will be preserved at lower energies. In that case, the performance of an assessment of the value of the cross-section, for example, at energy of 1 μeV (10^{-6} eV = 10^{-9} keV), gives the value of 1.3 b [220].

2.5 The radiative capture in the $n^{12}C$ and $n^{13}C$ systems

Earlier, the processes of the neutron capture on ^{12}C to the GS and three ESs were considered in the model of direct capture [221–223] where good description of the available experimental data in the energy range from 20 to 200 keV was obtained. In [161], also based on the model of direct capture, the dependence of the total cross-sections of the neutron capture on ^{12}C for the transitions from different partial scattering waves is shown. In addition, in [224], the possibility of description of the neutron capture on ^{12}C at the energy range from 20 to 600 keV was considered based on the general optical model.

Considering the neutron capture on ^{13}C, it is possible to cite work [225], wherein the model of the direct capture the total capture cross-section to the GS and some ES of ^{14}C are considered. Consequently, a general good agreement with the experimental data [226] is obtained, but only in the energy range of 25–60 keV.

Crossover to the research of capture reactions for more heavy nuclei we will consider the possibility of the description of experimental data for the total cross-sections for the neutron radiative capture on ^{12}C and ^{13}C for the energy range from 25 meV to 1.0 MeV. Therefore, the same MPCM with the FS will be used, which has been used previously for other reactions of the radiative capture. Furthermore, we will show that for the obtaining of the acceptable description of the experimental data on the total capture cross-sections are sufficient to consider only the *E1* transitions from the certain states, for the scattering on the ground state and some excited states of ^{13}C in cluster $n^{12}C$ channel.

For neutron radiative capture on ^{13}C with the formation of ^{14}C by its consideration in the $n^{13}C$ channel the transitions from some scattering states to the ground and first excited state of this nucleus were also considered. Accounting for the resonance $^3P_2$ scattering wave for the energy of 153 keV, it is possible to obtain a resonance form of capture total sections, which in the absence of the experimental data in this energy range, in fact, predicts the value of such total cross-section.

2.5.1 Total cross-sections of the neutron capture on ^{12}C

In the present calculations of the neutron radiative capture on ^{12}C the *E1* transitions are considered, which are caused by the orbital part of the electric operator $Q_{JM}(L)$

[22,24]. One such transition to the $n^{12}C \to {}^{13}C\gamma$ process is possible between the doublet ${}^2S_{1/2}$ scattering state and the ground ${}^2P_{1/2}$ bound state of ${}^{13}C$ in the $n^{12}C$ channel.

Furthermore, we consider the *E1* transitions not only to the ground state of ${}^{13}C$, i.e., the reaction of ${}^{12}C(n,\gamma_0){}^{13}C$ type, but also the capture on the first three excited levels, i.e., the processes ${}^{12}C(n,\gamma_1){}^{13}C$, ${}^{12}C(n,\gamma_2){}^{13}C$ and ${}^{12}C(n,\gamma_3){}^{13}C$. The two-body potentials of the interaction, as usual, are constructed on the basis of the description of phase shifts of the elastic $n^{12}C$ scattering in the initial channel and the reasonable reproduction of the main characteristics of the bound state of ${}^{13}C$ in the $n^{12}C$ cluster configuration for the output channel [12,14,136].

Classification of the $n^{12}C$ states and phase shifts of the elastic scattering

The classification of the orbital states of clusters according to Young tableaux for the $n^{12}C$ and $p^{12}C$ systems was considered by earlier [227] where it was shown that the possible orbital Young tableaux for a complete system of the 13 nucleons have the form $\{1\} \times \{444\} = \{544\} + \{4441\}$ [28]. The first of them is compatible with the orbital angular momentum $L = 0,2$, and is forbidden as in the *s*-shell there cannot be five nucleons. The second tableaux is allowed and compatible with the orbital angular momentum $L = 1$, which is determined based on Eliot's rule [28].

This state corresponds to the ground bound allowed state of ${}^{13}C$ in the $n^{12}C$ channel with the moment and the isospin of $J^\pi, T = 1/2^-, 1/2$, and for ${}^{12}C$ the characteristics of $J^\pi, T = 0^+, 0$ [228] are known. Thus, in the potential of the ${}^2S$ wave the forbidden BS has to present, and the ${}^2P$ waves have only the allowed states in the $n^{12}C$ channel. Furthermore, the bound allowed state for the ${}^2P_{1/2}$ wave corresponds to the ground state of ${}^{13}C$ and has the $n^{12}C$ channel binding energy of -4.94635 MeV [229].

However, as we have no full tables of multiplication of Young tableaux for systems with number of particles more than eight [134] which were used by us previously for the similar calculations [12,22,136], the results obtained above should be considered only as the quality standard of possible orbital symmetry in the ground state of ${}^{13}C$ for the $n^{12}C$ channel. Simultaneously, based on such classification, it was possible to explain the available experimental data on the radiative proton capture on ${}^{12}C$ quite acceptable [227].

Therefore, considering the $n^{12}C$ system, we will use the classification of states by orbital symmetry given above, which gives certain number of the FSs and ASs in the partial interaction potentials that allows to fix their depth, as well as the possibility of describing the channel AC, which allows us to choose the width of such potentials quite unambiguously.

In our earlier works [19,23,227], the ${}^2S_{1/2}$ potential of the $p^{12}C$ scattering wave was constructed so that it can describe the corresponding partial elastic scattering phase shift, which has an expressed resonance at 0.42 MeV. The $n^{12}C$ system considered here, according to results of review [229], has no resonances at the energies to

1.9 MeV; therefore its $^2S_{1/2}$ phase shift has to behave itself in this area of energies rather smoothly. An earlier phase analysis of the elastic n^{12}C scattering at energies below 1.0–1.5 MeV [150,151] has not been reported earlier, although its results should be notably different from the similar analysis for the p^{12}C scattering [227].

Therefore, for determining the exact course $^2S_{1/2}$ of the phase shift required for the upcoming calculations, we made the phase analysis of the elastic n^{12}C scattering at astrophysical energies, namely, from 50 keV to 1.0 MeV [230], the detailed results are shown in [13]. Experimental measurement of differential sections of the elastic n^{12}C scattering for the energy range from 0.05 to 2.3 MeV was reported in [231]. The results of our phase-shift analysis for the $^2S_{1/2}$ elastic scattering phase shift to 1.0 MeV are presented in Fig. 2.5.1a denoted by the black points.

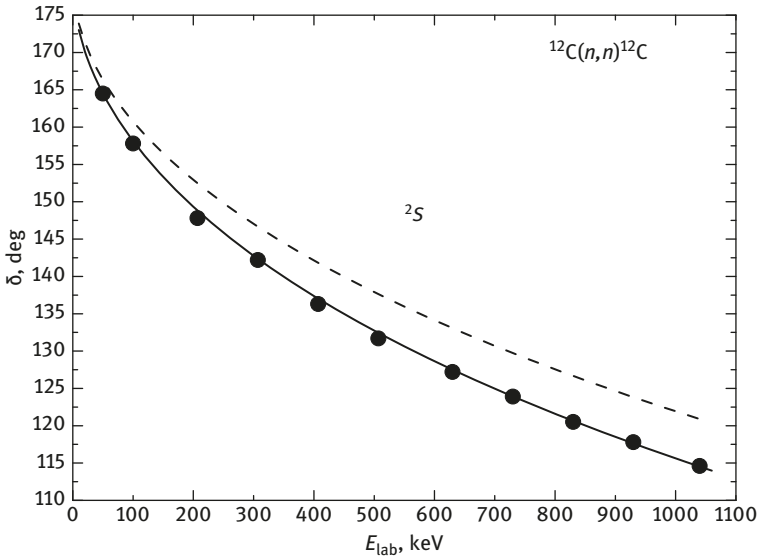

Fig. 2.5.1a: $^2S_{1/2}$ phase shift of the n^{12}C elastic scattering at low energies. Results of our phase shift analysis of the ^2S phase shift are presented by the black points (●) and obtained in work [230]. Curves – the calculations with different potentials, the parameters of which are specified in the text.

Interaction potentials

The potential of the ground state of ^{13}C in the n^{12}C channel for the $^2P_{1/2}$ wave without the FS was constructed based on the results obtained earlier by us for the p^{12}C systems [227]. This potential has to reproduce the binding energy of ^{13}C in the n^{12}C channel correctly describes the root-mean square radius of ^{13}C, which is equal to 2.4628(39) fm [229]. For the charge and mass radius of ^{12}C, the value of 2.472(15) fm [228] is accepted, the charge radius of neutron is necessary to be equal to zero, and its mass radius was accepted, as usual, equal to radius of proton of 0.8775(51) fm [126].

Using the results obtained earlier for the p^{12}C channel of ^{13}N for the n^{12}C system considered here, we find the parameters $^2P_{1/2}$ of the GS potential of ^{13}C with $J^\pi, T = 1/2^-, 1/2$

$$V_{\text{g.s.}} = -135.685683 \quad \text{MeV}, \quad \gamma_{\text{g.s.}} = 0.425\,\text{fm}^{-2}. \tag{2.5.1}$$

The potential leads to the binding energy of –4.946350 MeV with an accuracy of FDM of 10^{-6} MeV [24] to the root-mean square charge radius of $R_{\text{ch}} = 2.48$ fm and to the mass radius of $R_{\text{m}} = 2.46$ fm. The value of AC on an interval of 5–16 fm was equal to 0.99(1). The given error of the AC is determined by its averaging the specified interval of distances.

We will note that according to previous worl [195] where the selection of results on the AC is given, value of this constant 1.54(3) fm$^{-1/2}$ which after recalculation to dimensionless value with $\sqrt{2k_0} = 0.971$ is 1.59(3). This recalculation is made under the condition of equality of 1 spectrofactor of the n^{12}C channel GS of ^{13}C. Once again, such recalculation is required as in these works determination of an asymptotic constant (1.7.2) different from ours (1.2.5) at a value $\sqrt{2k_0}$was used. At the same time, in [94] for the AC in dimensionless form (1.2.5) the value of 1.60(3), which may well be used as a basic value when compared with the results obtained is shown.

In the later work [197] for the considered system in the GS of ^{13}C the interval of spectrofactor 0.531–0.633 with an average 0.58 is given. The theoretical value of ANC is 1.50 fm^{-1} and experimental value is 2.46 (31) fm^{-1}. Using (1.7.1) with the experimental ANC and average $S_{\text{f}} = 0.58$ for the AC C_{w} we will obtain the value of 2.12. If to use the S_{f} interval given above, for the C_{w} we will obtain 2.03–2.15. If to consider the ANC errors, we will obtain an interval of values of the AC 1.90–2.35. For the theoretical value of the ANC and average S_{f} we will have the AC of 1.65, and the whole interval 1.58–1.73 which well coincides with conclusions of [94].

In general, it is possible to consider that all these results will be coordinated among themselves, except that experimental data of work [197]; therefore, it is necessary to consider one more n^{12}C option of potential of the GS of ^{13}C in the n^{12}C channel and parameters

$$V_{\text{g.s.}} = -72.173484 \quad \text{MeV}, \quad \gamma_{\text{g.s.}} = 0.2\,\text{fm}^{-2}. \tag{2.5.2}$$

Using an accuracy of FDM of 10^{-8} MeV [24], the binding energy was –4.94635034 MeV, the charge radius of 2.48 fm, the mass radius of 2.50 fm, and the AC was 1.52(1) at an interval of 5–18 fm, which are consistent with previous works [94,195]. The form of wave function of such $^2P_{1/2}$ potentials is shown in Fig. 2.5.1b by the solid curve.

For the additional control of calculation of the binding energy the variation method [24] was used, which already on a grid with dimension $N = 10$ and an independent variation of parameters for the potential of the GS (2.5.2) allowed to obtain the energy of –4.94635032 MeV. The asymptotic constant C_{w} of the variation WF the parameters of which are specified in Table 2.5.1, at distances of 5–15 fm is at

Table 2.5.1: Variation parameters and coefficients of expansion of radial GS wave function of ^{13}C in the n^{12}C channel for potential (2.5.2). The normalization on an interval of 0–25 fm is N_0 = 0.9999999999697765.

i	α_i	C_i
1	1.500426018861289E–002	1.223469853688857E–004
2	1.002841633851088E–001	3.503273917493124E–002
3	1.981842450457470E–001	1.115174300485543E–001
4	3.011361231511710E–002	1.898077834207565E–003
5	1.460253375610869E–001	2.604340601242970E–002
6	5.115290090973104E–001	9.245769209919236E–002
7	9.742057085044215E–001	–2.382087077902581E–003
8	3.220854607507809E–001	1.870518591470587E–001
9	8.801958230927104E–001	7.197537136787223E–003
10	5.612447142811238E–002	1.050288601397638E–002

the level of 1.52(2), and the value of the residuals does not exceed 10^{-12} [24]. Charge radius does not differ from the value obtained in the previous finite-difference calculations.

As discussed already, for the real binding energy in such potential, it is possible to accept the average value obtained by the VM and FDM and equal in this case to –4.94635033(1) MeV. It is clear that the accuracy of the determination of the two-body binding energies based on two different mathematical methods, and calculated on the basis of two various computer programs is at the level of $\pm 10^{-8}$ MeV = ±10 meV.

Coming back to the description of scattering processes, we will notice that to accept the potential of the $^2S_{1/2}$ wave of the n^{12}C scattering the parameters obtained earlier for the p^{12}C systems

$$V_S = -102.05 \quad \text{MeV}, \quad \gamma_S = 0.195\,\text{fm}^{-2},$$

which on changing Coulomb potential do not lead to resonance, as shown by the dotted curve in Fig. 2.5.1a, the total cross-sections for the radiative capture for the potential of the GS (2.5.1) we will obtain the values some orders lower than the experimentally observed values at all considered energies from 25 meV to 1.0 MeV.

We use now the potential describing the $^2S_{1/2}$ phase shift of the elastic n^{12}C scattering (the result is shown in Fig. 2.5.1a by the solid curve) with parameters [230]

$$V_S = -98.57558 \quad \text{MeV}, \quad \gamma_S = 0.2\,\text{fm}^{-2}, \tag{2.5.3}$$

the wave function of which at 10 keV is shown in Fig. 2.5.1b by the dashed line. The parameters of the potential (2.5.3) are given and specified with a great accuracy for the correct description of energy of the first excited state of ^{13}C in the $^2S_{1/2}$ wave, which is bound and is at the depth of –1.856907 MeV relatively to the threshold of the

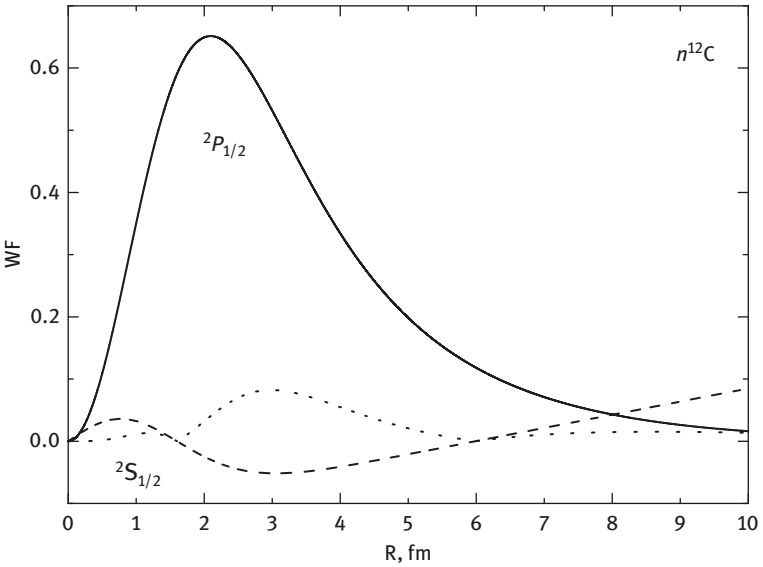

Fig. 2.5.1b: The $^2P_{1/2}$ wave function of the GS of ^{13}C in the n^{12}C channel and the $^2S_{1/2}$ WF of the elastic n^{12}C scattering at energy of 10 keV.

n^{12}C channel. Therefore, for the potential of the scattering processes and FES the same potential as that obtained previously for the n^9Be system in the S wave is used.

From these results, it is clear that when in the $^2S_{1/2}$ potential of the p^{12}C scattering describing the superthreshold resonance at 0.42 MeV correctly the Coulomb interaction is switched off, such state is bound. The potential except the forbidden one has now the allowed bound state corresponding to the first excited state of ^{13}C at energy of 3.089 MeV with $J^\pi = 1/2^+$ relatively to the GS. Such potential describes correctly not only the elastic scattering phase shift, but, as will be seen below, the main characteristics of the BS in the partial wave.

Total cross-sections for the radiative capture

The calculation of capture total cross-sections for the scattering potential (2.5.3) and the GS interaction of (2.5.1) are shown by the dotted curve in Fig. 2.5.2a. The calculated cross-section are twice below than data at 25 meV from work [159,232], and for the energy range of 20–200 keV are much below than the data [161,163–165]. It should be noted here that new data from [184] lie higher than results of older work [159] (the lower circle at 25 meV), but correspond with data [232], shown in Fig. 2.5.2a by the upper circle at 25 meV.

For comparison, we will consider the results with the same potential of scattering process (2.5.3), but with the GS interaction (2.5.2), which describes the AC correctly,

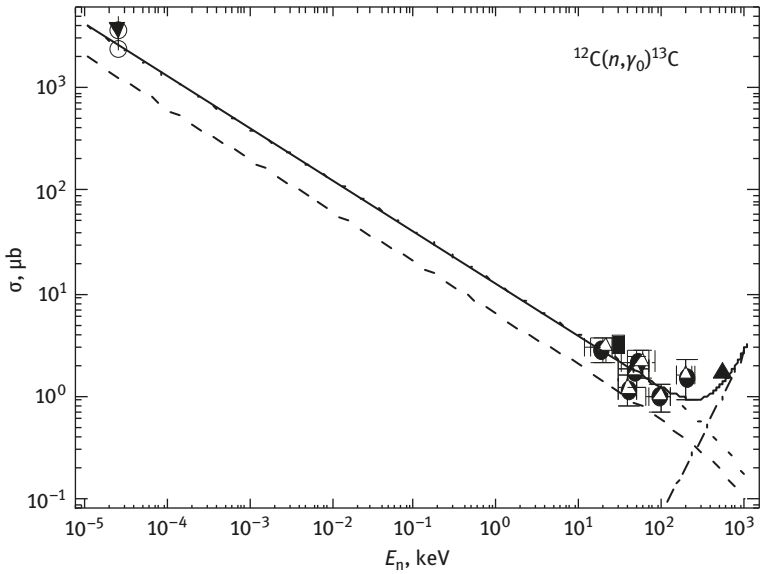

Fig. 2.5.2a: Total cross-sections for the neutron radiative capture on ^{12}C at low energies to the ground $1/2^-$ state of ^{13}C. The experimental data are taken from works: ● – [165], ○ – [159,232], ■ – [164], Δ – [163] and ▲ – [161], ▼ – [184]. Curves – calculations with different potentials, parameters which are given in the text.

which are shown in Fig. 2.5.2a by the dotted curve. It is clear that they lead to the correct description of the total cross-sections obtained in various experimental studies, starting with the energy of 25 meV from [159], and approximately up to the range 100 keV.

The results of calculation for the transition from $^2D_{3/2}$ scattering wave with potential (2.5.3) at $L = 2$ and the correct coefficient in the cross section for $J = 3/2$ to the GS of ^{13}C with potential (2.5.2) are shown by the dashed-dotted curve. The $^2D_{3/2}$ phase shift of the scattering wave does not exceed 1° at energy less than 1.0 MeV. The solid curve is the sum of dotted and dashed-dotted curves, i.e., the sum of transitions

1. $$^2S_{1/2} \rightarrow {}^2P_{1/2}$$

and

2. $$^2D_{3/2} \rightarrow {}^2P_{1/2}.$$

We will emphasize that these results are obtained for the (2.5.2) and (2.5.3) potentials, which correspond with characteristics of the GS of ^{13}C in the $n^{12}C$ channel, as well as with the AC and the phase shifts of the elastic $n^{12}C$ scattering at low energies and have no fitting parameters.

Moving to the consideration of the transitions to the excited states, we will notice that in work [206] the AC for the first excited $1/2^+$ state of ^{13}C in the n^{12}C channel, which was equal in these calculations to 1.61 fm$^{-1/2}$ that after recalculation with $\sqrt{2k_0} = 0.76$ at $S_f = 1$ in a dimensionless look gives 2.12. Simultaneously, in one of works [142] for the first excited state 1.84(16) fm$^{-1/2}$ was obtained that after recalculation at $S_f = 1$ leads to the value 2.42(21).

In this case, it is possible to consider the *E1* transition from the $^2P_{1/2}$ and $^2P_{3/2}$ scattering waves to the $^2S_{1/2}$ first excited state, bound in the n^{12}C channel

3. $$^2P_{1/2} + {}^2P_{3/2} \rightarrow {}^2S_{1/2}.$$

As the ^2P waves have no FSs, and in the spectra of ^{13}C there are no resonances of the negative parity at energy less than 1.0 MeV, the ^2P wave potentials can be simply equalized to zero. The potential of the FES (2.5.3) as its width weakly influences on the root-mean square radii of nucleus is constructed to correctly reproduce the AC given above.

Consequently, for the excited BS in the $^2S_{1/2}$ wave with the FS we will use the potential (2.5.3) which leads to the binding energy of –1.856907 MeV at an FDM of accuracy of 10^{-6} MeV [24], to the charging radius of 2.49 fm, mass radius of 2.67 fm and the AC 2.11(1) at distances of 6–24 fm. The values of the AC practically do not differ from the results of works [206], and the total cross-sections of this process are shown in Fig. 2.5.2b by the solid curve with the experimental data of [161,163–165]. In this case, the used potentials ^2P of scattering, meanwhile with zero depth, and excited BS (2.5.3) allow one to correctly reproduce the available experimental data at low energies.

The AC of the second excited $3/2^-$ state of ^{13}C, which was equal to 0.23 fm$^{-/2}$, is given in the same work [206] that after recalculation with $\sqrt{2k_0} = 0.69$ at $S_f = 1$ in a dimensionless form gives 0.33. For the correct reproduction of such AC the potential of the FES has to be very narrow

$$V_{P3/2} = -681.80814 \quad \text{MeV}, \quad \gamma_{P3/2} = 2.5\,\text{fm}^{-2}.$$

This potential gives the binding energy of –1.261840 MeV with an accuracy of FDM of 10^{-6} MeV, the charge radius of 2.47 fm, mass radius of 2.44 fm, and the AC is 0.30(1) at a distance of 2–24 fm. Such $^2P_{3/2}$ potential has no FS and reproduces the value of the AC [206]. The calculation of the total cross-sections of the neutron capture on ^{12}C from the $^2S_{1/2}$ scattering state with potential (2.5.3) to the second excited level $^2P_{3/2}$

4. $$^2S_{1/2} \rightarrow {}^2P_{3/2}$$

are provided in Fig. 2.5.2c by the dotted curve together with the experimental data of works [159, 161, 163–165].

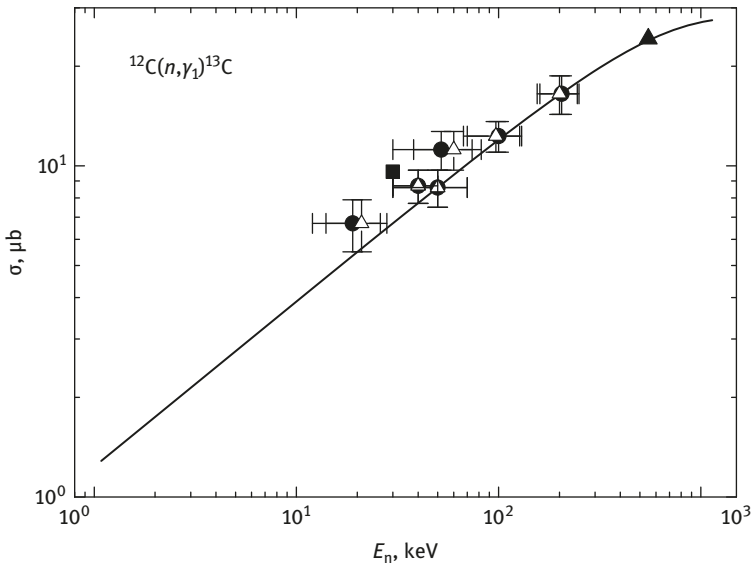

Fig. 2.5.2b: Total cross-sections for the neutron radiative capture on ^{12}C at low energies to the first excited level $1/2^+$ of ^{13}C. Experimental data are taken from works: ● – [165], ■ – [164], □ – [163] and ▲ – [161]. Curves – calculations with different potentials which parameters are specified in the text.

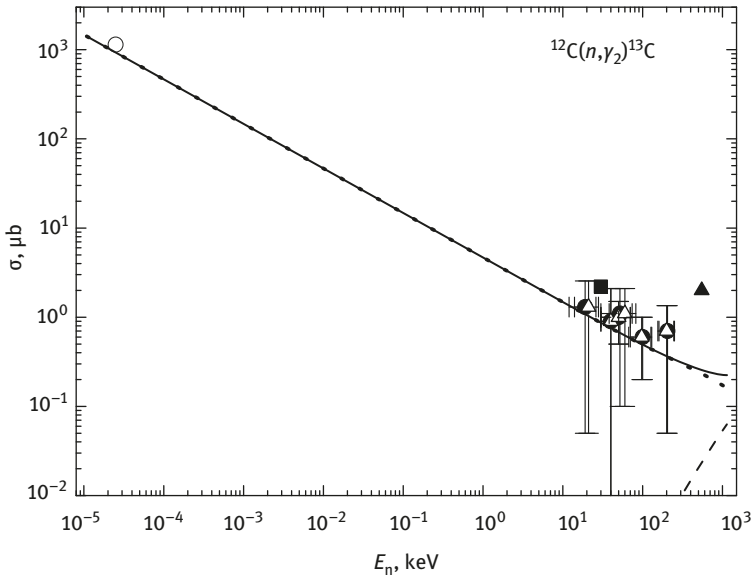

Fig. 2.5.2c: Total cross-sections of the neutron radiative capture on ^{12}C at low energies to the second excited level $3/2^-$ of ^{13}C. The experimental data are taken from: ● – [165], ○ – [159], ■ – [164], □ – [163] and ▲ – [161]. Curves – calculations with different potentials, which parameters are given in the text.

On the right in the bottom of Fig. 2.5.2c the calculation results of cross-section with transition to this ES from the $^2D_{3/2}$ and $^2D_{5/2}$ scattering waves for potential (2.5.3) are shown by the dashed curve at $L = 2$ and exact coefficients in cross sections for $J = 3/2$ and 5/2, and the solid curve shows the sum of these cross-sections. It is clear that the used approach in this case allows one to obtain the acceptable results on the description of the total cross-section at the transition to the second ES of ^{13}C. Meanwhile, the intercluster potentials correspond with the scattering phase shifts and generally reproduce the main characteristics of the nucleus correctly, namely the AC of the considered BS, which is the second ES of ^{13}C.

For the consideration of the transition from the $^2P_{3/2}$ scattering wave to the bound $^2D_{5/2}$ state

5. $$^2P_{3/2} \rightarrow {}^2D_{5/2}$$

at energy of −1.09254 MeV relatively to the threshold of the n^{12}C channel which is the third ES of ^{13}C, we will give the value of the AC. So in work [206] the value of 0.11 fm$^{-1/2}$, and in [142] 0.15(1) fm$^{-1/2}$ were obtained that after recalculation with $\sqrt{2k_0} = 0.665$ at $S_f = 1$ to the dimensionless form leads to the 0.16 and 0.23 values. For the $^2P_{3/2}$ scattering wave, still, we use zero potential, and for the potential of the bound $^2D_{5/2}$ state with one FS in the considered channel we use the same geometry as for the GS of ^{13}C (2.5.2).

Then for the potential of the third ES of ^{13}C in the n^{12}C channel we have the parameters

$$V_D = -263.174386 \quad \text{MeV}, \quad \gamma_D = 0.2\,\text{fm}^{-2},$$

which give the binding energy of −1.092540 MeV with an accuracy of FDM of 10^{-6} MeV, the charging radius of 2.49 fm, mass radius of 2.61 fm, and the AC is 0.25(1) at distance of 6–25 fm. Such potential has the bound FS and reproduces the value of the AC correctly.

The calculation results of the total cross-sections for the neutron capture on ^{12}C from the $^2P_{3/2}$ scattering state to the bound $^2D_{5/2}$ level shown in Fig. 2.5.2d by the solid curve with the experimental data of [159,161,163–165]. Thereby, in this case, the used MPCM allows one to obtain the acceptable results on the description of the cross-sections of the capture to the third ES of ^{13}C. Meanwhile, the intercluster potentials are, still, coordinated with elastic scattering phase shifts and in general reproduce the main characteristics of the considered BS of ^{13}C in the n^{12}C channel.

Thereby, the used combinations of potentials, describing the main characteristics of discrete and continuous spectra for the n^{12}C system, allows to well reproduce the available data on the experimental cross-sections of the neutron radiative capture on ^{12}C to the GS and to the three first excited states at energies from 25 meV to

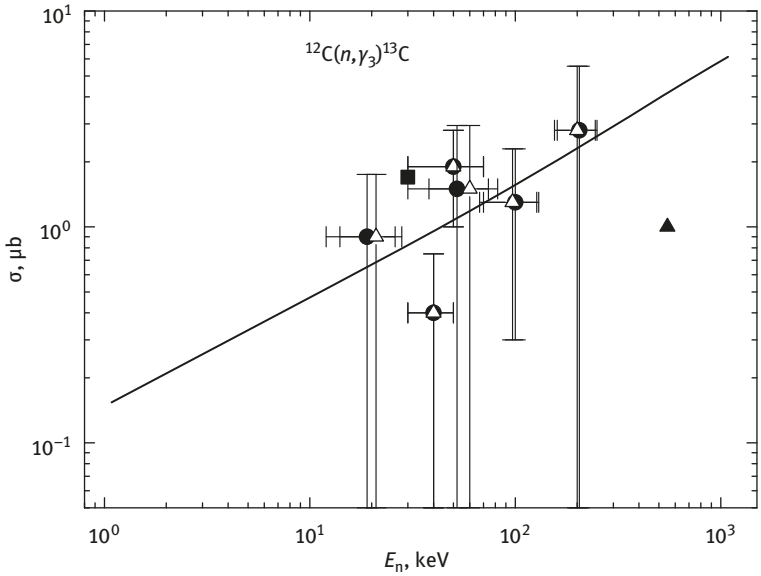

Fig. 2.5.2d: Total cross-sections of the neutron radiative capture on ^{12}C at low energies to the third excited $5/2^+$ level of ^{13}C. Experimental data are taken from works: ● – [165], ■ – [164], □ – [163] and ▲ – [161]. Curves – calculations with different potentials which parameters are specified in the text.

0.5 MeV, i.e., in the energy range of covering nearly seven orders. All considered potentials have no fitting parameters which vary at calculations of the total cross-sections, all these parameters are fixed previously according to the characteristics of the BS and the scattering processes.

At the energies from 10^{-5} to 10 keV the calculation cross section is practically a straight line (dotted curve in Fig. 2.5.2a), for the area of low energies it can be approximated by a simple function of the form (2.1.3) with a constant A = 12.7292 μb · keV$^{1/2}$, determined by one point in sections at the minimum energy equal to 10^{-5} keV (ls). The module of a relative deviation of the settlement theoretical cross section and approximation of this cross section the function (2.1.4) given above in the range from 10^{-5} to 10 keV has a value of less than 1.0%. It is possible to assume that this form of dependence of the total cross section of the energy will be preserved at lower energies. Therefore, when performing an estimation of the cross section value, for example, at energy of 1 μeV (10^{-6} eV = 10^{-9} keV) we find 402.5 mb [233].

2.5.2 The total cross-sections of the n^{13}C capture

By considering the radiative capture the *E1* transition was taken into account, which in $n^{13}\mathrm{C} \to {}^{14}\mathrm{C}\gamma$ process is possible between the triplet $^3S_1$ scattering state and the

ground $^3P_0$ bound state of ^{14}C in the n^{13}C channel. Besides, the possible *E1* transition from the resonance scattering wave $^3P_2$ at 153 keV to the $^3S_1$ first excited state of ^{14}C with energy of 6.0938 MeV relatively to the GS of ^{14}C will be considered at $J^\pi = 1^-$ or at –2.0827 MeV relatively to the threshold of the n^{13}C channel. Recall that for ^{13}C is known J^π,T=1/2$^-$,1/2 and for ^{14}C is known J^π,T=0$^+$,1 [229].

Classification of orbital states and interaction potentials

The classification of the orbital states of p^{13}C, and n^{13}C system according to Young tableaux was considered by us earlier in [141]. Therefore, in brief we will remind that for the p^{13}C system, we obtain {1} × {4441} → {5441} + {4442} [28]. The first of these Young tableau is compatible with the orbital angular momentum L = 1 and is forbidden, as in the *s*-shell there cannot be five nucleons, however, the second tableaux is allowed and compatible with the orbital angular moments 0 and 2 [28].

Thus, being limited only by the lowest partial waves, it is possible to tell that in the potential of the $^3S_1$ wave the forbidden state is absent, but the bound AS for the {4442} tableau can be present. The ^3P waves have the forbidden state with the {5441} tableaux and allowed state, which corresponds to the GS of ^{14}C in the n^{13}C cluster channel with $J^\pi = 0^+$ ($^3P_0$ state), the binding energy of n^{13}C system in ^{14}C is equal to -8.1765 MeV [229].

For calculating the total cross-sections for the radiative capture of the nuclear part of intercluster potential of n^{13}C interaction, as usual, is presented in the form of a Gaussian function (1.2.2) without the Coulomb member. For the potential of the $^3S_1$ scattering wave without FS in the beginning were used the values obtained in the p^{13}C scattering [141,234] with parameters

$$V_S = -265.4 \quad \text{MeV}, \quad \gamma_S = 3.0\,\text{fm}^{-2}. \tag{2.5.4}$$

The calculation results of the $^3S_1$ phase shift of the elastic scattering with such p^{13}C potential without Coulomb interaction, i.e., for the n^{13}C system, is shown in Fig. 2.5.3 by the dotted curve. Now it has not resonance character [234], and represents smoothly drooping function of energy.

The potential with one bound FS of the triplet $^3P_0$ state has to reproduce the binding energy of the ground state of ^{14}C in the n^{13}C channel correctly and reasonably describe the root-mean square radius of ^{14}C, the experimental value of which is equal to 2.4962(19) fm [229]. Consequently, the following parameters which are the changed variant of the potential of the bound p^{13}C state in ^{14}N were obtained

$$V_{\text{g.s.}} = -399.713125 \quad \text{MeV}, \quad \gamma_{\text{g.s.}} = 0.45\,\text{fm}^{-2}. \tag{2.5.5}$$

The potential leads to the binding energy of –8.176500 MeV with an accuracy of FDM of 10^{-6}, to the root-mean square charge and mass radii of 2.47 fm. For the radii of

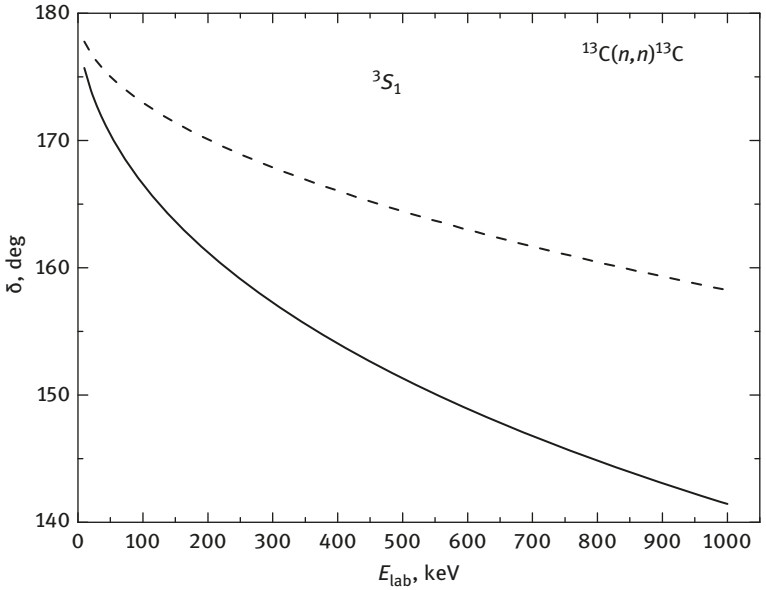

Fig. 2.5.3: $^3S_1$ phase shift of the elastic $n^{13}C$ scattering at low energies. Curves – calculations of phase shifts with the potentials given in the text.

neutron and ^{13}C the values specified in the previous part of this paragraph are used. For the asymptotic constant, which is written in a dimensionless form (1.2.5), the value of 1.85(1) on an interval of 4–13 fm was obtained. The error of this constant is determined by averaging by the interval of distances stated above.

We will notice that in work [215] for the AC of this channel in ^{14}C the value of 1.81 (26) $fm^{-1/2}$ was obtained, which after the recalculation at $\sqrt{2k_0} = 1.102$ and $S_f = 1$ gives the dimensionless (1.2.5) value of 1.64(24), that is quite acceptable will be coordinated by the results obtained for the potential (2.5.5). However, the interval of a spektrofactor 1.573–1.87 with average value of 1.72 is given in later work [197] for the GS of ^{14}C in the $n^{13}C$ channel at theoretical ANC of 1.67 fm^{-1}. In that case, for average C_W it is found the value of 2.83 that is almost twice more than in the previous results.

For the additional control of the calculation of energy of the GS, the two-body variation method [24] was used, which already on a grid with the dimension $N = 10$ and with independent variation of parameters for the potential of BS (2.5.5) allowed to obtaining the energy of –8.176498 MeV. The parameters of variation radial wave function are specified in Table 2.5.2, and the values of residuals do not exceed 10^{-11} [24]. The charge radius and the AC do not differ from the values obtained for this potential in the FDM calculations above.

Consequently, for the real binding energy in such potential it is possible to accept the average FDM and VM value of -8.176499(1) MeV, i.e., the accuracy of the

Table 2.5.2: The variation parameters and expansion coefficients of the variation wave function of ^{14}C for the n^{13}C channel and the GS potential (2.5.5). Wave function normalization on an interval of 0–30 fm is N_0 = 1.000000000000000.

i	α_i	C_i
1	3.491469469267236E–002	1.603503246684095E–003
2	8.137782371906017E–002	2.247604868653303E–002
3	1.702453936681754E–001	1.028690037355076E–001
4	2.936860230901219E–001	1.924715189471573E–001
5	4.639996320920978E–001	4.910563075348197E–001
6	1.240165593327286	–2.532914988637461
7	2.291957256255444	–3.347540732339817
8	2.670822833331601	4.750289923787678
9	3.031209229832412	–3.492655828236482
10	3.331758094832779	1.069432486749043

determination of the binding energy of ^{14}C of the n^{13}C channel by two methods according by two various computer programs for the potential (2.5.5) is at the level of ±1.0 eV. We will notice that it coincides with the initially set by the accuracy in the determination of the binding energy in the set potential.

Total cross-sections for radiative capture

For describing the total cross-sections, as well as earlier in work [141], we used only the *E1* transition from the non-resonance, in this case, $^3S_1$ and $^3D_1$ scattering waves with potential (2.5.4) to the triplet $^3P_0$ bound state of the n^{13}C clusters in ^{14}C for potential (2.5.5)

1. $$^3S_1 + {}^3D_1 \rightarrow {}^3P_0.$$

It is compared to the ground state of ^{14}C with $J^\pi = 0^+$ in the n^{13}C channel, because ^{13}C has the moment and an isospin of $J^\pi, T = 1/2^-, 1/2$ [229]. For calculating the $^3D_1$ waves the $^3S_1$ scattering potential with orbital angular momentum L = 2 was used. The available experimental data for the total cross sections for the neutron radiative capture on ^{13}C to the GS [159,226,235–237] were obtained by us from the EXFOR database [150] and for the energy range of 25 meV–100 keV are shown further in Figs. 2.5.4 and 2.5.6.

As discussed already, at the consideration of the radiative capture the *E1* transition, which in the $n^{13}\text{C} \rightarrow {}^{14}\text{C}\gamma$ process is possible between the triplet $^3S_1$ scattering state and the bound basic $^3P_0$ state of ^{14}C in the n^{13}C channel, was taken into account. However, the results of calculation of total cross-sections for the neutron radiative capture on ^{13}C to the ground state of ^{14}C with the potentials

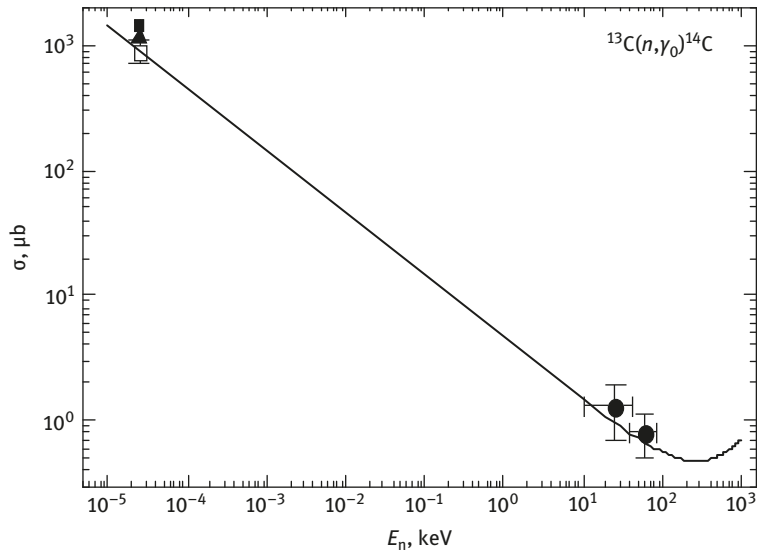

Fig. 2.5.4: Total cross-sections for the neutron radiative capture on ^{13}C to the GS of ^{14}C. Experimental data: ● – [226], □ – [237], ▲ – [159], ■ – [184]. Curve – calculation of the total cross-section for the potentials given in the text.

specified above almost an order of magnitude higher than the data on the cross-sections of [159,237] with the energy of 25 meV and are much higher than the results of [226] in the 10–100 keV.

To describe the experimental data properly it is necessary to change a little the potential of the $^3S_1$ wave (2.5.4) and to accept its depth

$$V_S = -215.770460 \quad \text{MeV}, \quad \gamma_S = 3.0 \quad \text{fm}^{-2}. \tag{2.5.6}$$

The scattering phase shift calculated with the modified potential is shown in Fig. 2.5.3 and the total cross-section is shown in Fig. 2.5.4 by the solid curve.

The specified scattering potential (2.5.6) allows to describe correctly the location of the $^3S_1$ bound state in the n^{13}C channel, but excited at 6.0938 MeV with $J^\pi = 1^-$ levels, and leads with an accuracy of 10^{-6} MeV to the binding energy of –2.082700 MeV relatively to the threshold of the n^{13}C channel, which precisely coincides with the experimental value [229]. For charge and mass radius, the value of 2.47 fm is obtained, and the AC is equal to 1.13(1) on an interval of 2–22 fm. Here the situation similar to the previous system when the superthreshold resonance state in the p^{13}C system at switching off Coulomb interaction becomes the bound allowed $^3S_1$ state of the n^{13}C system with the {4442} tableaux is observed.

Thus, it is clear that some change of depth of the scattering potential from (2.5.4) to (2.5.6) and its coordination with the energy of the bound level, which is present in the $^3S_1$ wave allows one to describe the experimental data for the total cross sections

for the capture from 25 meV to 100 keV. Delay of dropping of the cross sections at 0.2–1.0 MeV is caused by the contribution of the *E1* transition from the $^3D_1$ scattering wave, which is visible only in this energy range.

It is necessary to emphasize that unlike the previous n^{12}C system, we did not manage to find the independent results for the AC of the first ES in the bound $^3S_1$ wave. Therefore, the used scattering potential (2.5.6) may contain a certain ambiguity in its parameters. Other set of parameters of this potential, which describes the characteristics of the bound state correctly, in particular, the binding energy and the total capture cross-section, but leading to slightly different value of the AC is possible.

An estimate of the cross-section of the *M2* transition from the resonance with $J^\pi = 2^+$ at 152.9(1.4) keV (l.s.) $^3P_2$ scattering wave with very small width of 3.4(7) keV (c.m.) [229] to the $^3P_0$ GS led to the value less than 1% from the *E1* cross-section. However, the *E1* transition from the resonance $^3P_2$ scattering wave to the $^3S_1$ first ES of ^{14}C with energy of 6.0938 MeV is possible here at $J^\pi = 1^-$, for which the potential is already obtained (2.5.6)

2. $$^3P_2 \rightarrow {}^3S_1.$$

The cross-section of such process has to have a narrow resonance, which may reach a value of 1–2 mb. In the beginning of these calculations we will give the potential of resonance $^3P_2$ wave without the FS, which has the parameters

$$V_P = -10719.336 \quad \text{MeV}, \quad \gamma_P = 40.0 \quad \text{fm}^{-2}. \tag{2.5.7}$$

This potential leads to the resonance energy of 153 keV (ls) and the width of 3.7 keV (cm), and its phase shift is shown in Fig. 2.5.5 by the solid curve.

For the potential of the resonance $^3P_2$ wave, having the bound FS the parameters are found

$$V_P = -46634.035 \quad \text{MeV}, \quad \gamma_P = 60.0 \quad \text{fm}^{-2}. \tag{2.5.8}$$

It leads to a resonance at 153 keV with a width of 4.0 keV, and the phase shift for such potential is shown in Fig. 2.5.5 by the dotted curves. This potential will be coordinated with the classification according to Young tableaux if we assume that the AS in this partial scattering wave is not bound.

In both cases, the phase shift of the potentials at the resonance energy is set to 90.0(5) degrees, and the widths of the resonances are quite consistent with the experimental data and are in the error range 3.4(7) keV, as well as resonance energy of 152.9(1.4) keV [229]. In both cases, the parameters of the potentials are determined completely unambiguously if the quantity of the bound FSs is given, even though their values have large magnitudes. Depth of the potential defines the provision of the resonance, and its width gives the width of this resonance.

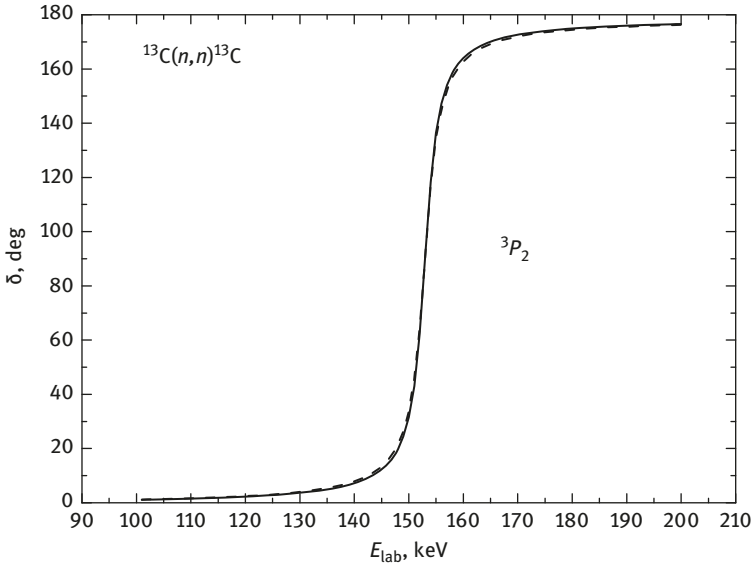

Fig. 2.5.5: $^3P_2$ phase shift of the elastic n^{13}C scattering at low energies. Curves – solid for the potential without the FS and with resonance width of 3.7 keV and dotted with one bound FS and with resonance width of 4.0 keV.

Now, we will present the results of the $E1$ transition with these two potentials. In the first case for the potentials (2.5.6) and (2.5.7), the results are presented in Fig. 2.5.6 by the dotted curves. The dotted curve represents the results for the total cross sections for the transition to the GS shown in Fig. 2.5.4 by the solid line. The solid curve in Fig. 2.5.6 represents the sum of these cross-sections.

At the resonance energy the total calculation cross-sections have the value of 1.42 mb, which can be used for the comparison if in the future will be made new measurements of the total capture cross sections in the resonance region. The experimental data for the total sections with transition to the GS and to all ES are given in works [226,238,239] and shown in Fig. 2.5.6 by the black squares and light triangles at 30 [238] and 40 keV [239], black invert triangles from work [240]. These experimental data become known to us only in the middle of 2017, and the calculation of such resonance were done and published by us in 2014 [241]. To clarify, the resonance its range in details is shown in Fig. 2.5.7.

The results of similar calculations for the scattering potential (2.5.8) practically do not differ from given in Fig. 2.5.6. Only at resonance energy the total sections have a little smaller value of 1.40 mb that can be caused by some increase in width of resonance for the potential containing the bound FS (2.5.8). Thus, the results of both calculations practically do not depend on the presence of the bound FS at the resonance $^3P_2$ potential. They are completely defined by the correctness of the reproduction of resonance energy of level and, first of all, the right description of its width and energy.

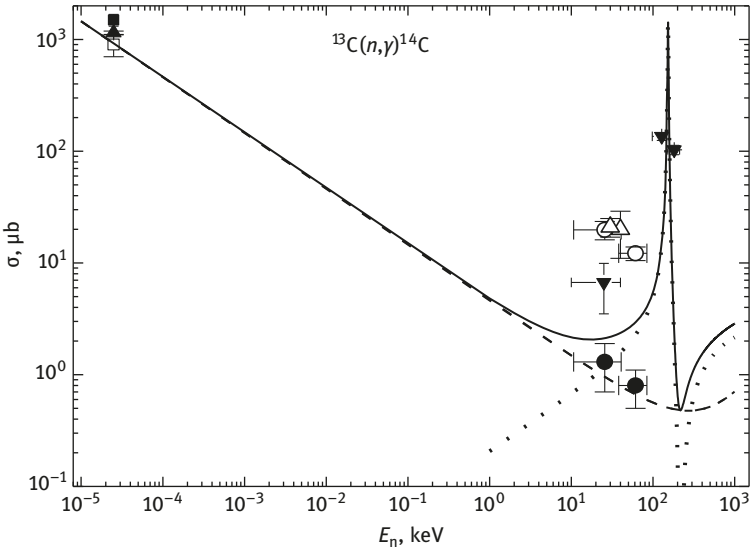

Fig. 2.5.6: The total cross-sections of the neutron radiative capture on ^{13}C from the $^3P_2$ wave for potential without the FS to the GS and the first ES of ^{14}C. Experimental data: ● – [226], □ – [237], ▲ – [159], ■ – [184] and Δ – at 30 keV from work [238], at 40 keV from [239], ○ – [226] for total capture cross-sections, black invert triangles from work [240]. Curves: the dashed – the calculation of the total cross-sections to the GS, the dotted – transition to the FES and solid – summarized cross-section.

Furthermore, we will notice that we did not manage to find the results of the phase-shift analysis of the $n^{13}C$ elastic scattering or experimental data on the differential cross sections of the elastic scattering at energies up to 1.0 MeV. The available data higher than 1.26 MeV [242] are measured with a big step on energy, which does not allow to make the phase shift analysis now as reported by us, for example, for $p^{12}C$, $n^{12}C$ or $p^{13}C$ scattering at energies less than 1.0 MeV [13,167,230,234,243].

We will notice that for the elastic $p^{13}C$ scattering in the field of the resonance at 0.55 MeV (l.s.) and its width of 23(1) keV there were about 30 measurements of the differential cross sections executed in different works at four scattering angles. Such details allow us to reproduce in the phase shift analysis [234] the resonance shape at $J^\pi,T = 1^-,1$ and 8.06 MeV relatively to the GS of ^{14}N or 0.551(1) relatively to the threshold of the $p^{13}C$ channel [229] precisely.

In this case, the available differential sections of the elastic $n^{13}C$ scattering [242] higher than 1.26 MeV because of a big interval of measurements of cross-sections on energy, do not allow to detect a resonance shape with $J^\pi = 1^-$ at 9.8 MeV relatively to the GS or 1.75 MeV (ls) relatively to the $n^{13}C$ threshold the characteristics of which are provided in Table 14.7 of work [229], not to mention a resonance with $J^\pi = 2^+$ at 153 keV (ls) is higher than the threshold with a width of 3.4 keV. Therefore, there is no opportunity to obtain the $^3P_2$ and $^3S_1$ scattering phase shift of the experimental data

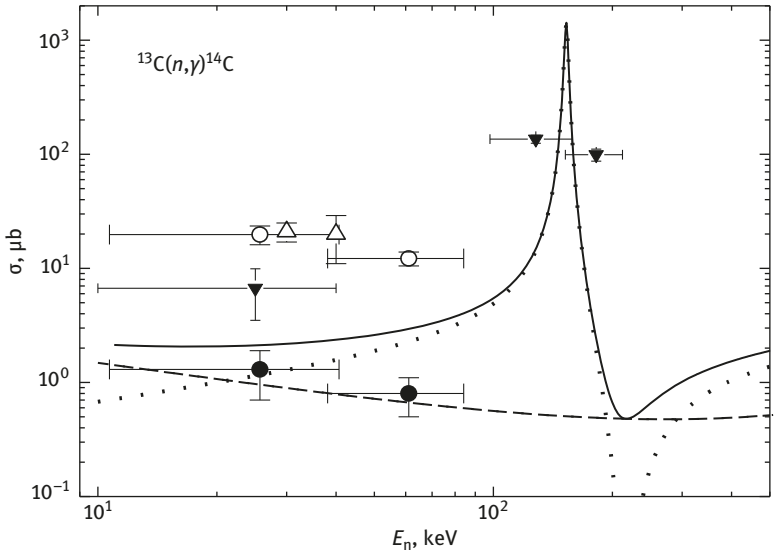

Fig. 2.5.7: The total cross-sections of the neutron radiative capture on ^{13}C from the $^3P_2$ wave for potential without the FS to the GS and first ES of ^{14}C. Experimental data: ● – [226], □ – [237], ▲ – [159], ■ – [184] and Δ – at 30 keV from work [238], at 40 keV from [239], ○ – [226] for total capture cross-sections, black invert triangles from work [240]. Curves: the dashed – calculation of the total cross-sections to the GS, the dotted – transition to the FES and solid – summarized cross-section.

on the differential cross-sections at low energies, and to construct a scattering potential on their basis. However, the use of some other criteria for creation of intercluster potentials allows one to find their parameters which lead to the acceptable description of the available experimental data.

Thus, the BS interaction of the n^{13}C system reproduces the characteristics of the GS of ^{14}C quite acceptable, just as it was obtained earlier for the p^{13}C channel in ^{14}N [141]. However, the lack of results for the AC makes it impossible to draw any definite and final conclusions about the parameters of the ES potential in the $^3S_1$ wave (2.5.6). For the remaining, the situation here is similar to the previous n^{12}C system, when for the scattering process the changes of the S phase shift are not limited by the changing of only the Coulomb interaction. The real S phase shift of the n^{12}C scattering, obtained in the phase shift analysis and shown in Fig. 2.5.1by points had a little smaller values, than a calculated phase shift for the p^{12}C potential at the switched-off Coulomb interaction, given above in Fig. 2.5.1a by the dashed curve.

Thus, in the used approach almost all potentials (2.5.5)–(2.5.8) are constructed quite unambiguously. The exception makes only the $^3S_1$ potential (2.5.6), the parameters of which, first of all, depend on the value of the AC of this bound state, which is not known now. However, in this system for the $^3S_1$ wave, as before in certain cases, it is possible to construct a single potential for a certain bound state with a given moment

and scattering processes in the corresponding partial wave. Then, it is used to calculate the characteristics of the continuous and discrete spectra of the clusters of states, which are under consideration, including the total cross sections for radiative capture.

In conclusion, as at the energies from 25 meV to 10 keV, the calculated cross-section shown in Fig. 2.5.4 is practically a straight line, it can also be approximated by a simple function of form (2.1.3) with constant value A = 4.6003 μb keV$^{1/2}$. It was determined by one point in calculation cross-sections at the minimum energy equal to 10 meV (ls). The module $M(E)$ (2.1.4) of a relative deviation of the calculated theoretical cross-section and approximation of this cross-section by a function (2.1.3) in area from 25 meV to 10 keV does not exceed 0.4%. It is still possible to assume that this form of dependence of the total cross-section on energy (2.1.3) will be preserved at lower energies too. Therefore, the evaluation of the cross-section, for example, at an energy of 1 μeV (10^{-6} eV = 10^{-9} keV), gives a value of 145.5 mb [241].

2.6 Radiative capture in the n^{14}C and n^{14}N systems

Let us consider the reactions of the neutron capture on ^{14}C and ^{14}N at the energies of 23 keV–1.0 MeV though only the first of them is a part of chain of the processes of primordial nucleosynthesis (2.0) which led to the existence of the Sun, stars and all our universe [3]. The cross-section of the first process smoothly reduces with decreasing energy and obeys the law of $\sqrt{E}$. Therefore, the process of the neutron capture on ^{14}C makes the greatest contribution at the very beginning of primordial nucleosynthesis, i.e., at big energies of particles interaction. The cross-section of the second reaction as function of energy in thermal range increases under the law of $1/\sqrt{E}$. Thereby, the processes considered here ^{14}C$(n,\gamma)^{15}$C и ^{14}N$(n,\gamma)^{15}$N show two types of behavior of capture cross-sections as functions of energy at thermal and astrophysical energies.

Though the capture reaction $n^{14}\mathrm{N} \rightarrow {}^{15}\mathrm{N}\gamma$ does not include directly into any chain of reactions of primordial nucleosynthesis or thermonuclear cycles [3,12,14,136,138], it leads to the formation and accumulation of ^{15}N nuclei. Thereby, this reaction is additional to the ^{14}C$(n,\gamma)^{15}$C$(\beta^-)^{15}$N process, which is present at a chain (2.0) and increases the quantity ^{15}N participating in further reactions of synthesis of heavier elements. The value of the total cross-section of these two reactions is comparable with the energy of 100 keV and is at the level of 10 μb.

2.6.1 Classification the n^{14}C and n^{14}N states and n^{14}N scattering potentials

Passing to the analysis of the total cross-sections of the neutron capture on ^{14}C and ^{14}N with the formation of ^{15}C and ^{15}N in the GS, we will notice that the classification of orbital states of nuclei ^{14}C in the n^{13}C system or ^{14}N in the p^{13}C channel according to

Young tableaux was considered by us earlier earlier works [136,141,244] and the previous paragraph. However, we have not have production tables of Young tableaux for systems with the particle number more than eight [134], which were used by us earlier for similar calculations [12], the results obtained further must be considered only as qualitative estimation of possible orbital symmetries in the ground state of ^{15}C and ^{15}N nuclei for considered channels. Simultaneously, based on the similar classification, it is possible to explain available experimental data on neutron [244] and proton [136,141] radiative capture on ^{13}C quite reasonable. Therefore, we will classify the cluster states according to orbital symmetries, which leads us to fixed number of FSs and ASs in partial intercluster potentials and, so, to the definite number of nodes in the wave function of the cluster relative motion.

Furthermore, we will assume that for ^{14}C it is possible to accept the orbital Young tableaux in the form of {4442}, therefore for the $n^{14}C$ system within a $1p$-shell we have $\{1\} \times \{4442\} \to \{5442\} + \{4443\}$ [134]. The first of the obtained tableaux is compatible with the orbital momentum $L = 0$ and 2 is forbidden as in a s-shell there cannot be five nucleons [11], and the second tableau is allowed and compatible with orbital momentum $L = 1$ [28]. As it was already told, the absence of product tables of the Young tableaux for number of particles 14 and 15 makes it impossible to classify the cluster states in the considered system of particles accurately. However, even so quality standard of the orbital symmetry allows one to define the existence of the FSs in the ^2S wave and its absence for the ^2P states. Such structure of the FSs and ASs in different partial waves allows further to construct potentials of intercluster interaction, which lead to possibility of the description of available experimental data.

Thus, being limited only by the lowest partial waves with the orbital momentum $L = 0$ and 1, it is possible to tell that for the $n^{14}C$ system (for ^{14}C we have $J^\pi, T = 0^+1$) in the potential of the $^2S_{1/2}$ wave there are forbidden and allowed states. The last of them corresponds to the GS of ^{15}C with $J^\pi, T = 1/2^+, 3/2$ and is at binding energy of the $n^{14}C$ system of −1.21809 MeV [229]. At the same time the potentials of the ^2P elastic scattering waves have no bound FSs. In such system, first two *E1* transitions from $^2P_{1/2}$ and $^2P_{3/2}$ scattering waves without the FSs to the GS of ^{15}C in the $^2S_{1/2}$ wave with the bound FS are possible

1. $$^2P_{1/2} + {}^2P_{3/2} \to {}^2S_{1/2}.$$

Now, we will consider the process of the radiative capture in the $n^{14}C$ system at energies from 20 keV to 1.0 MeV, approximately, where the experimental data exist, the information about them is given in the base of the MSU [150]. For creation of the potential of the $^2P_{1/2}$ wave of $n^{14}C$ scattering without FS at first it is possible to use the representations obtained based on data on the resonance at 3.103(4) MeV with $J^\pi = 1/2^-$ relatively to the GS of ^{15}C or, approximately, to 1.9 MeV (cm) higher than threshold of the $n^{14}C$ channel and the width of about 40 keV. In this case its parameters can be written down in the form

$$V_P = -787.0 \quad \text{MeV}, \quad \gamma_P = 3.0 \quad \text{fm}^{-2},$$

The calculation result of the $^2P_{1/2}$ scattering phase shift with n^{14}C potential leads to the resonance at an energy of 1.88 MeV (cm), though its width is in 15 times more of known value [229]. Because this potential does not contain the FS, its phase shift starting from zero degree [21,42]. For the obtaining of the correct width of this resonance with $J^\pi = 1/2^-$ the further decrease of width of the potential will be required, i.e., the increase in parameter of width γ, and the value of the phase shift of such potential in the resonance range will decrease. As we consider only the energy range which is not exceeding 1.0 MeV, it is quite possible to consider that the $^2P_{1/2}$ phase shift in this area is simply equal to zero. That means that the depth of the V_0 potential, because it has the FS, can be equalized to zero – this variant of interaction of the n^{14}C input channel is used further in our calculations. The same applies to the potential of the $^2P_{3/2}$ scattering wave as the appropriate response of ^{15}C is at even greater energy 4.66 MeV.

The $^2S_{1/2}$ GS potential with one bound FS has to correctly reproduce the binding energy of ^{15}C with $J^\pi, T = 1/2^+, 3/2$ in the n^{14}C channel at –1.21809 MeV [229], reasonably describe the root-mean square radius of ^{15}C, the value of which, apparently, should not exceed the ^{14}C radius that is equal to 2.4962(19) fm [229] and reproduce the AC in the n^{14}C channel obtained earlier in independent researches [206,245,246] significantly.

For realization of the conditions stated above it is possible to offer the variant of the GS potential of ^{15}C in the n^{14}C channel with one FS and the following parameters

$$V_{\text{g.s.}} = -93.581266 \quad \text{MeV}, \quad \gamma_{\text{g.s.}} = 0.2 \quad \text{fm}^{-2}, \tag{2.6.1}$$

This leads to the AC of 1.85(1) at the range of 7–27 fm, gives the binding energy of –1.2180900 MeV with an FDM accuracy of 10^{-7} MeV, charge radius of 2.52 fm and mass radius of 2.73 fm. As the neutron charge radius has the value of zero, and its mass radius was accepted equal to proton radius. The constant error is determined by its averaging by the interval of distances stated above.

In the review [206] with the reference to work [245] for the AC was given 1.13 $\text{fm}^{-1/2}$, that after the recalculation to the dimensionless value gives 1.65 at $\sqrt{2k_0}$= 0.686 and the assumption that $S_f = 1$ (1.7.1). In one of the most recent studies [246] devoted to the determination of the AC from the characteristics of various reactions, the detailed review of values of such constant is provided. It is shown that its values obtained in different works are within limits from 1.22(6) $\text{fm}^{-1/2}$ to 1.37(5) $\text{fm}^{-1/2}$, that after recalculation gives 1.8–2.0 with the recommended value in a dimensionless form 1.87(13), which will completely be coordinated with the value obtained by us.

For additional control of the calculation of energy of the GS of ^{15}C for the potential given above, the variation method [24] was used, which already on a grid with dimension of N = 10 and an independent variation of parameters for the BS potential (2.6.1) allowed one to obtain the energy of –1.2180898 MeV. The parameters of variation radial WF are specified in Table 2.6.1, and the residual value have an order of 10^{-12}

[24]. The charge radius and the AC in the range of 5–25 fm do not differ from the values obtained above in the FDM calculations.

Table 2.6.1: The variation parameters and expansion coefficients of the radial WF in the $n^{14}C$ system for potential of the GS of ^{15}C (2.6.1). The WF normalization on an interval of 0–30 fm is equal to N_0 = 9.999975198490593E-001

I	α_i	C_i
1	4.400254682811078E-003	−1.911899202003393E-003
2	1.080053848380744E-002	−1.812966082174055E-002
3	2.564236030232376E-002	−5.667440751622722E-002
4	5.871946600420144E-002	−1.100036773570067E-001
5	1.272854480145382E-001	−1.689491422977194E-001
6	2.722367794808272E-001	−8.927563832717325E-002
7	3.451311294813448E-001	4.976170503854868E-001
8	5.153383537797701E-001	4.660987945089151E-001
9	7.170517147157914E-001	1.389709903982375E-001
10	1.048194029972669E-000	5.167447028899066E-003

For the real binding energy in such potential it is possible to accept the average value of −1.2180899(1) MeV obtained by two methods – FDM and VM. Thus, the accuracy of determination of the two-body binding energy of the GS of ^{15}C in the $n^{14}C$ channel for potential (2.6.1), obtained on the basis of two various computer programs, each of which are based on different numerical methods, is at the level of ±0.1 eV and coincides with the accuracy, which is initially defined with accuracy in the FDM.

In the given calculations the following value of mass of $m(^{14}C)$ = 14.003242 amu was used [214], and the mass of neutron is given in §1.6 earlier.

2.6.2 Total cross sections for the neutron capture on ^{14}C

Passing to the description of the results of our calculations, we will notice that the available experimental data for the total cross section of the neutron radiative capture on ^{14}C [247–251], found by using of the database of MSU [150], show the presence of large ambiguities of these cross sections measured in different studies. For example, at energy of 23 keV [248,250] the distinction of cross sections makes two or three times, and uncertainty of various data in the energy range of 100–1000 keV reaches three or four times [247,249–251]. The experimental results of the works stated above for energy range of 23 keV–1.0 MeV are shown in Figs. 2.6.1 and 2.6.2.

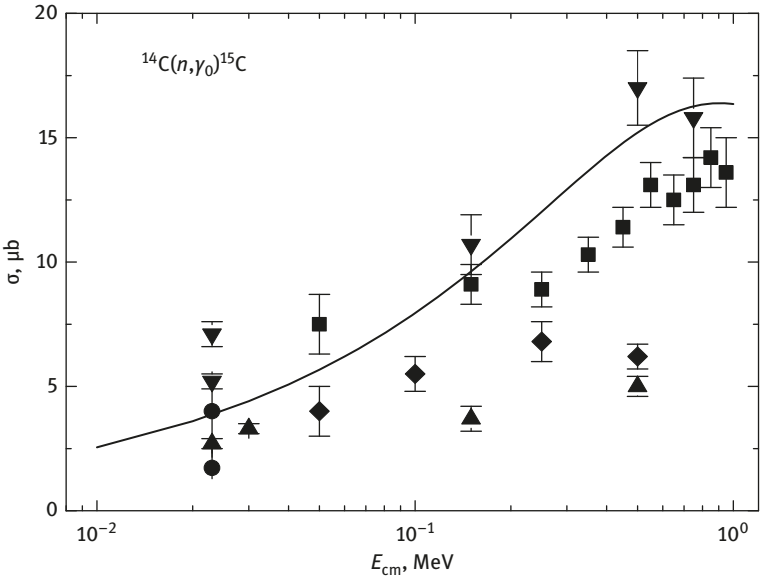

Fig. 2.6.1: The total cross sections for the neutron radiative capture on ^{14}C at energies of 10 keV–1 MeV. Experimental points: ■ – [247], ● – [248], ▲ – [249], ▼ – [250], ♦ – [251]. Curves: calculation of total cross sections for the potentials given in the text.

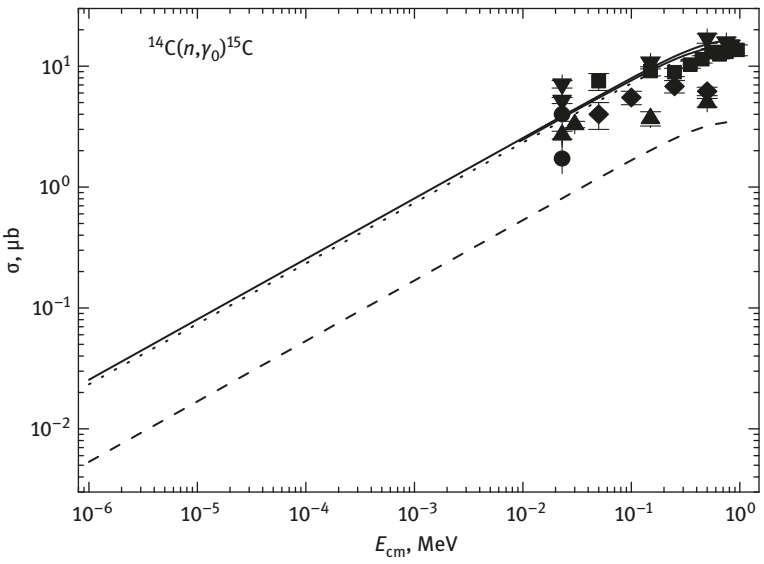

Fig. 2.6.2: Total cross sections for the neutron radiative capture on ^{14}C at energies of 1 eV–1 MeV. Experimental points: ■ – [247], ● – [248], ▲ – [249], ▼ – [250], ♦ – [251]. Curves: calculation of total cross sections for the potentials given in the text.

In this system we consider only the *E1* capture from the ^2P scattering states to the $^2S_{1/2}$ GS of ^{15}C – in §2.6.1 it is designated as process No.1. It become possible because in work [252] was shown that the contribution of the process of the radiative *E2* capture with transition from the ^2P waves scattering to the first excited state with $J^\pi = 5/2^+$ which can be compared with $D_{5/2}$ level, is less in 25–30 times. Therefore, if the available experimental errors and uncertainties in the measurements of the total cross sections it can quite be neglected.

Thus, for the total cross sections, as well as earlier in works [141,244], we considered only the *E1* transition from the non-resonance at the energies lower than 1.0 MeV $^2P_{1/2}$ and $^2P_{3/2}$ scattering waves with the potential of zero depth without FS to the $^2S_{1/2}$ bound GS of $n^{14}C$ clusters in ^{15}C for potential (2.6.1) with one FS. The calculation results of total cross sections for the neutron radiative capture on ^{14}C with the GS potential (2.6.1) specified above at energies lower than 1.0 MeV are shown in Figs. 2.6.1 and 2.6.2 by the solid curves, and in Fig. 2.6.2 calculation results starting from 1 eV.

As can be seen from these figures, the obtained results are located between various experimental data known in the energy range from 23 keV to 1.0 MeV, but best of all are coordinated, apparently, with results of works [247,250], which are measured at the very end of the 2000th years. Thus, the total capture cross sections entirely depend on the form of potential of the ground state of ^{15}C in the $n^{14}C$ channel, because at the considered energies the $^2P_{1/2}$ and $^2P_{3/2}$ scattering potentials of the input channel without the FS can be simply equalized to zero.

Note that if you use the potential of the GS of ^{15}C without FS, for example, with the parameters

$$V_{\text{g.s.}} = -19.994029 \quad \text{MeV}, \quad \gamma_{\text{g.s.}} = 0.2 \quad \text{fm}^{-2},$$

leading to the binding energy of –1.218090 MeV, the AC is equal to 1.46(1) on an interval of 5–30 fm, the charge radius of 2.51 fm and the mass radius of 2.63 fm, the calculation results of the total cross section shown in Fig. 2.6.2 by the dotted curves, which is located much below than all known experimental data.

In order to get the results in this case, describing the experiment correctly, the GS potential of ^{15}C without the FS with the next parameters is required

$$V_{\text{g.s.}} = -4.593639 \quad \text{MeV}, \quad \gamma_{\text{g.s.}} = 0.02 \quad \text{fm}^{-2}.$$

Such parameters lead to very large width and small depth of interaction, and the results of cross section calculations are shown in Fig. 2.6.2 by the dotted curves, which practically merge with the solid line. This potential brings to the charge radius of 2.53 fm and to the mass radius of 2.92 fm, and its AC on an interval of 15–30 fm is equal to 3.24(1), which is almost twice different from the results for the potential (2.6.1) and the conclusion of [206,245,246]. Thereby, it is clear from the obtained results that both the latest version of such GS potentials give the value of the AC incorrectly, though the last from them allows one to reproduce the experimental total capture cross sections.

Thus, the available experimental data manage to be described on the basis of only the $E1$ transition from the ^2P scattering waves from the zero potentials in the GS of ^{15}C, which is described by the interactions coordinated with the main characteristics of this state – the root-mean square radius, the AC in the considered n^{14}C channel and two-body binding energy.

However, for all the previously reviewed processes of the neutron radiative capture by light nuclei the total cross sections have been measured, starting with the area of 5–25 meV (see, for example, [244]). Therefore, it would be interesting to execute the measurements of cross section of this capture reaction, at least, at energy of 1 eV, for which the calculations given above give the cross section value about 0.025 μb.

Because, at energies from 1 eV to 1 keV the calculation cross section practically is a straight line (the solid curve in Fig. 2.6.2), it can be approximated by the simple function of the form [178,253]

$$\sigma_{ap}(\mu\text{b}) = A\sqrt{E_{\text{n}}(\text{keV})}, \tag{2.6.2}$$

this, however, differs from the usually used expression (2.1.3).

The value of the given constant A = 0.7822 μb keV$^{-1/2}$ was determined by one point in cross sections at the minimum energy equals 1 eV (c.m.).Then it turned out that the module $M(E)$ (2.1.4) the relative deviation of the calculated theoretical and approximation of this cross section the function given above at the energies less than 1 keV does not exceed 0.4%.

If to assume furthermore that this form of dependence of the total cross section by energy will be preserved at lower energies, it is possible to estimate, as usual, the value of the total cross section for the radiative capture, which, for example, at energy 1 meV (10^{-3} eV = 10^{-6} keV), gives the value about 0.78 10^{-3} μb [178,253].

2.6.3 The n^{14}N scattering potentials

Coming back to the classification of states according to Young tableaux, we will notice that in case of the n^{14}N system (for ^{14}N we have $J^\pi, T = 1^+0$) in the potentials of S scattering waves the forbidden bound state is present, and the $P_{1/2}$ wave has only the AS, which corresponds to the GS of ^{15}N with J^π, T = 1/2$^-$,1/2 and is at the binding energy of the n^{14}N system equal to −10.8333 MeV [229]. Such bound state can be mixed according to spin with S = 1/2 and 3/2, i.e., be the $^{2+4}P_{1/2}$ state. Then the $E1$ transitions from two S scattering waves with the bound FS to the $P_{1/2}$ GS of ^{15}N without the FS of the following form are possible here

2. $$^2S_{1/2} + {}^4S_{3/2} \rightarrow {}^{2+4}P^{g.s.}_{1/2},$$

Therefore, further the *E1* transitions to the GS from the non-resonance energy range up to 0.5–0.6 MeV doublet ${}^2S_{1/2}$ and quartet ${}^4S_{3/2}$ scattering waves with one bound FS will be considered, i.e., the following total cross sections of the capture reaction will be calculated

(A) $$\sigma_0(E1) = \sigma(E1, {}^2S_{1/2} \rightarrow {}^2P^1_{1/2}) + \sigma(E1, {}^4S_{3/2} \rightarrow {}^4P^1_{1/2}).$$

Thereby, as for the n^7Li capture, the transitions to the doublet and quartet parts of the WF of the GS, which in this approach do not differ and correspond to the BS in one potential are considered. Furthermore, we will be limited only by the transitions to the BS with the minimum values $J^\pi = 1/2^\pm$. For example, at the energy of 9.2221 MeV a spectrum of ^{15}N there is excited, but bound in the n^{14}N channel at −1.6112 MeV with $J^\pi = 1/2^-$ level (first ES). Therefore, it is possible to consider the additional transitions of the form

3. $$ {}^2S_{1/2} + {}^4S_{3/2} \rightarrow {}^{2+4}P^{e.s.}_{1/2},$$

i.e., to consider total cross sections of the following two *E*1 processes for the transition to the first ES

(B) $$\sigma_1(E1) = \sigma(E1, {}^2S_{1/2} \rightarrow {}^2P^2_{1/2}) + \sigma(E1, {}^4S_{3/2} \rightarrow {}^4P^2_{1/2}).$$

Besides, we will consider the possible transitions from the $P_{1/2}$ and $P_{3/2}$ scattering states to the second ES, the seventh ES and the ninth ES of ^{15}N with $J^\pi = 1/2^+$ at energy of 5.298822, 8.31262 and 9.04971 MeV, bound in the n^{14}N channel which can be carried to the doublet ${}^2S_{1/2}$ wave. And we will consider the ${}^{2+4}P_{1/2}$ scattering state, which has a resonance at 492.6(0.65) keV and with a width about 8(3) keV (see, for example, Table 15.14 and Table 15.4 of work [229] – resonance at 11.2928(7) MeV).

Located near the resonant state at 430(5) KeV with $J \geq 3/2$ and width of about 3 keV (energy of 11.235 (5) MeV in Table 15.4 [229]), but the parity [229] which is not defined so far, will not be taken into account. The ${}^{2+4}P_{3/2}$ potentials of scattering waves as they do not contain the FSs and have no resonances lower than 1.0 MeV, we will accept equal to zero. Zero, if not to take into account the presence of the resonance, can be considered the ${}^{2+4}P_{1/2}$ scattering potential too.

Then it is possible to analyze the *E1* processes of the next form

4. $$ {}^2P_{1/2} + {}^2P_{3/2} \rightarrow {}^2S^{e.s.}_{1/2}$$

and to present the summarized total cross sections for all transitions to the second ES, the seventh ES and the ninth ES in the form

(C)
$$\sigma_2(E1) = \sigma(E1,{}^2P_{1/2}\to{}^2S^1_{1/2}) + \sigma(E1,{}^2P_{3/2}\to{}^2S^1_{1/2}) + \\ + \sigma(E1,{}^2P_{1/2}\to{}^2S^2_{1/2}) + \sigma(E1,{}^2P_{3/2}\to{}^2S^2_{1/2}) + \\ + \sigma(E1,{}^2P_{1/2}\to{}^2S^3_{1/2}) + \sigma(E1,{}^2P_{3/2}\to{}^2S^3_{1/2}).$$

Here and earlier the figure on the right above designates the serial number of the level with the specified orbital momentum, for example, ${}^2S^1_{1/2}$.

Passing to the creation of the potentials of all these states, we will notice that the doublet ${}^2S_{1/2}$ levels with one bound FS obviously differ by the binding energy and for each of them the interaction potentials will be obtained. The ${}^2S$ and ${}^4S$ potentials of the scattering wave with one bound FS, having the resonances at the different energies, also have to differ obviously, but here we did not manage to construct the potentials which consider the resonances in these waves. Namely, the first resonance in the ${}^2S_{1/2}$ wave is at energy of 11.4376(0.7) MeV with $J^\pi = 1/2^+$ or 0.639(5) MeV (c.m.) above the n^{14}N channel threshold with a width of 34 keV (l.s.).

The resonance in the ${}^4S_{3/2}$ wave at the energy of 11.763(3) MeV with $J^\pi = 3/2^+$ or 0.998(5) MeV above the n^{14}N channel threshold with a neutron width about of 45 keV (l.s.) [229]. Therefore, furthermore we will consider that these potentials have to lead to the phase shifts close to zero and use for them the identical parameters of potentials, i.e., resonances which are present at these partial waves are not considered in the calculations.

So, for potentials of doublet ${}^2S_{1/2}$ and quartet ${}^4S_{3/2}$ scattering waves with one bound FS further the values of parameters which do not consider the presence of resonances at the considered energy range were used

$$V_S = -19.0 \quad \text{MeV}, \quad \gamma_S = 0.06\,\text{fm}^{-2}, \tag{2.6.3}$$

and the calculation results of the ${}^2S_{1/2}$ and ${}^4S_{3/2}$ phase shifts with the potential for energies up to 1.0 MeV lead to values of 0±2°.

The ${}^{2+4}P$ scattering states or the bound ${}^{2+4}P$ levels are mixed up by spin, therefore further the ${}^{2+4}P_J$ potentials of states are constructed for the states of the total angular momentum J. In particular, for the resonance at 493 keV potential of the $P_{1/2}$ wave without the FS the next parameters are used

$$V_P = -13328.317 \quad \text{MeV}, \quad \gamma_P = 50.0\,\text{fm}^{-2}, \tag{2.6.4}$$

which lead to the resonance energy of 493 keV at the level width of 18.2 keV, which is somewhat higher measured value [229]. Let us notice that for obtaining the correct value of the level width, we should make such potential narrower, and width parameter already has unusually high value.

Now we will consider the potentials of all stated above BSs of the $n^{14}N$ system in ^{15}N. The potential of the ground bound $^{2+4}P_{1/2}$ state without the FS has to reproduce the binding energy of ^{15}N in the $n^{14}N$ channel at −10.8333 MeV [229] correctly and it is reasonable to describe the root-mean square radius of ^{15}N, the experimental value of which is equal to 2.612(9) fm [229], at the experimental radius of ^{14}N equals 2.560(11) fm [150]. As a result, for the potential of the GS of ^{15}N in the $n^{14}N$ channel without the FS the parameters were obtained

$$V_{\text{g.s.}} = -55.442290 \quad \text{MeV}, \quad \gamma_{\text{g.s.}} = 0.1\,\text{fm}^{-2}. \tag{2.6.5}$$

The potential leads to the binding energy of −10.83330001 MeV with the FDM accuracy of 10^{-8} MeV, to the root-mean square charge radius of 2.57 fm and the mass radius of 2.59 fm. For the asymptotic constant on an interval of 7–13 fm the value 4.94(1) is obtained. The error of a constant is determined by its averaging by the interval of distances stated above. The value equaling 5.69(7) $\text{fm}^{-1/2}$ is given in works [195], that after the recalculation to dimensionless value at $\sqrt{2k_0}$= 1.184 and the spektrofactor S_f equals unit gives 4.81(6). This value agrees well with the above value for the potential of the GS.

In review paper [197] the spektrofactor interval is given in limits from 1.231 to 1.48 with average value of 1.36 and the ANC equal to 5.35 $\text{fm}^{-1/2}$. In that case, taking into account (1.7.1), (1.7.2), (1.2.5) for C_w we find the value of 3.87, slightly less than the obtained for potential (2.6.5). If to consider an interval of values of spektrofactor, we obtain an interval of the dimensionless AC of 3.71–4.07, the top value of which is also slightly less than obtained value.

For the additional control of calculation of the energy of GS the variation method, which already on a grid with dimension N = 10 and an independent variation of parameters for the potential (2.6.5) allowed to obtain the energy of −10.83330000 MeV, was used. The parameters of the variation radial WF are specified in Table 2.6.2, and the value of residuals does not exceed 10^{-8} [24]. The value of the AC in the range of 7–14 fm was equal to 4.9(1), and the charge radius does not differ from the value obtained above in FDM calculations.

Consequently, for real binding energy in such potential it is possible to accept the average value −10.833300005(5) MeV. Thus, the accuracy of the determination of the binding energy of ^{15}N for the intercluster potential (2.6.5), obtained by two methods (FDM and VM), according to two various computer programs, can be given as $\pm 5 \cdot 10^{-9}$ MeV = ±5 meV. It practically coincides with the initially accuracy of the finite-difference method of search of the binding energy equal to 10^{-8} MeV.

The potential parameters of the FES of ^{15}N at energy of −1.6112 MeV in the $n^{14}N$ channel with $J^\pi = 1/2^-$ [229], which coincides with the moment of the GS have values

$$V_{\text{e.s.}} = -33.120490 \quad \text{MeV}, \quad \gamma_{\text{e.s.}} = 0.1\,\text{fm}^{-2}. \tag{2.6.6}$$

Table 2.6.2: The variation parameters and expansion coefficients of the radial WF in the n^{14}N system for potential of the GS of ^{15}N (2.6.5). The WF normalization on an interval of 0–30 fm is equal to N_0 = 1.000000000000001.

i	α_i	C_i
1	2.763758363387135E-002	−3.542736101468866E-004
2	5.252886535294879E-002	−6.584466560462019E-003
3	9.444752983481111E-002	−4.679747477384075E-002
4	1.088660404093062E-001	1.318491526218144E-002
5	1.503486884800729E-001	−1.087314408835770E-001
6	2.226413018972464E-001	−8.992256982354141E-002
7	2.684402252313877E-001	−5.745985900990638E-002
8	3.736191607656845E-001	−2.834463978909703E-002
9	7.499707281247036E-001	−1.302287964205851E-004
10	6.009438691088970	2.060489845515652E-006

The potential leads to the binding energy of −1.611200 MeV with an FDM accuracy of 10^{-6} MeV, to the root-mean square charge radius of 2.58 fm and the mass radius of 2.71 fm. For the asymptotic constant, which is written down in a dimensionless form (1.2.5) on an interval of 8–30 fm the value 1.19(1) is obtained.

For potentials of the ES with $J^\pi = 1/2^+$ in ^{15}N, which are compared to the bound $^2S_{1/2}$ levels in the n^{14}N channel, the same width, as for the GS or the potential of FES (2.6.6) was also used. For example, for the potential of the first bound in the n^{14}N channel $^2S_{1/2}$ state, designated above the SES at the energy of 5.298822 MeV, relatively to the GS or −5.534478 MeV relatively to the threshold of the n^{14}N channel these values are used

$$V_{1S} = -66.669768 \quad \text{MeV}, \quad \gamma_{1S} = 0.1\,\text{fm}^{-2}. \tag{2.6.7}$$

The potential leads to the binding energy of −5.534478 MeV, to the charge radius of 2.57 fm, the mass radius of 2.69 fm and the AC of 5.65(1) on an interval of distances of 8–20 fm.

For the potential of the second bound $^2S_{1/2}$ state in the n^{14}N channel, designated above as seventh ES at the energy of 8.31263 MeV, relatively to the GS or −2.52068 MeV relatively to the threshold of the n^{14}N channel these values are used

$$V_{2S} = -56.271191 \quad \text{MeV}, \quad \gamma_{2S} = 0.1\,\text{fm}^{-2}. \tag{2.6.8}$$

The potential leads to the binding energy of −2.520680 MeV, to the charge radius of 2.58 fm, the mass radius of 2.77 fm and the AC of 3.34(1) on an interval of distances of 8–21 fm.

For the potential of the third bound $^2S_{1/2}$ state in the n^{14}N channel, designated above as ninth ES at the energy of 9.04971 MeV, relatively to the GS or −1.78362 MeV relatively to the threshold of the n^{14}N channel these values are used

$$V_{3S} = -53.1402573 \quad \text{MeV}, \quad \gamma_{3S} = 0.1\,\text{fm}^{-2}. \tag{2.6.9}$$

The potential leads to the binding energy of –1.783620 MeV, to the charge radius of 2.58 fm, the mass radius of 2.82 fm and the AC of 2.78(1) on an interval of distances of 8–27 fm.

In the calculations given here the following value of mass of $m(^{14}\text{N}) = 14.003074$ amu was used [214], and the mass of neutron is specified in chapter 1 §1.6.

2.6.4 Total cross sections of the neutron capture on ^{14}N

Passing to the direct description of the results of our calculations, we will notice that all used experimental data for the total cross sections for the neutron radiative capture on ^{14}N were obtained from the database [150], and data are given in works [152,254–256]. These data are obtained for the energy range of 25 meV–65 keV and shown in Fig. 2.6.3.

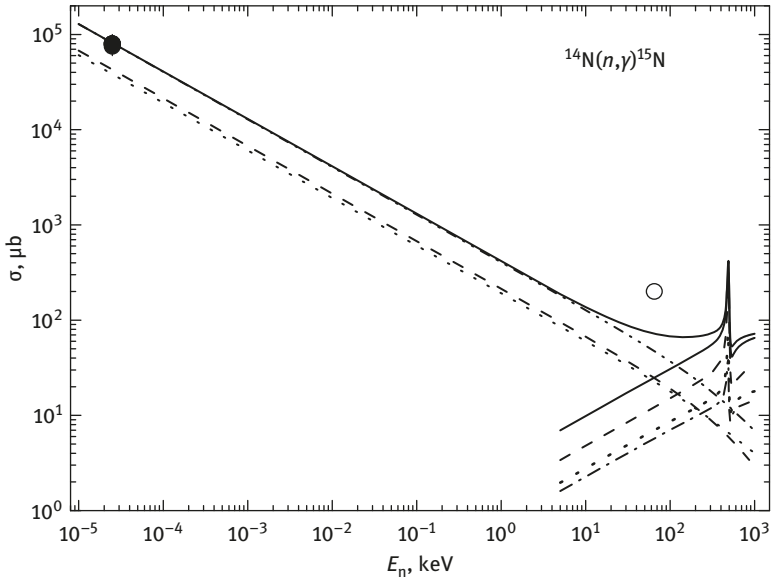

Fig. 2.6.3: Total cross sections of the neutron radiative capture on ^{14}N. Experimental points: ● – [152, 254, 255], ○ – [256]. Curves: calculation of the total cross sections for the given in the text potentials.

In the same place the results of our calculation of total cross sections of the neutron radiative capture on ^{14}N to the considered above two bound $^{2+4}P_{1/2}$ levels and three $^2S_{1/2}$ states of ^{15}N are given at energies lower than 1.0 MeV. The experimental results of different works at energy of 25 meV have the values of the total cross sections in the

range of 77–80 mb. They are given in Fig. 2.6.3 by one point and, for example, in one of the work [255] for this energy value 80.3(6) mb was obtained. At the latest work [184] the value of 80.0(4) mb was given.

In Fig. 2.6.3 by the dotted curves in non-resonance area are shown the calculations of cross sections for transition from S scattering waves (2.6.3) to the GS (2.6.5), i.e., the cross section designated above as process "A". By the dotted curve the results of calculations with the transition to the first excited ${}^{2+4}P_{1/2}$ state with the potential (2.6.6) are given, i.e., the cross section designated above as "B" process. By the double dotted-dashed line designates their sum, which well describes the total cross section at thermal energy 25 meV.

The resonance part of cross sections for the ${}^{2}P_{1/2}$ scattering potential (2.6.4) and the zero potential ${}^{2}P_{3/2}$ wave of a continuous spectrum defined by the transitions to the 1, 2 and 3 bound ${}^{2}S_{1/2}$ states (second ES, seventh ES, ninth ES) with the potentials (2.6.7) – (2.6.9), i.e., the cross section designated above by a "B" symbol. These cross sections are designated by the dashed, dotted and dashed-dotted curves, respectively, and by the solid line in the resonance range, i.e., about 5–1000 keV, their sum is shown. Other solid curve in all energy range, i.e., from 10^{-5} keV to 1.0 MeV, shows the total cross sections of all the transitions considered above – "A + B + C".

From the given Fig. 2.6.3 it is clear that results of our calculation describe the data on the capture cross sections at 25 meV, but do not reproduce the measurement of work [256] at energy of 65 keV, shown by open circle. The reason of it, perhaps, consists in the absence of the accounting of transitions from the resonance ${}^{2}S_{1/2}$ and ${}^{4}S_{3/2}$ of the scattering waves with rather large width which did not manage to be constructed, to the GS and first excited ${}^{2+4}P_{1/2}$ states with $J^{\pi} = 1/2^{-}$.

Furthermore, we will notice that if for the comparison we will use the ${}^{2}S_{1/2}$ and ${}^{4}S_{3/2}$ scattering potentials with the zero phase shifts and zero depth, which do not contain the FS, i.e., would not be coordinated with the classification of the FS and AS according to Young tableaux given above, then the results of calculation of cross sections for the potentials of the GS (2.6.5) and the ES (2.6.6) are above than all experimental data, more than an order of magnitude.

This result shows that the scattering potentials in this system have to comply with the classification according to Young tableaux. Only in that case it is possible to obtain the interactions, owing to which there is possible to describe the cross section at thermal energy. Meanwhile, apparently, only this cross section is determined rather precisely that is confirmed by the numerous measurements executed in works [254,255] at energy of 25 meV.

From the obtained results it is clear that in this system it is quite possible to agree the description of the total cross sections of the radiative capture process at the lowest energy and BS characteristics of ^{15}N, including the AC in the n^{14}N channel based on the consideration of the combination of potentials (2.6.3) and (2.6.5) (2.6.6). In other words, if to fix the parameters of the GS potential of ^{15}N in the n^{14}N channel on the basis of the correct description of its characteristics, on the basis of

classification of the FS and AS according to Young tableaux, is quite possible to find the $^{2+4}S_{1/2}$ of the scattering potentials. Such potentials allow one to describe elastic scattering phase shifts, which have the zero value and the value of total cross sections for the neutron radiative capture on ^{14}N at energy of 25 meV correctly. Furthermore, measurements of total cross sections at other energies would enable more specifically to find out the quality of the description of such cross sections in the model for the potentials with the FS.

Because at energies of 10 meV to 10 keV, the calculated cross-section shown in Fig. 2.6.3 by the solid curve is almost a straight line, they can be approximated by a function of the form by energy (2.1.3). The value of the constant $A = 406.4817$ μb keV$^{1/2}$ in this expression was determined by a single point in cross-sections with a minimum energy of 10 meV = 10^{-3} eV (ls). The module (2.1.4) of a relative deviation of the calculated theoretical cross-section and approximation of this cross-section by the used function (2.1.3) in the range of up to 10 keV does not exceed 0.9%. The cross-section value at energy of 1 μeV (1 μeV = 10^{-6} eV = 10^{-9} keV), gives the value of approximately 12.8 b [257].

2.7 The radiative neutron capture on ^{15}N

Continuing the study of neutron capture reactions on light nuclei, we get to the thermonuclear processes, we will discuss the capture reaction $n^{15}\text{N} \to {}^{16}\text{N}\gamma$ at low energies. This process is included in the main chain of reactions of the primordial nucleosynthesis (2.0) determine the development of the universe. For this, the methods of calculations based on the MPCM of light atomic nuclei with forbidden states will be used. The existence of the FSs in wave functions is determined based on the classification of orbital states of clusters according to Young tableaux.

In the approach used by us, the potentials of intercluster interactions for scattering processes are based on the reproduction of the elastic scattering phase shifts of considered particles concerning their resonance behavior or based on the structure of the spectra of resonance states of the final nucleus. For bound or ground states of the nuclei, which are formed as a result of the reaction in the cluster channel, coinciding with initial particles, the intercluster potentials are constructed on the basis of the description of binding energy of these particles in a final nucleus and some main characteristics of such states.

2.7.1 The potentials of the n^{15}N scattering

Moving to analysis of the total cross-sections of the neutron capture on ^{15}N, we will notice that the classification of orbital states of ^{15}N in the n^{14}N channel according to Young tableaux was considered by us above as well as in [257]. Therefore, for the n^{15}N system we

have {1} × {4443} → {5443} + {4444} [11]. The first of the obtained tableaux is compatible with the orbital moments L = 1, 3, and is forbidden because it has five cells in the first row, and the second tableaux is allowed and compatible with the orbital moment 0 [11]. Thus, being limited only by the lowest partial waves, it is possible to consider that in potentials of S and D waves the forbidden states are absent, and the P wave contains the bound FS. We will further consider that in the D wave there is an allowed state, which corresponds to the GS of ^{16}N and is at the binding energy of the n^{15}N system of −2.491 MeV [258]. Because the moment of ^{15}N is $J^{\pi},T = 1/2^{-},1/2$ [229], and for ^{16}N characteristics of $J^{\pi},T = 2^{-},1$ [258] are known, the GS of ^{16}N in the n^{15}N channel can be the mixed of singlet and triplet $^{1}D_2$ and $^{3}D_2$ states with total angular moment $J = 2$. Moreover, the potential of the partial S wave may also contain the bound AS.

As we do not have complete product tables of Young tableaux for the system with the number of particles of more than eight [134], which were used by us earlier for the similar calculations [12,14,19,183,230]. The result obtained above should be considered only as the quality standard of the possible orbital symmetry for the bound states of ^{16}N in the n^{15}N channel. Simultaneously, based on similar classification, it was possible to explain available experimental data on the proton radiative capture on ^{13}C [141,259], and the neutron radiative capture on ^{12}C, ^{13}C [244], ^{7}Li [207] and ^{14}N [257] quite acceptable. Therefore, here, we will use the similar classification of cluster states by the orbital symmetry, which gives a certain number of the FSs and ASs in various partial intercluster potentials of interaction. The number of such states determines the number of nodes of the radial wave function of the relative motion of the clusters with a certain orbital momentum [12,14].

To describe the total cross-sections for the neutron radiative capture on ^{15}N, as in previous studies [12,14,19,257,259], we mainly considered the $E1$ transitions. In this process, such transition is possible from the nonresonance $^{3}P_2$ scattering waves with the zero phase shift at energies of up to 1.0 MeV at $^{3}D_2$ triplet part of the wave function of the ground bound state in the n^{15}N cluster channel of ^{16}N

1. $$^{3}P_2 \rightarrow {}^{3}D_2.$$

Moreover, the $E1$ transitions from the resonance P_1 scattering wave at 0.921 MeV (ls) with a width of 14 keV (ls) and $J^{\pi} = 1^{+}$ at 3.3528(26) MeV [258], which is a mixture of the triplet $^{3}P_1$ and singlet $^{1}P_1$ states, to the triplet $^{3}D_2$ and singlet $^{1}D_2$ part of wave function of the GS, respectively

2. $$\begin{matrix} {}^{3}P_1 \rightarrow {}^{3}D_2 \\ {}^{1}P_1 \rightarrow {}^{1}D_2 \end{matrix}.$$

Earlier in §2.3.3, we already considered similar processes for the neutron capture on ^{7}Li. The total cross-section is the sum of the cross-sections for the transitions from the

various S-scattering waves in the different parts of the wave function of the GS wave function mixed by the spin, i.e., total cross-section can be written as

$$\sigma(E1) = \sigma(E1,^3 S_1 \rightarrow ^3 P_2) + \sigma(E1,^5 S_2 \rightarrow ^5 P_2).$$

However, here we have another situation because mixing by the spin is observed not only for the GS, but also in the initial scattering state. Therefore, the notation of capture cross-sections for the transition of No. 2 will be considered further using two different ways in more detail.

For the calculations of the total cross-section of the radiative capture, the nuclear part of the intercluster potential of n^{15}N interaction is presented in the form of Gaussian function (1.2.2) [19]. For the resonance potential at 0.921 MeV [258] $^{1+3}P_1$ of scattering waves, with one FS was not successful in obtaining the potential which can describe the resonance width. For example, the Gaussian potential with the parameters and FS

$$V_{P1} = -7687.40 \quad \text{MeV}, \quad \gamma_{P1} = 10.0\,\text{fm}^{-2}$$

leads to the resonance width at energy of 0.921 MeV of 138 keV (cm) which is approximately 10 times more of the experimental value of 14 keV (Is) specified in Table 16.10 of work [258]. We will notice that according to these, Table 16.5 from the same review [258], this width is equal to 15(5) keV (cm).

The calculation of the P_1 phase shift of the elastic n^{15}N scattering with such potential at energies ranging from 0.2 MeV to 1.25 leading to its resonance shape

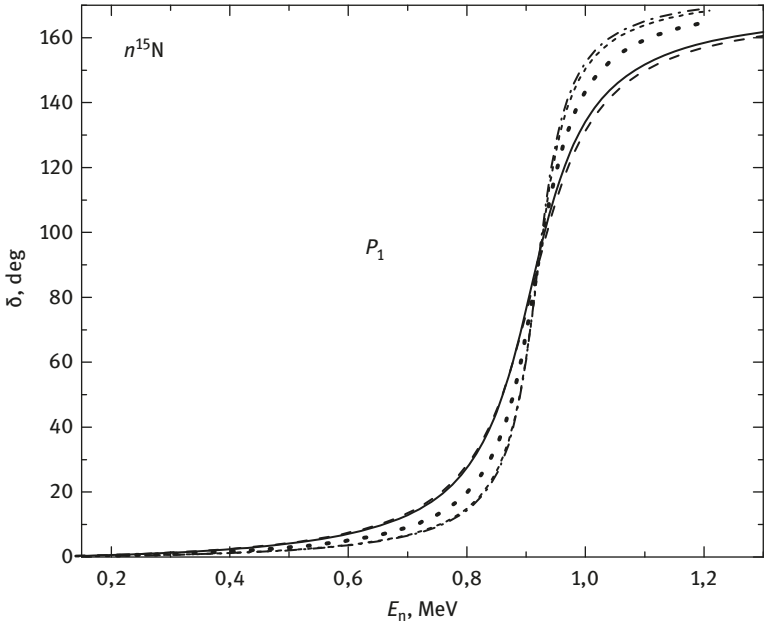

Fig. 2.7.1: Phase shifts of the n^{15}N elastic scattering in the P_1 wave. The curves obtained for different potentials, described in the text.

shown in Fig. 2.7.1 by the solid curve. To reproduce the width of the resonance correctly it is necessary to considerably increase the parameter γ, i.e., reduction in the potential width. For example, the parameters

$$V_{P1} = -15385.47 \quad \text{MeV}, \quad \gamma_{P1} = 20.0\ \text{fm}^{-2}$$

lead to the resonance width of approximately 98 keV (cm), and the phase shift of such potential is shown in Fig. 2.7.1 by the dotted curve.

The parameters of the narrower potential with one bound forbidden state

$$V_{P1} = -30781.774 \quad \text{MeV}, \quad \gamma_{P1} = 40.0\ \text{fm}^{-2}. \tag{2.7.1}$$

lead to the width of the resonance of 70 keV in cm, and its phase shift is presented in Fig. 2.7.1 by the dashed-dotted curve. The relative accuracy of calculation of the P_1 scattering phase shift in these calculations is approximately 10^{-3} and for the resonance energy of 921 keV this potential leads to the phase shift of 90.0(1)° value.

As seen from these results, even for very approximate description of width of this resonance in the elastic n^{15}N scattering, the P_1 potential has a very large depth and exclusively small width. Therefore for independently verifiying the results, another calculation program of phase shifts was used, which was developed independently by another author based on other numerical methods of determination of the wave function and a bit different ways of jointing the wave function with an asymptotics. Based on the potential (2.7.1) at the resonance energy of 921 keV (ls) and at 500 thousand steps for calculating wave function, at its joining with an asymptotics at 30 fm the scattering phase shift equals 89.9° is obtained [260]. This result differs from the value given above only on 0.1°, i.e., approximately at the value of an error of its determination, given in our program with an automatic choice of a step and distances for joining the wave function [261].

Thereby, the results obtained according to two independent programs completely validate creation of such potential and the accuracy of the search of a phase of scattering. For the comparison of such results it is necessary to remember that the constant $\hbar^2/m_0$ was accepted equal to 41.4686 MeV fm^2, for the value of ^{15}N mass the value of 15.000108 amu was used [214], and the exact mass of a neutron is specified in chapter 1 of §1.6 [126]. This computer program [261] was used in all calculations of the nuclear scattering phase shifts given in this book.

Now, once again we notice that the known resonance energy level in the spectra of ^{16}N and its potential width with the FS is constructed unambiguously. It is impossible to find other V_0 and γ parameters, which would be capable to describe the resonance energy of level and its width if the quantity of the FS, which in this case is equal to unity is set correctly. The depth of the potential uniquely identifies the resonance position, i.e., the resonance energy of the level, and its width gives a certain width of this resonance state (see §1.7 in Chapter 1).

However, we did not manage to find any physical explanation of such a small width and a large depth of this potential – the entire mass of 16 nucleons in ^{16}N is

approximately 15 GeV, and the potential depth (2.7.1) is of the order of 30 GeV. Therefore, the potentials used here should be considered for approximation within the potential approach of experimentally observed width of the considered level at 921 keV, which presents at the elastic n^{15}N scattering (see data from Table 16.10 of review [258]).

For comparison, we will give the similar P_1 scattering potential without FS, i.e., which is not consistent with the above in §2.7.1, classification according to Young tableaux, and parameters

$$V_{P1} = -1321.18 \quad \text{MeV}, \quad \gamma_{P1} = 5.0\,\text{fm}^{-2}.$$

which gives the width of the resonance of approximately 148 keV (cm), and its phase shift is shown in Fig. 2.7.1 by the dashed curves. It differs slightly from the solid line, the results of which for the first variant of this potential with the FS are shown. Thus, it is clear that the potential without the FS, which does not coordinate with the classification according to Young tableaux, will also require a very small width to describe the observed width of the resonance [258].

For example, another variant of the potential without the forbidden state and parameters

$$V_{P1} = -5302.745 \quad \text{MeV}, \quad \gamma_{P1} = 20.0\,\text{fm}^{-2} \tag{2.7.2}$$

has a width of the resonance of approximately 74 keV (cm), and its phase shift is shown in Fig. 2.7.1 by the short-dashed curve. Such scattering phase shift practically does not differ from the dashed-dotted curve for the potential (2.7.1) containing the FS.

This potential will be used further for comparing the results of capture cross-sections calculated for the interactions, satisfying the classification of the FSs according to Young tableaux (2.7.1) as both of them give the approximately identical width of the resonance at the energy of 921 keV. We will notice that the wave function of the potential given above at energy of the elastic scattering, for example, 10 eV has smooth character and does not contain the node. At the same time, the wave function of the continuous spectrum for the n^{15}N scattering at the same energy for the potential with the FS (2.7.1) contains the node approximately at 0.14 fm.

For the potentials of the nonresonance $^3P_2$ and $^3P_0$ waves with one FS, the parameters based on the assumption that in the considered energy range of up to 1.0 MeV, the phase shifts of zero were used. Such assumption is submitted reasonably and was used earlier as in the spectra of ^{16}N in the n^{15}N channel, which is not observed with resonance levels with $J^\pi = 2^+$ and 0^+ (see Table 16.10 in work [258]).

In particular, for the parameters of such potential with the forbidden bound state, the following is obtained

$$V_{P2} = -500.0 \quad \text{MeV}, \quad \gamma_{P2} = 1.0\,\text{fm}^{-2}. \tag{2.7.3}$$

The calculation of the P phase shifts with such potential at energy up to 1.0 MeV gives values no more than 0.1°. Here, it is necessary to remember that as potential has the

bound level (FS or AS – see, for example, [11], it has to lead to the scattering phase shift starting from 180° because such phase shift obeys to the generalized Levinson theorem. Therefore, the record of the scattering phase shift discussed above gives a value of 180.0°±0.1°.

The potential without the FS of the bound $^{1+3}D_2$ states has to reproduce the binding energy of the ground state of ^{16}N with $J^{\pi},T = 2^{-},1$ in the n^{15}N channel at –2.491 MeV [258], and it is reasonable to describe the root-mean square ^{16}N radius correctly. Its experimental value should not exceed the ^{16}O radius equaling 2.710(15) fm [258], and the experimental radius of ^{15}N is equal to 2.612(9) fm [229]. For a neutron, the zero charge radius with its mass radius of 0.8775(51) fm equaling the radius of proton was used from work [126].

The following parameters for the potential of the ground state of ^{16}N in the n^{15}N channel, which describes all requirements given above obtained as

$$V_{\text{g.s.}} = -49.5356532 \quad \text{MeV}, \quad \gamma_{\text{g.s.}} = 0.07\,\text{fm}^{-2}. \tag{2.7.4}$$

The potential leads to the binding energy of –2.49100003 MeV with an FDM accuracy of 10^{-8} MeV [261], to the root-mean square charge radius of 2.63 fm, and the mass radius of 2.76 fm. For the asymptotic constant defined in work [94] described in a dimensionless form at the value of 0.96(1) on an interval of 6–19 fm was obtained. The error for the constant is determined by averaging the interval of distances stated above.

In [206], for this AC, the value of 0.85 $\text{fm}^{-1/2}$ is given, recalculation to the dimensionless value at $\sqrt{2k_0} = 0.821$ in the assumption of $S_{\text{f}} = 1$ from the expression (1.7.1), we obtain 1.04. This value only for 10% differs from the obtained above for potential (2.7.4). Once again we will pay attention that recalculation of the AC is required similar to [206] other determination of the AC (1.7.2), which differs from used here (1.2.5) on a multiplier $\sqrt{2k_0}$ was used.

For additional control of calculation of the GS energy the variation method [22,24,261], on a grid with dimension of $N = 10$ and an independent variation of the parameters for the potential (2.7.4) allowed to obtain the energy of –2.49100001 MeV was used. The parameters of the variation radial wave function are specified in Table 2.7.1, and the value of residual does not exceed 10^{-13} [24, 261]. The value of the AC is 0.96(1) at 9–24 fm, and charging radius does not differ from the value obtained above using FDM calculations.

Let us remember that the variation energy with the increase in the dimension of basis decreases and approached the top limit of thetrue binding energy, and finite-difference energy while reducing the value of step and increasing the number of steps [24,261]; thus, for real binding energy,in such potential it is possible to accept average value of –2.49100002(1) MeV. Thus, the accuracy of the determination of the two-body binding energy of ^{16}N in the n^{15}N channel with a potential (2.7.4) by two methods (FDM and VM) according to two various and independent computer programs [261] at the

Table 2.7.1: Variation parameters and expansion coefficients of the variation wave function in the n^{15}N system for the GS potential of ^{16}N (2.7.4). Wave function normalization on an interval of 0–30 fm is N_0 = 9.999999994380500E⁻001.

i	α_i	C_i
1	1.007315112666127E–002	7.788913416706688E–006
2	2.114166815403187E–002	1.840350354408430E–004
3	4.065632994643584E–002	1.624635313928398E–003
4	6.341390294306766E–001	4.554526693691232E–005
5	7.371125591230167E–002	8.955183950318307E–003
6	1.284454542085454E–001	3.511639379823815E–002
7	1.828031977711215E–001	–2.448510312616634E–001
8	2.023555602680635E–001	2.154064966258853
9	2.100279381326923E–001	–4.331318884909111
10	2.143212946811676E–001	2.442239109862597

level of $\pm 10^{-8}$ MeV = ±10 meV. This value coincides with accuracy initially set in FDM when determining the binding energy of two-cluster system equals 10^{-8} MeV.

Furthermore, we will notice that for the first three excited states of ^{16}N with $J^\pi = 0^-, 3^-$, and 1^-, bound in the n^{15}N channel, in [206] AC values of 1.10, 0.29, and 1.08 fm$^{-1/2}$, respectively, were obtained. After recalculation to a dimensionless form we have 1.36 at $\sqrt{2k_1} = 0.811$ ($J^\pi = 0^-$), 0.36 at $\sqrt{2k_2} = 0.795$ ($J^\pi = 3^-$) and 1.37 at $\sqrt{2k_3} = 0.786$ for level with $J^\pi = 1^-$. In all cases $S_f = 1$ of expression is expected (1.7.1). The potentials of these three first bound ES obtained further were constructed to approximately reproduce the obtained results of work [206], as well as the above-mentioned values of the asymptotic constants.

Thus, except the GS interaction (2.7.4), the potentials of first three excited states at energies of 0.12042 MeV with $J^\pi = 0^-$, 0.29822 MeV with $J^\pi = 3^-$ and 0.39727 MeV with $J^\pi = 1^-$ [258] relative to the GS of ^{16}N were found. They correspond to the energy of –2.37058 MeV ($J^\pi = 0^-$), –2.19278 MeV ($J^\pi = 3^-$) and –2.09373 MeV ($J^\pi = 1^-$) relative to the threshold of the n^{15}N channel. These bound states can be matched the next $^1S_0$, $^3D_3$, and $^3S_1$ levels of ^{16}N by considering the n^{15}N cluster channel.

For the first of these ESs, the parameters of the $^1S_0$ potential without the FS in the n^{15}N channel were obtained

$$V_{S0} = -54.454312 \quad \text{MeV}, \quad \gamma_{S0} = 0.6\,\text{fm}^{-2}. \tag{2.7.5}$$

The potential leads to the binding energy of –2.370580 MeV with an FDM accuracy of 10^{-6} MeV [261], to root-mean square charge radius of 2.62 fm, and mass radius of 2.63 fm, and AC value of 1.35(1) at an interval of 3–22 fm which is consistent with previously published results [206].

For the second ES bound in the n^{15}N channel the $^3D_3$ potential is obtained without the FS and with parameters

$$V_{D3} = -126.14123 \quad \text{MeV}, \quad \gamma_{D3} = 0.2\,\text{fm}^{-2}. \tag{2.7.6}$$

Potential gives the binding energy of –2.192780 MeV with an FDM accuracy of 10^{-6} MeV [261], the root-mean square charge radius of 2.62 fm, and mass radius of 2.64 fm. For the AC at an interval of 5–22 fm the value of 0.32(1), which differs from the above-mentioned value as well as work [206] approximately for 10% was obtained.

For the potential of the third ES without the FS which corresponds to the $^3S_1$ level, the parameters were obtained

$$V_{S1} = -53.170538 \quad \text{MeV}, \quad \gamma_{S1} = 0.6\,\text{fm}^{-2}. \tag{2.7.7}$$

The potential leads to the binding energy of –2.093730 MeV with an FDM accuracy of 10^{-6} MeV [261], to root-mean square charge radius of 2.62 fm, mass radius of 2.64 fm, and for the AC at an interval of 3–23 fm the value of 1.33(1), which differs slightly from the results of work [206].

Consequently, for these excited states together with the GS of ^{16}N in the n^{15}N channel in addition to the transition No.s 1 and 2 it is possible to consider the following five *E1* transitions from nonresonance $^3P_2$ and $^3P_0$ waves and resonance mixed according to spin $^{1+3}P_1$ scattering states to these ES

3. $$\sigma_{ex}(E1) = \sigma(E1,{}^3P_0 \to {}^3S_1) + \sigma(E1,{}^3P_2 \to {}^3S_1) + \sigma(E1,{}^3P_1 \to {}^3S_1) + \\ + \sigma(E1,{}^1P_1 \to {}^1S_0) + \sigma(E1,{}^3P_2 \to {}^3D_3)$$

Therefore, based on certain assumptions, the intercluster potentials were constructed, i.e., their parameters for correctly describing the spectra of resonance levels and characteristics of the BSs, in particular, the ACs, are fixed. In general, it is possible to reproduce the available experimental data on the spectrum of ^{16}N levels, along with characteristics of the bound states of this nucleus in the n^{15}N channel. Furthermore, the offered scattering potentials and the BS quite satisfy the classification of orbital cluster states according to Young tableaux mentioned above. The obtained potentials allow one to consider further eight *E1* transitions from the various *P* states of the n^{15}N scattering to four *S* and *D* bound states in the n^{15}N channel of ^{16}N.

2.7.2 Total cross-sections of the neutron capture on ^{15}N – first variant

For the direct examination of the results for the stated above *E1* transitions to the GS and the first three ESs of ^{16}N, we will notice that we managed to find [150,262–264] the experimental data for the total cross-sections neutron capture process on ^{15}N only at three energies of 25, 152, and 370 keV [265]. These results are presented in Fig. 2.7.2–2.7.4 using black points.

Here, we consider the first variant of our calculations of cross-sections for transitions No. 1 and No. 2 to the GS. In this case, the transition No. 2 of the *P* scattering waves

with potentials (2.7.1) and (2.7.4) is presented in the form of the simple sum of cross-sections

4. $$\sigma_{02} = \sigma(E1, {}^3P_1 \rightarrow {}^3D_2) + \sigma(E1, {}^1P_1 \rightarrow {}^1D_2).$$

The calculation results of this cross-section is presented in Figs. 2.7.2 by the dashed curve, the dotted shows the cross-section of transition No.1 ${}^3P_2 \rightarrow {}^3D_2$ for potentials (2.7.3) and (2.7.4)

$$\sigma_{01} = \sigma(E1, {}^3P_2 \rightarrow {}^3D_2),$$

and the solid is their sum.

From results shown in Figs. 2.7.2 [266], it is clear that it is enough to consider only these three transitions to the GS for describing the total cross-sections of the radiative capture, described in [265]. Therefore, for representing the total section of process No. 2 in the form of No. 4, it is not required to consider the transition to the excited states of ^{16}N of the form No. 3. The measured cross-section almost completely is determined by the simple sum of cross-sections for two obvious transitions No. 2, if the cross-section is represented in the form of No. 4.

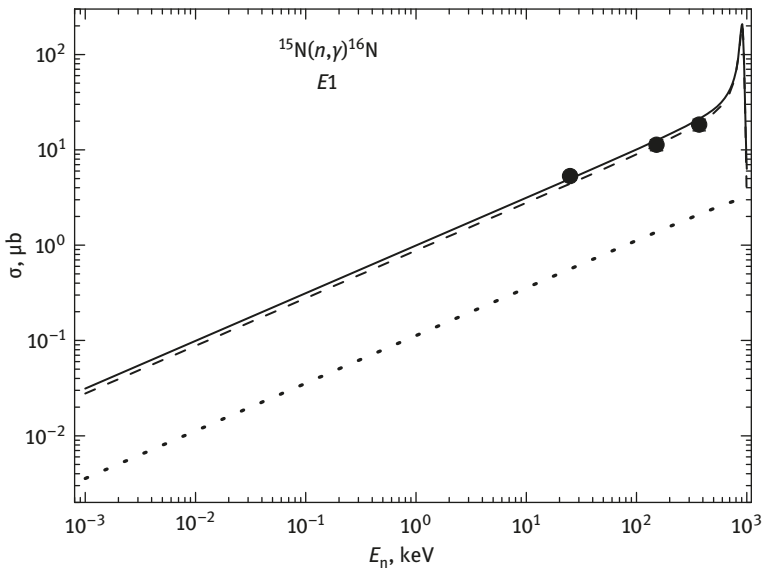

Fig. 2.7.2a: Total cross-sections of the neutron capture on ^{15}N at the energy of 1 eV. Experimental points: ● – [265]. Curves – calculation of the total cross-sections.

We will also pay attention because of the large width of the resonance phase shift of P_1 potential (2.7.1) the width of the resonance of total cross-sections in the calculations are slightly overestimated. It leads to slightly inflated cross-section value at the energy of 370 keV [265], which is close to a resonance of 921 keV, as it is clear in Fig. 2.7.2b.

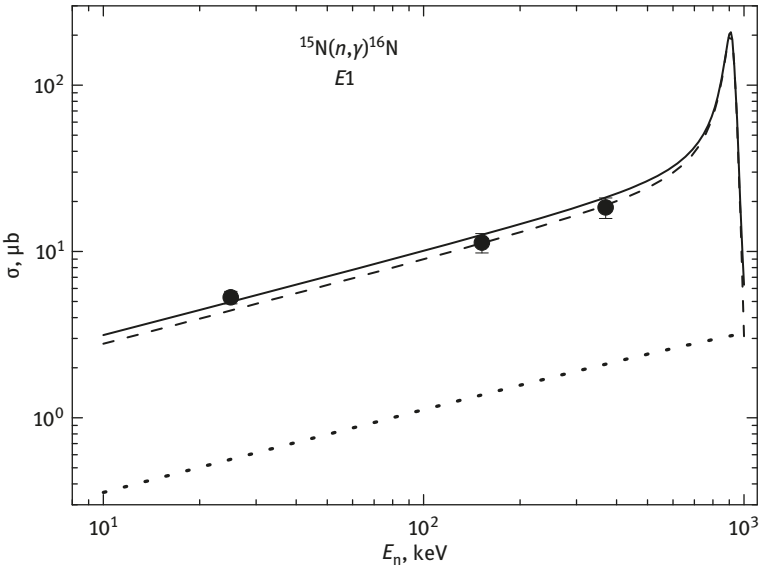

Fig. 2.7.2b: Total cross-sections of the neutron capture on ^{15}N at the energy of 10 keV. Experimental points: ● – [265]. Curves – calculation of the total cross-sections.

Now we will note that if the parameters of the resonance P_1 potential are fixed on the phase-shift resonance rather unambiguously, and for the bound state, they are definitely based on the description of its characteristics, including the AC, for the $^3P_2$ potential with the FS (2.7.3) leading to zero phase shifts, including other values of the parameters are possible. However, the narrower potential with parameters are used as

$$V_{P1} = -1000\,\text{MeV}, \quad \gamma_{P1} = 2.0\,\text{fm}^{-2},$$

which also leads to the elastic scattering phase shifts close to zero, calculation results of cross-sections for the transition No. 1 to the GS of ^{16}N shown in Fig. 2.7.2a of the dotted curve differ at the value of approximately 1%. This result shows a weak influence of the geometry of such scattering potential on the total capture cross-sections. In this case, only the value of the corresponding scattering phase shift, close to zero, is important.

Additionally, if were to use the P_1 potential without the FS (2.7.2), which leads almost to the same width of the resonance at 921 keV as potential (2.7.1), it is not consistent with the classification of the FSs given above, the calculated results of the total capture cross-sections to the GS of the considered reaction practically does not differ from the dashed line in Fig. 2.7.2 obtained for the P_1 scattering potential (2.7.1). Therefore, for this system, the existence of node in the resonance P_1 scattering wave practically does not influence on the calculation results of the total capture cross-sections on ^{16}N to the GS.

2.7.3 Total cross-sections of the neutron capture on ^{15}N – second variant

Furthermore, we will consider another variant of calculation of the total cross-section of the neutron capture reaction on ^{15}N. *For this purpose, we will notice that if the potential is constructed based on the scattering phase shifts or spectra of levels of nucleus, i.e., on the basis of observed results, which contain all possible effects of such system, and the wave function obtained at the solution of the Schrödinger equation with such potential also considering all possible states of particles, including the mixing of the spin. In the employed MPCM approach with the FS, it is not possible to extract the parts of the wave function, pure according to spins, as for scattering states and GS of the nucleus. Therefore, the total cross-section as a sum can apparently be considered as a simple doubling of the cross section; for calculation of each part of such summand the same wave function are used. Only the spin multipliers in the expression for a matrix element (1.6.2) are various.*

Thereby, as there is only one transition from the mixed state of scattering to the bound mixed GS of nucleus, but not two different *E1* processes, such cross-section can be presented as

5. $$\sigma_0(E1) = \sigma(E1, {}^3P_2 \to {}^3D_2) + [\sigma(E1, {}^3P_1 \to {}^3D_2) + \sigma(E1, {}^1P_1 \to {}^1D_2)]/2.$$

Here, the transitions from the mixed P_1 scattering wave to the mixed D_2 bound GS of ^{16}N in the n^{15}N channel are averaged. This is another variant of the record of total sections for the n^{15}N states in a continuous and discrete spectrum. Such variant with averaging of cross-sections is represented in reality; furthermore, we will consider this case in more detail.

The results of our calculation of the total cross-section ${}^3P_2 \to {}^3D_2$ of the *E1* capture process to the ground state No. 1 are shown in Fig. 2.7.3a using the dotted curve that coincides with the same curve on the Fig. 2.7.2 and cross-sections for transitions

6. $$[\sigma(E1, {}^3P_1 \to {}^3D_2) + \sigma(E1, {}^1P_1 \to {}^1D_2)]/2$$

to the GS are shown in Fig. 2.7.3a denoted by the dashed curve. This cross-section is twice less than the corresponding cross-section in Fig. 2.7.2, also presented by the dashed curve. The solid curve in Fig. 2.7.3a was presented as their sum – in these calculations the scattering potentials and the GS (2.7.1), (2.7.3) and (2.7.4) specified above are used.

Furthermore, the calculated total cross-sections of all five *E*1 transitions No. 3 to three ESs of ^{16}N are shown in Fig. 2.7.3b as:

(A) $\sigma(E1, {}^3P_0 \to {}^3S_1)$– transition is presented by the dashed-dotted curve,
(B) $\sigma(E1, {}^3P_1 \to {}^3S_1)$ – process is shown by the dotted curve,
(C) $\sigma(E1, {}^3P_2 \to {}^3S_1)$ – double dashed-dotted curve,
(D) $\sigma(E1, {}^3P_2 \to {}^3D_3)$ – usual dashed curve,

(E) $\sigma(E1, {}^1P_1 \to {}^1S_0)$ – transition is shown by the short dashes, which practically coincide with the dotted line for the $\sigma(E1, {}^3P_1 \to {}^3S_1)$ process given above at number "B."

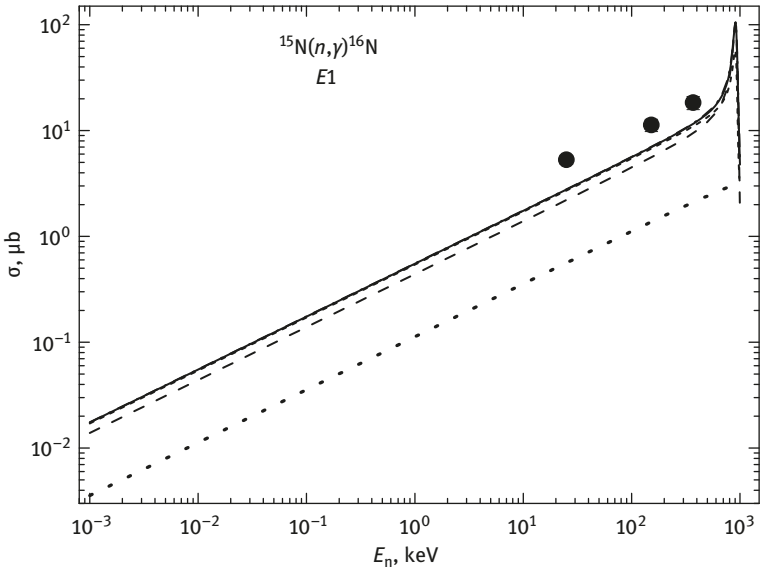

Fig. 2.7.3a: Total cross-sections for the radiative neutron capture on ^{15}N to the GS. Experimental points: ● – [265]. Curves – calculation of the total cross-sections.

The solid curve in Fig. 2.7.3b shows the total summarized capture cross-section for all five *E1* transitions to three ESs of ^{16}N considered above. For these calculations, the scattering potentials (2.7.1) and (2.7.3) of the ground state (2.7.4), as well as the potentials of the excited states (2.7.5)–(2.7.7) are used.

Finally, Figs. 2.7.4 show the total cross-sections for transitions to the ground state (dotted line is the cross section shown in Fig. 2.7.3a by the solid line) and fifth considered above $E1$ transitions to the three excited state – dashed line, which correspondent to the solid line in the given above Fig. 2.7.3b. The sum of all eight described processes is presented in Fig. 2.7.4a and Fig. 2.7.4b by the solid line, which well describe the available experimental data of work [265].

Thus, the intercluster potentials of various bound states constructed based on obvious requirements for describing the binding energy, root-mean square radii of ^{16}N, and values of the AC in the $n^{15}N$ channel allow reproducing the available experimental data for the total cross-sections of the neutron radiative capture on ^{15}N at low energies [265].

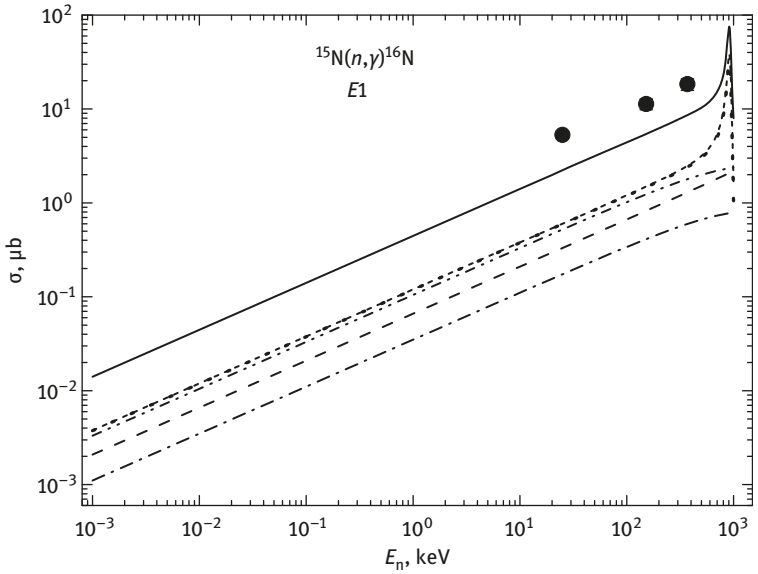

Fig. 2.7.3b: Total cross-sections for the neutron radiative capture on ^{15}N to the first three ESs. Experimental points: ● – [265]. Curves – calculation of the total cross-sections.

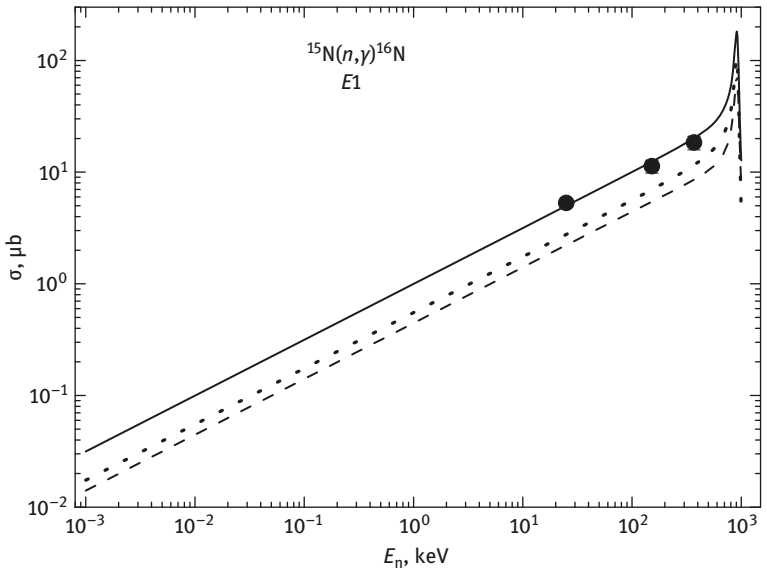

Fig. 2.7.4a: Total cross-sections for the neutron radiative capture on ^{15}N to the ground and excited states at energies from 1 eV to 1 MeV. Experimental points – ● are given in [265]. Curves – calculation of the total sum cross-sections for transitions to the GS and three ESs.

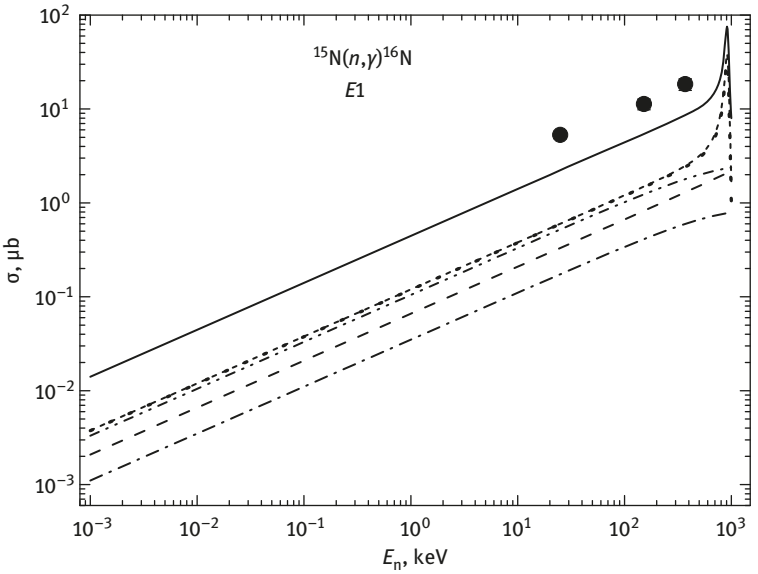

Fig. 2.7.4b: Total cross-sections for the neutron radiative capture on ^{15}N to the ground and the excited states at the energy from 10 keV to 1.0 MeV. Experimental points – ● are given in [265]. Curves – calculation of the total sum cross-sections for the transitions to the GS and ES

Moreover, all used n^{15}N potentials were constructed based on the classification of cluster states given above with FSs and ASs according to Young tableaux. The quality of describing the cross-sections in Fig. 2.7.2b (the solid curve) and Fig. 2.7.4b, which are also shown by the solid curve, practically coincide and give a cross-section value at resonance energy of approximately 200 μb.

However, it is difficult to draw definite conclusions based on only three experimental points in total capture cross-sections in a relatively narrow energy range of 25–370 keV [265]. Therefore, more detailed measurement of such cross-sections in the energy range from 1–10 eV to 1.0–1.2 MeV is desirable. Such measurements have to completely determine the width of the resonance of this reaction at 921 keV [258], and the value of the cross-section at resonance energy that will allow one to compare it with the results of these calculations.

For further comparison of the obtained results it is possible to use the GS potential, for example, with one FS, i.e., not consistent with the given above classification of the ASs and the FSs according to Young tableaux. We will consider the option of the parameters

$$V_{\text{g.s.}} = -151.424599 \quad \text{MeV}, \quad \gamma_{\text{g.s.}} = 0.11\,\text{fm}^{-2}, \tag{2.7.8}$$

leading to the binding energy of –2.491000 MeV with an FDM accuracy of 10^{-6} MeV, to charge and mass radii of 2.63 fm and 2.77 fm, respectively, and practically the

same, as for the potential (2.7.4), the AC value equals 0.97(1). In this case, the calculation results of the total capture cross-sections to the GS shown in Fig. 2.7.3a denoted by short dashes that do not differ from the results shown in this Fig. 2.7.3a by the solid line for the GS potential (2.7.4) without the FS.

The presence of FS in the GS potential of ^{16}N in the n^{15}N channel practically does not affect the calculation of the total cross-sections for radiative capture. Such results depend only on the correctness of the description of the value of binding energy and AC in the considered channel.

The weak difference in calculation results turns out at using, for example, the $^3S_1$ potential of the excited state with one FS and the parameters

$$V_{S1} = -636.795577 \quad \text{MeV}, \quad \gamma_{S1} = 1.5\text{fm}^{-2}. \tag{2.7.9}$$

Such potential leads to the binding energy of –2.093730 MeV with an FDM accuracy of 10^{-6} MeV, to the root-mean square charge radius of 2.62 fm and the mass radius of 2.64 fm, respectively, and the AC value of 1.35(1) at an interval of 3–23 fm, which practically coincides with our previous results for potential (2.7.7).

Here, it is necessary to notice that the AC value depends on the width of potential very strongly and to obtain the demanded AC for potential (2.7.9) it was necessary to reduce its width by 2.5 times in comparison with interaction (2.7.7), i.e., to increase the parameter of width γ from 0.6 to 1.5 fm^{-2}. The calculated total cross-section for the transition with such potential practically does not differ from the results obtained above for potential (2.7.7).

Similar results, i.e., slightly different from the previous ones, are obtained using the potentials of other ESs with one FS, the presence of which is not consistent with the above classification of orbital states according to Young tableaux. The result is that the total cross-sections for the neutron capture reaction on ^{15}N at low energies are weakly dependent on the number of FSs in the potentials of the BS. In other words, if we use the equivalent phase shift scattering potentials and BS interaction, resulting in same quality of description of the main characteristics of the BS, namely, AC, the results of the calculation of the total capture cross-sections are essentially independent of the number of the FSs.

This conclusion is in general contrary to the observations made previously in the analysis of many other light atomic nuclei in the cluster channels and capture reactions with them [12,14,136]. The system considered here and the capture process are exception to commonly observed strong dependence of the total cross-sections from the number of FSs in a certain partial potential, i.e., inter-cluster interaction for a given orbital moment [12,14,19]. As a rule, the potentials with the “wrong” number of FSs resulted in significantly larger difference in the total cross-sections.

Because at the lowest energies, namely, from 1 eV to 10 keV, the calculated cross-section is almost a straight line (see the solid curve in Fig. 2.7.4a), it can be approximated by a simple function of the form (2.6.2). The value of the given

constant $A = 0.9968$ μb keV$^{-1/2}$ was determined by one point in cross-sections at the minimum energy equal to 1 eV. Furthermore, it appeared that the module (2.1.4) of a relative deviation of settlement theoretical cross-section and approximation of this cross-section by the function given above at energies less than 10 keV is at the level of 0.1%.

If we assume that this form of dependence of the total cross-section of energy will be preserved at lower energies, it is possible to estimate the value of the cross-section, which at the energy of 1 meV (1 meV = 10^{-3} eV = 10^{-6} keV), gives a value of order 10^{-3} μb. The coefficient for the solid curve in Fig. 2.7.2a in the approximation of cross section in a form given above to 10 keV is equal to 0.9907 μb keV$^{-1/2}$, the module of a relative deviation has approximately the same value, and the cross section at 1 meV is equal to 9.9 10^{-4} μb [267].

2.8 The radiative capture in the n^{16}O system

Now, we will consider the ^{16}O(n,γ)^{17}O process, which participates in the chain of primordial nucleosynthesis (2.0) and represents additional interest because this is the reaction on the last nucleus of the 1p-shell with the formation of ^{17}O going beyond its limits. As usual, we assume that the BS of ^{17}O is caused by the cluster channel consisting of initial particles, which participate in the capture reaction, i.e., n and ^{16}O clusters.

Progressing to analysis of the total cross-sections of the neutron capture on ^{16}O, we will consider the classification of orbital states of the n^{16}O system according to Young tableaux initially. The ground bound state of ^{16}O corresponds to the Young tableaux {4444} [11,19,42], and hence, for the n^{16}O system we have {1} × {4444} → {5444} + {44441} [134]. The first of the obtained tableaux compatible with the orbital moment $L = 0$ is forbidden, as in the s-shell there cannot be five nucleons, and the second tableau is allowed and compatible with the orbital moment $L = 1$ [11,28].

Thus, in the potential of the $^2S_{1/2}$ wave, which corresponds to the first excited state of ^{17}O in the n^{16}O channel and the scattering states of these clusters, there is forbidden bound state, and ^2P scattering waves do not contain the bound FSs, but the allowed state with {44441} can be both in continuous and discrete spectrum. The ground state of ^{17}O in the n^{16}O channel, which is at an energy of −4.1436 MeV [258] belongs to the $^2D_{5/2}$ wave and also does not contain the FS.

However, as discussed already, we do not have complete product tables of Young tableaux for the system with the number of particles more than eight [134], which were used by us earlier for similar calculations in easier cluster systems [12,14,19,22]. Therefore, the result obtained above should be considered only as the quality standard of the possible orbital symmetry in the bound states of ^{17}O for the n^{16}O channel.

2.8.1 Phase shifts and n^{16}O scattering potentials

For calculating radiative capture within the MPCM, it is required to know the potentials of the elastic n^{16}O scattering in the $^2S_{1/2}$, $^2P_{1/2}$, $^2P_{3/2}$, $^2D_{3/2}$, and $^2D_{5/2}$ waves, as well as the interaction of the ground $^2D_{5/2}$ and the first excited $^2S_{1/2}$ bound states of ^{17}O. For the transition to these BSs, there are experimental data for the total cross-sections for radiative capture, as obtained in [267].

As usual, the potentials of the scattering processes are constructed based on the elastic scattering phase shifts, higher than 1.1 MeV were obtained in works [268,269]. For energy range of 0.2–0.7 MeV, phase-shift analysis [270] based on the measurements of differential cross-sections of the elastic n^{16}O scattering [271] in the range of the resonance at 0.433 MeV [258]. In [270], some preliminary results of the phase-shift analysis have been discussed in the resonance area of $^2D_{3/2}$ at energy range of 750–1200 keV.

Later, new experimental data [272] regarding the excitation function at energies from 0.5 to 6.2 MeV are listed in the database [151], and, as far as we know, at the energies in the range of the $^2D_{3/2}$ resonance of 1.0 MeV [258] have not been considered in the phase-shift analyses. The data [272] were used futher for phase-shift analysis and the extraction of the form of the phase shift in the resonance $^2D_{3/2}$ wave of the n^{16}O scattering. The used excitation functions at 40° (ls) or 42.3° (cm) [272] MeV are shown by open circles in Fig. 2.8.1 at energies ranging from 0.75 to 1.25. The

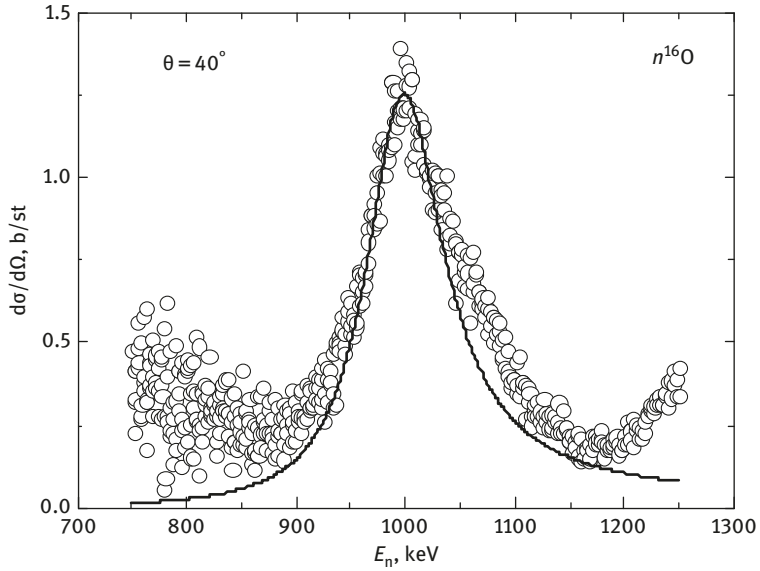

Fig. 2.8.1: Excitation functions in the elastic n^{16}O scattering in the range of the $^2D_{3/2}$ resonance at 1.0 MeV are shown by the open circles [272]. Curve - calculation of the cross-sections with potential given in the text.

experimental errors, reaching 25% in some cases, are not given in Fig. 2.8.1. The indication of such large errors clutters the figure because our analysis has been used more than 500 points for cross-sections at different energies of the excitation functions obtained in [272].

Note that the ambiguity of data [272] lower than 0.7–0.8 MeV increases sharply; however, for the extraction of the $^2D_{3/2}$ scattering phase shifts, it is sufficient to consider the energy range shown in Fig. 2.8.1, which has relatively small ambiguities, and such data may well be used for implemented the phase-shift analysis. Earlier, we already conducted similar phase-shift analyses, for example, in the n^{12}C [230], p^{12}C [167], p^6Li [145], and p^{13}C [234,259] systems generally at astrophysical energies and all these results are given in the new book [13].

Details of the phase shifts used by us in the elastic scattering of particles with the spins 1/2 + 0 and the main expressions for the cross-sections used in the phase-shift analysis have been previously reported [13,261]. Results of the present analysis of the n^{16}O elastic scattering in the energy range of 0.75 to 1.25 MeV are shown in Fig. 2.8.2 by open circles. In Fig. 2.8.2, using the black squares, the results of the phase-shift analysis from work [268], obtained higher than 1.1 MeV, and by the triangles the results of the analysis from [270] are given.

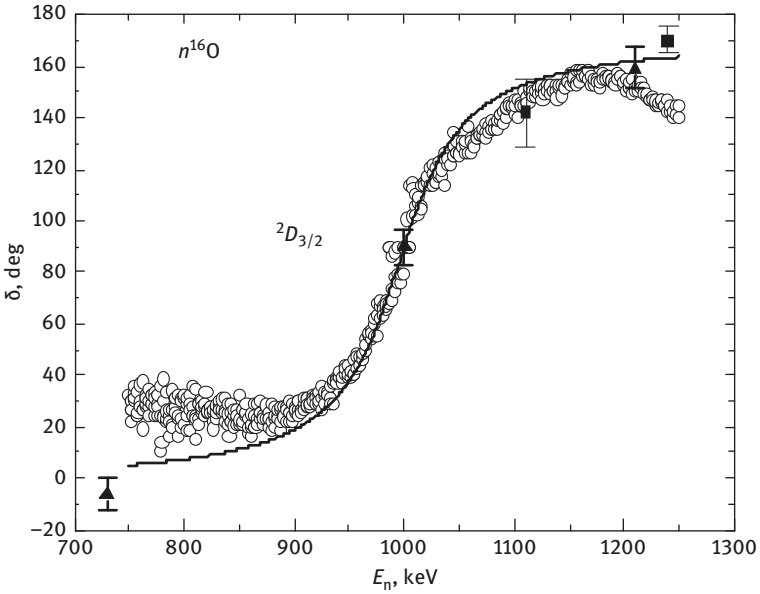

Fig. 2.8.2: $^2D_{3/2}$ phase shift of the n^{16}O elastic scattering at low energies. The open circles (O) – results of our phase-shift analysis made on the basis of data [272], the black squares (■) - results of the phase-shift analysis from work [268], the triangles (▲) – results of the analysis from work [270], the solid curve – calculation of the phase shift with a potential specified in the text.

For describing the cross-sections in excitation functions [272], at energies up to 1.20–1.25 MeV, it is not required to consider the $^2S_{1/2}$ scattering phase shift because its presence does not change the value of χ^2, i.e., its values can be accepted equal to zero. The values χ^2, regarded as only one point in the cross-sections for each energy has an average value 4.7×10^{-3} with a maximum partial value of $\chi^2_i = 0.6$ at an energy of 999.5 keV.

For the description obtained as a result of the phase-shift analysis of the $^2D_{3/2}$ scattering phase shift, it is possible to use a simple Gaussian potential (1.2.2) with the following parameters

$$V_{D3/2} = -95.797 \quad \text{MeV}, \quad \gamma_{D3/2} = 0.17\,\text{fm}^{-2}, \tag{2.8.1}$$

which does not have the bound FS and leads to the resonance energy of 1000 keV at a phase shift of 90.0(1)° with the level width of 88 keV (ls) or 83 keV (cm). At the same time, in Table 17.17 of [258], the width value is 96 keV (cm) or 102 keV (ls) at the energy of 1000±2 keV (ls).The energy dependence of the $^2D_{3/2}$ scattering phase shift of potential (2.8.1) is shown in Fig. 2.8.2 by the solid curve. Such potential well describes the behavior of the phase shift obtained by us in the resonance range and corresponds with the previous scattering phase shift, discussed previously in [268,270]. The shape of the cross-sections in excitation functions is calculated with the $^2D_{3/2}$ phase shift of potential (2.8.1) at zero values of other phase shifts, as shown in Fig. 2.8.1 by the solid curve. From these results, it is clear that exactly the $^2D_{3/2}$ scattering phase shift is almost completely defines the behavior of such cross-sections in excitation function in the resonance range.

Furthermore, we will consider the total cross-sections for radiative capture taking into account the *E1* transitions from the $^2P_{3/2}$ resonance in the $n^{16}O$ scattering at 433 keV to the $^2D_{5/2}$ ground and $^2S_{1/2}$ first excited state of ^{17}O. For constructing the $^2P_{3/2}$ scattering potential, except location data and width from an earlier review [258] (see Table 17.17), we use the results of the phase-shift analysis [270] denoted by triangles in Fig. 2.8.3. Consequently, we find that for describing the resonance $^2P_{3/2}$ scattering phase shift at 433(2) keV (ls) with the width of 45 keV (cm) or 48 keV (ls) [258] the potential without forbidden or allowed BS with the following parameters are required

$$V_{P3/2} = -1583.545 \quad \text{MeV}, \quad \gamma_{P3/2} = 6.0\,\text{fm}^{-2}, \tag{2.8.2}$$

which leads to the width level of 44 keV (cm) or 47 keV (ls) at the resonance of 433 keV (ls). The phase shift of such potential at the resonance energy is 90.0(0.2)°, and the complete dependence of the scattering phase shift from energy in the resonance range is shown in Fig. 2.8.3 denoted by the solid curve.

Here, according to the well-known resonance energy level in the spectra of ^{17}O and its width, the potentials are constructed entirely unambiguously. In other words, it is impossible to find other V_0 and γ parameters which can correctly describe the resonance energy level and its width if the number of the BSs is given, which in this

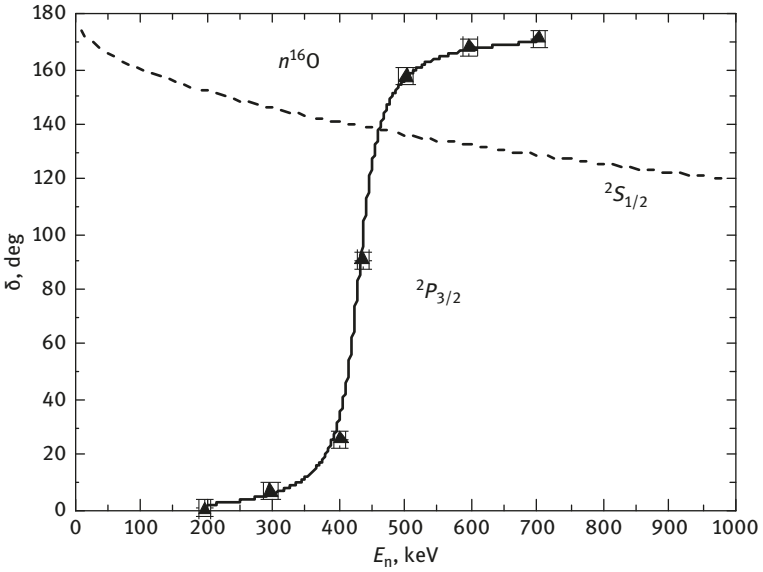

Fig. 2.8.3: $^2S_{1/2}$ and $^2P_{3/2}$ of phase shifts of the n^{16}O scattering at low energies. Triangles (▲) – results of the phase-shift analysis from work [270]. The solid curve – calculation of the phase shift with potential specified in the text, the dashed curve – the $^2S_{1/2}$ scattering phase shift of potential (2.8.4).

case is zero. The depth of such potential unambiguously defines the location of the resonance, i.e., the resonance energy of level, and its width defines a certain width of this resonance state.

In spectra of ^{17}O lower than 1.0–1.3 MeV, there are no resonance levels with moment $J^\pi = 1/2^-$ and $5/2^+$ [258], which could be compared to the n^{16}O channel. Therefore, the $^2P_{1/2}$ and $^2D_{5/2}$ potentials of scattering waves, as expected to be the first variant, having no bound FSs or ASs and can have zero depth, i.e., zero scattering phase shifts. Such an assumption was already used by us earlier, as discussed previously and completely acquitted itself for some other systems of particles by the consideration of other processes of radiative capture.

Furthermore, for calculations of radiative capture within the MPCM, we need the potentials of interaction of n^{16}O clusters in the BS. We will consider the electromagnetic transitions to the ground state with $J^\pi, T = 5/2^+, 1/2$ at an energy of –4.1436 MeV and first excited with $J^\pi = 1/2^+$ at –3.2729 MeV of ^{17}O in the n^{16}O channel [258]. The width of such potentials was fixed based on the correct description of the binding energy and the charge radius of ^{17}O equals 2.710(15) fm [258], and the calculated asymptotic constants of the n^{16}O channel were compared with other independent data.

Consequently, for the $^2D_{5/2}$ potential of the GS of ^{17}O the parameters are found in the n^{16}O channel without the FSs

$$V_{\text{g.s.}} = -102.2656782 \quad \text{MeV}, \quad \gamma_{\text{g.s.}} = 0.15\,\text{fm}^{-2}, \tag{2.8.3}$$

which allow to obtain the binding energy of –4.1436000 MeV with an accuracy of 10^{-7} MeV [261], the charge radius of 2.71 fm, the mass radius of 2.73 fm, and the dimensionless asymptotic constant (1.2.5) at an interval of distances of 6–16 fm was equal to $C = 0.75(1)$. The scattering phase shift of such potential with one bound AS smoothly reduces and at energy of 1.0 MeV becomes 179.6º, i.e., a value of zero. As the charge radius of neutron was zero as usual, and its mass radius of 0.8775(51) fm was equal to the charge radius of proton specified in database [126]. In work [206] for the AC GS the value 0.9 $\text{fm}^{-1/2}$ was obtained that after recalculation with $\sqrt{2k_0} = 0.933$ at $S_f = 1$ (1.7.1) to dimensionless value of 0.96. In [94], for the GS in the dimensionless form (1.2.5) it is becomes 0.77(8) taking into account the errors will completely be coordinated with the value obtained above.

For the $^2S_{1/2}$ potential of the first excited state of ^{17}O in the $n^{16}O$ channel with a bound forbidden state the following parameters are obtained

$$V_{S1} = -81.746753\text{MeV}, \quad \gamma_{S1} = 0.15\,\text{fm}^{-2}, \tag{2.8.4}$$

which gives the binding energy of –3.2729000 MeV relative to the threshold of the $n^{16}O$ channel or 0.8707 MeV relative to the GS of ^{17}O with an accuracy of 10^{-7} MeV [261], to the charge radius of 2.71 fm, the mass radius of 2.80 fm, and the AC of 3.09(1) at an interval of distances of 6–17 fm. The scattering phase shift of such potential is shown in Fig. 2.8.3 by the dashed curve, which smoothly reduces and at 1.0 MeV reaches 119.6°. For this $^2S_{1/2}$ level in work [206] for the AC the value of 3.01 $\text{fm}^{-1/2}$ is obtained, that after recalculation with $\sqrt{2k_0} = 0.88$ at $S_f = 1$(1.7.1) gives 3.42. In this case, for an asymptotic constant the acceptable consistence between the different results, with the difference between them of approximately 10%.

For additionally controlling the energy of the bound state, the variation method was used [24,261], which for the ground state is already on the grid with dimension $N = 10$ at an independent variation of parameters for the potential (2.8.3) allowed to obtain the energy of –4.1435998 MeV. The parameters of variation wave function are specified in Table 2.8.1, and the residual value does not exceed 10^{-8} [261]. The charge radius and asymptotic constant at an interval of 6–16 fm do not differ from the values, which have been obtained above in the FDM.

For the real binding energy in such potential, it is possible to accept the average value of –4.1435999(1) MeV, the accuracy of determining the binding energy using two methods (FDM and VM) according to two various computer programs is at the level of ±0.1 eV, which is in full compliance with the FDM program within the error of searching binding energy of 10^{-7} MeV.

For energy of the first excited state but bound in the $n^{16}O$ channel, on a grid with dimension $N = 10$ and an independent variation of parameters for the potential (2.8.4) the energy of –3.2728998 MeV is obtained. The parameters of the variation wave function are specified in Table 2.8.2, and the residual value does not exceed 10^{-10}

Table 2.8.1: The variation parameters and the expansion coefficients of the radial wave function in n^{16}O system for the ground $5/2^+$ state for the potential (2.8.3). The normalization of the wave function on interval 0–30 fm is N_0 = 9.999999999996603E −001.

i	α_i	C_i
1	2.970820484267648E−002	5.999898648526680E−002
2	1.355376641105716E−002	−5.268187781652860E−006
3	2.971441871730051E−002	−6.024647870785407E−002
4	6.553466412237838E−002	−3.087819670804185E−003
5	1.253831431831826E−001	−1.906462762571792E−002
6	2.156627509028788E−001	−6.585296562529887E−002
7	3.393826502547065E−001	−1.006636861923295E−001
8	5.166966410860497E−001	−4.627970949895152E−002
9	1.063579836670607	−1.116683372038532E−003
10	1.639614546923715	2.440471375269290E−004

[261]. The charge radius and asymptotic constant at an interval of 6–20 fm do not differ from the values obtained for the FDM. Here, for the real binding energy it is possible to accept the average value −3.2728999(1) MeV, i.e., the accuracy of determining the energy by two methods according to two various computer programs is also at the level of ±0.1 eV = ±100 meV.

Table 2.8.2: The variation parameters and expansion coefficients of the radial wave function in n^{16}O system for the potential of the first excited $1/2^+$ states for potential (2.8.4). The normalization of the wave function on interval 0–30 fm is N_0 = 9.999999975230215E−001.

i	α_i	C_i
1	1.268144327251019E−002	7.701423164869143E−003
2	4.193709029136675E−003	4.794229107401904E−005
3	2.881642596445175E−002	5.677769979981124E−002
4	6.245243687002310E−002	1.570309903921747E−001
5	1.259974114760052E−001	2.619817602771229E−001
6	2.163927688688810E−001	−4.833513946049395E−002
7	3.383830162751630E−001	−7.529455791580352E−001
8	5.187698913796229E−001	−4.062518687767323E−001
9	1.062316903143099	−5.106918680411997E−003
10	1.867671209905880	4.235490376362463E−004

For all these calculations the mass value of ^{16}O equal to 15.994915 amu was used [214], and the mass of neutron is specified in §1.6. (Chapter 1).

2.8.2 Total cross-sections of the radiative capture

Earlier the radiative capture reaction on ^{16}O was considered based on the model of direct capture in work [223], where the possibility of describing available experimental data [267] in the range of 20–280 keV. Furthermore, based on the convolution model [273], it was possible to describe the available experimental data [267] in the energy range of 20–60 keV. Subsequently, based on the generator coordinate method (GCM), taking into account only the *E1* transition in [274], a correct description of the total cross-section [267] in the range of 20–280 keV was obtained.

Finally, in [275] on the basis of GCM and microscopic R-matrix analysis on the basis of the *E1* and *M1* processes, the experimental total cross-sections were successfully reproduced at energies of 25 meV [276] to 280 keV [267], i.e., to a resonance at 433 keV, corresponding to the $^2P_{3/2}$ wave of $n^{16}O$ scattering [258], and predict the possible behavior of cross-sections within the range of the $^2D_{3/2}$ resonance. However, as we know, until now the energies of approximately $^2P_{3/2}$ resonance have not been considered, wherein there are a relatively new experimental data [189] from 160 to 560 keV.

Here, based on MPCM taking into account FSs [12,14,24,178], using data [189], the total cross-sections of the neutron capture on ^{16}O in the energy range from 10 meV to 1.3 MeV will be considered. Thus the following *E1* transitions are considered

1. from the resonance $^2P_{3/2}$ scattering wave to the $^2D_{5/2}$ ground state of ^{17}O in the $n^{16}O$ channel, i.e., the transition of the form $^2P_{3/2}\rightarrow{}^2D_{5/2}$.
2. from the $^2P_{1/2}$ and $^2P_{3/2}$ scattering waves to the first $^2S_{1/2}$ excited state, which is bound in the $n^{16}O$ channel of ^{17}O, i.e., the transitions of the form $^2P_{1/2}+{}^2P_{3/2}\rightarrow{}^2S_{1/2}$.

Besides, the *M1* processes were considered.

3. from the resonance $^2D_{3/2}$ wave to the $^2D_{5/2}$ GS of ^{17}O, i.e., the $^2D_{3/2}\rightarrow{}^2D_{5/2}$ transition.
4. from the $^2S_{1/2}$ scattering wave to the first $^2S_{1/2}$ excited state, i.e., $^2S_{1/2}\rightarrow{}^2S_{1/2}$ transition, which plays a main role at lowest energies.

Separate consideration of transitions to the GS and first ES was possible due to measurements described in [267] within the energy range of 20–280 keV, which is shown further in Figs. 2.8.4 and 2.8.5 by points. Moreover, the results of measurements [267] showed noticeable predominance of capture cross-sections on the first $^2S_{1/2}$ ES before capture to the $^2D_{5/2}$ GS of ^{17}O as it will be clear further in Figs. 2.8.4 and 2.8.5.

The total cross-sections of other possible transitions such as *E2* from the resonance $^2D_{3/2}$ wave to the first excited $^2S_{1/2}$ level or *M*1 from the nonresonance $^2D_{5/2}$ scattering wave to the ground $^2D_{5/2}$ state and few others were at least 2–3 orders of magnitude smaller. Meanwhile, to use the similar potentials (2.8.3) for continuous

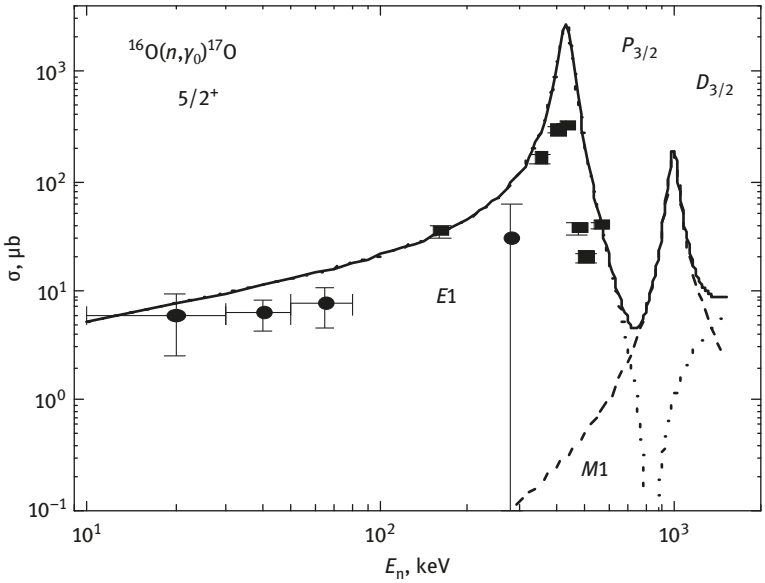

Fig. 2.8.4: Total cross-sections of the $E1$ neutron radiative capture on ^{16}O to the ground $5/2^+$ state. The experimental data are taken from: ● – [267], ■ – [189]. The solid curve – our calculation for the potentials (19–21).

and discrete spectra for $M1$ transitions from the $^2D_{5/2}$ scattering wave to the ground $^2D_{5/2}$ state, these cross-sections have to be equal to zero because the matrix element of the $M1$ transition overlap the integral of wave functions of these states.

The results of our calculations of total cross-sections for the *M1* and $E1$ transitions to the GS with the potentials specified above in comparison with the experimental data [189,267] are presented in Fig. 2.8.4 by the solid curve. The cross-sections of *M1* transition from the resonance $^2D_{3/2}$ scattering wave (transition No. 3) at energies up to 1.3 MeV, i.e., in the range of the $^2D_{3/2}$ resonance, are presented by a dashed curve, and for the *E1* $^2P_{3/2}\rightarrow{}^2D_{5/2}$ process (transition No.1) in the range of 433 keV resonance denoted by the dotted curve.

From Fig. 2.8.4, it is clear that the calculations, taking into account the *M1* and *E1* transitions No. 1 and No. 3, well describe the results of the experimental data published previously in [189,267] for the total capture cross-section to the GS of ^{17}O, which in this range smoothly reduces with the decreasing energy. In Fig. 2.8.4, the squares show the measurement results of the total cross-sections executed in the resonance range from 160 to 560 keV [189], wherein the total data for transitions to the GS and the first excited state are provided.

Here, the $^2P_{3/2}$ and $^2D_{3/2}$ potentials of scattering waves, as well as the $^2D_{5/2}$ bound state of the $n^{16}O$ system of clusters, which do not contain the FS, are constructed based on simple assumptions. The consistency of the scattering potential with the

scattering phase shifts, and the BS potential with the main characteristics of these states for ^{17}O was required (the binding energy, charge radius, AC).

The calculations of cross-sections for the *E1* transitions from the $^2P_{3/2}$ and $^2P_{1/2}$ scattering waves at energies ranging from 10 keV to 1.3 MeV without the second resonance in $^2P_{3/2}$ wave at 1312 keV [258] to the first ES of ^{17}O, i.e., the process No. 2, ass shown in Fig. 2.8.5 by solid curve. Here, using the points, the measurement results of the cross-sections from works [267] for transition to the first excited $1/2^+$ level in the energy range of 20–280 keV, and squares denote the measurement of total cross-sections from [189] are shown.

It appears that the measurements mentioned earlier [189] correspond with the earlier experimental results for transitions to the first ES [267] and, as seen from Fig. 2.8.5, are described in our calculations at all considered energies raning from 20 to 560 keV. At the energy of 430 keV, the value of resonance cross-section reaches the value of 767 μb.

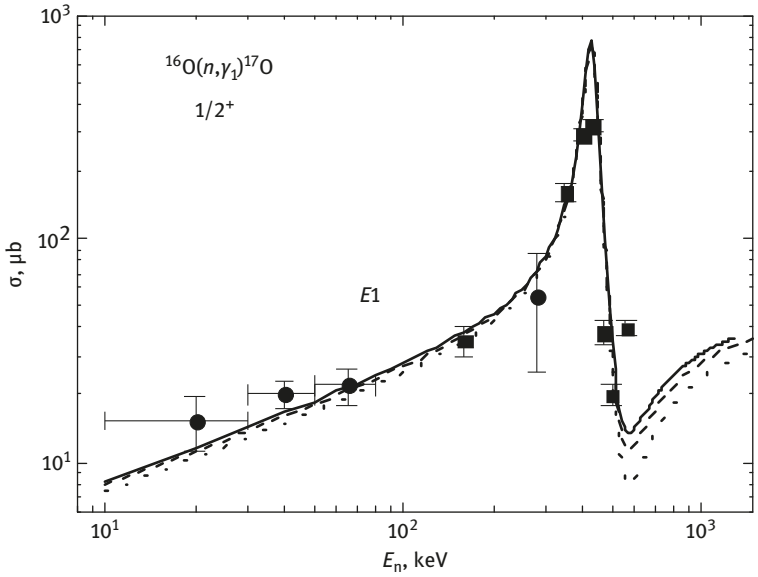

Fig. 2.8.5: Total cross-sections *E*1 of the neutron radiative capture on ^{16}O to the first excited $1/2^+$ state of ^{17}O. Experimental data: ● – from 267], ■ – 189]. Curves – our calculation of the total cross-section for the potentials given in the text.

From the above classification of the FS and AS according to Young tableaux, in the *P* wave, the allowed BS can be present. Therefore, according to the n^{12}C system considered earlier, it is possible to consider that the second excited state of ^{17}O with $J^\pi = 1/2^-$ at the energy of 3.055 MeV relative to the GS corresponds to the $^2P_{1/2}$ wave and can be the BS; the scattering potential has been considered further. Then,

as the second variant of the $^2P_{1/2}$ potential, it is necessary to accept the presence of the bound allowed state in this partial wave, resulting in a scattering phase shift close to zero.

In that case, we accept the parameters for the potential $^2P_{1/2}$ in more details, than were used for the $^2P_{3/2}$ interaction (2.8.2)

$$V_{P1/2} = -1593.43535 \quad \text{MeV}, \quad \gamma_{P1/2} = 6.0\,\text{fm}^{-2}. \tag{2.8.5}$$

Such potential gives phase shifts close to zero ranging up to 1.0 MeV (from 180° to 177.6°), leading to the binding energy of –1.08824 MeV, relative to the n^{16}O threshold with an FDM accuracy of 10^{-5} MeV [261]. The charge radius of ^{17}O in the second excited $1/2^-$ state turns out 2.70 fm, the mass radius of 2.65 fm, and the dimensionless AC is 0.22 at an interval of 2–18 fm.

Using the (2.8.5) potential for the scattering process in the $^2P_{1/2}$ wave and the resonance potential (2.8.2) in the $^2P_{3/2}$ wave of the total capture cross-sections for *E1* transitions of the form $^2P_{1/2} + {}^2P_{3/2} \to {}^2S_{1/2}$, we canl obtain the results shown in Fig. 2.8.5 by the dashed curve. This figure shows almost complete agreement between the calculated cross-sections for potential (2.8.5) with previous results obtained for zero values of the depth of this potential.

Because we did not manage to find the AC values for the second excited state at 3.055 MeV with $J^\pi = 1/2^-$, it is not possible to compare the value obtained here with independent results and the potential may contain some uncertainty of parameters. To get rid of the available ambiguity of this scattering potential, at least partially, we will consider another variant, with a wider interaction as

$$V_{P1/2} = -270.71124 \quad \text{MeV}, \quad \gamma_{P1/2} = 1.0\,\text{fm}^{-2}, \tag{2.8.6}$$

which also leads to the phase shifts close to zero (from 180° to 173.9° at 1.0 MeV). The binding energy is equal to –1.08824 MeV with an FDM accuracy of 10^{-5} MeV, the charge radius of 2.70 fm, radius mass of 2.69 fm, and AC of 0.39 at an interval of 3–23 fm, which is almost twice more than the results for the previous potential.

The total capture cross-sections with such potential are shown in Fig. 2.8.5 by the dotted curve. It is clear that the cross-sections do not strongly depend on the existence of bound AS in the $1/2^-$ wave and the width of such potential. Although it is comparable with a width of interaction of the $^2P_{3/2}$ wave and is in the 1.0–6.0 fm range, and the AC values lie in the range of 0.2 to 0.4. Thus, it does not manage to use this transition for an unambiguous choice of the form of interaction potential in the scattering $^2P_{1/2}$ wave. The potential of zero depth without the BS and the variants of interactions (2.8.5) and (2.8.6) given above, wherein there is the AS at $J^\pi = 1/2$, resulting in same results for total cross-sections.

The summarized total cross-section for all the transitions to the GS with $J = 5/2^+$ considered above (Fig. 2.8.4 – the solid curve) and to the first ES with $J = 1/2^+$ (Fig. 2.8.5 – the solid curve) is shown in Fig. 2.8.6 by the solid curve. It is clear that

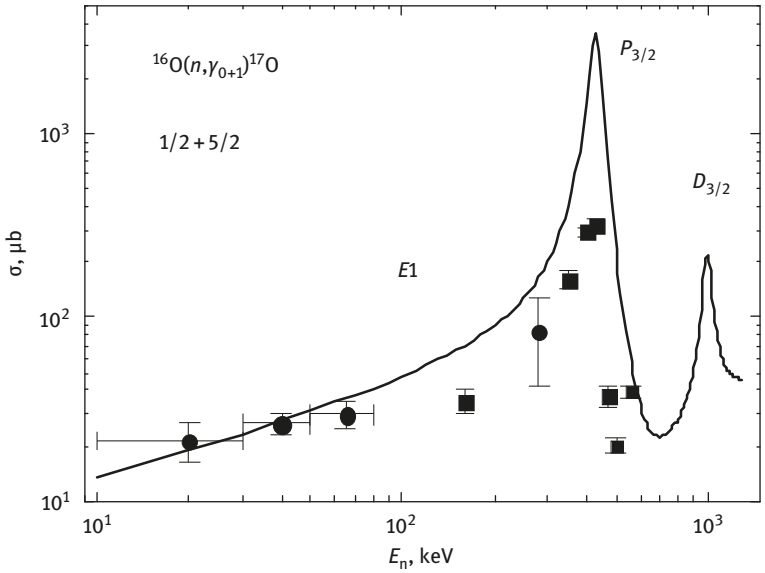

Fig. 2.8.6: Total cross-sections of the *E1* neutron radiative capture on ^{16}O to the $5/2^+$ GS and the first excited $1/2^+$ state of ^{17}O. Experimental data: ● – from [267], ■ – [189]. Solid curve – our calculation of the total cross-section for the potentials is explained in the text.

the calculation results reproduce data published previously [267] for total cross-sections, and measurement results [189] lie slightly below than the calculated curve. Thus, the methods of constructing interaction potentials of clusters considered above allow reproducing the experimental data for total cross-sections of the neutron radiative capture on ^{16}O at the energy range from 10–20 keV and to 550–600 keV.

However, considering the *M1* transition No. 4 of the form $^2S_{1/2} \rightarrow {}^2S_{1/2}$ at the thermal energy range for describing the capture cross-sections in this cluster system of the criteria used above is insufficient for the unambiguous determination of the scattering potential in the $^2S_{1/2}$ wave. As discussed below, it is necessary to vary some the parameters for accurately described experimental data [276] at the lowest capture energy of 25 meV, which is considered as the thermal energy of the reaction.

For the consideration of the range of the smallest energies, note that lower than 10 eV capture cross-section is completely determined by the *M*1 process with the transition from the $^2S_{1/2}$ scattering wave to the first ES $^2S_{1/2}$ state of ^{17}O, i.e., the process No. 4 described above. The potential of the $^2S_{1/2}$ wave of the $n^{16}O$ scattering containing the FS, as it follows from the classification of cluster states considered above, at the considered energies practically leads to a zero scattering phase shift; however, as it has the FS, its depth cannot simply be zero.

The form of such potential was specified only for describing the cross-section at 25 meV, and its parameters were

$$V_S = -10.0 \quad \text{MeV}, \quad \gamma_S = 0.03\,\text{fm}^{-2}, \tag{2.8.7}$$

The calculated total cross-sections taking into account the $M1$ transition in the energy range from 10 meV to 1.0 MeV are presented in Fig. 2.8.7 by the solid curve.

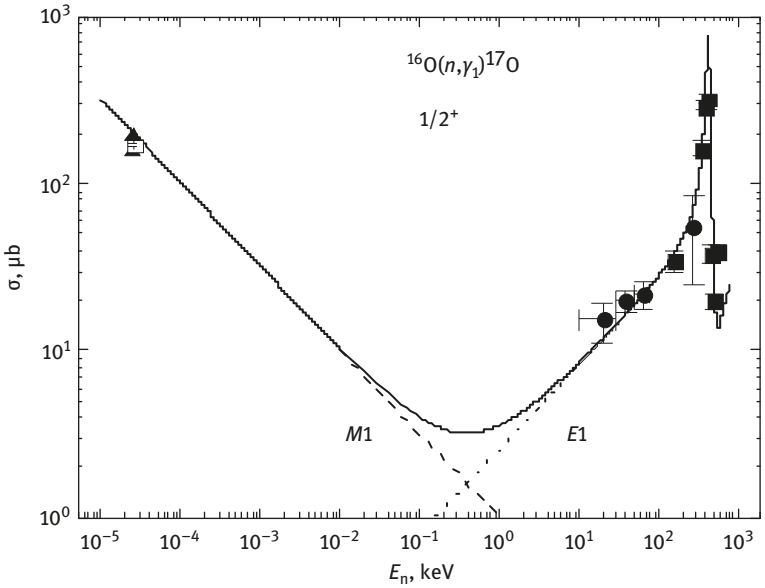

Fig. 2.8.7: Total cross-sections of the *E1* and *M1* neutron radiative capture on ^{16}O to the first excited $1/2^+$ state of ^{17}O. Experimental data: ● – from [267], ■ – [189], ▲ – [276], π – [184]. Solid curve – our calculation of the total cross section for the potentials is explained in the text.

The results of the experimental measurements from works [276], which are in an interval of values of cross section of 150–200 μb are shown at 25 meV by triangles. The dashed curve in Fig. 2.8.7 shows the results for the cross sections of the $M1$ process with potential (2.8.7), and dotted curve for the $E1$ transition at the energies higher than 100 eV, shown in Fig. 2.8.5 by the solid curve.

Thus, it is clear that the $E1$ cross-section sharply reduces and at 100 eV is approximately three times less than the $M1$ transition cross-section. At an energy of 25 meV for potential (2.8.7) of the $^2S_{1/2}$ scattering phase shift is equal to 0.00812° (when using more modern value of the constant $\hbar^2/m_0 = 41.8016$ MeV fm^2 for the value of the phase shift which becomes 0.00692°), and the cross-section of radiative capture is 202 μb.

It is especially necessary to emphasize that only $^2S_{1/2}$ scattering potential with the FS allows one to describe the total capture cross-sections at energies of 25 meV. To use the potential without the bound FS, its parameters cannot describe the behavior of the total cross-section at this energy. For example, to use the $^2S_{1/2}$ potential without

the FS and to accept V_0 = 0 MeV, the phase shift will be equal to zero, and cross-section at 25 meV increases to 12.5 mb. Another variant of the $^2S_{1/2}$ potential without the FS, for example, using the parameters V_0 = 3.18 MeV и γ = 0.1 fm^{-2}, which gives just the same scattering phase shift of 0.00812°, resulting in even bigger increase in cross-section to 37.9 mb. Thereby, the value of cross-section described at an energy of 25 meV within the MPCM methods is possible only when using the $^2S_{1/2}$ scattering potential, which contains the bound FS. Such behavior of the cross-section is explained by the wave function of the $^2S_{1/2}$ scattering wave, which in the presence of the FS oscillates even at an energy of 25 meV, leading to its minimum value, as shown in Fig. 2.8.7.

However, note that to use at such $M1$ transition for the states of continuous and discrete spectra identical $^2S_{1/2}$ potentials of the bound state in the form of (2.8.4), the cross-section of this process approaches zero because of the orthogonality of the wave function. However, just this transition in the $n^{16}O$ system defines the behavior of the total capture cross-sections at small energies. Therefore, in case of its absence, in the used model simply it is not possible to explain the cross-section value at thermal energy. Therefore, in case of its absence, the used model cannot explain the magnitude of the cross-sections with thermal energy. At the same time, in this system, because there are no product tables of Young tableaux, which is similar to the n^2H capture, the potentials can be dependent, for example, from different tableaux in a continuous and discrete spectrum. This can explain the difference of potential is a reason for their use in such calculations.

New experimental measurements are needed in the future for the total capture cross-sections at 10 eV–10 keV, where the calculations predict the defined behavior of cross-sections with a smooth minimum at an energy of 0.4 keV and the value of approximately 3 μb (Fig. 2.8.7). Besides, at energy of approximately 1.0 MeV, i.e., in the range of the $^2D_{3/2}$ resonance, with the fixed value of the second maximum of cross-sections (Fig. 2.8.4) is also obtained. In both cases, our obtained results differ from thoseobtained earlier in work [275] and only new experimental measurements can eliminate such divergence.

As at energies ranging from approximately 10 meV to 10 eV, the calculated cross-section presented in Fig. 2.8.7 by the solid curve is practically a straight line, it can be approximated by the simple function of the form (2.1.3). The value of constant A = 1.0362 μb keV$^{1/2}$ was determined by one point in cross-sections at a minimum energy of 10^{-5} keV. Furthermore, it is possible to consider the module (2.1.4) of the relative deviation of the calculated theoretical cross-section and approximated cross-section of such a function in the range from 10 meV to 10 eV. At energies lower than 10 eV, the deviation is at the level of 2.5%, and up to 1 eV but does not exceed 0.5%. It is quite possible to assume that this form of dependence of the total cross-section on energy will be preserved, and at lower energies and the performance of an assessment of the value of section, for example, at energy of 1 μeV (10^{-6} eV = 10^{-9} keV), gives the value of 32.8 mb [178, 277].

Conclusion

Total cross-sections were calculated for the neutron radiative capture on ^{2}H at energies ranging from 10 meV to 15 MeV based on the principles of the MPCM described above, which are consistent with the known experimental data. The MPCM with the forbidden states and classification of orbital states of clusters according to Young tableaux could well describe the description of astrophysical S-factor of the proton capture on ^{2}H [12,14,19,278] to transfer the general course of the total cross-sections of the neutron capture on ^{2}H at a wide energy range covering nine orders of magnitude. Small changes in depth of the ^{2}S potential for this system are admissible as the data on the p^{2}H phase-shift analysis with large ambiguities and errors, whereas the data on the n^{2}H phase-shift analysis were absent. These results with some uncertainties of the potential parameters of the n^{2}H interactions, discussed above, is at the level of 5% [178,183,253,278].

The MPCM and intercluster potentials specified above used here for light nuclei and radiative capture of charged particles [12,14,136] allows one to obtain the results for describing the neutron capture process on ^{6}Li at astrophysical energies [178]. The results of the calculations of the total cross-sections of the neutron capture on ^{6}Li obtained based on *E1* transitions at energies ranging from 25 meV to 1.5 MeV, which agrees well with the experimental data, as for the capture process, and the recalculated data for the measurements of the total cross-sections of the two-body photodisintegration of ^{7}Li in the n^{6}Li channel.

For the n^{7}Li system in the MPCM [12,14,136,178,253], it is possible to describe the magnitude of the total capture cross-sections in the resonance energy region. Additionally, it was possible to describe the location and the magnitude of the $^{5}P_{3}$ resonance at low energy. In general, the obtained results allow one to consider that the S and P potentials can satisfy the second variant of classification of the FSs and contain only one bound FS, and the P wave of the GS includes also the AS at the binding energy of nucleus in the considered channel. Consequently, the use of the described ideas of potentials with the forbidden states coordinated with the phase shifts of the elastic scattering of clusters and characteristics of the BS of ^{8}Li allows one to describe the available experimental data for the neutron radiative capture on ^{7}Li in a wide energy range.

Within certain assumptions of general characteristics concerning the interaction potentials in the n^{9}Be channel of ^{10}Be, it is possible to describe the available experimental data on the total cross-sections for the neutron capture on ^{9}Be at energies ranging from 25 meV to 25 keV. However, as there are no data on the phase-shift analysis of the n^{9}Be elastic scattering, the scattering potentials were constructed based on general information about the structure of resonances of ^{10}Be in the n^{9}Be channel, and the GS potentials are obtained relatively approximately as the data on radii as well as the AC of ^{10}Be [178,217].

Based on MPCM, which was used by us earlier for the consideration of 15 similar processes with charge particles [14], as well as the potentials satisfying classification of the FSs and ASs calculated based on orbital Young tableaux, it is possible to obtain quite acceptable results at the description of the total cross-sections of the neutron radiative capture on ^{12}C. The possibility of creating n^{12}C potential of the scattering process correspond with the n^{12}C scattering phase shifts [178,230,233], characteristics of the bound in this channel $^2S_{1/2}$ ES and allowing to describe in general the available experimental data is less than 100–200 keV. Meanwhile, it does not significantly differs from the p^{12}C analog, which is also obtained based on the corresponding elastic scattering phase shifts [12,14,136,227].

For the used MPCM intercluster potentials of the n^{13}C interaction in the $^3S_1$ wave and GS of ^{14}C provide quite acceptable results for describing the total cross-section of neutron radiative capture on ^{13}C [178]. The considered version of the n^{13}C scattering potential, the parameters of which differ by approximately 10–15% of its p^{13}C analogue [12,14,136], allow the description of the experimental data at energies ranging from 25 meV to 100 keV. Such difference in parameters can be explained by the absence of results on the n^{13}C phase-shift analysis within the considered range of astrophysical energies.

It has been shown that the total capture cross-section entirely depends on the shape of the potential of the ground state of ^{15}C in the n^{14}C channel because at the considered energies the ^2P potentials of the input channel without the FS can simply be set equal to zero [217]. Thus, the potential of the BS allowing to describe the available experimental data for the total cross-sections for the neutron radiative capture on ^{14}C, resulting in a correct description of the main characteristics of the GS, i.e., the binding energy, the charge radius and the value of the asymptotic constant [178,253].

Using the calculations of total cross-sections of the neutron capture on ^{14}N [217] it is clear that it is possible to agree the description of these cross-sections with the lowest energy, scattering phase shifts and the characteristics of the BS. For this purpose it is required to fix the parameters of the GS potential of ^{15}N in the n^{14}N channel on the basis of the correct description of the AC and other characteristics. Then it is quite possible to find such $S_{1/2}$ scattering potentials, which allow to describe the phase shifts of the elastic n^{14}N scattering close to zero, so the value of total cross-sections for the neutron radiative capture on ^{14}N at the energy of 25 meV [178,253,257].

By considering the processes of radiative capture in the n^{15}N system [217,266], it has been shown that it is possible to correctly describe the total cross-sections of this reaction $n^{15}\text{N}\rightarrow{}^{16}\text{N}\gamma$ at low energies, and the results weakly depend on the number of FSs in the interaction potentials. However, such conclusion is contrary to the results obtained earlier in the analysis of many other light atomic nuclei in the cluster channels and capture reactions with them, which were considered in works [12,14,136].

It is shown that the considered variants of intercluster potentials of the n^{16}O interaction, satisfying the classification of states according to Young tableaux allow one to obtain quite acceptable results for describing the total experimental cross-

sections of the neutron radiative capture on ^{16}O at energy ranging from 25 meV to 560 keV [217]. The potential of the $^2S_{1/2}$ scattering wave with the FS, the phase shift of which is close to zero, allowing one to correctly describe the behavior of experimental sections at thermal energy. It is shown that the description of low-energy cross-sections is possible only in the presence of such potential of the bound FS. The interaction of the $^2S_{1/2}$ scattering wave without the FS does not allow one to describe the value of the capture cross-section at such a low energy [277].

III New results for radiative capture

Over the past 50 years, the microscopic model RGM has become an important tool in the development of nuclear physics. However, the possibilities of simple-potential two-cluster models, if they use the concept of forbidden states, which follows from the classification of states according to Young tableaux are not yet investigated completely and directly consider the resonance behavior of elastic scattering phase shifts of interacting particles at low energies. Such variants of the model can be termed the modified potential cluster model [178].

Recently, new results were obtained for various processes of neutron radiative capture of protons and some light atomic nuclei at astrophysical and thermal energies, which will be discussed here. First, we will present the results of neutron capture on ^{8}Li, ^{10}Be, and ^{10,11}B nuclei [178], followed by the description of proton capture on ^{16}O. The last reaction is described in the Appendix as it does not involve capture process of neutrons.

In this chapter, we will also demonstrate the use of the obtained based on the phase-shift analysis of intercluster potentials for calculating total cross-sections and astrophysical *S*-factors of radiative capture processes on light nuclei. Not all reactions of neutron and proton radiative capture directly enter stellar thermonuclear cycles or even the main reactions of primordial nucleosynthesis. These reactions are considered here as companion reactions, which occurred during the formation and development of our universe.

We will pay attention to the 15 thermonuclear reactions considered in the present book; 15 similar capture reactions of charged particles on light nuclei were discussed in previous books by the author. The first book is titled “Thermonuclear processes of the Universe” and was published in 2011 in Russian [12]; the book can be found on the website http://arxiv.org/abs/1012.0877. Subsequently, the American publishing house NOVA Sci. Publ. in 2012 published its reduced English edition, titled “Thermonuclear processes of the Universe” [136], which is available on the website http://www.novapublishers.org/catalog/product_info.php?products_id=31125. Recently, this book was republished in Germany in Russian and titled “Thermonuclear processes in stars and the Universe” [14], and can be found at https://www.morebooks.shop/store/gb/book/Термоядерные-процессы-в-Звездах/isbn/978-3-659-60165-1, and in English titled as “Thermonuclear processes in stars and the Universe” – https://www.morebooks.de/store/en/book/thermonuclear-processes-in-stars/isbn/978-3-639-76478-9.

3.1 Neutron radiative capture on ^{10}B

Continuing the investigation of radiative capture processes [12,14,136,147,171,178, 207,217], we will consider the capture reaction $n + {}^{10}\mathrm{B} \rightarrow {}^{11}\mathrm{B} + \gamma$ at thermal and astrophysical energies within the framework of the modified potential cluster model

https://doi.org/10.1515/9783110619607-004

(MPCM) with the forbidden states and classification of orbital cluster states according to Young tableaux. Such a reaction can play a role in some models of the Big Bang (2.0) [142], with an additional chain of the form

$$^{7}\mathrm{Li}(^{3}\mathrm{H}, n)^{9}\mathrm{Be}(n, \gamma)^{10}\mathrm{B}(n, \gamma)^{11}\mathrm{B}(n, \gamma)^{12}\mathrm{B}(\beta^{-})^{12}\mathrm{C}(n, \gamma)^{13}\mathrm{C}(n, \gamma)^{14}\mathrm{C}. \tag{3.0}$$

although its contribution is rather small in comparison with a chain (2.0).

3.1.1 Structure of cluster states of n^{10}B system

Note that we have no full product tables of Young tableaux for a system with more than eight particles [134], which were earlier used by us for similar calculations [136, 178]. Therefore, the results described in this chapter should be considered only as the quality standard of possible orbital symmetry for the nuclei considered in two-body channels. However, based on similar classification, the available experimental data of neutron and proton radiative capture can be explained for a wide range of reactions [12, 14, 136, 147, 171, 178, 207, 217]. Therefore, here, we will use classification of cluster states according to orbital symmetry, which gives certain number of FSs and ASs in partial intercluster potentials, as well as certain number of nodes of wave function of the relative movement of clusters – in this case, neutron and ^{10}B.

Further, we assume that, for ^{10}B, the orbital Young tableaux can be accepted in the form of {442}. This is because here specific channels of ^{10}B are not considered, and it is not obligatory to take the orbital tableaux in the form of {4411}, which was obtained earlier for the n^{9}Be channel of ^{10}Be with $J^{\pi}, T = 0^{+}$,1 or for the p^{9}Be channel of ^{10}B with $J^{\pi}, T = 3^{+}$,0. Therefore, for the n^{10}B system, we have {1} × {442} = {542} + {443} + {4421} [28, 134]. The first of the obtained tableaux is compatible with the orbital moments L = 0,2,3,4, and is forbidden because there cannot be more than five nucleons in the nuclear s-shell. The second tableaux is allowed and is compatible with orbital moments L = 1,2,3,4, and the third also appears to be allowed, and is compatible with L = 1,2,3 [28].

As discussed already, the absence of product tables of Young tableaux 10 and 11 particles makes it impossible to precisely classify the cluster states in the considered system of particles. However, the quality standard of orbital symmetry allows one to define the existence of the FSs in the S and D waves and the absence of the FS for P states. Such a structure of FSs and ASs in different partial waves allows one to construct the potentials of intercluster interaction necessary for calculating the total cross-sections of the radiative capture reaction at low energies.

Thus, being limited by the lowest partial waves with the orbital moments L = 0,1 we can say that, for the n^{10}B system, for P wave potentials only allowed state is present and for the S wave only forbidden state is present. Meanwhile, the P wave corresponds to two allowed Young tableaux, namely, {443} and {4421}. This is similar

to the N^{2}H system described in §2.1 where potentials for scattering processes depend on two, whereas for BS only on one Young tableaux. Therefore, we will consider here that the GS potential corresponds to one tableau {443} – it defines the most low-lying allowed level for the BS in the given partial potential with $L = 1$ [11,20,21,28].

Consequently, there are various potentials of the BS and scattering processes as they depend on a different set of Young tableaux. Here, we consider that for discrete spectrum the allowed states in P waves, corresponding to the GS and ES of ^{11}B are bound, whereas for the scattering processes they are not bound. For the S scattering waves in the n^{10}B system, the forbidden state is the bound state.

However, we still notice that, for ^{10}B in the p^9Be channel or n^9Be channel of ^{10}Be, the orbital Young tableaux in the form of {4411} has been obtained earlier [12,14,178,217]. Therefore, for the N^{10}B system, which is only limited by the 1p-shell nuclei, we obtain {1} × {4411} = {5411} + {4421} [28]. The first of the obtained tableaux is compatible with the orbital moments $L = 1,3$, and is forbidden because there cannot be five nucleons in the nuclear s-shell. The second tableaux is allowed and compatible with the orbital moments $L = 1,2,3$ [28]. This is another variant of the classification of orbital states according to Young tableaux for the n^{10}B system.

Thus, for orbital moments $L = 0,1$, in case of the N^{10}B system in the potentials of P waves, the FS is presented by the {5411} tableaux and the allowed state with {4421}, corresponding to the GS of ^{11}C with $J^\pi = 3/2^-$ or ^{11}B also with $J^\pi = 3/2^-$, and in the S waves the FSs are absent. The potentials and capture cross-section results for such variants of the classification will be discussed in the future. The upcoming chapters will consider the N^{11}B system's two Young tableaux {443} and {4421} the GS of ^{11}B.

Coming back to the first classification variant, a state in the $^6P_{3/2}$ wave (in standard notations $^{(2S+1)}L_J$) corresponds to the GS of ^{11}B at $J^\pi,T = 3/2^-,1/2$, to the Young tableaux {443} is at the binding energy of the n^{10}B system of –11.4541(2) MeV [228]. Additionally, some n^{10}B scattering states and discrete spectrum can be mixed up to spin with $S = 5/2$ ($2S+1 = 6$) и $S = 7/2$ ($2S+1 = 8$), which will be discussed in the future.

Now, we will consider the available ^{11}B excited states but bound in the n^{10}B channel.

1. At an energy of 2.1247 MeV, higher than the GS, or –9.3329 MeV [228], relative to the threshold of the n^{10}B channel, the first ES exists, although bound at this channel with moment $J^\pi = 1/2^-$, which can be compared to the $^6F_{1/2}$ wave with the FS. We will not consider this because the cross-section of such a transition is suppressed as result of of the large centrifugal barrier.
2. The second ES at an energy of 4.4449 MeV [228], relative to the GS, or –7.0092 MeV, relative to the threshold of the n^{10}B channel, has moment $J^\pi = 5/2^-$, which can be compared with a mixture of $^6P_{5/2}$ and $^8P_{5/2}$ waves without the bound FSs or ASs. As the used model does not allow dividing the states with different spins, a single potential of such a mixed state, namely, the $P_{5/2}$ wave, will be constructed below. For both the states stated above, the same potential at $J = 5/2$ will be used.

The wave function obtained using such a potential at the solution of the Schrödinger equation consists of two components for the different spin channels; however, it is not explicitly divided into these components. Therefore, for all calculations of the $P_{5/2}$ wave, we use the full form.

3. The third ES at an energy of 5.0203 MeV [228], relative to the GS, or −6.4338 MeV, relative to the threshold of the n^{10}B channel has $J^{\pi} = 3/2^{-}$, and can be considered pure by spin $^{6}P_{3/2}$ wave without bound FSs.
4. The fourth ES at an energy of 6.7429 MeV [228], relative to the GS, or −4.7112 MeV, relatively to the threshold of the n^{10}B channel, has momemt $J^{\pi} = 3/2^{-}$, and can be compared to a mix of $^{6}P_{7/2}$ and $^{8}P_{7/2}$ without bound FSs. The potential for $J = 7/2$ will be constructed here, considering the wave function of the $P_{7/2}$ wave.
5. In addition, it is possible to consider the ninth ES at an energy of 8.9202 MeV with the moment $5/2^{-}$, i.e., at −2.5339 MeV relative to the n^{10}B threshold, which can be compared to a mixture of $^{6}P_{5/2}$ and $^{8}P_{5/2}$ states without the bound FSs – the situation here is similar to that described in 2. For capture in this state, experimental data have been published [279], therefore, we include this in further consideration of neutron radiative capture processes on ^{10}B. Numerical values of total experimental cross-sections from [279] have been taken from the MSU database [150].

Now, we will consider the spectrum of resonance states in the n^{10}B system, i.e., states at positive energies:

1. The first resonance state (RS) of ^{11}B in the n^{10}B channel is at 0.17 MeV, and has a neutron width of 4 keV and a moment of $J^{\pi} = 5/2^{+}$ (see Table 11.11 in [228]), which can be compared to the $^{6}S_{5/2}$ scattering wave with the bound FS. However, we did not construct the potential with such a small resonance width. Therefore, we will consider this scattering wave as nonresonance, resulting in zero phase shifts; however, the presence of the bound FS leads to non-zero potential depth. Moreover, in this energy range, there are no experimental data on the cross-sections of radiative capture [150].
2. The second RS has an energy of 0.37 MeV – its neutron width is 0.77 MeV and has a moment of $J^{\pi} = 7/2^{+}$ [228]; therefore, it can be compared to the $^{8}S_{7/2}$ scattering wave with the bound FS. Because of such a large resonance width, which is twice more than the resonance energy for scattering wave potential, we use nonresonance values of parameters with the bound FS, coinciding with the parameters for previous $^{6}S_{5/2}$ potentials.
3. The third RS has an energy of 0.53 MeV; its neutron width is 0.031 MeV (cm) and the moment is $J^{\pi} = 5/2^{-}$ [228]. Therefore, it can be compared with the mixed scattering waves $^{6}P_{5/2} + {}^{8}P_{5/2} = {}^{6+8}P_{5/2}$ without the BS, i.e., without FSs and ASs. These resonance characteristics are listed in Table 11.11 in [228]. However, an energy of 0.495(5) MeV and width of 140(15) keV is mentioned in the note to this table at this resonance. Simultaneously, 0.475(17) MeV with a width of 200(20)

keV are given in Table 11.3 in [228] for this resonance (). As these results differ considerably, in the first variant of such a potential, we will not consider this resonance. Instead, we will consider the $P_{5/2}$ scattering phase shift as zero and all P scattering states as not supporting the BSs; the depth parameter of the V_0 potential (1.2.2) can possibly approach zero.

Because the following resonance is at an energy higher than 1.0 MeV, we will not consider it (Table 11.11 in [228]). At energies 1.0 MeV in the spectra of ^{11}B, resonance levels are absent, which could be compared with $P_{3/2}$ and $P_{7/2}$ states [228]. Therefore, their phase shifts can approach zero, and as in these waves, they are not bound FSs or ASs. These potentials can also approach zero, as in case of $P_{5/2}$ scattering state discussed above [136,147,171,178,207]. Thus, we will first consider all electromagnetic transitions to the GS as well as to four (second, third, fourth and ninth) excited states in the P waves without FSs and from the S scattering states with the FS.

Because the ground state is compared with the $^6P_{3/2}$ level, it is possible to consider $E1$ transitions from $^6S_{5/2}$ scattering wave to this state of ^{11}B

1. $$^6S_{5/2} \to {}^6P_{3/2}.$$

Furthermore, it is possible to consider the $E1$ transitions from the $^6S_{5/2}$ and $^8S_{7/2}$ scattering waves to the second ES of ^{11}B, which is a mixture of two $P_{5/2}$ states

2. $$\begin{matrix} {}^6S_{5/2} \to {}^6P_{5/2} \\ {}^8S_{7/2} \to {}^8P_{5/2} \end{matrix}.$$

Because, here, we have a transition from different spin states of the initial S to different parts of the wave function of this second ES, the cross-section of these transitions can be summarized asx

$$\sigma = \sigma({}^6S_{5/2} \to {}^6P_{5/2}) + \sigma({}^8S_{7/2} \to {}^8P_{5/2}).$$

This has been discussed earlier, for example, for the neutron capture on ^{7}Li.

In the third ES, the pure level is compared with the spin $^6P_{3/2}$ level; therefore, for the GS, it is possible to consider $E1$ transitions from the $^6S_{5/2}$ scattering wave to the third ES of ^{11}B

3. $$^6S_{5/2} \to {}^6P_{3/2}.$$

Another $E1$ transition from the $^6S_{5/2}$ and $^8S_{7/2}$ scattering waves to the fourth ES of ^{11}B is possible at $J^\pi = 7/2^-$

4. $$\begin{matrix} {}^6S_{5/2} \to {}^6P_{7/2} \\ {}^8S_{7/2} \to {}^8P_{7/2} \end{matrix}.$$

The cross-section of two of these transitions can also be summarized as for reaction No. 2.

The last $E1$ transition considered here is the capture from ${}^{6}S_{5/2}$ and ${}^{8}S_{7/2}$ of scattering waves to the ninth ES of ^{11}B at $J^{\pi} = 5/2^{-}$

5. $$\begin{matrix} {}^{6}S_{5/2} \rightarrow {}^{6}P_{5/2} \\ {}^{8}S_{7/2} \rightarrow {}^{8}P_{5/2} \end{matrix}.$$

The cross-section of these transitions can be summarized, as it has been already explained for the reaction given above (2) for transition to the second ES.

Furthermore, it is possible to consider $M1$ transitions to the GS from resonance at 0.475(17) MeV for the ${}^{6}P_{5/2}$ scattering wave, as well as from nonresonance for ${}^{6}P_{3/2}$ wave

6. $$\begin{matrix} {}^{6}P_{5/2} \rightarrow {}^{6}P_{3/2} \\ {}^{6}P_{3/2} \rightarrow {}^{6}P_{3/2} \end{matrix}.$$

Furthermore, ${}^{6}P_{3/2} \rightarrow {}^{6}P_{3/2}$ transition from the nonresonance for ${}^{6}P_{3/2}$ scattering potential with zero depth is at the level of 1–2 μb. Such transitions from nonresonance for $P_{3/2}$ and $P_{7/2}$ scattering waves to the ground state or $P_{5/2}$, $P_{7/2}$ ES will not be considered.

$M1$ transitions to the second ES from the resonance of ${}^{6}P_{5/2}$ and ${}^{8}P_{5/2}$ scattering waves can also be considered

7. $$\begin{matrix} {}^{6}P_{5/2} \rightarrow {}^{6}P_{5/2} \\ {}^{8}P_{5/2} \rightarrow {}^{8}P_{5/2} \end{matrix}.$$

Because this is a single transition from the mixed spin state by $P_{5/2}$ scattering wave to the mixed second spin ES, the cross-section will be averaged by the above-mentioned transitions, i.e., we will use the following expression

$$\sigma = 1/2\left\{\sigma({}^{6}P_{5/2} \rightarrow {}^{6}P_{5/2}) + \sigma({}^{8}P_{5/2} \rightarrow {}^{8}P_{5/2})\right\}.$$

This expression was previously described for the neutron capture on ^{15}N.

The potentials in the same partial wave $P_{5/2}$ for both continuous and discrete spectrum are different because of different Young tableaux for these states. As discussed already, the possible transition of ${}^{6+8}P_{7/2} \rightarrow {}^{6+8}P_{5/2}$ from the nonresonance ${}^{6+8}P_{7/2}$ scattering wave, with zero potential on second ES, is not considered here because of its small cross-section.

$M1$ transitions to the third ES ${}^{6}P_{3/2}$ from the resonance ${}^{6}P_{5/2}$ scattering wave can be considered as

8. $${}^{6}P_{5/2} \rightarrow {}^{6}P_{3/2}.$$

$M1$ transitions to the fourth ES $^6P_{7/2} + {}^8P_{7/2}$ from the resonance $^6P_{5/2} + {}^8P_{5/2}$ scattering wave are also possible

9. $$\begin{matrix} {}^6P_{5/2} \to {}^6P_{7/2} \\ {}^8P_{5/2} \to {}^8P_{7/2} \end{matrix}.$$

Such a cross-section can averaged by two transitions, as shown earlier for reaction No. 7.

Finally, it is possible to consider $M1$ transitions to the ninth ES $^6P_{5/2} + {}^8P_{5/2}$ as experimental data for this transition are already available [279] from the resonance $^6P_{5/2} + {}^8P_{5/2}$ scattering wave

10. $$\begin{matrix} {}^6P_{5/2} \to {}^6P_{5/2} \\ {}^8P_{5/2} \to {}^8P_{5/2} \end{matrix}.$$

The cross-section of this transition can also be averaged by two processes specified here on the considered ES, as discussed in reaction No. 7.

Now, we progress to the direct construction of intercluster potentials of interaction in both continuous and discrete spectra.

3.1.2 Intercluster potentials

For all n^{10}B interaction potentials, i.e., all partial waves with known JLS, the Gaussian potential of the form (1.2.2) was used. Here, as discussed previously, we will not consider the influence of the first resonance at 0.17 MeV in the $^6S_{5/2}$ wave. Instead, we will use it for the potential with bound FS leading to zero scattering phase shift

$$V_{S5/2} = -160.5 \text{ MeV}, \ \gamma_{S5/2} = 0.5 \text{ fm}^{-2}. \tag{3.1.1}$$

At energies up to 1.0 MeV, $^6S_{5/2}$ scattering phase shift of is less than 0.5°. For the $^8S_{7/2}$ scattering wave without second resonance at 0.37 MeV and with a very large width of 0.77 MeV, we will also use these potentials.

For the potential of the third RS at 0.475(17) MeV and the width of 200(20) keV [228] for the $^6P_{5/2} + {}^8P_{5/2}$ waves as the second variant of potential (the first variant has zero depth) the following can be obtained

$$V_{P5/2} = -106.615 \text{ MeV}, \ \gamma_{P5/2} = 0.4 \text{ fm}^{-2}. \tag{3.1.2}$$

Such potentials lead to resonance, i.e., the scattering phase shift becomes 90.0° (1) at 475(1) keV with a width of 193(1) which is consistent with previous studies [228,280]. This scattering phase shift is illustrated in Fig. 3.1.1. For calculating the width of the resonance level for scattering phase shift, expression (2.3.6) was used.

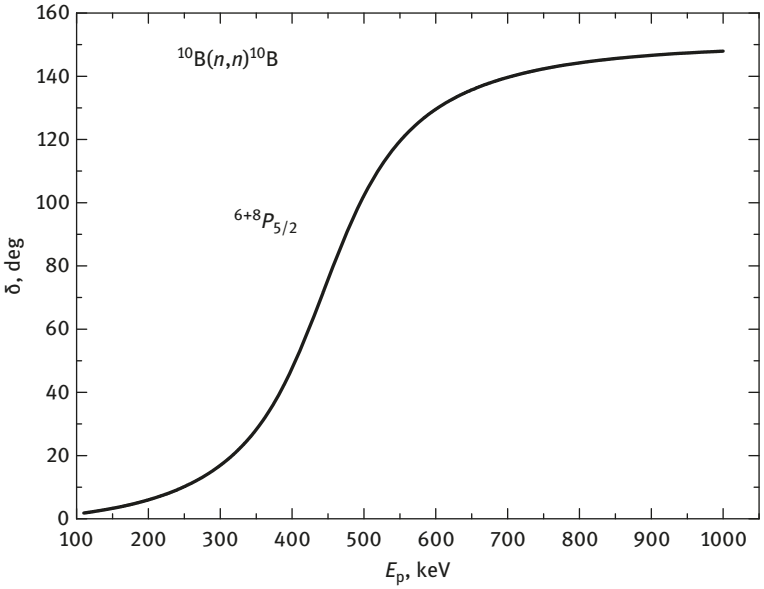

Fig. 3.1.1: Phase shift of elastic n^{10}B scattering in the $^{6+8}P_{5/2}$ wave.

Note that the partial phase shift, i.e., phase shift with an orbital moment L, of potential with bound states, with M (allowed) or N (forbidden) states is dominated by the generalized Levinson theorem [11]. Therefore, at zero energy, such phase shift starts from $(N + M)\pi$ where $N + M$ is the number of the bound levels. However, here and elsewhere in this book, we present the drawing of the scattering phase shift from zero degrees, in which is habitual for a majority of physicists.

Here, it is necessary to remember that for analyzing resonance scattering, for the considered partial wave at energies up to 1.0 MeV, there is narrow resonance; however, at given number of BSs (both allowed or forbidden), potential is constructed entirely unambiguously. Its depth is unambiguously fixed by the resonance energy level, and the width is defined by the width of such a resonance. The error of its parameters usually does not exceed the error width determination, usually ranging 3–5%. It also belongs to the creation of partial potential on the scattering phase shifts and determination of its parameters on two-body resonances in the spectra of the final nucleus.

Now, we will discuss the creation of potentials of the BS into n^{10}B system, including the GS and several ESs. For the potential pure by spin with S = 5/2 the GS of ^{11}B in the n^{10}B channel, corresponding to the $^6P_{3/2}$ wave, the following partial parameters can be accepted

$$V_{\text{g.s.}} = -165.3387295 \text{ MeV}, \ \gamma_{\text{g.s.}} = 0.45 \text{ fm}^{-2}. \tag{3.1.3}$$

Using this potential, we obtain the AC = 1.53(1) on an interval of 3–10 fm, a charge radius of 2.44 fm, and a mass radius of 2.39 fm at the binding energy of 11.454100 MeV with an FDM accuracy of $\varepsilon = 10^{-6}$ MeV [261]. The AC error, as usual, is associated with its averaging on the interval of distances, as stated above. The scattering phase shift of this potential smoothly reduces to 179° when energy changes from zero to 1.0 MeV. ^{10}B radius has the value 2.428(50) fm for both charge and mass [214], and the corresponding value for ^{11}B radius is 2.406(29) fm [214]. The charge radius of neutron was zero, and its mass radius was considered to be the radius of proton of 0.8775(51) fm, whose value has been specified in [126].

For the AC of the GS of ^{11}B in the n^{10}B cluster channel in [215], the value of 1.72 fm$^{-1/2}$ has been reported, where the coefficient of identity of the $\sqrt{7}$ nucleons has been already allocated (see expression 83b in [96]). In [215], a slightly different determination of the AC was used (1.7.2). This expression differs from our determination (1.2.5) [94,136] at $\sqrt{2k_0}$ which, in this case, is equal to 1.19. Therefore, in the dimensionless form, the AC value becomes 1.44.

In recent results involving this constant [281], the specified value has been 1.82 (15) fm$^{-1/2}$, which after recalculation gives 1.52(12) in a dimensionless form; this is consistent with the obtained higher value for potential (3.1.3). These conclusions are correct if the spectroscopic factor (S_f) of the GS of ^{11}B in the n^{10}B channel is close to unity. For example, in [197], an average value of 0.88 has been reported for S_f. Using expression (1.7.1) for A_{NC} and the value 1.82(15) fm$^{-1/2}$, for the dimensionless AC in the form of (1.2.5), we obtain 1.62(13), which is also consistent with the results of the GS potential (3.1.3).

As mentioned above, parameters of the GS potential or any BS in the considered channel at known number of allowed and forbidden states bound in this partial wave are fixed quite unambiguously according to the binding energy, nuclear radius, and asymptotic constant. The accuracy with which the BS potential parameters are determined is first connected with the AC, which typically ranges 10–20%. Such potentials do not contain other ambiguities because the classification of states according to Young tableaux allow fixing the number of the BSs, which completely determines its depth; the width of the potential is entirely dependent on the AC values and the final nucleus charge radius.

The first ES is not considered because of the large orbital moment $^6F_{1/2}$. For the parameters $^6P_{5/2} + {}^8P_{5/2}$ of the potential without bound FS of the second ES of ^{11}B in the n^{10}B channel at $J^\pi = 5/2^-$, the following values have been obtained

$$V_{P5/2} = -151.61181 \text{ MeV}, \quad \gamma_{P5/2} = 0.45 \text{ fm}^{-2}. \tag{3.1.4}$$

With such potentials, the binding energy is –7.0092 MeV at an FDM accuracy of $\varepsilon = 10^{-4}$ MeV [261]. The obtained energy well coincides with the experimental value [228]; the charge radius is 2.44 fm, and the dimensionless AC is 1.15(1) on

an interval of 3–13 fm. The scattering phase shift for this potential smoothly reduces from 180° to 179° with increase in energy from 0 to 1.0 MeV.

The potential of the third pure by spin ${}^6P_{3/2}$ ES with $J^\pi = 3/2^-$ without the bound FS parameters were obtained as

$$V_{P3/2} = -149.70125 \text{ MeV}, \ \gamma_{P3/2} = 0.45 \text{ fm}^{-2}. \tag{3.1.5}$$

The binding energy of –6.4338 MeV was found at $\varepsilon = 10^{-4}$ MeV, which is consistent with the results of [228], AC was 1.10(1) on an interval of 3–13 fm, and charge and mass radii were 2.44 fm and 2.41 fm, respectively. The scattering phase shift for such potential decreased to 179° at an energy of 1.0 MeV.

For parameters ${}^6P_{7/2} + {}^8P_{7/2}$ of potential without the bound FS of the fourth ES of ^{11}B in the n^{10}B channel with $J^\pi = 7/2^-$ the following parameter values were obtained

$$V_{P7/2} = -143.72353 \text{ MeV}, \ \gamma_{P7/2} = 0.45 \text{ fm}^{-2}. \tag{3.1.6}$$

With such potentials, a binding energy of –4.7112 MeV is found at $\varepsilon = 10^{-4}$ MeV, which is consistent with the experimental results of [228], charge radius of 2.44 fm, and dimensionless AC is 0.94(1) at an interval of 3–15 fm. The scattering phase shift for such potentials smoothly decreases to 178° at an energy of 1.0 MeV.

For parameters ${}^6P_{5/2} + {}^8P_{5/2}$ of potential without the FS of the ninth ES of ^{11}B in the n^{10}B channel at $J^\pi = 5/2^-$ the following was obtained

$$V_{P5/2} = -135.39620 \text{ MeV}, \ \gamma_{P5/2} = 0.45 \text{ fm}^{-2}. \tag{3.1.7}$$

This potential gives a binding energy of –2.5339 MeV at $\varepsilon = 10^{-4}$ MeV, which is consistent with the experimental results of [228], charge radius of 2.44 fm, and dimensionless AC of 0.70(1) at an interval of 4–24 fm. The scattering phase shift of such potential smoothly decreases to 178° at an energy of 1.0 MeV.

In all calculations, the mass of ^{10}B is 10.012936 amu [214], and the mass of the neutron is given in §1.6. Hereinafter, the magnetic moments of clusters obtained from [126, 282] are used.

3.1.3 Total capture cross-sections

To analyze neutron capture on ^{11}B, first, $E1$ transition ${}^6S_{5/2} \to {}^6P_{3/2}$ from the S scattering waves with potential (3.1.1) to GS with potential (3.1.3) was considered. The obtained capture cross-section is shown in Fig. 3.1.2 denoted by short dashes (process No.1 in the §3.1.1). In Fig. 3.1.2, the capture cross-section from ${}^{6+8}S$ scattering waves of (3.1.1) to the ${}^{6+8}P_{5/2}$ to the second ES with potential (3.1.4), discussed above in 2 is denoted by dashed curves.

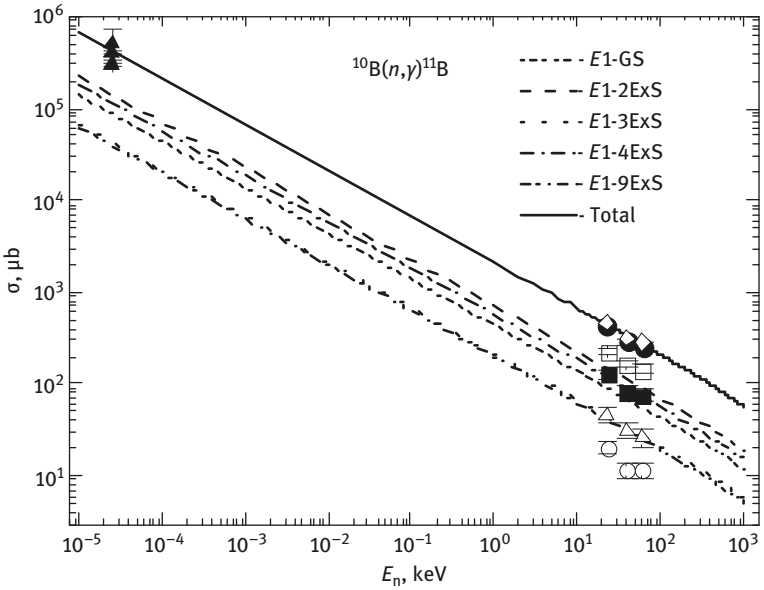

Fig. 3.1.2: The total cross-section of the neutron radiative capture on ^{10}B. Experimental data: black triangle (▲) – from [184], [232], and [283]; (●) – total summarized cross-section for the neutron capture on ^{10}B from [279]; circles (o) – total cross-sections for capture to the GS from [279]; open squares (□) – total capture cross-section to the second ES from [279]; black squares (■) – total capture cross-section to the fourth ES; open triangles (Δ) – total capture cross-section to the ninth ES from [279]; open rhombus (◊) – total cross-section for the capture from [279], taking into account transition to the third ES. Curves: short dashes – the cross-section of the $E1$ transition $^6S_{5/2}\rightarrow{}^6P_{3/2}$ from the ^6S scattering wave with potential (3.1.1) to the GS with potential (3.1.3); dashed curve – capture cross-section from the ^6S wave to the second ES (3.1.4); the dotted curve – the transition cross-section $^6S_{5/2}\rightarrow{}^6P_{3/2}$ to the third ES (3.1.5); the dashed-dotted curve – the transition cross-section from the S waves to the fourth ES (3.1.6); double dashed-dotted curve – the transition cross-section from the S scattering waves to the ninth ES with potential (3.1.7); the solid curve – summarized total cross-section of all listed transitions.

The cross-section of transition $^6S_{5/2}\rightarrow{}^6P_{3/2}$ to the third ES for the potential (3.1.5) is shown by the dotted curve at the bottom of Fig. 3.1.2, this transition is discussed above in 3.

The dashed-dotted curve shows the transition cross-section to the fourth ES with potential (3.1.6), which is discussed above in No. 4. The double dashed-dotted curve which almost merges with the dotted line shows the transition from the S scattering waves to the ninth ES with potential (3.1.7); i.e., No. 5. The solid curve shows the total summarized cross-section of all above transitions, which is generally reproduce the experimental data [279, 283] in the energy range of 25 meV to 61 keV.

The summarized total capture cross-section at 23, 40, and 61 keV is shown in Fig. 3.1.2 denoted (●)and (▲); the data from [184, 232, 279, 283] at 25 meV is

represented. In Fig. 3.1.2, the experimental results of [279] for transitions to various ES of ^{11}B are also shown. In particular, the circles (o) are total capture cross-sections to the $^{6}P_{3/2}$ GS, open squares (□) denote the total capture cross-section to the second ES with the $^{6+8}P_{5/2}$, black squares (■) denoted the total capture cross-section to the fourth ES from the $^{6+8}P_{7/2}$, and open triangles (Δ) denote the total capture cross-section to the ninth ES with $^{6+8}P_{5/2}$.

As seen, the calculation curve for the transition to the fourth ES, denoted by the dotted-dashed line, is consistent with the experimental data denoted black squares. The good agreement of the calculation, shown by the dotted-dotted-dashed line, is also observed for the transition to the ninth ES, which is denoted by open triangles.

At the same time, measurements for the transition to the second ES are shown in Fig. 3.1.2 denoted by open squares which lie much above the corresponding calculation curve, which is denoted by the dashed line. The measurements for the transition to the GS denoted by the open circles lie much below than the calculation curve, which is denoted by short dashes. Thus, for transitions to various excited levels of ^{11}B, the following two calculations are consistent with the experimental results of [279] – these include transitions to the fourth ES and the ninth ES. The two reactions that are not coordinated include transitions to the second ES and ground state. However, the total summarized cross-sections denoted black points are described by the calculation curve, i.e., the solid line in Fig. 3.1.2.

The measurements published previously in [279] regarding transition to the third ES were not considered here. Our calculations provide approximately identical cross-sections of the transition to the second ES and the ninth ES, as shown in Fig. 3.1.2 by the dotted curve and the dotted-dotted-dashed line. To obtain accurate summarized total cross-sections, it is necessary to add the cross sections of the transition to the ninth ES to the summarized total cross-sections obtained from [279], as it will be equivalent to the transition to the third ES. Such cross-sections are shown in Fig. 3.1.2 by the open rhombs (◊); these are possibly consistent with the results of our calculations and new values of asymptotic constant from [197,281].

As the value of the asymptotic constant for the second ES is unknown, it is possible to construct the potential by transferring the capture cross-sections to this state, shown in Figs. 3.1.2 and 3.1.3, which is by open squares [279]. For example, it is possible to use the potential with parameters

$$V_{P5/2} = -108.37443 \text{ MeV}, \ \gamma_{P5/2} = 0.3\,\text{fm}^{-2}, \tag{3.1.8}$$

which leads to a binding energy of –7.0092 MeV, charge radius of 2.44 fm, and AC of 1.45(1) at an interval of 4–13 Fm. The calculation results of the capture cross-sections

to the $^{6+8}P_{5/2}$ of the second ES from the ^{6+8}S scattering waves are also shown in Fig. 3.1.3 denoted by the dashed curve, which is consistent with the results of [279], denoted as open squares.

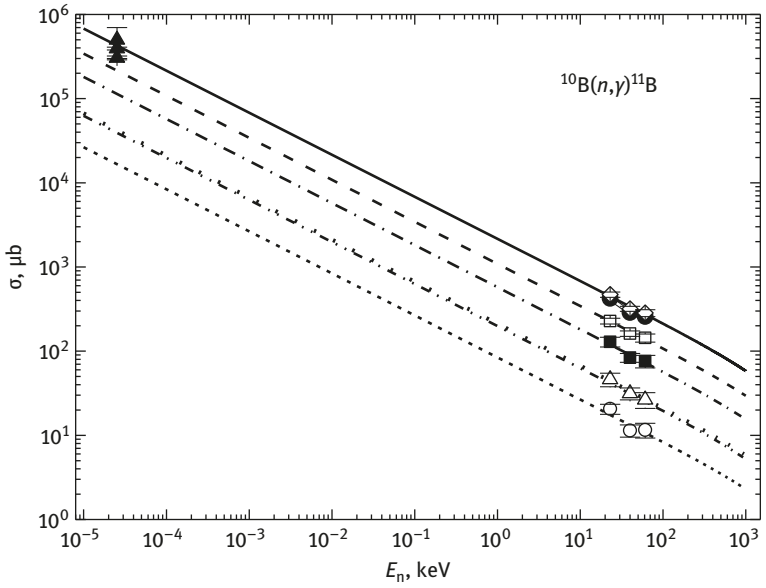

Fig. 3.1.3: Total cross-sections of the neutron radiative capture on ^{10}B. Experimental data: the same as in Fig. 3.1.2. Curves: short dashes – the cross-section of the $E1$ transition $^6S_{5/2}\rightarrow{}^6P_{3/2}$ from the ^6S scattering wave with potential (3.1.1) to the GS with potential (3.1.9); usual dashed curve – capture cross-section to the second ES (3.1.8); dotted curve – the cross-section of the$^6S_{5/2}\rightarrow{}^6P_{3/2}$ transition to the third ES (3.1.5); dashed-dotted curve – the cross-section of the transition to the fourth ES (3.1.6); dotted-dotted-dashed curve – the cross-section of the transition from the ^6S scattering waves to the ninth ES with potential (3.1.7); solid curve – the summarized total cross-section of all listed transitions.

Simultaneously, another variant of the GS potential, which describes the total capture cross-sections to the GS, shown in Fig. 3.1.2–3.1.3 by the open circles correctly, does not correspond with the known and above-mentioned AC for the ground state. For example, the following parameters

$$V_{\text{g.s.}} = -602.548373 \text{ MeV}, \ \gamma_{\text{g.s.}} = 2.0 \text{ fm}^{-2} \tag{3.1.9}$$

describe the available experimental measurements of the cross-sections of such transition [279], as shown in Fig. 3.1.3 by short dashes. Other curves, shown in Fig. 3.1.3, coincide with the results presented earlier in Fig. 3.1.2, and the solid

curve describes the summarized total capture cross-sections denoted by black points and rhombs.

However, such potentials, though lead to the correct binding energy of –11.454100 MeV, are acceptable and describe the charge radius of ^{11}B as 2.43 fm and the AC value as 0.71(1) at an interval of 2–8 fm. This is twice less than the results available by the extraction of this constant from experimental data iin [197,215,281]; the results for the potential of the ground state are specified above (3.1.3).

Such results could be explained by the imperfection of the MPCM used here; however, in similar cases, MPCM correctly described the cross-sections for both the transitions to the GS and for the summarized total cross-sections of capture processes [12,136,171,178]. Therefore, it is possible to assume that the experimental measurements of the transitions to various ESs of ^{11}B, including transition to the third ES, at neutron radiative capture on ^{10}B must be specified in future studies. It is also interesting to obtain new experimental data in the energy range of possible resonances, i.e., approximately 100–600 keV.

Because at energy range of 10 keV to 10 meV, the calculation cross-section is practically a straight line, and can be approximated by the simple function of the form (2.1.3). The value of the constant A = 2123.4694 μb keV$^{1/2}$ was determined by one point in the calculation cross-sections (solid curve in Fig. 3.1.2) at a minimum energy of 10 meV. The relative deviation (2.1.4) of the calculated theoretical cross-section (σ_{theor}) and the approximated (σ_{ap}) cross-section by the function given above to 10 keV is approximately 0.2%.

Thus, it can be assumed that this dependence of the total cross-section on energy will also hold at lower energies. Therefore, based on the given expression for the approximation of cross-section, it is possible to estimate the cross-section, for example, at 1 μeV (1 μeV = 10^{-6} eV = 10^{-9} keV), which gives a value of approximately 67.2 b. For the solid curve in Fig. 3.1.3, the coefficient of approximation (2.1.3) of cross-sections is slightly different, i.e., A = 2150.3488 μb keV$^{1/2}$.

Further, we can consider a possible contribution of various magnetic $M1$ transitions. In particular, Fig. 3.1.4 shows the considered $M1$ transitions to the ground and different excited states of ^{11}B, along with the summarized cross-section for $E1$ processes, which is shown in Fig. 3.1.4 by the dashed curve and in Fig. 3.1.2 by the solid line.

The dotted curve denotes the cross-section of the $M1$ transition to the $^6P_{3/2}$ of the GS with potential (3.1.3) from the resonance $^6P_{5/2}$ scattering waves for potential (3.1.2), which was discussed above at No. 6. The cross-section, denoted by the dashed-dotted curve is the transition from the resonance $^6P_{5/2}$ scattering waves (3.1.2) to the second ES with potential (3.1.4), which is designated in §3.1.1 as No. 7. The curve designated in Fig. 3.1.4 by a dotted-dotted-dashed line denoted the cross-section of $M1$ $^6P_{5/2}\rightarrow{}^6P_{3/2}$ transition to the third ES with potential (3.1.5), discussed above at No. 8.

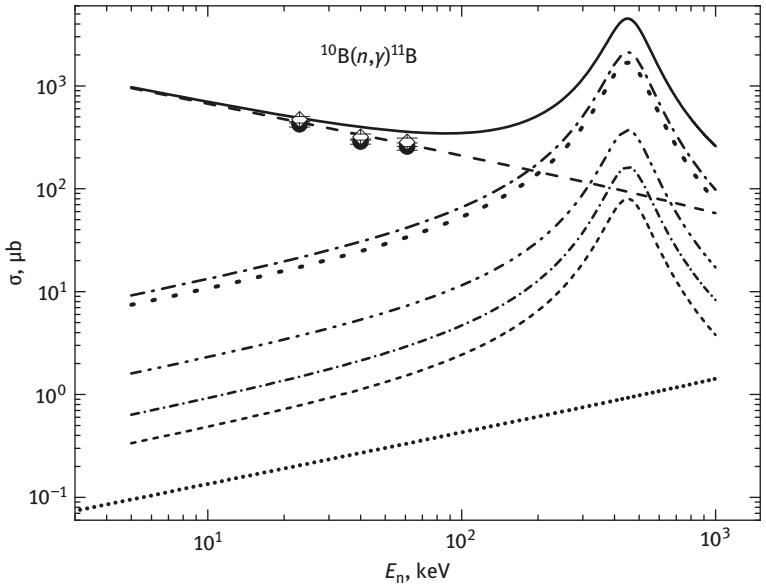

Fig. 3.1.4: Total cross-section of neutron radiative capture on ^{10}B. Experimental data: Points (●) – total summarized capture cross-section on ^{10}B from [279]; open rhombs (◊) – total capture cross-section from [279], taking into account the transition to the third ES. Curves: dashed curve – the total cross-section for the $E1$ processes, shown in Fig.3.1.2 by the continuous curves; dotted curve – cross-section the $M1$ transition to the GS (3.1.3) from the resonant $^6P_{5/2}$ scattering wave for the potential (3.1.2) is shown, cross-sectional transition is shown by the dashed-dotted curve from the resonance $P_{5/2}$ scattering wave (3.1.2) to the second ES with potential (3.1.4); the dotted-dotted-dashed line shows the cross-section of the $M1$ transition to the third ES with potential (3.1.5); short dashes – $M1$ transition to the fourth ES (3.1.6); dashed-dotted curve with often located dashes –$M1$ transition to the ninth ES (3.1.7). The dotted line with often located points at the very bottom of Fig. 3.1.4 shows $M1$ transition from the nonresonance $^6P_{3/2}$ scattering wave to the GS; the solid curve shows the sum of above-described $E1$ and $M1$ transitions.

Another possible $M1$ transition to the fourth ES (3.1.6), designated above as No. 9, has been shown in Fig. 3.1.4 by short dashes. Additionally, the $M1$ transition to the ninth ES (3.1.7) is discussed above as No. 10, and is shown in Fig. 3.1.4 by the dashed-dotted curve with often located dashes, which goes slightly above the curve designated by the short dashes. The sum of all $E1$ and $M1$ transitions described above is presented in Fig. 3.1.4 by the solid curve, which is quite acceptable considering the behavior of the experimental data denoted by points and rhombs.

Furthermore, for $M1$ transition from nonresonance $^6P_{3/2}$ scattering wave to the GS with the first potential variant of the zero depth, the second transition at No. 6 has been considered. This is shown by the dotted line with often located dots at the very bottom of Fig. 3.1.4. Its maximum value approaches 1.5 μb and does not influence the calculation of the cross-sections in the resonance range of 475 keV, which almost approaches 4.5 mb.

A slight excess of the calculated cross-sections over the experimental value at 40 and 61 keV (see Fig. 3.1.4) can be attributed to the used potential of the $P_{5/2}$ resonance wave (3.1.2) which leads to the overestimated resonance width value in this scattering wave, i.e., 193 keV. As discussed earlier, different values of the energy and width of this resonance are presented in [228]; it is also possible to construct the new potential, which will be coordinated, for example, with energy of 530 keV or 475 keV, but with a width of 31 keV, as presented in Table 11.11 in [228].

Use of such potential can significantly change the calculation of resonance cross-sections, having an impact on the total summarized cross-section in the energy range of 40–60 keV, as reported previously in [279]. For example, we will use the resonance potential of the $P_{5/2}$ scattering wave in the form

$$V_{\mathrm{P5/2}} = -3555.983\ \mathrm{MeV},\ \ \gamma_{\mathrm{P5/2}} = 13.0\,\mathrm{fm}^{-2}. \tag{3.1.12}$$

This potential leads to resonance at 475 keV, however, its width is reduced to 32 keV, which is accordance with the data of Table 11.11 in [228]. The resonance energy remains unchanged, i.e., the minimally possible to strengthen its influence on the cross-section at 61 keV. These experimental cross-sections obviously do not belong to the resonance part of the cross-sections, even though a slight increase at energy of 61 keV can be expected. The calculation results of the total capture cross-sections with the potential (3.1.12), given above, are presented in Fig. 3.1.5.

The dashed curve, as in Fig. 3.1.4, represents the summarized cross-sections for all $E1$ processes shown in Fig. 3.1.2 by the solid curve. The dotted curve shows the cross-section of the $M1$ transition to the GS with potential (3.1.3) from the resonance $^6P_{5/2}$ scattering wave for new potential (3.1.12), and the dashed-dotted curve shows the cross-section of the transition from the resonance $P_{5/2}$ scattering wave of the form (3.1.12) to the second ES with potential (3.1.4). The solid curve represents the summarized cross-sections for the transitions described above.

All other transitions, shown in Fig. 3.1.4, result in cross-sections that do not essentially contribute to the total summarized cross-sections at resonance energy. From Fig. 3.1.5, it is clear that the resonance part of the cross-section calculation does not change the total summarized cross-sections at 40–60 keV. The results of these calculations correspond with the available experimental data of [279].

This is shown in detail in Fig. 3.1.6, where the calculated and experimental cross-sections in the energy range of 10–100 keV are shown [279]. From Fig. 3.1.6, it is clear that calculated total cross-section well coordinates with the summarized experimental data [279], taking into account their contribution to the transition to the third ES, as described above. The calculated cross-section is almost completely consistent with the experimental errors shown in Fig. 3.1.6 using open rhombs. Thus, based on the considered $M1$ transitions, shown in Figs. 3.1.4 to 3.1.6, the total summarized cross-sections at resonance energy of 0.475 MeV and resonance width

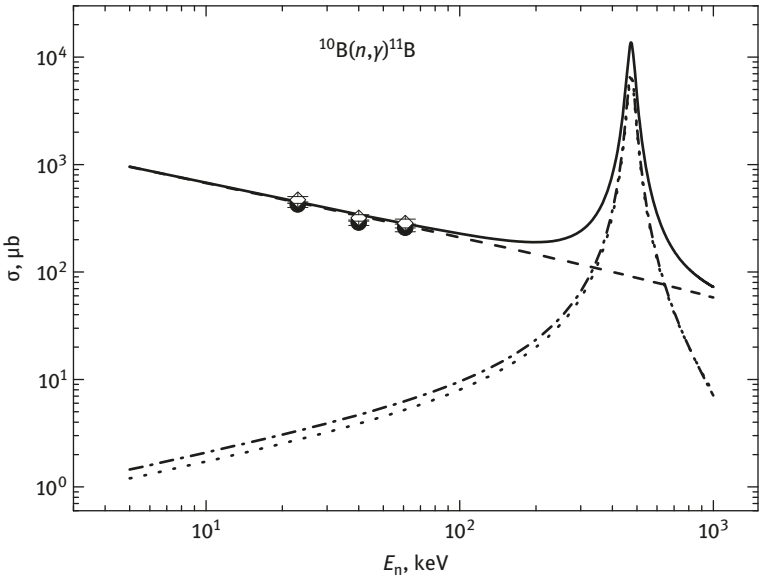

Fig. 3.1.5: Total cross-section of neutron radiative capture reaction on ^{10}B. Experimental data: as in Fig. 3.1.4. Curves: dashed curve – the summarized cross-section for the $E1$ processes shown in Fig. 3.1.2 by the solid curve; the cross-section of $M1$ transition to the GS (3.1.3) is shown by the dotted curve from the resonance $^6P_{5/2}$ scattering wave for (3.1.12) potential; the cross-section of the transition from the resonance $P_{5/2}$ scattering wave to the second ES with (3.1.4) potential is shown by the dashed-dotted curve (3.1.12); the solid curve – summarized cross-sections.

of 193 keV reach 4.5 mb, and with a width of 32 keV the cross-section value reaches 13.7 mb. In the latter case, the transition to the GS from the resonance $P_{5/2}$ wave gives a cross-section value of 6.5 mb.

Here, it is necessary to note that if the distinction of the Young tableaux for the potentials of the continuous and discrete spectra is not used, then as another variant for the $^6P_{3/2}$ and $^{6+8}P_{7/2}$ potentials of nonresonance scattering, it is possible to use BS potentials which correspond to these moments. Such potentials have different number of BSs, allowed or forbidden, and are, in fact, phase-equivalent. In other words, it is possible to use the identical interactions for a continuous and discrete spectrum in states with $J = 3/2$ and $7/2$. In particular, for the $^6P_{3/2}$ scattering wave, the GS potential can be used in the form of (3.1.3), and for the $^{6+8}P_{7/2}$ scattering wave of the fourth ES potential (3.1.6) can be used.

In the first case, the matrix element of the $M1$ transition $^6P_{3/2} \rightarrow {}^6P_{3/2}$ (the second transition detailed above at No. 6), calculated from the product of the GS wave function and the wave function of the corresponding scattering wave, gives cross-sections of approximately 10^{-11} μb, i.e., orthogonality of the numerical wave function of both continuous and discrete spectrum obtained in one potential is observed.

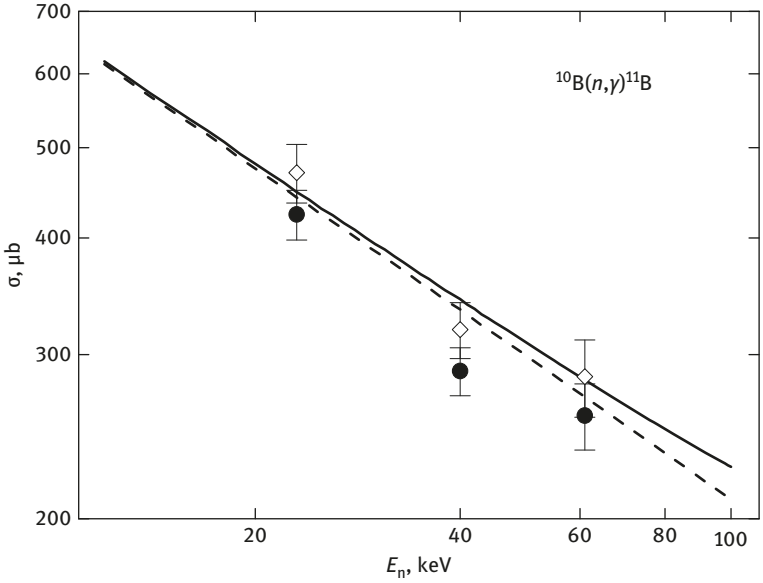

Fig. 3.1.6: Total cross-sections of neutron radiative capture on ^{10}B. Experimental data: as in Fig. 3.1.4. Curves: dashed line – total cross-section of the $E1$ processes shown in Fig. 3.1.2 by the solid curve and by the dashed curve in Fig .3.1.5; the solid curve – summarized cross-sections taking into account the $M1$ transitions, illustrated in detail in Fig. 3.1.5.

On transitions of the form $^6P_{3/2} \to {}^6P_{5/2}$, i.e., from the nonresonance $^6P_{3/2}$ scattering waves with potential (3.1.3) to the second ES, which is bound in the n^{10}B channel with potential (3.1.4), and transition of the form $^{6+8}P_{7/2} \to {}^{6+8}P_{5/2}$, capture cross-sections have an order of 10^{-2} μb and do not significantly contribute to the general summarized capture cross-sections. However, these processes and on using different potentials of discrete and continuous spectra did not provide a real contribution to the total cross-sections, instead leading to other cross-section values.

On the other hand, for the $P_{5/2}$ resonance scattering wave, it is impossible to use potentials of the $P_{5/2}$ bound states as they do not result in the resonance form of the phase shift. It is not possible to construct the potential, which gives the resonance of the phase shift and allowed BS (the second or ninth ES); meanwhile, it is also not possible for these interactions to use different parameters, corresponding to a different set of Young tableaux for this system. Therefore, such potentials for continuous and discrete spectrum can vary.

Thereby, from the given results, it is clear that for describing the experiment, there are enough obvious assumptions about the construction methods of the n^{10}B interaction potentials, i.e., they need to contain the FS, describe the scattering phase shifts or resonances in the spectra of the final nucleus and the characteristics of the

BS, and obey the Young tableaux classification. Consequently, such potentials allow one to obtain the description which is consistent with the available experimental data for the total cross-sections of the neutron capture on ^{10}B previously discussed in [279,283] at energies ranging from 25 meV to 61 keV.

The possibility of describing all experimental data, both on the cross-sections and according to the GS characteristics, allows one to fix the parameters of the GS potential (3.1.3) rather precisely. It is necessary to note that the AC values are known only for the GS of ^{11}B in the n^{10}B channel; AC values for all ESs are absent, therefore, the calculation results with transitions to the second, third, fourth, and ninth ES should be considered first [284].

3.2 Neutron capture on ^{11}B

Neutron radiative capture reaction on ^{11}B can possibly play a role in some models of the Big Bang. Such models consider that the primordial nucleosynthesis of the universe occurred as per a chain of nuclear reactions of the form (3.0) [142], including the below process as

$$^{11}\mathrm{B}(n,\gamma)^{12}\mathrm{B}(\beta^-)^{12}\mathrm{C}$$

Therefore, to study the radiative capture processes that are possible at the primordial nucleosynthesis of the universe [12,14,136], we will consider the $n^{11}\mathrm{B} \to {}^{12}\mathrm{B}\gamma$ reaction at thermal and astrophysical energies in the MPCM framework.

Here, for constructing intercluster potentials, we adhere to the methods and principles stated in Chapter 1 of this book. As there are no results available for the phase-shift analysis of the elastic n^{11}B scattering, the potentials of intercluster interactions for the scattering processes are constructed based on the structure of the spectra of the resonance states of final nucleus ^{12}B considering them to be resonances in the two-body n^{11}B channel.

For the bound excited states and the ground state of ^{12}B, formed as a result of the capture reaction in the considered cluster channel, the initial intercluster potentials are constructed based on the description of the binding energy of these particles in the final nucleus as well as some important characteristics of such states, for example, the charge radius and asymptotic constant.

3.2.1 Classification of cluster states in the n^{11}B system

As discussed above, for the GS of ^{11}B with $J^\pi, T = 3/2^-, 1/2$ moments, it is possible to accept the orbital Young tableaux in the form of {443}; therefore, for the n^{11}B system,

we have {1} × {443} = {543} + {444} + {4431} [28,134]. The first of the obtained tableaux {543} is compatible to the orbital moments of L = 1,2,3,4 and is forbidden because in the s-shell there cannot be five nucleons [11]. The second Young tableaux {444} is allowed and compatible with the orbital moments of L = 0,2,4, and the third {4431}, is also and compatible to L = 1,2,3 [28].

Thus, being limited only by the lowest partial waves with the orbital moment of L = 0, 1, and 2, it is possible to state that for the n^{11}B system in the potential of the $^3S_1$ wave for the tableaux {444}, there is only allowed state, which does not have to be necessarily bound for the scattering states. The same situation can exist for the ^3D waves, which have the FS, as well as the mixed allowed state according to Young tableaux. Furthermore, for the sake of definiteness, we will consider that the FS corresponding to the tableaux {543} in this scattering wave is bound, whereas AS for the tableaux {444} is not. However, there is one exception, which is described below for the second ES.

In the ^3P waves for tableaux {543} and {4431}, there are forbidden and allowed bound states respectively. The last of them, namely, for the $^3P_1$ wave, corresponds to the GS of ^{12}B with $J^\pi, T = 1^+, 1$ and is at a binding energy of −3.370 MeV for the n^{11}B system [228]. Here, we will also consider that in the ^3P scattering waves, the FSs are bound and there is no AS. In general, some n^{11}B scattering states and BSs can be mixed by spins 1 and 2. However, here, we assume that all states have the same spin S = 1, i.e., they are pure triplet states.

If the orbital Young tableaux in the form {4421} can be accepted for ^{11}B, then for the n^{11}B system, we have {1} × {4421} = {5421} + {4431} + {4422}. The first of the obtained tableaux is forbidden and corresponds to the orbital moments with L = 1, 2, 3; the second is allowed for moments L = 1, 2, 3; the also is also allowed for moments L = 0, 2. Thus, only considering waves in the orbital moment L = 0, 1, 2, it can be considered that for the n^{11}B system in the potential of the $^3S_1$ and ^3D waves, only AS exists. In every ^3P waves, there is forbidden and allowed states; the last can be unbound for the discrete spectrum. As can be seen from this classification, in this case, the existence and number of the bound ASs and FSs in these partial waves, as opposed to the previous case, now another Young tableaux correspond to both ASs and FSs.

Now, we will consider the available ^{12}B excited states relative to the GS but bound in the n^{11}B channel, to which the transitions from the continuous spectrum are possible.

1. At an energy of 0.95 MeV above the GS of ^{12}B or −2.4169 MeV [228] relative to the threshold of the n^{11}B channel, the first excited state exists, however, bound in this channel with $J^\pi = 2^+$ moment, which can be compared to the triplet $^3P_2$ wave with the bound FS.
2. The second ES at an energy of 1.67 MeV [228], relative to the GS, or −1.6964 MeV, relative to the threshold of the n^{11}B channel, has $J^\pi = 2^-$ and can be compared to the triplet $^3D_2$ wave with the bound FS. This allowed state is mixed according to

Young tableaux, and similarly n^2H system can be considered as the state of a discrete spectrum, corresponding to the Young tableaux {444}. Moreover, the ^3D scattering waves correspond to two Young tableaux.

3. The third ES at an energy of 2.62 MeV [228], relative to the GS, or −0.7492 MeV, relative to the threshold of the n^{11}B channel, has $J^\pi = 1^-$, which can be compared to the triplet $^3S_1$ wave without the forbidden BS.
4. The fourth ES at an energy of 2.72 MeV, relatively to the GS, or −0.647 MeV [228], relatively to the threshold of the n^{11}B channel, has $J^\pi = 0^+$, which can be compared to the triplet $^3P_0$ wave with the bound FS.

If the bound state has a small binding energy, i.e., less than 1.0 MeV, contribution from transitions, for example, $E1$, to such a level can be usually neglected as its cross-section has a small value. However, we continue to study these transitions.

Except the excited state, in the bound states in the n^{11}B system, there are several resonance levels, i.e., states at positive energies.

1. The first resonance state of ^{12}B in the n^{11}B channel is at an energy of 20.8 (5) keV, with a width of less than 1.4 keV and a moment of $J^\pi = 3^-$ [228] – it can be compared to the $^3D_3$ scattering wave with the forbidden bound state, but without the bound AS. Moreover, similarly, for the n^2H system the scattering state for both Young tableaux {444} and {4431} correspond; therefore, its potential differs from the ^3D wave interactions of the second ES.
2. The second resonance state has an energy of 430(10) keV,width is equal to 37(5) keV, and moment is $J^\pi = 2^+$ [228]. Therefore, it can be compared to the $^3P_2$ scattering wave with the bound FS, but without the bound AS.
3. The third resonance state is at an energy of 1027(11) keV with very small width of 9(4) keV and the moment 1^- [228], which can be compared to the $^3S_1$ scattering wave without the bound forbidden or allowed state.

From the scheme of levels described above, at energies up to 1.0 MeV, considered in our calculations, in the spectra of ^{12}B, there are no resonance levels, which could be compared to the $^3S_1$ scattering wave [228]; the third resonance state is at a higher energy and is not considered here. Therefore, the $^3S_1$ phase shift in this energy range can be accepted to be close or equal to zero, and because $^3S_1$ scattering wave does not comprise bound FSs or ASs, its potential as the first variant possibly approach zero [12].

As the second variant of such potential for the $^3S_1$ scattering wave, we will compare to the third ES of ^{12}B with $J^\pi = 1^-$, i.e., to the level with the bound AS at −0.7492 MeV, relative to the threshold of the n^{11}B channel, as it has been seen for the n^9Be or n^{12}C systems earlier (see §2.4 and §2.5). Consequently, the minimum set of electromagnetic transitions to the ground state and some ESs will be considered, which aid in the description of the general behavior of experimental total cross-sections of the neutron radiative capture on ^{11}B to the GS.

As the GS is compared to the $^3P_1$ level, it is possible to consider $E1$ transitions from nonresonance to 1.0 MeV $^3S_1$ scattering wave, for example, with zero potential to the GS of ^{12}B

1. $$^3S_1 \rightarrow {}^3P_1.$$

The $E1$ transition to the first ES $^3P_2$ at 0.95 MeV from the resonance at 20.8 keV $^3D_3$ scattering wave (the first resonance) is also possible

2. $$^3D_3 \rightarrow {}^3P_2.$$

Therefore, the transitions from other nonresonance ^3D scattering waves to any BSs (GS or ES) practically do not contribute to the summarized total cross-sections and transitions, which are not considered.

Furthermore, the $E1$ transition to the third ES $^3S_1$ at 2.62 MeV will be considered from the resonance $^3P_2$ wave at 0.43 MeV (the second resonance), as well as the nonresonance $^3P_1$ and $^3P_0$ waves

3. $$^3P_2 \rightarrow {}^3S_1,$$
$$^3P_1 \rightarrow {}^3S_1,$$
$$^3P_0 \rightarrow {}^3S_1.$$

Another $E1$ transition is possible from the nonresonance $^3S_1$ scattering wave to the first ES $^3P_2$ at an energy of 0.95 MeV

4. $$^3S_1 \rightarrow {}^3P_2$$

We will also consider the nonresonance $E1$ transition at energies lower than 1.0 MeV from the $^3S_1$ scattering wave to the fourth ES $^3P_0$ of ^{12}B in the n^{11}B channel at 2.72 MeV

5. $$^3S_1 \rightarrow {}^3P_0$$

The $E1$ transition is also possible between the second $^3P_2$ scattering resonance state at 0.43 MeV and the second $^3D_2$ excited state at 1.67 MeV

6. $$^3P_2 \rightarrow {}^3D_2,$$

In addition, it is possible to consider the $M1$ transitions to the GS from the resonance $^3P_2$ scattering wave at 0.43 MeV

7. $$^3P_2 \rightarrow {}^3P_1.$$

Furthermore, the $M1$ transition from the resonance will be considered at 0.43 MeV $^3P_2$ scattering wave to the first $^3P_2$ ES at 0.95 MeV

8. $$^3P_2 \rightarrow {}^3P_2.$$

Finally, we will consider $M1$ transition to the third $^3S_1$ ES at 2.62 MeV from the nonresonance in the considered energy range of $^3S_1$ scattering wave

9. $$^3S_1 \to {}^3S_1.$$

The cross-section of such processes, if zero potential of scattering the potential (3.2.9) obtained for the third ES is used, is small and does not significantly contribute to the summarized total calculated cross-sections.

In addition, the $M1$ process from the first $^3D_3$ resonance has been considered at 20.8 keV to the second $^3D_2$ ES at 1.67 MeV

10. $$^3D_3 \to {}^3D_2,$$

This does not make a significant contribution to the summarized total cross-sections of the neutron radiative capture on ^{11}B.

To use $M1$ transitions as Nos. 8 and 9, i.e., for transitions between identical partial waves and identical potentials in continuous and discrete ranges, the cross-section of these processes approach zero. In a numerical form, such cross-sections have a value of order 10^{-10} μb. It follows from the form of matrix elements (1.6.3) of the electromagnetic $M1$ transitions, which are simply overlap integrals of wave functions of the initial and final states. A similar situation was previously considered in the n^{10}B system for some $M1$ transitions.

The construction methods used here for intercluster partial potentials at given orbital L and total J moments were discussed in Chapter 1 of this book as well as in previous studies [12, 14, 136, 178]. In the given calculations, the mass value of ^{11}B of 11.0093052 amu was used [214], the neutron mass is specified in Chapter 1 (§1.6).

3.2.2 Interaction n^{11}B potentials

For all n^{11}B potentials, the Gaussian form given in Chapter 1 (1.2.2) was used. Now, we will determine the potential parameters for the GS, of all excited and resonance states of the n^{11}B system of ^{12}B, considering their triplet states with spin $S = 1$. First, we will consider the n^{11}B scattering potentials, which can correspond to some resonance levels of ^{12}B in the cluster n^{11}B channel.

For the potential of the first resonance $^3D_3$ waves at 20.8 keV with the bound FS and unbound AS, it is possible to use the parameters of the form

$$V_{D3} = -129.305 \text{ MeV}, \ \gamma_{D3} = 0.1 \text{ fm}^{-2}, \tag{3.2.1}$$

which lead to the scattering phase shifts shown in Fig. 3.2.1 and give the resonance at 20.9(1) keV with the width less than 1 keV, which well coincides with published data [228].

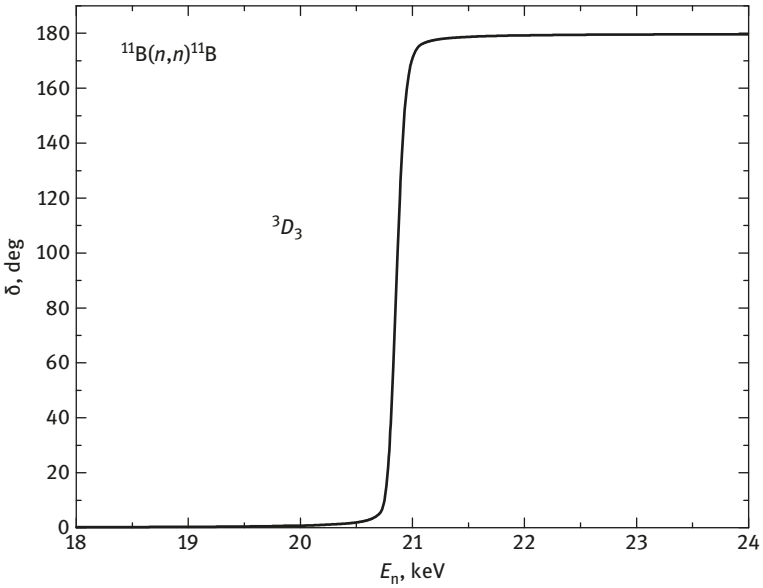

Fig. 3.2.1: The n^{11}B phase shift of the elastic $^3D_3$ scattering with the resonance at 20.9(1) keV.

For the potentials of nonresonance $^3D_2$ and $^3D_1$ scattering waves only with the bound FSs, it is possible to use the following parameters

$$V_{D1/2} = -78.0 \text{ MeV}, \ \gamma_{D1/2} = 0.1 \text{ fm}^{-2}, \tag{3.2.2}$$

which lead to the phase shifts for the $^3D_2$ and $^3D_1$ scattering states less than 0.1° at energies of up to 1.0 MeV.

For the potential of the second resonance in the $^3P_2$ wave at 0.43 MeV in a continuous spectrum with the bound FS and unbounded AS, the following parameters can be obtained

$$V_{P2} = -11806.017 \text{ MeV}, \ \gamma_{P2} = 15.0 \text{ fm}^{-2}. \tag{3.2.3}$$

With such potential, the resonance energy of the level is 430(1) keV with width of 37 (1) keV, which well coincides with the experimental data [228]. For this energy, the scattering phase shift was 90.0°(1). The $^3P_2$ phase shift is shown in Fig. 3.2.2 denoted by the solid curve.

Here, it is necessary to remember that, if the potential contains $N + M$ forbidden and allowed bound states, it obeys the generalized Levinson theorem [11] and its phase shift at zero energy starts from $\pi (N + M)$ [11,20]. However, in Figs. 3.2.1 and 3.2.2,

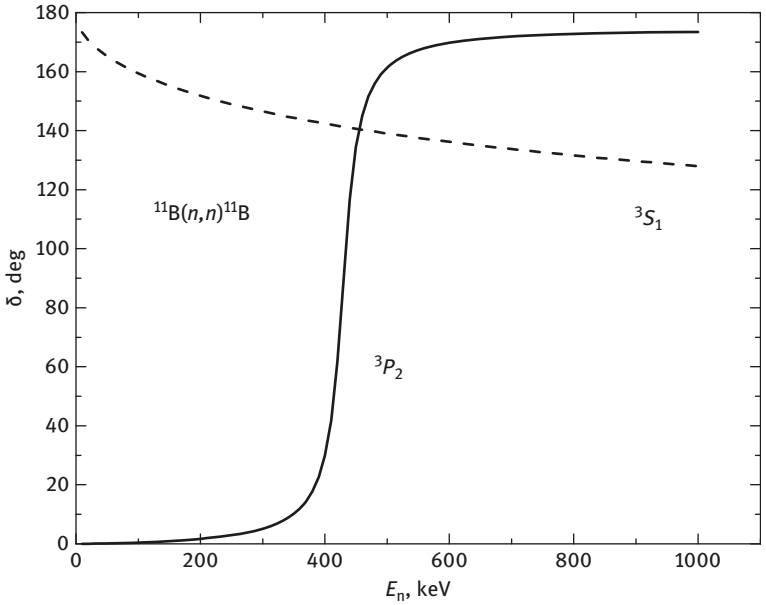

Fig. 3.2.2: The n^{11}B phase shift of the elastic $^3P_2$ scattering with resonance at 430 keV.

the P and D of scattering phase shifts are shown from zero for the usual representation of results.

For potentials of nonresonance $^3P_0$ and $^3P_1$ scattering waves with the bound FSs, it is possible to use the following parameters

$$V_{P01} = -11000.0 \text{ MeV}, \ \gamma_{P01} = 15.0 \text{ fm}^{-2}. \tag{3.2.4}$$

Such potential leads to the scattering phase shifts less than 0.5° at energies ranging up to 1.0 MeV.

Now, we will progress to the construction of the potentials of BSs of ^{12}B in the n^{11}B channel considered above. For potential $^3P_1$ GS with the bound FS and bound AS of ^{12}B in the n^{11}B cluster channel, the following parameters are obtained

$$V_{g.s.} = -3183.6365 \text{ MeV}, \ \gamma_{g.s.} = 4.0 \text{ fm}^{-2}. \tag{3.2.5}$$

Such potential allows to obtain the mass radius as $R_m = 2.36$ fm, and charge radius as $R_{ch} = 2.41$ fm, the binding energy of –3.3700 MeV at an experimental value of –3.370 MeV [228], and accuracy ε by the finite-difference method of 10^{-4} MeV [24,261]. The asymptotic constant (1.2.5) in the dimensionless form [94] is 0.43(1) at an interval of 2–14 fm. The calculation error of the constant is defined by averaging on the specified intervals of distances. The scattering phase shift for such potential smoothly reduces to 178° when energy changes to 1.0 MeV. The ^{11}B radius is specified in the previous

chapter, and the ^{12}B radius should not differ strongly from ^{11}B and ^{12}C radii; the last is known as 2.4702(22) fm [214].

For the asymptotic coefficient of the ground state of ^{12}B in the cluster n^{11}B channel in [215], a dimensional value of 0.245 fm^{-1} or 0.495 fm$^{-1/2}$ was obtained. In [215], another definition of the AC (1.7.2), which differs from our C_w by the value $\sqrt{2k_0}$ (1.2.5), in this case being 0.88 for the GS, was used. Therefore, in a dimensionless form at $S_f = 1$ of (1.7.1), the value of AC was 0.56, which did not significantly differed from an asymptotic constant for the potential specified above (3.2.5).

The known ratio (1.7.1) and the spectroscopic factor can be used; their values for the GS of ^{12}B is given, for example, in the review [228] and is 1.1(2). Thus, we have $A^2_{NC} = 0.245$ fm^{-1} and at $S_f = 1.1$, we obtain $C = 0.472$ fm$^{-1/2}$ (1.7.2). Consequently, for the dimensionless AC (1.2.5) C_w, a value of 0.54 has been obtained. As the spectrofactor ranges from 0.9 to 1.3, the C_w values also range from 0.49 to 0.59, with an average value of 0.54.

As the second variant for the potential of the GS we use the following parameters, which describe an average asymptotic constant [215,228]

$$V_{g.s.} = -1606.331 \text{ MeV}, \ \gamma_{g.s.} = 2.0 \text{ fm}^{-2}. \tag{3.2.6}$$

With such a potential, AC = 0.55(1) at an interval of 2–16 fm, the charge radius is 2.37 fm and mass radius is 2.41 fm at a binding energy of −3.3700 MeV with an FDM accuracy of 10^{-4} MeV [24]. The scattering phase shift of such potential smoothly reduces to 178° with increase in energy up to 1.0 MeV.

For parameters of the $^3P_2$ potential with the forbidden bound state of the first ES of ^{12}B in the n^{11}B channel at $J^\pi = 2^+$, the following values have been obtained

$$V_{P2} = -3174.75797 \text{ MeV}, \ \gamma_{P2} = 4.0 \text{ fm}^{-2}. \tag{3.2.7}$$

With such a potential, the binding energy of −2.4169 MeV is obtained at an FDM accuracy of $\varepsilon = 10^{-4}$ MeV, which is consistent with the experimental value of −2.41686 MeV [228], charge radius of 2.41 fm, and AC of 0.38(1) at an interval of 2–14 fm.

The AC for this ES have been reported to be 0.098 fm^{-1} or 0.313 fm$^{-1/2}$ are given in work [215], and after recalculation to the dimensionless value with $\sqrt{2k_0} = 0.81$, a value of 0.386 can obtained, which is consistent with the value obtained for the potential (3.2.7). The scattering phase shift for such potential smoothly reduces to 177° on increasing energy up to 1.0 MeV.

For the parameters of the $^3D_2$ potential of the second ES at 1.67 MeV with the bound FS and $J^\pi = 2^-$, the following parameters are obtained

$$V_{D2} = -5187.0744 \text{ MeV}, \ \gamma_{D2} = 4.0 \text{ fm}^{-2}. \tag{3.2.8}$$

In such conditions, binding energy of –1.6964 MeV is found at an FDM accuracy of $\varepsilon = 10^{-4}$ MeV, which is consistent with the experimental value of –1.69635 MeV [228]; AC is 0.033(1) at an interval of 2–12 fm, charge and mass radii are 2.41 fm and 2.33 fm, respectively. The scattering phase shift for such potential is almost 180° when energy changes from 0 to 1.0 MeV.

For the parameters of the $^3S_1$ potential without the forbidden states of the third ES at 2.62 MeV of ^{12}B in the n^{11}B channel with $J^\pi = 1^-$, the following values of parameters have been obtained

$$V_{S1} = -266.3015 \text{ MeV}, \ \gamma_{S1} = 4.0 \text{ fm}^{-2}. \tag{3.2.9}$$

Such potential leads to a binding energy of –0.7492 MeV at an FDM accuracy of $\varepsilon = 10^{-4}$ MeV, which is consistent with the experimental value [228]; the charge radius is 2.43 fm and the dimensionless AC is 1.07(1) at an interval of 2–30 fm. The scattering phase shift with such potential is shown in Fig. 3.2.2 by the dashed curve; it smoothly reduces to 130– at energy of up to 1.0 MeV.

For parameters of the $^3P_0$ potential with the bound FS of the fourth ES at 2.72 MeV of ^{12}B in the n^{11}B channel with $J^\pi = 0^+$, the following paramters are obtained

$$V_{P0} = -3156.9385 \text{ MeV}, \ \gamma_{P0} = 4.0 \text{ fm}^{-2}. \tag{3.2.10}$$

Such potential gives the binding energy of –0.6470 MeV at $\varepsilon = 10^{-4}$ MeV, which is consistent with the experimental results of [228]; the charge radius is 2.41 fm and the dimensionless AC is 0.25(1) at an interval of 2–24 fm. The scattering phase shift for such potential smoothly reduces to 175° at energy of up to 1.0 MeV.

3.2.3 Total cross-sections of the neutron radiative capture on ^{11}B

To analyze the total cross-sections of the radiative capture, first, $E1$ transition of the form $^3S_1 \to {}^3P_1$ from the $^3S_1$ scattering wave with zero potential to the $^3P_1$ GS (process No.1 in the first paragraph of this section) with the first variant of potential of the GS (3.2.5) was considered. The obtained capture cross-section is shown in Fig. 3.2.3 by the solid curve at an energy range of 10^{-5}–10^3 keV. Furthermore, these results are denoted by the dashed curve at 1–1000 keV, which well describes the experimental results of [232] and [184] in Figs. 3.2.4 and 3.2.5 at an energy of 25 meV (black triangles and squares) and in the energy range of 23–61 keV (open circles) [279].

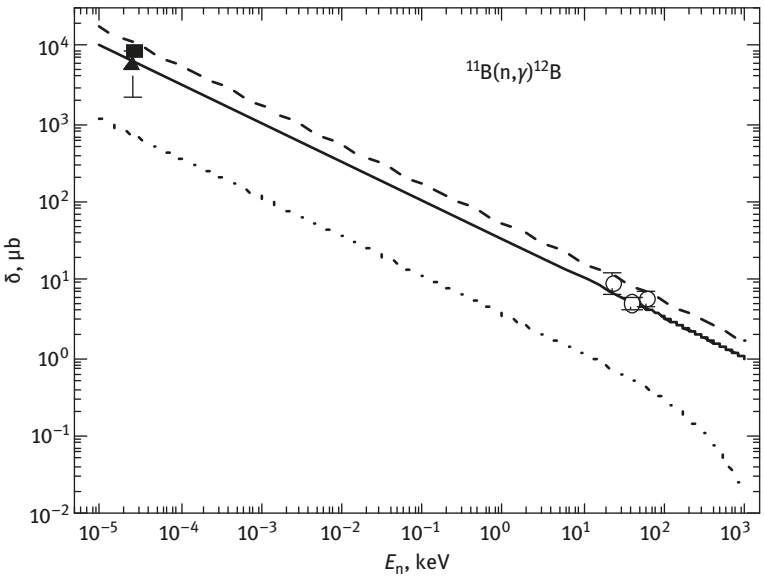

Fig. 3.2.3: Total cross-sections of neutron radiative capture reaction on ^{11}Be for the transition to the GS in the energy range of 10^{-5}–10^{3} keV. Experimental data: black triangle (▲) – from work [232], open circles (o) – total capture cross-sections to the GS from [279], square (■) from work [184]. Curves – calculation results for different electromagnetic transitions with potentials given in the text.

In comparison, in Fig. 3.2.3, the dashed curve show similar results for the same process; however, for the second variant of the GS potential (3.2.6), AC is 0.55, which well coincides with previous studies [215], and zero potential for a $^3S_1$ wave. Here, an increase in cross-sections is observed both at 25 meV and 23–61 keV. These calculations do not agree with [232, 279], but agree with [184]. Therefore, the first variant of the GS potential (3.2.5) should be considered as the most acceptable – its parameters were selected only for correctly describing the cross-section for 25 meV from [232].

Using such parameters without any additional variations or specifications, measurements for the transition to the GS at 23–61 keV [279] have been well described. In other words, the GS potential (3.2.5), because $^3S_1$ potential is, defines the inclination and location of the curve in Fig. 3.2.3, explaining the calculation cross-section of the $^3S_1 \rightarrow {}^3P_1$ transition. Moreover, the AC of the GS potential (3.2.5) does not significantly differ from those reported previously [215, 228]. However, this AC value was obtained 25–35 years ago, being subject to further specification using modern experimental data.

In addition, in Fig. 3.2.3, the dotted curve denotes the calculation results of the total cross-sections with capture to the GS from the $^3S_1$ scattering wavewhen the third ES potential (3.2.9) is sued. Apparently, this cross-section is almost an order of

magnitude lesser than the previous results. The calculation of the cross-section for this variant of the $^3S_1$ wave and the second variant of the GS potential (3.2.6) does not significantly differ from the dotted curve in Fig. 3.2.3. Consequently, at this stage of neutron capture on ^{11}B, unlike the n^9Be system, it is not possible to combine the $^3S_1$ scattering potential with the third ES potential because the parameters of the GS potentials are precisely fixed according to the binding energy and the asymptotic constant at this level.

Furthermore, in Fig. 3.2.4, the dashed-dotted curve denotes the cross-section of the $E1$ transition $^3D_3 \to {}^3P_2$ from the resonance in the range of 20.8 keV and the $^3D_3$ scattering wave with potential (3.2.1) to the first $^3P_2$ ES with potential (3.2.7); process No. 2 described above. The transitions from the nonresonance $^3D_2 \to {}^3P_2$ and $^3D_1 \to {}^3P_2$ waves (3.2.2) to the first $^3P_2$ ES (3.2.7) result in cross-sections smaller than 10^{-3} μb at 1.0 MeV, and do not significantly contribute to the total capture cross-sections.

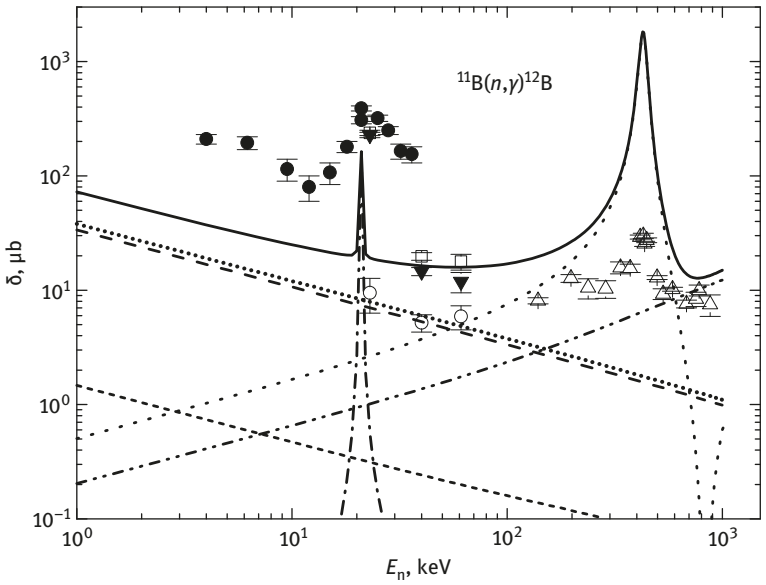

Fig. 3.2.4: Total cross-sections for the neutron radiative capture on ^{11}Be in the energy range of 1–1000 keV taking into account the resonances for transitions No. 1–5. Experimental data: black triangles (▼) – transition to the second ES at –1.6964 MeV from work [279], points (●) – summarized cross-sections from [285], open squares (□) – summarized total cross-sections from [279], open triangles (Δ) – [286], open circles (o) – total capture cross-sections to the GS from [279]. Curves – the calculation results for different electromagnetic transitions with the potentials specified in the text.

The following $E1$ transition flows from the resonance scattering $^3P_2$ wave at 430 keV to the third ES, which is the $^3S_1$ level; process No. 3 discussed above (§3.2.1). The results of this calculation are shown in Fig. 3.2.4 by the dotted curve in the range of 430 keV;

the cross-section exceeds 1 mb and significantly affects the summarized total cross-sections at resonance energy. The cross-sections of transitions from the nonresonance $^3P_1$ and $^3P_0$ scattering waves to the third ES (other processes from No.3) are shown in Fig. 3.2.4 by the dotted-dotted-dashed line, and play a role only at energies of an order or higher than 1.0 MeV.

Transition cross-section from the $^3S_1$ scattering wave with zero potential to the first $^3P_2$ ES (process No.4) are presented by the dotted curve with often located dots, which is parallel to the dashed line for the transition $^3S_1 \rightarrow {}^3P_1$, discussed above in No. 1. The solid curve denotes the sum of all of the $E1$ transitions, described above for the neutron capture on ^{11}B.

Another possible $E1$ transition $^3S_1 \rightarrow {}^3P_0$ with zero scattering potential to the fourth ES (3.2.10) has a cross-section illustrated in Fig. 3.2.4 by short dashes at the very bottom of the figure; process No. 5 discussed above which does not significantly contribute to the total capture cross-sections. The experimental data for total cross-sections of the neutron radiative capture on ^{11}B with transitions to the ground state (open circles) are discussed in [279], and summarized with transitions to all bound states of ^{12}B and total capture cross-sections in [279,285,286].

In Fig. 3.2.5 using similar curves, the cross-sections of transitions No.1,2,4 of §1 are shown, and the results for some additional processes are also presented. Instead of the process No. 3, $E1$ transition of the form $^3P_2 \rightarrow {}^3D_2$ with the scattering potential (3.2.3) to the second ES (3.2.8), i.e., process No. 6, is considered. The cross-section of such transition exceeds 1 mb; moreover, for the $E1$ transition $^3P_2 \rightarrow {}^3S_1$, the cross-section is much higher than the available experimental data, as shown in Fig. 3.2.5 by the dotted curve. The solid curve denotes the sum of four cross-sections specified above. Here, it is necessary to notice that the obtained results can point to an incorrect comparison of the second ES $^3D_2$ wave. This state can be compared to $^5S_2$ level. Here, we do not consider the state with spin $S = 2$. If for this ES the value of the AC is known, more concrete conclusions can be drawn on its relationship with certain partial waves.

The $M1$ transition cross-section from the $^3P_2$ resonance scattering wave for the potential (3.2.3) to the $^3P_1$ of the GS (3.2.5), i.e., process No. 7, is shown by the dashed-dotted curve with often located dashes in the resonance energy range at 430 keV (Fig. 3.2.5). The accounting of the $M1$ transitions from the nonresonance $^3P_1$ and $^3P_0$ scattering waves with potentials (3.2.4) leads to cross-sections of approximately 10^{-2} μb at 1.0 MeV in comparison with the resonance cross-section of 77.5 μb. Therefore, as already mentioned, their contribution can be neglected.

The $M1$ transition cross-section from the resonance $^3P_2$ scattering wave (3.2.3) to the first $^3P_2$ ES with potential (3.2.7), i.e., process No. 8, is shown by the dashed curve with often located dashes. At the resonance energy, the calculated cross-section is approximately 98 μb. These transitions give summarized cross-section of less than 10% from the cross-section considered above $^3P_2 \rightarrow {}^3D_2$ of the $E1$ process No.6. The

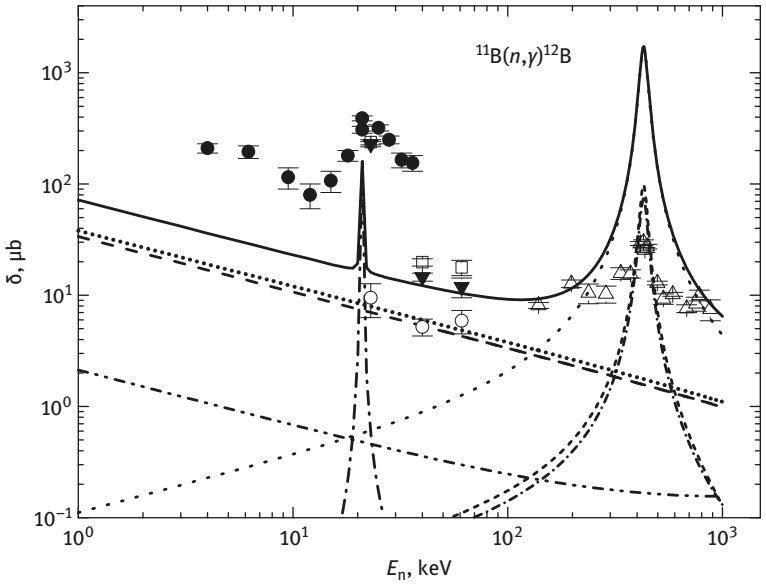

Fig. 3.2.5.: Total cross-sections of the neutron radiative capture reaction on ^{11}Be in the energy range of 1–1000 keV taking into account the resonances for the transitions 6–10. Experimental data: black triangles (▼) – transition to the second ES at –1.6964 MeV from work [279], points (●) – summarized cross-sections from [285], open squares (□) – summarized total cross-sections from [279], open triangles (Δ) – [286], open circles (o) – total capture cross-sections to the GS from [279]. Curves – calculation results for different electromagnetic transitions with the potentials specified in the text.

situation for this transition is similar to the previous n^{10}B system, when for the same potential in the discrete spectrum and in continuous spectrum, different parameters are used.

However, there is no mixing of states according to Young tableaux [11]. Therefore, it is possible to prove the distinction of parameters only by the fact that currently it is not possible to obtain the potential with the bound AS, which leads to the resonance in the $^3P_2$ scattering wave. However, if this can be achieved, then the cross-section of such transitions would simply approach zero because of the orthogonality of wave function with an identical set of the moments of LSJ, as shown for some transitions in the previous system.

The curve designated in Fig. 3.2.5 by a dotted-dotted-dashed line denotes the cross-section of the $M1$ transition from the $^3S_1$ scattering wave with zero potential to the third ES $^3S_1$ at an energy of –0.7492 MeV with potential (3.2.9), i.e., $^3S_1 \rightarrow {}^3S_1$ (process No. 9). This cross-section is 10 times less than the cross-section of the $E1$ transition from the same scattering wave to the GS (3.2.5), as shown by the dashed curve. To use for the scattering potential as the potential of the third ES, such cross-section tend to approach zero, as mentioned previously.

Moreover, $M1$ transitions from all ^3D scattering waves (3.2.1) and (3.2.2), including the first resonance, to the second $^3D_2$ ES (3.2.8) have been considered (process No. 10). The resonance cross-section value reaches 5 μb and does not significantly affect the calculated cross-section, having a value of 144 μb for the $E1$ transition $^3D_3 \rightarrow {}^3P_2$ at resonance of 20.8 keV (process No.2). Other $M1$ transitions from the nonresonance ^3D scattering waves (3.2.2) to the second $^3D_2$ ES (3.2.8) have cross-sections of less than 10^{-5} μb.

From Figs. 3.2.3–3.2.5, it is clear that the cross-sections at 25 meV and 23–61 keV for transitions to the GS are acceptable, and so are the summarized cross-sections in the resonances. However, in the nonresonance range, the experimental results [285] for summarized cross-sections are almost 10 times more than the calculated values. Note that we only know the AC for the GS and the first ES, and their values are nonexistent for all other ESs; therefore, it is necessary to consider these as preliminary calculation results of transitions to the second, third, and fourth ES. It is also possible to note that all available experimental studies [285, 286] were conducted in 1960s, and require further clarification, especially in the field of the resonances.

Because at energies in the range of 10 meV to 10 keV, the calculated cross-section (shown in Fig. 3.2.3 by the solid curve) is practically a straight line, and can be approximated, as before, by the simple function of the form (2.1.3). The value of the given constant A = 33.8364 μb keV$^{1/2}$ was determined by one point in the calculation of cross-sections (solid curve in Fig. 3.2.3) at a minimum energy of 10 meV. The module (2.1.4) of the relative deviation of the calculated theoretical cross-section (σ_{theor}) and approximation (σ_{ap}) of this cross-section by the function given above in the range up to 10 keV is at the level of 0.3%. It can be assumed that this dependence of total cross-section on energy, as in the case of neutron capture on ^{10}B, will hold at lower energies. Therefore, it is possible to estimate the cross-section at energies of 1 μeV (10^{-6} eV = 10^{-9} keV), giving a value of 1.1 b.

Thus, the assumptions about the construction methods of the n^{11}B interaction potentials with FSs are obvious. It allows to obtain acceptable results for describing the available experimental data of the total cross-sections of the neutron capture on ^{11}B to the GS [232, 279, 285, 286] at energies ranging from 25 meV to 61 keV. In general, this cross-section is defined by the $^3S_1 \rightarrow {}^3P_1$ transition No. 1. The possibility of describing these experimental cross-sections allows one to preceisly fix the parameters of potential $^3P_1$ of the GS (3.2.5) rather. Further, based on the processes considered above, in general, the provision of the resonances in total summarized cross-sections of the neutron radiative capture on ^{11}B is described at all considered energies.

Thus, MPCM, along with the potentials for a spectrum of resonance levels and in some partial waves FSs, allows one to describe the behavior of the experimental cross-sections of the neutron capture on ^{11}B to the GS at energies in the range of 10^{-5}–10^2.

Simultaneously, the GS potential is consistent with the main characteristics of ^{12}B in the n^{11}B channel, including the binding energy, charge radius, and AC. Based on the considered $E1$ transitions, the total summarized cross-sections for the resonance energies are also described [287]. However, it is necessary to note that the non-resonance cross sections are not described. Although, the available experimental data of works [232,285,286] designated in Figs. 3.2.3–3.2.5 by the top black triangle, points and open triangles hardly can be approximated by rather smooth curve even in the non-resonance energy range.

3.3 Neutron radiative capture on ^{8}Li

To continue to study the radiative capture, we will now consider the reaction of $n + {}^{8}\mathrm{Li} \rightarrow {}^{9}\mathrm{Li} + \gamma$ within the MPCM framework at thermal and astrophysical energies. Some other calculation results of total cross-sections of this reaction executed using different models and methods, which describe the available experimental data [288], can be found [288,289]. Very few studies have been reported in this area such as [150] and experimental data in [288]. Very few theoretical calculations of cross-sections have been reported [288–290], and the results of these studies considerably differ from each other.

3.3.1 Astrophysical aspects

$n + {}^{8}\mathrm{Li} \rightarrow {}^{9}\mathrm{Li} + \gamma$ reaction can be of significant astrophysical interest as it participates in one of the variants of the primordial nucleosynthesis of the universe and the thermonuclear reactions in supernova of type II [289]. In such synthesis processes, after the formation of nuclei with $A = 7$, another method of formation of elements with $A = 11$, and even higher can be described, for example, with the help of the reactions

$$^{7}\mathrm{Li}(n,\gamma)^{8}\mathrm{Li}(\alpha,n)^{11}\mathrm{B}$$

or owing to less probable $^{7}\mathrm{Li}(\alpha,\gamma)^{11}\mathrm{B}$ [291,292]. However, as shown previously [293], for the neutron capture on ^{8}Li, i.e., the reaction of $n + {}^{8}\mathrm{Li} \rightarrow {}^{9}\mathrm{Li} + \gamma$, it is possible to reduce the quantity of these nuclei in the chain of reactions mentioned above, which can reach 50%. In other words, there are two variants of the primordial synthesis of elements with the mass of $A = 11$–12 and further. Specifically, this synthesis is possible not only because of the reaction chain

$$^{7}\mathrm{Li}(n,\gamma)^{8}\mathrm{Li}(\alpha,n)^{11}\mathrm{B}(n,\gamma)^{12}\mathrm{B}(\beta^{+})^{12}\mathrm{C},$$

but also according to the following reactions [294]

$$^{7}\mathrm{Li}(n,\gamma)^{8}\mathrm{Li}(n,\gamma)^{9}\mathrm{Li}(\alpha,n)^{12}\mathrm{B}(\beta^{+})^{12}\mathrm{C}.$$

The base of this chain is the reaction ^{8}Li(n,γ)^{9}Li. For supernovas of the type II, immediately after collapse, there is an opportunity "to produce" heavy isotopes by the *r*-process. In particular, at the initial expansion stage, the mass gap of elements at $A = 8$ can be eliminated by reactions such as $\alpha + \alpha + \alpha \rightarrow {}^{12}\mathrm{C}$ or $\alpha + \alpha + n \rightarrow {}^{9}\mathrm{Be}$ [295]. However, at this stage, the overcoming of such mass gap is possible through the following chain of reactions [296,297]

$$^{4}\mathrm{He}(2n,\gamma)^{6}\mathrm{He}(2n,\gamma)^{8}\mathrm{He}(\beta^{-})^{8}\mathrm{Li}(n,\gamma)^{9}\mathrm{Li}(\beta^{-})^{9}\mathrm{Be},$$

where the considered here process is presented.

The problem in studying the ^{8}Li(n,γ)^{9}Li reaction lies in the direct experimental measurement of the cross-sections, which is impossible as the half-life of ^{8}Li is too small at 838 ms [294]. Microscopic calculations have allowed us to obtain the rate of this reaction [290,298,299], however, such results differ considerably. For example, in the comparative table from work [300] the reaction rates of the neutron capture on ^{8}Li, the values ranging from 5300 to 790 $\mathrm{cm^3 s^{-1} mol^{-1}}$ are given. Therefore, recently, experimental efforts have been directed to reaction researches ^{8}Li(n,γ)^{9}Li employing indirect approaches, for example, the Coulomb dissociation [301] and (d,p) transfer reactions [294,302].

Consequently, the total cross-sections of the neutron capture on ^{8}Li were obtained [288], which we further used for comparison with our theoretical calculations. Large ambiguities in the study of such reactions using different methods make it an interesting study topic. Therefore, we will consider the reaction of the neutron capture on ^{8}Li within the MPCM [171, 178, 303], and define it as far as the criteria of this model allow the correct description of the total cross-sections of the neutron radiative capture on ^{8}Li at thermal and astrophysical energies, namely from 25.3 meV (1 meV = 10^{-3} eV) up to 1.0 MeV.

3.3.2 Classification of n^{8}Li states according to Young tableaux

For ^{8}Li, as well as for ^{8}Be, the orbital Young tableaux {44} can be accepted; therefore, for the n^{8}Li system we obtain {44} + {1} = {54} + {441}. This shows that in the state with $L = 0$, which will be needed later, there is the FS with tableaux {54}. The allowed state corresponds to the configuration {441} at $L = 1$, i.e., the orbital moment is determined using the Eliot's rule [28]. The first of the obtained tableaux is forbidden because there cannot be five nucleons in the *s*-shell, and the second is allowed and compatible with the orbital moment of $L = 1$, to which the GS of ^{9}Li in the n^{8}Li channel [205] corresponds.

Thus, being limited only by the lowest partial waves with the orbital moment of $L = 0,1$ it is possible to state that, for the n^8Li system ($J^\pi, T = 2^+, 1$ [205] for ^{8}Li) in the potentials of P waves, only AS is present, and in the S-waves bound FS exists. The state in the $P_{3/2}$ wave corresponds to the ground state of ^{9}Li with $J^\pi, T = 3/2^-, 3/2$ and is at the binding energy of the n^8Li system of −4.0639 MeV [205]. Some n^8Li scattering states and BS can be mixed up by spin with $S = 3/2$ ($2S + 1 = 4$) and $S = 5/2$ ($2S + 1 = 6$). However, here, we consider that the GS of ^{9}Li in the n^8Li channel most probably is the $^4P_{3/2}$ level (in designations of $^{(2S+1)}L_J$), though in both spin states for $L = 1$ the total moment of $J = 3/2$ is possible. For clarity, we will consider that in the potentials of the ^4P scattering waves the AS is not bound.

In this case, we have no full tables of products for Young tableaux for the system with more than eight particles [134], which were used earlier for similar calculations [171,178,303]. Therefore, the obtained results should be considered as the quality standard of the possible orbital symmetries in the ground state of ^{9}Li in the n^8Li channel. However, remember that, only on the basis of a similar classification, it was possible to explain the available experimental data on radiative capture of neutrons and other particles for a wide range of 1p-shell nuclei with masses ranging from 3 to 17 [12,14,136,171,178,217,303] as quite acceptable.

Therefore, here, we use the classification of the cluster states according to orbital symmetry, which results in a certain number of FS and AS in the partial intercluster potentials, as well as a certain number of nodes of wave function of the relative motion of clusters – in this case, neutron and ^{8}Li. The quality standard of orbital symmetry allows one to define the existence of the FS in the S wave and the absence of the FS for the P states. Such FS and AS structures in different partial waves allows one to further construct potentials of the intercluster interaction, which are necessary for calculating the total cross-sections of the considered radiative capture reaction.

3.3.3 Structure of the n^8Li states

Now, we will consider the structure of the excited and resonance states of ^{9}Li in the n^8Li channel. Furthermore, we will consider the first excited state, but bound in the n^8Li channel, and the first resonance state of ^{9}Li, as moments and parity are known only for these states [205]. The first ES of ^{9}Li with $J^\pi = 1/2^-$ is at an energy of 2.691(5) MeV, relative to the GS or −1.3729(5) MeV, relative to the threshold of the n^8Li channel. Such a state is the quartet $^4P_{1/2}$ level, and its potential has one bound AS.

The first RS is located at 4.296(15) MeV, relative to the GS or 0.2321(15) MeV, relative to the threshold of the n^8Li channel. For this level $J^\pi = 5/2^-$ [205] is given, which allows to accept $L = 1$ for it, i.e., to consider it as the quartet $^4P_{5/2}$ resonance at 0.261(17) MeV. The width is $\Gamma_{cm} = 100(30)$ keV, as previously mentioned in [205]. According to these data, it is possible to construct the quite unambiguous $^4P_{5/2}$

potential of elastic scattering. Ambiguity of its parameters does not contain the bound FSs or ASs, and is caused only by an error of width of such resonance.

Based on these data, it is possible to consider that the $E1$ capture is possible from the ${}^4S_{3/2}$ scattering wave with the bound FS to the ${}^4P_{3/2}$ GS of ^{9}Li. As we consider the GS with ${}^4P_{3/2}$ and the first ES with ${}^4P_{1/2}$ quartet states, the main contribution gives the transition of the form

1. $$ {}^4S_{3/2} \to {}^4P_{3/2}. $$

For the radiative capture to the first ES, the similar $E1$ transition is possible

2. $$ {}^4S_{3/2} \to {}^4P_{1/2}. $$

As the results of the phase-shift analysis of the elastic $n{}^8$Li scattering could not be successfully determined, several variants of the ${}^4S$ potential with the bound FS and different width will be further considered. Such potentials result in the ${}^4S$ scattering phase shifts close to zero because in the spectra of ^{9}Li there are no ${}^4S$ resonances. The classification presented above allows to determine the existence of the FS, but does not give the chance to establish whether it will be bound in this partial wave.

The GS potentials will be constructed further to describe the channel binding energy, charge radius of ^{9}Li, as well as its asymptotic constant (AC) in the $n{}^8$Li channel. As the known values of the asymptotic normalization coefficient (A_{NC}) and the spectroscopic factors S_{f}, by which the AC is determined (1.7.1), have quite a big error, the GS potentials also have several variants with different width parameters.

In further calculations, the ^{8}Li radius is 2.327 ± 0.0298 fm [214]. For ^{9}Li, the known value of radius is 2.2462 ± 0.0315 fm [214]. In [304], for the radii of these nuclei the following values were reported: 2.299(32) fm for ^{8}Li and 2.217(35) fm for ^{9}Li. In [305], for these radii 2.30(4) fm and 2.24(4) fm, respectively, were obtained. All these data are consistent with each other, even after accouting for errors. For masses of nucleus and neutrons, exact values were used: $m({}^8\text{Li})$ = 8.022487 amu [306]; the mass of the neutron was specified in Chapter of this book (§1.6). The charge radius of neutron approached zero, and its mass radius of 0.8775(51) fm coincided with the known radius of the proton [126]. The spectroscopic factor S_{f} data of the GS and asymptotic normalizing coefficients of A_{NC} are provided in [294]. The magnetic moment of 1.653560 μ_0 for ^{8}Li was given in [307], where μ_0 is the nuclear magneton.

3.3.4 Interaction $n{}^8$Li potentials

As reported previously [171, 178, 303], for the $n{}^8$Li interaction in each partial wave with given orbital moment of L, we used the potential of Gaussian form (1.2.2) with the dotted Coulomb term. The ground state of ^{9}Li in the $n{}^8$Li channel is the ${}^4P_{3/2}$ level, and such potential needs to describe the AC for this channel. To take this constant C

in the form of (1.7.2) or C_w (1.2.5) from the available experimental data, we will consider the data on the spectroscopic factors (S_f) and asymptotic normalizing coefficients of the A_{NC}. For example, in [308] they are given, not only their results, but the data of previous works, which is relatively small for the considered system. If these results are allocated with similar values of the spectrofactor, it is possible to present them in the form of Table 3.3.1.

Table 3.3.1: Data of the S_f spectroscopic factor given for the GS of ^{9}Li in the n^{8}Li channel obtained from previous studoes [308–311].

The reaction from which S_f was defined	Values of spectroscopic factor for the $n + {}^{8}\mathrm{Li}_{g.s.}$ channel	Ref.
^{2}H(^{9}Li,^{3}H)	0.65(15)	[308]
^{2}H(^{9}Li,^{3}H)	0.59(15)	[308]
^{2}H(^{8}Li,^{1}H)	0.90(13)	[309]
^{2}H(^{8}Li,^{1}H)	0.68(14)	[310]
^{9}Be(^{8}Li, ^{9}Li)	0.62(7)	[311]
Average	*0.69*	—
Interval of values	*0.44–1.03*	—

Furthermore, in two known works, the square of the A_{NC} of the GS was defined [294],where A^2_{NC} = 0.92(14) fm^{-1} [A_{NC} = 0.96(8) fm$^{-1/2}$] are obtained and [302], in which A^2_{NC} = 1.33(33) fm^{-1} [A_{NC} = 1.15(14) fm$^{-1/2}$] is given. The average between them is equal to A_{NC} = 1.06 fm$^{-1/2}$ – this value well coincides with the results of a previous review [197]. The calculated value of 1.08 fm$^{-1/2}$ and the experimental value of 1.15 fm$^{-1/2}$ is given for the A_{NC} GS. There are three theoretical values of spectrofactor in the range from 0.6 to 1.1 with an average value of 0.92. Note that in *ab initio* calculations, a spectrofactor value of 0.99 was obtained [312], which is close to the previously reported values [197]. These spectrofactor values are at an interval of the ambiguities of S_f from Table 3.3.1. Consequently, based on the expression (1.7.2) and average S_f from Table 3.3.1, for the AC GS we find C = 1.28 fm$^{-1/2}$ and as $\sqrt{2k_0}$ = 0.915, the dimensionless AC determined as $C_w = C/\sqrt{2k_0}$ is becomes C_w = 1.39(15).

Furthermore, to use the top A_{NC} value of 1.29 fm$^{-1/2}$ from [302] and a lower value of 0.88 fm$^{-1/2}$ from [294], then at average S = 0.69 for the dimensionless constant C_w we will obtain wider interval of values 1.43(27). It is possible to estimate another interval of values of the AC on using the interval given mentioned above for the A_{NC} and the interval for the S_f spectrofactor shown in Table 3.3.1. Then, for the dimensionless C_w, the wider interval of values are obtained as 1.54(58).

Note that the A_{NC} of the GS of ^{9}Li in [206] at S_f of 0.8 is 1.12 fm$^{-1/2}$, i.e., $C = 1.25$ fm$^{-1/2}$ which slightly differs from the average value of the AC given above $C = 1.28$ fm$^{-1/2}$. In [206] for the first ES of ^{9}Li the $A_{NC} = 0.4$ fm$^{-1/2}$ was obtained at $S = 0.55$ that gives $C = 0.54$ fm$^{-1/2}$ or in the dimensionless form of $C_w = 0.77$ at $\sqrt{2k_0} = 0.698$. In [196], for the GS A_{NC} of 1.140(13) fm$^{-1/2}$ was obtained, and for the first ES the A_{NC} is 0.308(7) fm$^{-1/2}$, whichi is generally well coordinated with all previous values.

The GS potential, which allows one to obtain the dimensionless constant C_w close to 1.39 has the following parameters

$$V_{3/2} = -65.788593 \text{ MeV}, \ \gamma_{3/2} = 0.18 \text{ fm}^{-2}. \tag{3.3.1}$$

This gives a binding energy of –4.063900 MeV with an FDM accuracy of 10^{-6} MeV [24], $C_w = 1.40(1)$ on an interval of 5–20 fm, to the mass radius of 2.42 fm and charge radius of 2.36 fm. Remember that the definition of calculation expressions for these radii has been previously given [14,22]. The error of the AC given above is determined by averaging the specified distance intervals. The elastic scattering phase shift of such potential smoothly reduces and at 1.0 MeV has a value of approximately 174(1)°.

Such GS potential has no FS in full accordance with the classification of states according to Young tableaux. The parameters of the GS potential were chosen only for correctly describing the obtained value of the AC as 1.39. However, as it was clear, the A_{NC} and spectrofactor S_f have large errors, therefore, we will consider two more variants of the GS potentials, leading to similar results for binding energy with different AC values.

The has smaller width and parameters

$$V_{3/2} = -71.714957 \text{ MeV}, \ \gamma_{3/2} = 0.2 \text{ fm}^{-2} \tag{3.3.2}$$

This also gives the same binding energy of –4.063900 MeV with an accuracy of 10^{-6} MeV [24], AC of 1.31(1) at an interval of 5–20 fm, mass radius of 2.41 fm, and charge radius of 2.35 fm. The elastic scattering phase shift of such potential smoothly reduces, and at 1.0 MeV has a value of 174(1)°.

Another GS potential is wider than the previous and has the following parameters

$$V_{3/2} = -56.827345 \text{ MeV}, \ \gamma_{3/2} = 0.15 \text{ fm}^{-2}. \tag{3.3.3}$$

This allows us to obtain the same binding energy of –4.063900 MeV with an accuracy of 10^{-6} MeV [24], AC of 1.56(1) at an interval of 5–18 fm, mass radius of 2.44 fm, and charge radius of 2.36 fm. The elastic scattering phase shift of such potential reduces

and at 1.0 MeV has a value of 173(1)°. These three potentials reflect the first interval of errors of determination of the dimensionless C_w = 1.39(15), and potential (3.3.3) corresponds with the last assessment of the average value of the asymptotic constant C_w = 1.54(58).

The potential of the first excited state $^4P_{1/2}$ is obtained by the simple reduction of the depth of the GS potential (3.3.1) and has the following parameters:

$$V_{1/2} = -56.727582 \text{ MeV}, \ \gamma_{1/2} = 0.18 \text{ fm}^{-2}. \tag{3.3.4}$$

This potential leads to the binding energy of –1.372900 MeV with an accuracy of 10^{-6} MeV [24], AC of 0.80(1) at an interval of 5–28 fm, mass radius of 2.53 fm, and charge radius of 2.37 fm. The AC value is consistent with previous studies [206]. The elastic scattering phase shift of such potential reduced and at 1.0 MeV has a value of 168(1)°.

We will describe another variant of potential of the first ES obtained based on (3.3.2)

$$V_{1/2} = -62.433328 \text{ MeV}, \ \gamma_{1/2} = 0.2 \text{ fm}^{-2}. \tag{3.3.5}$$

This potential gives the binding energy of –1.372900 MeV with an accuracy of 10^{-6} MeV [24], AC of 0.76(1) at an interval of 5–30 fm, mass radius of 2.51 fm, and charge radius of 2.37 fm. For this potential, the AC value coincides with previously published results [206]. The elastic scattering phase shift of such potential smoothly reduced and at 1.0 MeV has a value of 169(1)°.

Now, we will consider the criteria of the construction of the potential for the ^4S scattering wave. First, as shown above, such potential need to have a forbidden state, which need not necessarily be bound. Further, as there are no results of the phase-shift analysis of the elastic n^8Li scattering, and in the spectra of ^{9}Li at energy lower than 1.0 MeV there are no resonances of positive parity, we will consider that the $^4S_{3/2}$ potential approaches zero scattering phase shifts at this energy range.

The potential of nonzero depth with the bound FS should be rather narrow to obtain smoothly changing scattering phase shifts close to zero. The parameters of such potential can have the form

$$V_S = -327.0 \text{ MeV}, \ \gamma_S = 1.0 \text{ fm}^{-2}. \tag{3.3.6}$$

The potential leads to the scattering phase shift, as shown in Fig. 3.3.1 by the solid curve, which at energies of up to 1.0 MeV is in the range from +0.03° to –0.12°.

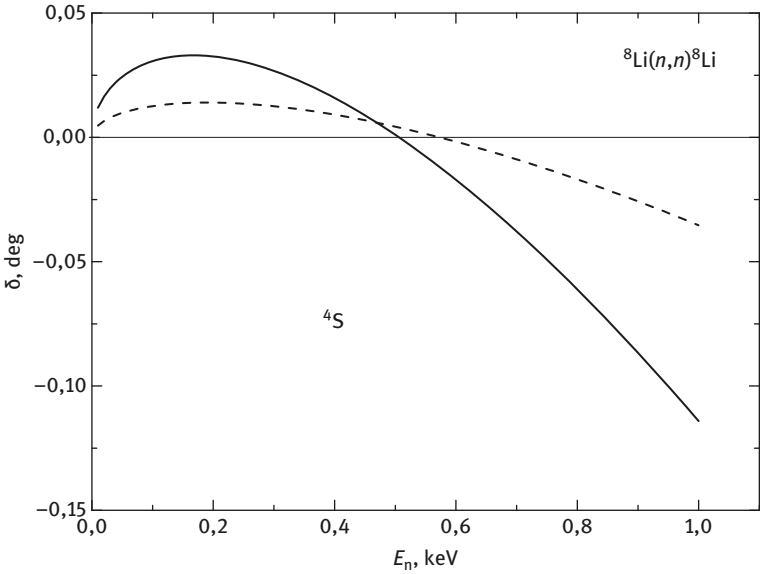

Fig. 3.3.1: The phase shift of the elastic n^8Li scattering in the ^4S wave at low energies. Curves are explained in the text.

The second variant of the scattering potential with the bound FS has the following parameters

$$V_S = -653.5 \text{ MeV}, \ \gamma_S = 2.0 \text{ fm}^{-2}, \tag{3.3.7}$$

Its phase shift is presented in Fig. 3.3.1 by the dashed curve, and at considered energies has values of less than ±0.05°. Except these two variants of the ^4S scattering potential, the variant of such interaction of zero depth will be considered, which leads to the zero scattering phase shifts and does not contain the FS.

The potential without the bound FS for the $^4P_{5/2}$ scattering resonance has the following parameters

$$V_P = -54.446 \text{ MeV}, \ \gamma_P = 0.2 \text{ fm}^{-2} \tag{3.3.8}$$

and leads to the resonance energy of 0.261(1) MeV with the width of Γ_{cm} = 106(1) keV with a scattering phase shift of 90.0°(1) which is consistent with previous studies [205].

3.3.5 Total cross-sections of the neutron radiative capture on ^{8}Li

As discussed earlier, we will consider that the radiative capture for the $E1$ process occurs from the $^4S_{3/2}$ scattering wave (3.3.6) to the $^4P_{3/2}$ of the GS of ^{9}Li in the n^8Li

channel. Our calculations of the total cross-sections for the GS potential (3.3.1) lead to the results shown in Fig. 3.3.2 by the solid curve.

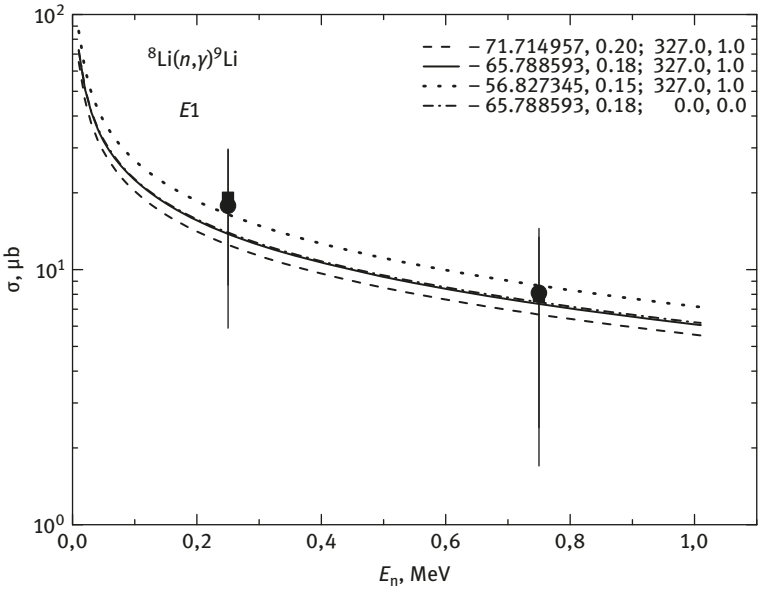

Fig. 3.3.2: Total cross-sections for the radiative ^{8}Li(n,γ)^{9}Li capture to the ground state of ^{9}Li. Black points – the experimental data of [288] to Pb, squares – data from [288] to U. Curves are explained in the text.

The results for the GS potential (3.3.2) are presented by the dashed curve, and for the potential (3.3.3) by the dotted line. In all these calculations for the potential of the elastic scattering, the parameters (3.3.6) were used. As seen from these results, the shape of the cross-sections poorly depend on the GS potential, and all offered variants acceptable reproduce the available experimental data of work [288].

For comparison, the results for the potential ^4S scattering wave of zero depth are given, i.e., without the FS and GS (3.3.1) – the dashed-dotted line in Fig. 3.3.2. They do not differ from the calculation results of the cross-sections for the scattering potential (3.3.6), with the same interaction of the GS (3.3.1) (Fig. 3.3.2, solid curve).

Now, we will present the calculation results of the total cross-sections of the radiative capture for the potential of the $^4S_{3/2}$ scattering wave (3.3.7). All are presented in Fig. 3.3.3 – curves are designated similar to Fig. 3.3.2. It is clear that total capture cross-sections not only poorly depend on the potential of the ground state but do not depend on the form and depth of scattering potential; moreover,

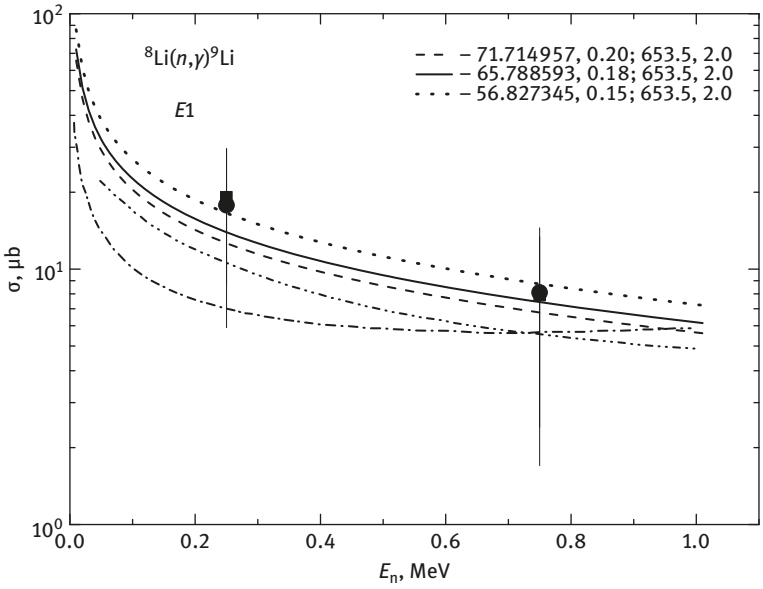

Fig.3.3.3: Total cross-sections for the radiative ^{8}Li(n,γ)^{9}Li capture to the ground state of ^{9}Li. Black points – experimental data of [288] to Pb, squares – data from [288] to U. Curves are explained in the text.

such potential does not necessarily has the bound FS – only zero scattering phase shifts is important.

In Fig. 3.3.3 the dashed-dotted curve shows the calculation results of such cross-sections from work [289], which are based on the Coulomb dissociation of ^{9}Li. We will notice that in [288] results are averaged at energies of 0–0.5 and 0.5–1.0 MeV. Additionally, in work [288], only the upper limit of the capture cross-sections is given, therefore, the results [289] well describe the such experimental data. Furthermore, the dotted-dotted-dashed line in Fig. 3.3.3 presents the results of work [299] based on the microscopic cluster model. These results slight differ from our results, shown in Fig. 3.3.2 and Fig. 3.3.3 by the dashed curve for the GS of ^{9}Li with parameters (3.3.2).

Our calculation of the E1 cross-section for the potential of the GS (3.3.2) and scattering (3.3.7) at thermal energy of 25.3 meV gives a value of 41.3 mb. Such calculation results as a function of energy in the range of 25 meV–1.0 MeV are shown in Fig. 3.3.4 by the solid curve. For the same GS potential and scattering potential (3.3.6), the thermal cross-section has a value of 41.2 mb, and for the potential of scattering of zero depth without FS, a value of 41.4 mb was obtained. Note that, in [299], for the total cross-section at thermal energy, the slightly smaller value of 37.9 mb is given.

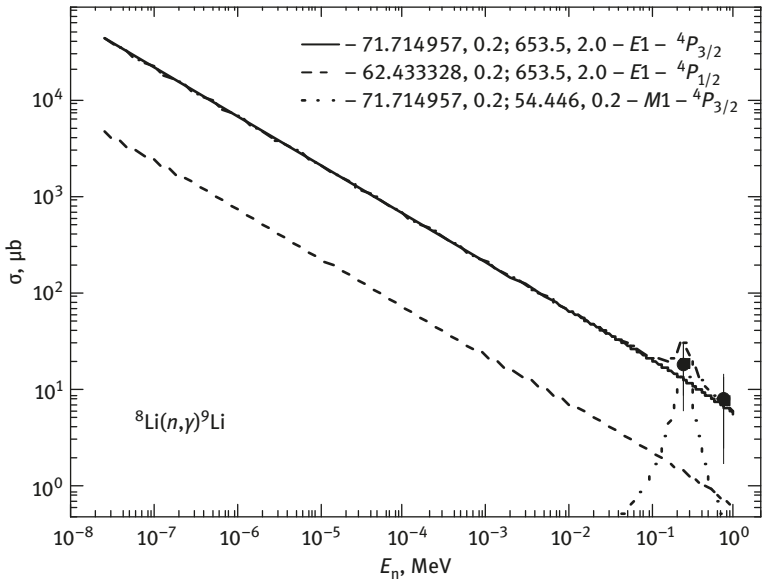

Fig. 3.3.4: Total cross-sections for the radiative ^{8}Li(n,γ)^{9}Li capture to the ground state of ^{9}Li. Black points – experimental data of [288] on Mb, squares – data from [288] on U. Curves are explained in the text.

The cross-section of the $E1$ transition to the first ES with potential (3.3.5) and scattering potential (3.3.7) is given in Fig. 3.3.4 by the dashed curve and at thermal energy of 25.3 meV has much more smaller value of 4.5 mb. For the potential of the first ES (3.3.4) and scattering potential (3.3.7), a little bigger value of the cross-section of 4.9 mb was obtained. Thereby, in the range of up to 1.0 MeV, this cross-section has values of almost 10 times less than that for the transition to GS.

In Fig. 3.3.4 the cross-section of the $M1$ transition $^4P_{5/2} \to {}^4P_{3/2}$ from the resonance scattering wave with potential (3.3.8) to the GS with potential (3.3.2) is shown by the dotted curve. The dashed-dotted curve with the resonance in the range of 0.26 MeV presents the summarized cross-section of the $E1$ and $M1$ transitions to the GS. From these results, it is clear that the accounting of the $M1$ transition leads to small resonance in the cross-sections, which, at such large errors of measurements does not significantly influence their value. The additional accounting of the $E1$ transition to the first ES $^4P_{1/2}$ increases the total summarized cross-sections approximately by 10%, leading to the thermal cross-sections of approximately 46 mb.

Furthermore, in Fig. 3.3.5 the solid curve denotes the reaction rate $N_A\langle\sigma v\rangle$ of the neutron capture on ^{8}Li, which corresponds to the solid curve in Fig. 3.3.2 and is presented in form (1.6.4) [15]. The cross-sections were integrated in the energy range of 0.1 keV–2 MeV, and expansion of this interval led to the change of the reaction rate

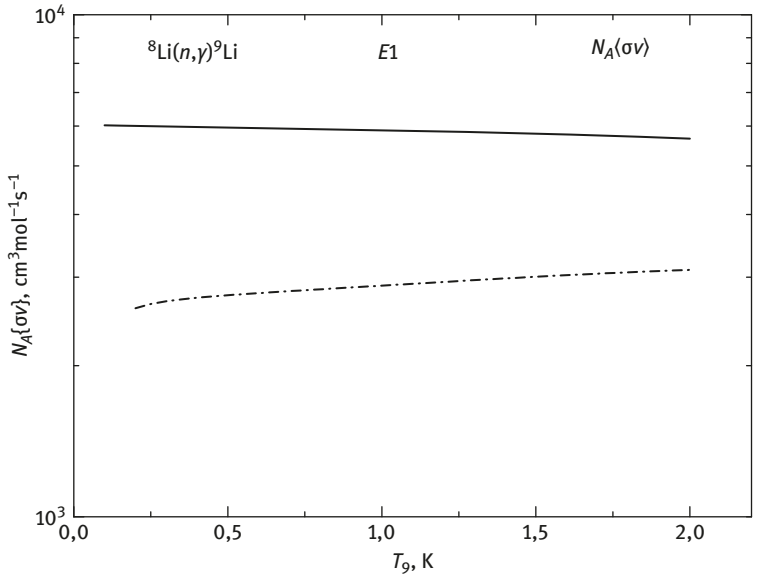

Fig. 3.3.5: Reaction rate of the neutron capture on ^{8}Li. Curves are explained in the text.

to no more than 1%. Here, the dashed-dotted line denotes the reaction rate for the results of work [289], the cross sections of which are presented in Fig. 3.3.3 by the dashed-dotted curve. In Figs. 3.3.3 and 3.3.5, the difference in total cross-sections and reaction rates is seen for these results.

Earlier we obtained all potentials of the ^4P waves, which can be used both for calculating the characteristics of the BSs, as well as elastic scattering phase shifts. Now, they can be used for considering the $E2$ transitions from the scattering states to the GS of the form

1. $$^4P_{1/2} \to {}^4P_{3/2}$$

2. $$^4P_{3/2} \to {}^4P_{3/2}$$

3. $$^4P_{5/2} \to {}^4P_{3/2}$$

In addition, the $E2$ capture to the first ES

4. $$^4P_{3/2} \to {}^4P_{1/2}$$

5. $$^4P_{5/2} \to {}^4P_{1/2}$$

The calculation results of total summarized cross-sections for the $E2$ transitions from all ^4P scattering wave to the GS are shown in Fig. 3.3.6 by the dashed-dotted curve. For process No. 1 with the scattering potential in the $^4P_{1/2}$ wave (3.3.5) and in the GS

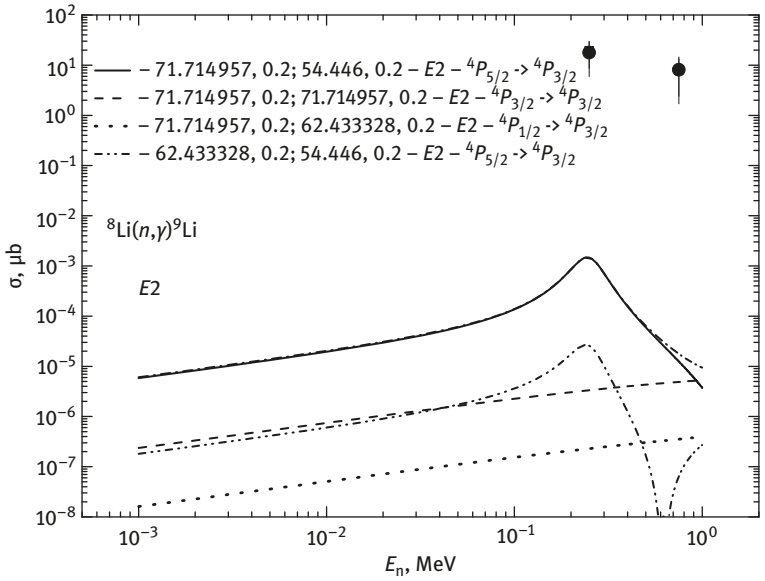

Fig. 3.3.6: Total cross-sections for the radiative ^{8}Li(n,γ)^{9}Li capture to the ground state of ^{9}Li. Black points – experimental data from work [288] on Pb, squares – data from [288] on U. Curves are explained in the text.

(3.3.2), the results are presented by the dotted curve. Transition No. 2 with the GS potentials (3.3.2) in continuous and discrete spectrum is denoted by the dashed line. Process No. 3 with the $^4P_{5/2}$ scattering potential (3.3.8) and the GS (3.3.2) is denoted by the solid curve.

Total cross-sections for the transitions to the first ES have a smaller value and for the resonance process No. 5 with scattering potentials (3.3.8) and first ES (3.3.5) are shown in Fig. 3.3.6 (dotted-dotted-dashed line). Thus, it is clear that in the used potential cluster model with the above potentials, the $E2$ transitions considered, even from the resonant $^4P_{5/2}$ wave, do not contribute to the total cross-sections of the neutron radiative capture on ^{8}Li.

At energies ranging from 25.3 meV to 100 keV, the calculation cross-section is a straight line (the solid curve in Fig.3.3.4), which can be approximated by the simple function in the form (2.1.3) [178,303]. Constant value of A = 207.8550 μb keV$^{1/2}$ was determined by one point in the calculation of cross-sections at minimum energy of 25.3 meV. The module of the relative deviation (2.1.4) of the calculated theoretical cross-section (σ_{theor}) and the approximated (σ_{ap}) cross-section using function (2.1.3) in the range to 10 keV has a value less than 0.2%, which increases to 1.5–2.0% when energy is increased up to 100 keV.

It can be assumed that this form of dependence of total cross-section on energy will also remain at lower energies. Therefore, based on the given expression for the

approximation of cross-section (2.1.3), it is possible to assess cross-section, for example, at energy of 1 μeV (1 μeV = 10^{-6} eV), which gives a value of approximately 6.6 b. If zero scattering potential is used for calcuating the cross-section, then the coefficient in expression (2.1.3) for the approximation of calculation results of total sections will be A = 208.1156 μb keV$^{1/2}$. Estimations of the accuracy of approximation of the capture calculation cross-section by function (2.1.3) in this case are at the same level.

Thus, in the MPCM framework, it is possible to construct two-body potentials of the n^8Li interaction, which allow us to describe the available experimental data for total cross-sections of the neutron radiative capture on ^{8}Li at low and ultralow energies correctly. Theoretical cross-sections are calculated from the thermal energy of 25.3 meV to 1.0 MeV and approximated by the simple function by energy, which can be used for calculating the cross-sections at energies ranging at 50–100 keV. The offered variants of the GS potentials of ^{9}Li in the n^8Li channel allow to obtain the AC within the limits, which are available, leading to reasonable description of ^{9}Li radii. Any of the offered variants of the GS potentials allow one to obtain the calculation capture cross-sections, which is consistent with previously reported studies [288]. The calculation results of cross-sections are not sensitive to the number of the bound FSs and to the width of the ^4S scattering potential. The obtained results for total cross-sections and static characteristics of ^{9}Li depend only on the parameters of the GS potential of this nucleus in the n^8Li channel.

Thereby, it is shown that due to the big cauterization of ^{9}Li in the n^8Li channel the simple two-body potential cluster model is not dependent on the FSs in the $^4S_{3/2}$ wave allows to correctly describe the main characteristics of ^{9}Li as poorly bound n^8Li system in the discrete spectrum (binding energy, radii, asymptotic constant for the n^8Li channel) and total cross-sections of the neutron capture on ^{8}Li process. Many of the results obtained earlier [14], and for the majority of the considered reactions, strongly depends on the existence of the bound FS in various partial waves. In this case, the independence of results for total cross-sections from the existence of the bound FS in the $^4S_{3/2}$ wave, which follows from the classification of states according to Young tableaux, is possible to consider, as confirmation of exclusively big cauterization of particles in the n^8Li channel of ^{9}Li.

3.4 Neutron radiative capture on ^{10}Be

To study the processes of the radiative capture, we will consider within the MPCM framework the $n + {}^{10}\text{Be} \rightarrow {}^{11}\text{Be} + \gamma$ reaction at thermal and astrophysical energies. This reaction is included in one of the variants of the chain of the primordial nucleosynthesis of the universe [313]

$$^{8}\mathrm{Li}(n,\gamma)^{9}\mathrm{Li}(\beta^{-})^{9}\mathrm{Be}(n,\gamma)^{10}\mathrm{Be}(n,\gamma)^{11}\mathrm{Be}(\beta^{-})^{11}\mathrm{B}(n,\gamma)\ldots$$

owing to which the elements with a mass of $A > 11$–12 can be formed (see, for example, [294]).

3.4.1 Structure of the n^{10}Be states

For ^{10}Be, as well as for ^{10}B, we accept the Young tableaux {442}; therefore, for the n^{10}Be system we have {1} × {442} → {542} + {443} + {4421} [28, 134]. The first of the obtained tableaux is compatible with the orbital moments of L = 0,2,3,4 and is forbidden because in an *s*-shell there cannot be five nucleons; the second tableaux is allowed and compatible with the orbital moments of L = 1,2,3,4; and the third is also allowed and compatible with L = 1,2,3 [28].

As mentioned above, lack of the product tables of Young tableaux for particle numbers 10 and 11 allow to exactly classify the cluster states in the considered system of particles. However, quality estimation of the orbital symmetries allows one to determine the existence of the FS in *S* wave and lack of the FS for the *P* states. Such structure of the FSs and ASs in the different partial waves allows to further construct the potentials of the intercluster interaction necessary for the calculations of total cross-sections of the considered reaction of radiative capture, as shown in the previous chapters.

Thus, being limited only by the lowest partial waves with the orbital moment of L = 0,1,2, it is possible to state that for the n^{10}Be system (for ^{10}Be is known that $J^{\pi},T = 0^{+},1$ [205]) at potentials of the ^{2}P waves there is only the allowed state, and the forbidden states are available in the ^{2}S and ^{2}D waves. The state in the $^{2}S_{1/2}$ wave with the FS corresponds to the GS of ^{11}Be with $J^{\pi},T = 1/2^{+},3/2$ and is at the binding energy of the n^{10}Be system of −0.5016 MeV [280].

Note that the ^{2}P waves correspond to two allowed {443} and {4421} Young tableaux. This situation is similar to the N^{2}H or N^{10}B systems when the potentials for the scattering processes depend on two Young tableaux, and for the BS only from one [20]. Therefore, we will consider here that the potential $^{2}P_{1/2}$ BS (the first ES) corresponds to one tableaux {443}. For the sake of definiteness, we will consider that for a discrete spectrum the allowed state in the $^{2}P_{1/2}$ wave is bound, and is unbound for the scattering processes. Therefore, the depth of such potential can approach zero. The FS is the bound state for the $^{2}S_{1/2}$ potential of the scattering wave or discrete spectrum in the n^{10}B system.

Now, we will consider the first ES, bound in the n^{10}Be channel and several resonance states (RS) of ^{11}Be [280], which are not bound in the n^{10}Be channel and correspond to the resonance in the n^{10}Be scattering:

1. The first ES of ^{11}Be is at the energy of 0.32004 MeV relatively to the GS with the moment of $J^{\pi} = 1/2^{-}$ or −0.18156 MeV relatively to the threshold of the n^{10}Be

channel. This state can be referred to as the doublet $^2P_{1/2}$ level without the FS (see Fig. 3.4.1.a).

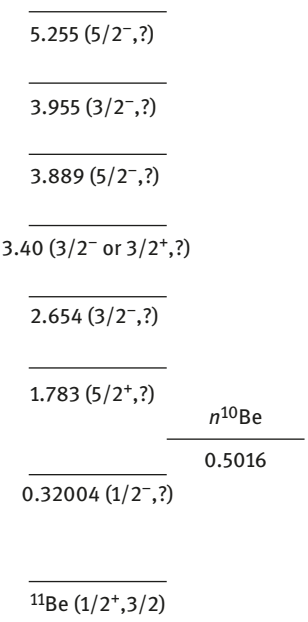

Fig.3.4.1a: Spectrum levels of ^{11}Be in MeV (c.m.) [280].

2. The first RS is located at 1.783(4) MeV, relative to the GS, or 1.2814 MeV, relative to the threshold of the n^{10}Be channel. For this level, the value of $J^\pi = 5/2^+$ [280] is given that allows to accept $L = 2$, i.e., to consider it the $^2D_{5/2}$ resonance in the n^{10}Be system at 1.41 MeV, and its potential has the FS. The width of such resonance is equal to 100(10) keV [280].
3. The second RS has energy of 2.654(10) MeV, relative to the GS, or 2.1524 MeV, relative to the threshold of the channel with the width 206(8) keV and moment $J^\pi = 3/2^-$ [280]. All these characteristics allow one to consider it as the $^2P_{3/2}$ resonance in the n^{10}Be system at 2.37 MeV, and its potential has unbound FS.
4. The third RS at 3.400(6) MeV with the width of 122(8) keV and the moment $J^\pi = 3/2^+$ (or $3/2^-$) [280] that allows $L = 2$, i.e., consider $^2D_{3/2}$ resonance in the n^{10}Be system at 3.19 MeV. However, uncertainty parity of this level is allowed, except $^2P_{3/2}$ state.
5. The next two resonances, shown in Fig. 3.4.1a, were not considered because they have widths of appproximately 10 keV and lower. The resonance at 5.255(3) MeV has the width of 45(10) keV, but is far from our considered range of 5.0 MeV, with energy of 5.23 MeV.

On the basis of these data, it is possible to consider that $E1$ capture is possible from the ^2P scattering waves without the bound FSs or ASs to the $^2S_{1/2}$ GS of ^{11}Be with the bound 3C

1.
$$\begin{matrix} ^2P_{1/2} \to {}^2S_{1/2} \\ ^2P_{3/2} \to {}^2S_{1/2} \end{matrix}.$$

For the radiative capture to the first ES, similar $E1$ transition from the $^2S_{1/2}$ and $^2D_{3/2}$ scattering waves with the bound FSs to the $^2P_{1/2}$ BS without the FS is possible

2.
$$\begin{matrix} ^2S_{1/2} \to {}^2P_{1/2} \\ ^2D_{3/2} \to {}^2P_{1/2} \end{matrix}.$$

The potentials of the GS and first ES will be further constructed to describe the channel binding energy, charge radius of ^{11}Be, and its asymptotic constant in the n^{10}Be channel correctly. As asymptotic normalizing coefficient and spectroscopic factor S_f values are known, asymptotic constant (1.7.2) can be calculated. The AC has a large error, the GS potentials have several variants with different width parameters of width, which strongly influence AC value. Asymptotic normalizing coefficients A_{NC} data have been reported previously [294]. For determining different ACs, we will use the known ratios (1.7.2) and (1.2.5).

In further calculations for the radius of ^{10}Be at GS the value of 2.357(18) fm [314] was used, and for the GS of ^{11}Be the known radius value of 2.463(15) fm [280] was used. The charge radius of neutron is zero, and its mass radius 0.8775(51) fm coincides with the known radius of proton [126]. Moreover, for the charge radius of the first ES of ^{11}Be calculated value of 2.43(10) fm is known [315], and for the GS in the same work 2.42(10) fm was obtained.

For the neutron radius in ^{11}Be, 5.6(6) fm [315] has been estimated. Similarly, in [316], for the neutron radius in the GS is given 7.60(25) fm, and for the first ES 4.58(25) fm. In all calculations, for the masses of nucleus and neutron the exact values were used: $m(^{10}\text{Be})$ = 10.013533 amu [306], and the mass of neutron is specified in §1.6.

3.4.2 Interaction n^{10}Be potentials

For the usual n^{10}Be interaction in each partial wave with the given orbital moment L, we use the potential of the Gaussian form with a Coulomb term (1.2.2). The ground state of ^{11}Be in the n^{10}Be channel is $^2S_{1/2}$ level, and such a potential should correctly describe the AC of this channel. To take this constant from the available experimental data, we will consider the spectroscopic factors and asymptotic normalizing coefficients. The results for the A_{NC}, which are presented in Table 3.4.1, obtained from [294] –some

Table 3.4.1: Data for the A_{NC} of ^{11}Be in the n^{10}Be channel.

Reaction from which A_{NC} was defined	A_{NC} value in fm$^{-1/2}$ for the GS	The A_{NC} value in fm$^{-1/2}$ for the FES	Refs.
(d,p_0) at 12 MeV	0.723(16)	0.133(4)	[294]
(d,p_0) at 25 MeV	0.715(35)	0.128(6)	[294]
(d,p_0) at 25 MeV	0.81(5)	0.18(1)	[313]
	0.68–0.86	*0.122–0.19*	Interval
	0.749	*0.147*	Average $\overline{A}_{NC}$

Table 3.4.2: Data of the spectroscopic factors S of ^{11}Be in the n^{10}Be channel.

The value S for the GS	The value S for the first ES	Refs.
0.42(6)	0.37(6)	[317]
0.72(4)	—	[318]
0.61(5)	—	[319]
0.56(18)	0.44(8)	[320]
0.73(6)	0.63(15)	[321]
0.77	0.96	[322]
0.36–0.79	*0.31–0.96*	*Interval*
0.64	*0.6*	*Average* $\bar{S}$

results from other previous studies are added [313]. Besides, the spectroscopic factors of the n^{10}Be channel of ^{11}Be [280] were successfully determined. Their values are listed separately in Table 3.4.2.

Furthermore, based on (1.7.1) for the GS, we find $\overline{A}_{NC}/\sqrt{\bar{S}} = \bar{C} = 0.94$ fm$^{-1/2}$, and as $\sqrt{2k_0} = 0.546$, thedimensionless AC can be defined as $\bar{C}_w = \bar{C}/\sqrt{2k_0}$ (1.2.5) and (1.7.2) is equal to $\bar{C}_w = 1.72$. However, the interval of values of the spectroscopic factor is so large that the value C_W for average A_{NC} can be in the range of 1.54–2.29. If the errors of A_{NC} are considered, then this interval is possible to be expand to a range of 1.40–2.63.

For the first ES at the value of $\sqrt{2k_0} = 0.423$, we found $\bar{C}_w = 0.45$, and the interval of values $\bar{C}_W$ for average A_{NC} was 0.35–0.62. To consider the A_{NC} errors, this interval extends till 0.29–0.81. These results were further used for constructing GS and FES potentials.

The potential $^2S_{1/2}$ GS with the FS, which allows one to obtain the dimensionless constant C_w close to average value 1.72 has the parameters

$$V_{1/2} = 47.153189\,\text{MeV},\ \ \gamma_{1/2} = 0.1\,\text{fm}^{-2}. \tag{3.4.1}$$

This leads to the binding energy of –0.501600 MeV with an FDM accuracy of calculation of the binding energy of 10^{-6} MeV [24], the AC $C_w = 1.73(1)$ at an interval of 7–30

fm, mass radius of 3.16 fm, and charge radius of 2.46 fm. The errors of the AC, as usual, are determined by averaging the specified distance intervals.

Such GS potential with the FS is in full accordance with the classification of states according to Young tableaux given above and gives the charge radius of ^{11}Be that well coordinates with the data [280]. The parameters of the GS potential were constructed based on the approximate description of the average value of the AC obtained above and equaled 1.72; its phase shift is shown in Fig. 3.4.1b by the solid curve. This potential at the orbital moment of $L = 2$ leads to the resonance ^2D scattering phase shift without spin-orbital splitting, shown in Fig. 3.4.1b by the dotted curve. In the same figure, the $^2S_{1/2}$ phase shifts of the n^{10}Be scattering obtained in the calculation [323] are shown by points.

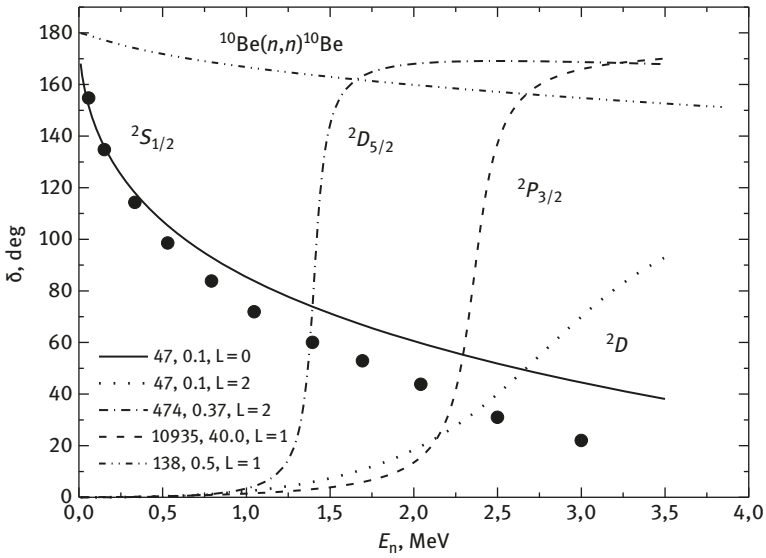

Fig.3.4.1b: The phase shifts of the elastic n^{10}Be scattering in the $^2S_{1/2}$ and ^2D waves. Curves and points are explained in the text.

Let us note that, for the potential of the resonance $^2D_{5/2}$ wave with FS, which will be required for the consideration of the $E2$ transitions, the following parameters were obtained

$$V_{D5/2} = 474.505 \text{ MeV and } \gamma_{5/2} = 0.37 \text{ fm}^{-2}. \tag{3.4.2}$$

The potential leads to the resonance at 1.41 MeV with the width $\Gamma_{c.m.} = 100$ keV which is consistent with the data [280], and its phase shift is shown in Fig. 3.4.1b by the dotted-dashed line.

The $^2P_{3/2}$ potential of the resonance state at the energy of 2.654 MeV with the width of 206(8) keV relatively to GS or 2.37 MeV above the threshold of n^{10}Be channel without FS can have the following parameters

$$V_{P3/2} = 10935.65 \text{ MeV and } \gamma_{1/2} = 40.0 \text{ fm}^{-2}. \quad (3.4.3)$$

It leads to the resonance energy of 2.37 MeV at the width of 204(1) keV, and its scattering phase shift is shown in Fig. 3.4.1b by the dashed line.

For potential of the $^2P_{1/2}$ first ES of ^{11}Be without FS, the following parameters were obtained

$$V_{P1/2} = 138.022609 \text{ MeV and } \gamma_{1/2} = 0.5 \text{ fm}^{-2}. \quad (3.4.4)$$

This potential leads to the energy of –0.181560 MeV with an FDM accuracy of 10^{-6} MeV [24], AC of 0.27(1) at an interval of 10–30 fm, mass radius of 2.61 fm, and charge radius of 2.40 fm. The phase shift of such potential is shown in Fig. 3.4.1b by the dashed-dashed-dotted line. The potential parameters of the first ES (3.4.4) were selected for the correct description of total cross-sections of the neutron capture on ^{10}Be at the thermal energy of 25.3 meV [313], and the value of its dimensionless asymptotic constant approximately lies at an acceptable interval of 0.29–0.81.

Let us note that in work [324] other parameters of this potential are given. In [324], the matrix elements (ME) were evaluated at the distances from zero to 30 fm for calculating the total cross-sections, and its parameters also fitted the description of total cross-section of the neutron capture on ^{10}Be at thermal energy of 25.3 meV from [313]. Hence, it is clear that from the exclusively small value of the GS binding energy and especially the first ES, the calculation of ME need to carry out at big distances. The values of total cross-sections of the capture to the GS and first ES and their precision from the distances of integrity are listed in the below Tables 3.4.3 and 3.4.4.

Table 3.4.3: Value of the total cross-section of the neutron capture on ^{10}Be for transition to the first ES at 1 keV for potential (3.3.4) depending on the final distance at ME integration.

R, fm	σ_{tot}, μb
30	0.15
50	0.83
100	1.43
150	1.45
200	1.45

Table 3.4.4: Value of the total cross-section of the neutron capture on ^{10}Be for transition to the GS at 1 keV for potential (3.3.1) depending on the final distance at ME integration.

R, fm	σ_{tot}, μb
30	0.46
50	0.96
100	1.09
150	1.09
200	1.09

It is clear from that ME is correctly calculated only at distances of 100–150 fm. Therefore, in all further calculations of total cross-sections of this system we use ME integration distance of 150 fm. Consequently, new parameters of potential (3.4.4), which fitted the correct description of the total cross-sections of the neutron capture on ^{10}Be at thermal energy of 25.3 meV. Other potentials do not change, only new potential (3.4.3) was added for considering the resonance in the second transition No. 1, which was not taken into account in work [324].

Let us return to the consideration of the criteria of construction of the $^2P_{1/2}$ scattering wave potential, which can differ from the first ES due to the difference in Young tableaux of these states [11]. Primarily, as it was shown above, such potentials do not have forbidden states. Thus, we do not have results of the phase shift analysis of the n^{10}Be elastic scattering, and in spectra of ^{11}Be at energy lower than 5.0 MeV above the threshold there is no resonance at $J^\pi = 1/2^-$, we will consider that $^2P_{1/2}$ potential practically approaches zero scattering phase shifts in this energy range; therefore, it can have zero depth.

The GS interaction for $^2S_{1/2}$ with FS will be used for $^2S_{1/2}$ scattering potential, i.e., potential (3.4.1), because well agrees with the scattering phase shifts reported in [323], shown by the solid and dot line in Fig. 3.4.1b.

3.4.3 Total cross-sections of the neutron radiative capture on ^{10}Be

As discussed above, we consider that the radiative $E1$ capture No. 1 occurs from the ^2P scattering waves to the $^2S_{1/2}$ of the GS of ^{11}Be in the n^{10}Be channel. The calculation of such cross-sections executed by us for the GS potential (3.4.1) gives the results shown in Fig. 3.4.2 by the solid line. In all these calculations for the $^2P_{1/2}$ potentials of the elastic scattering, the potential of zero depth was used, and for the $^2P_{3/2}$ scattering, the potential with parameters (3.4.3) was used.

The experimental data of the neutron radiative capture on ^{10}Be, shown in Fig. 3.4.2 by the points, are given in work [325] with reference to [326]. As seen from

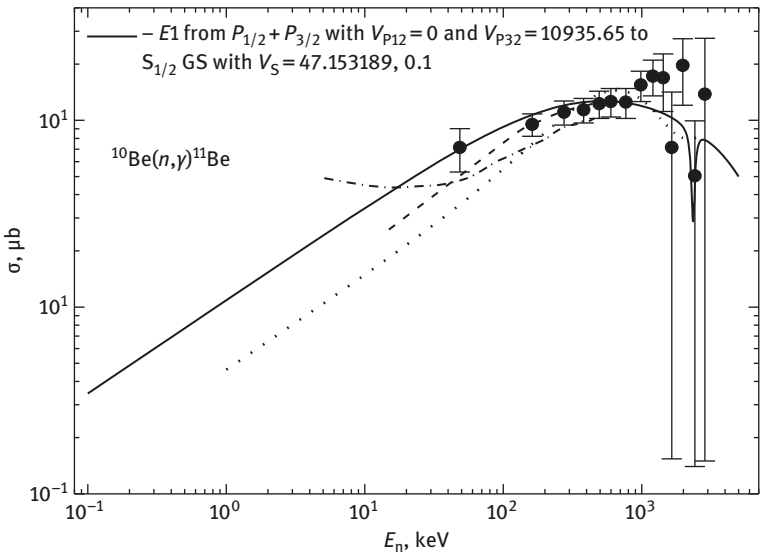

Fig. 3.4.2: Total cross-sections for the radiative ^{10}Be(n,γ)^{11}Be $E1$ capture to the GS. Points – experimental data of [325]. Curves are explained in the text.

these results, the calculated cross-sections describe the available experimental data in the whole energy range. The dashed line in Fig. 3.4.2 shows the results of [325]. The dotted-dashed line shows the results of work [313]. The dotted line shows our previous results [324].

It is seen from Fig. 3.4.2 that at energies of approximately 10 keV and lower, the calculated cross-section shown by the solid line reduces smoothly. It does not allow to describe its value at thermal energy of 290(90) μb, given in work [313]. Therefore, we will further consider the $E1$ transitions to the $^2P_{1/2}$ first ES of $^2S_{1/2}$ and $^2D_{3/2}$ scattering waves. In Fig. 3.4.3, the dashed curve presents the results for the $E1$ transition to the GS with potential (3.4.1) and with the zero $^2P_{1/2}$ scattering potential. The dotted curve shows the cross-sections for the $E1$ transition No.2 from $^2S_{1/2}$ and $^2D_{3/2}$ scattering waves with potential (3.4.1) for $L = 0$ and 2 to the $^2P_{1/2}$ first ES with potential (3.4.4). The solid curve shows the summarized cross-section of these two $E1$ processes, which correctly describe the general course of the available experimental data practically in the entire considered energy range, i.e., from the thermal energy of 25.3 meV to the energy of approximately 3.0 MeV.

The calculated cross-section at the thermal energy was 289 μb. The experimental data at thermal energy are taken from work [313] – triangle about value 290(90) μb and [232] – square, which shows the upper limit of the thermal cross-section os 1 mb.

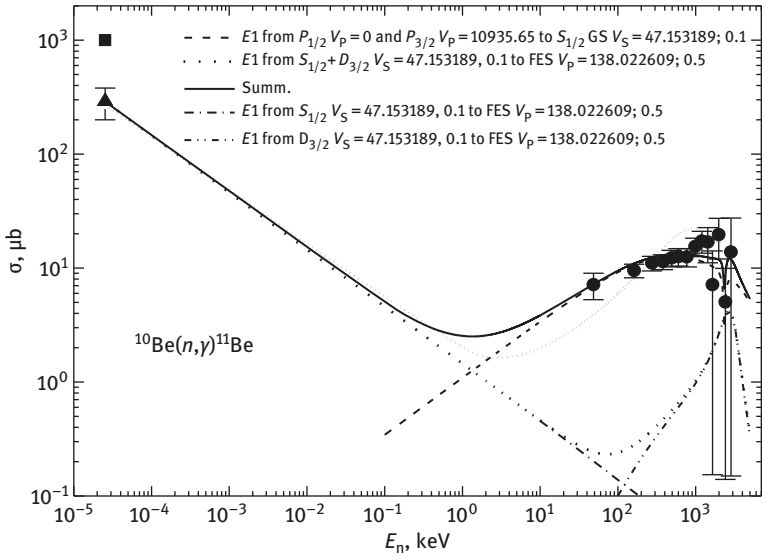

Fig. 3.4.3: Total cross-sections of the radiative ^{10}Be(n,γ)^{11}Be capture. Experimental data from works: [326] – points, [313] – triangle, [232] – square. Curves are explained in the text.

Separate contributions of the first and second transitions No. 2 are shown by the dotted-dashed and dotted-dashed-dashed lines in Fig. 3.4.3. Similar results from our previous work [324] were shown by the frequent dotted line for the GS potential (4.4.1) and the first ES with the following parameters

$$V_{P1/2} = 9.077594 \text{ MeV and } \gamma_{1/2} = 0.03 \text{ fm}^{-2}.$$

Meanwhile, in the capacity of both P scattering potentials for processes No. 1, the interactions of zero depth were used. These potentials lead to cross-sections of 272 μb at thermal energy [324].

The resonance at 2.7 MeV, which is shown by the dotted line in Fig. 3.4.3, is caused by the $^2D_{3/2}$ wave for which potential (3.4.1) is used. As discussed in 3.4.1, the $^2D_{3/2}$ resonance at 3.2 MeV can be located in this wave; however, the parity for this level cannot be determined unambiguously [280]. Therefore, we do not specify the parameters of this potential so that it accurately reproduces the resonance energy of this level.

The cross-section of the possible $M1$ transition from the $^2S_{1/2}$ scattering wave to the GS $^2S_{1/2}$ of ^{11}Be in the n^{10}Be channel with identical potential (3.4.1) in both states will tend to be zero because of the orthogonality of wave functions of continuous and discrete spectra in one potential. The real numerical calculation of such cross-sections leads to the value less than 10^{-2} μb in the energy range from 1 keV to 2.0 MeV, and at energy of 25.3 meV such cross-section appears slightly less than 1% of the cross-section of transition to the first ES shown in Fig. 3.4.3 by the dotted curve.

If to consider the $M1$ transitions from the ^2P scattering waves with zero potential for the $^2P_{1/2}$ and (3.4.3) for the $^2P_{3/2}$ waves to the $^2P_{1/2}$ first ES with potential (3.4.4), then cross-sections do not exceed 0.15 μb in all energy range. For the $E2$ transitions from the $^2D_{3/2}$ wave with potential (3.4.1) at $L = 2$ and the $^2D_{5/2}$ wave with potential (3.4.2) to the GS with $^2S_{1/2}$ even at the resonance energies the value of the cross-sections does not exceed 10^{-3} μb. Thus, it is clear that such transitions do not make a significant contribution to the total cross-sections of the considered process.

Because Fig. 3.4.3 well demonstrates difference in the total cross-sections at thermal energies. The value of 290(90) μb was obtained in [313], and in [232] the upper value of 1 mb was given, i.e., three times as much. Therefore, it is possible to suggest other potential of the first ES, for example, with parameters

$$V_{P1/2} = 28.38357 \text{ MeV and } \gamma_{1/2} = 0.1 \text{ fm}^{-2}.$$

This potential leads to the binding energy of –0.181560 MeV at an FDM accuracy of 10^{-6} MeV [24], AC of 0.45(1) at the interval 7–30 fm, mass radius of 3.01 fm, and charge radius of 2.44 fm. The AC value is within the possible limits of 0.29–0.81 obtained above. The total cross-sections with such potential are shown in Fig. 3.4.3 by the frequent dashed line and at thermal energies it leads to the cross section of 810 μb, i.e., two and a half times more than was obtained for the first ES potential (3.4.4). Consequently, it can be seen that large uncertainty in thermal cross-sections and big interval of possible AC values do not allow one to fix the first ES potential parameters unambiguously.

Furthermore, the reaction rate $N_A\langle\sigma v\rangle$ of the neutron radiative capture on ^{10}Be (solid line) in the range 0.01–5.0 T_9 and the form of (1.6.4) is shown in Fig. 3.4.4. It

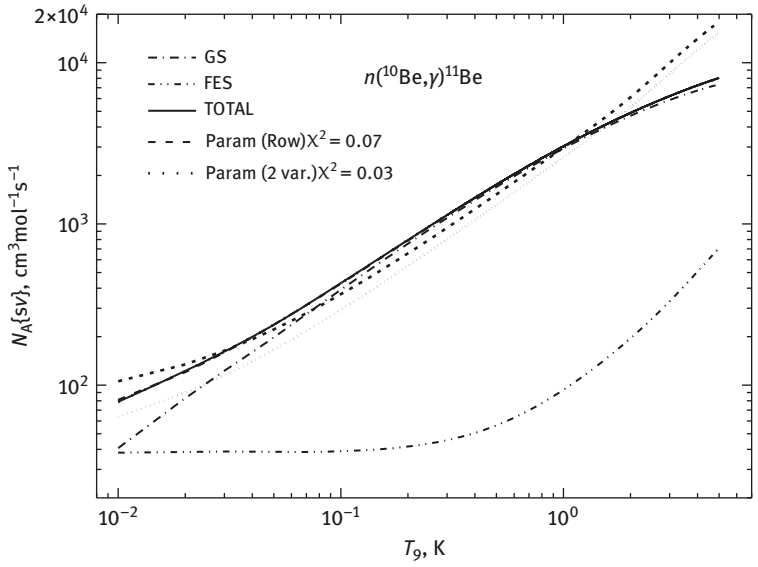

Fig. 3.4.4: The reaction rate of the neutron capture on ^{10}Be. Curves are described in the text.

corresponds to the solid line in Fig. 3.4.3. The total cross-section was calculated in the range 25.3 meV to 5.0 MeV for 5000 points with the period 1 keV. The dotted-dashed line shows the capture rate to the GS, and the dotted-dashed-dashed line shows the capture rate to the first ES.

Frequent dotted line shows the results of approximation of the calculated rate of the considered rate from work [313]. This curve shows slightly lower our results at temperatures smaller than 1.0 T_9. This can be explained by the absence of taking into account cross-sections at the lowest ([313]) cross-sections at energies above 1 keV. Furthermore, in Fig. 3.4.4, frequent dashed line shows the results of reaction rate from work [327], which well agrees with our results.

The solid line in Fig. 3.4.4 in the range 0.01–5.0 T_9 can be approximated by the following expression

$$N_A\langle\sigma v\rangle = \sum_{k=1}^{6} a_k T_9^{k-1}. \tag{3.4.5}$$

with parameters from Table 3.4.5.

Table 3.4.5: Extrapolation parameters of expression (3.4.5).

K	1	2	3	4	5	6
a_k	41.42579	3974.179	−1236.052	305.108	−42.60267	2.40722

Calculation results using these parameters are shown in Fig. 3.4.4 by the dashed line at an average value of $\chi^2 = 0.07$ at 1% error rate calculated from (1.6.4). Increase in expansion up to 7 leads to insignificant change in approximation quality. However, decrease in dimension down to 4 leads to sharp rise of χ^2.

It is possible to use another form of approximation of the calculated reaction rate [328]

$$\begin{aligned} N_A\langle\sigma v\rangle = {} & 10.5445/T_9^{2/3} \cdot \exp(-0.57427/T_9^{1/3}) \cdot (1.0 + 19.5585 \cdot T_9^{1/3} - \\ & 19.5087 \cdot T_9^{2/3} - 110.3739 \cdot T_9 + 883.6600 \cdot T_9^{4/3} - 264.5747 \cdot T_9^{5/3}) \end{aligned} \tag{3.4.6}$$

with $T_9 = 10^9$ K, which leads to $\chi^2 = 0.03$ at 1% errors of the calculated rate. Approximation results are shown in Fig. 3.4.4 by the dotted line.

As the energies from 25.3 meV and, approximately, to 10 eV, the calculated cross-section is a straight line (the solid curve in Fig. 3.4.3), it can be approximated by the simple function from the energy of the form (2.1.3). The value of the constant $A = 1.4522$ μb keV$^{1/2}$ was determined by one point in the settlement sections at the minimum energy equal to 25.3 meV. The module of a relative deviation (2.1.4) of the calculation theoretical cross-section (σ_{theor}) and approximation (σ_{ap}) of this cross-section by the

function (2.1.3) given above in the energy range up to 10 keV is at the level of 0.1%. It is quite real to assume that this form of the dependence of total cross-section on energy will hold at lower energies. Therefore, based on the given expression for approximation of the cross-section (2.1.3), it is possible to estimate the cross-section, for example, at energy of 1 μeV (1 μeV = 10^{-6} eV), which gives a value of approximately about 45.9 mb.

Thus, within the MPCM with the classification of states according to Young tableaux, it is quite possible to construct the potentials of the n^{10}Be interaction, which allows one to describe the general course the available experimental data for the total cross-sections of the neutron radiative capture on ^{10}Be at low and ultralow energies. The theoretical cross-sections are calculated from the thermal energy of 25.3 meV to 3.0 MeV and approximated by the simple function from the energy, which can be used for the calculation of cross sections at energies lower than 10–50 eV. The offered variants of the potentials of the ground and the first excited state of ^{11}Be in the n^{10}Be channel allows one to obtain the AC in the limits, which are available for errors and reasonably describe the radii of ^{11}Be.

Conclusions

The results discussed here show that on the basis of the principles of the MPCM, it is possible to construct the potentials, which allow us to correctly describe the general trend of the total radiative capture cross-sections of nucleons on the nuclei stated above. From these results, it is clear that for describing the experimental data on these reactions, there are enough obvious assumptions about the methods of creation of interaction potentials between nucleon or the lightest cluster and nucleus.

Such potentials have to contain FSs in certain cases, describe the scattering phase shifts or resonance states in the spectra of final nucleus, describe the characteristics of BSs of these nuclei in the considered cluster channels, and obey the classification of the orbital states according to Young tableaux. Thus, the construction methods of such potentials discussed is §1.7 are completely justified.

Conclusion

> *In result of numerous theoretical studies it has been shown that the modified potential cluster model can successfully explain many of the characteristics of light atomic nuclei, the structure of which is represented in two- or three-body channels* [13, 14].

Thus, knowing the calculation methods of the nucleus wave functions in continuous and discrete spectrum, which were given in Chapter 1, it is possible to use them for the calculations of some important characteristics of thermonuclear processes at low and ultralow energies in the modified potential cluster model [24]. However, for the performance of real calculations of nuclear characteristics of thermonuclear reactions, for example, of the cross sections of the radiative capture, at the solution of the Schrödinger equation it is necessary to know the interaction potentials between light atomic particles – clusters, which participate in the considered processes [12, 14]. Any model has some difficulties with the construction of the interaction potentials between particles, which are considered in it. Therefore, in Chapter 1 simple and even obvious criteria have been defined, on the basis of which the quite unambiguous potentials are constructed for the used here modified potential cluster model with the forbidden states [12, 14].

Namely, for the construction of the intercluster potentials of scattering processes the results of the phase shift analysis, which are partially given here and completely in the book [13] are usually used. At impossibility of the carrying out of the phase shift analysis or absence its results in the literature the potentials of the scattering processes are constructed on the basis of spectra of levels of the final nucleus, i.e., the existence of the resonance states of a two-cluster systems is considered. Besides, the classification of the orbital states according to Young tableaux used by us, in the form in which it is considered in the present book, and also described in works [12, 14, 22, 136, 171, 178], allows to define the number of the allowed and forbidden states in the interaction potentials of the nuclear particles.

It means that on the energy of the resonance, knowing the number of the bound states in this partial wave, it is possible to fix unambiguously the depth of the partial potential allowing one to describe the partial elastic scattering phase shift correctly. The form of the elastic scattering phase shift taken from the experiment, especially in the resonance energy range, where the values of the phase shift are sharply changed, allows to fix the width of such potential on the resonance quite unambiguously [12, 14, 136]. Consequently, the parameters of the scattering potential, especially, in the resonance energy range according to the location of the resonance of phase shift or resonance level of the final nucleus and its width are fixed completely unambiguously.

The intercluster potentials of bound in the nucleus states of clusters, which are required for the calculations, for example, of the electromagnetic transitions from the bound state of nucleus to the states of continuous spectrum or on the contrary,

https://doi.org/10.1515/9783110619607-005

usually are constructed on the basis of the description by them some characteristics of the ground or the bound excited states of nuclei in the cluster channels. They have to depend, as a rule, only on one certain Young tableau, i.e., to be pure on orbital symmetry [11, 14, 19, 22]. The depth of potentials of these bound states clearly fixed on the basis of the classification of the FSs and ASs and according to the position of the associated allowed level. The width of the acceptable potential is determined based on the data describing the nuclear characteristics, in particular, the AC of the ground or the bound excited state of the certain channel.

Thereby, the methods used here of obtaining the form and the depth of the intercluster interactions of scattering and BS allow to get rid from the discrete and continuous ambiguity of its parameters [12,14,136], inherent of the known optical model [93], and observed in usual approaches of the construction of intercluster potentials in continuous and discrete spectrum. Subsequently they can be used in any calculations connected with the solving of various nuclear-physics and astrophysical problems at thermal, ultralow and low energies [14,332].

Some variants of such interaction potentials of the Gaussian and Woods-Saxon type for the systems of nuclear particles of NN, N^2H, N^3H, N^3He, N^4He, N^6Li, N^7Li, N^9Be, $N^{10}B$, n^8Li, $n^{10}Be$, $N^{11}B$, $N^{12}C$, $N^{13}C$, $N^{14}C$, $n^{14}N$, $N^{15}N$, $N^{16}O$, $^2H^2H$, $^2H^3He$, $^2H^3H$, $^3H^3He$, $^3H^3H$, $^3He^3He$, $^2H^4He$, $^3H^4He$, $^3He^4He$, $^2H^6Li$, $^4He^4He$, $^4He^{12}C$ and some other have been obtained in original works of authors from SINP MGU and Almaty. Subsequently, they have been systematized, rechecked, specified, tested and given in the following articles, reviews and books, including the present book: [12–14, 19–24, 28, 34, 42, 136, 171, 178, 207, 261, 329–332]. In certain cases at construction of such intercluster interactions the concept of the forbidden and allowed states in the relative movement of clusters, which follows from the classification of orbital states according to Young tableaux [11] was used. It has allowed to get rid from the presence of the repulsive core at small distances, used earlier for the accounting of the effects of antisymmetrization of wave functions [21].

Now we will notice that in the book [13], except the phase shift analysis of the elastic scattering in the 10 systems, quite detailed consideration of the results of three-cluster single-channel model of some light atomic nuclei is given. It, in fact, is directed on the additional control and verification of the concept of the construction of pair intercluster potentials on the basis of the description of elastic scattering phase shifts and characteristics of the bound states in the discrete spectrum [92, 333]. As a result, it is possible to consider, apparently, that the interactions obtained on such basis can be used for calculations of astrophysical S-factors, total cross sections of radiative capture and other nuclear characteristics of thermonuclear processes on the Sun and stars of our Universe [12, 14, 136, 332].

Furthermore, in the second and third chapters of this book the calculation results of total cross sections of the neutron and proton radiative capture on some light nuclei at thermal and astrophysical energies are given in. The calculations of total cross sections of the considered reactions usually are carried out in the energy range

lower than 1.0 MeV and cover 7–9 orders on the energy. The calculation results of total cross sections at lowest energies will be parameterized by the functions of the simple form that facilitates their further application in problems of applied character. The considered reactions are usually included into processes of the primordial nucleosynthesis taking place in the Universe at different stages of its formation and development. Some enter into the CNO Solar cycle or are the accompanying reactions, which although make a smaller contribution, but nevertheless can be present at various variants of chain of the primordial nucleosynthesis, about which it was told, for example, in Chapter 3.

As a result, this book is an attempt to demonstrate certain methods of nuclear physics of low and ultralow, i.e., astrophysical energies, which can be used to calculate certain characteristics of thermonuclear reactions in the Sun, stars and the primordial nucleosynthesis processes of the Universe. It is shown, how on the basis of certain computing methods and the chosen representations of nuclear physics it is possible to obtain the nuclear intercluster potentials allowing to solve further some problems of the description of total cross sections of 15 thermonuclear reactions, which defined the formation and existence of all our Universe observed by us at present time [12, 14, 136, 332].

It is necessary to pay attention that the results only for 15 processes of the neutron and proton radiative capture are given in the this book (process of the proton capture on ^{16}O is given in the Appendix), and all there are 30 cluster systems considered by us earlier on the basis of the modified potential cluster model with classification of orbital states according to Young tableaux. Except this book, the new results for capture of protons and light clusters on the nucleus of 1*p*-cover are given in the book [14] in Russian and [334] in English languages. Is possible to obtain quite acceptable results on the description of the main characteristics of processes of radiative capture of nucleons or lightest clusters on the basis of the carried out classification of cluster states according to Young tableaux within the MPCM. Some properties of these cluster nuclei, their characteristics and the considered cluster channels are given below in the Table C.1 together with references to these results.

At the present moment, in the framework of the MPCM the preliminary results for capture reactions ^{2}H(^{3}He,γ)^{5}Li, p(^{7}Be,γ)^{8}B and n(^{11}B,γ)^{12}B were obtained already, but they are not yet are published in original papers. In such a way, already 33 reactions of the radiative capture form were considered and in all cases it is possible to describe their basic characteristics correctly, including total cross sections.

In conclusion, it is possible to notice that in the electromagnetic processes like the radiative capture or photodisintegration considered here and in books [14, 332, 334], the operator of electromagnetic transitions is well-known [25, 102]. Therefore there is a fine possibility of clarification of the form of strong interaction of two particles in the input channel when they are in a continuous spectrum, and the bound states of the same particles in the output channel, i.e., the states of their discrete spectrum. For example, the colliding particles ^{2}H and ^{4}He at low energies during the radiative

Table C.1: The characteristics of nuclei in the cluster channels and references to works, in which they were considered

No.	(J^{π},T) nucleus	Cluster channel	T_z	T	Reference
1.	^{3}He $(1/2^{+},1/2)$	p^{2}H	$+1/2+0=+1/2$	1/2	[12,14,19,136]
2.	^{3}H $(1/2^{+},1/2)$	n^{2}H	$-1/2+0=-1/2$	1/2	[178,183]
3.	^{4}He $(0^{+},0)$	p^{3}H	$+1/2-1/2=0$	0 + 1	[12,14,19,136,335]
4.	^{6}Li $(1^{+},0)$	^{2}H^{4}He	$0+0=0$	0	[12,14,136]
5.	^{7}Li $(3/2^{-},1/2)$	^{3}H^{4}He	$-1/2+0=-1/2$	1/2	[12,14,136]
6.	^{7}Be $(3/2^{-},1/2)$	^{3}He^{4}He	$+1/2+0=+1/2$	1/2	[12,14,136]
7.	^{7}Be $(3/2^{-},1/2)$	p^{6}Li	$+1/2+0=+1/2$	1/2	[12,14,136,193]
8.	^{7}Li $(3/2^{-},1/2)$	n^{6}Li	$-1/2+0=-1/2$	1/2	[194]
9.	^{8}Be $(0^{+},0)$	p^{7}Li	$+1/2-1/2=0$	0 + 1	[12,14,136]
10.	^{8}Li $(2^{+},1)$	n^{7}Li	$-1/2-1/2=-1$	1	[178,207]
11.	^{9}Li$(3/2^{-},3/2)$	n^{8}Li	$-1/2-1=-3/2$	3/2	[336]
12.	^{10}B $(3^{+},0)$	p^{9}Be	$+1/2-1/2=0$	0 + 1	[12,14,136]
13.	^{10}Be $(0^{+},1)$	n^{9}Be	$-1/2-1/2=-1$	1	[213,220]
14.	^{11}Be$(1/2^{+},3/2)$	n^{10}Be	$-1/2-1=-3/2$	3/2	[324]
15.	^{11}C $(3/2^{-},1/2)$	p^{10}B	$+1/2+0=+1/2$	1/2	[284]
16.	^{11}B $(3/2^{-},1/2)$	n^{10}B	$-1/2+0=-1/2$	1/2	[284,303]
17.	^{12}C $(0^{+},0)$	p^{11}B	$+1/2-1/2=0$	0	[303]
18.	^{12}B (1+,1)	n^{11}B	$-1/2-1/2=-1$	1	[287,303]
19.	^{13}N $(1/2^{-},1/2)$	p^{12}C	$+1/2+0=+1/2$	1/2	[12,14,136]
20.	^{13}C $(1/2^{-},1/2)$	n^{12}C	$-1/2+0=-1/2$	1/2	[178,244]
21.	^{14}N $(1^{+},0)$	p^{13}C	$+1/2-1/2=0$	0 + 1	[12,14,136,141]
22.	^{14}C $(0^{+},1)$	n^{13}C	$-1/2-1/2=-1$	1	[178,244]
23.	^{15}N $(1/2^{-},1/2)$	p^{14}C	$+1/2-1=-1/2$	1/2	[303,337]
24.	^{15}C $(1/2^{+},3/2)$	n^{14}C	$-1/2-1=-3/2$	3/2	[178,253]
25.	^{15}N $(1/2^{-},1/2)$	n^{14}N	$-1/2+0=-1/2$	1/2	[178,253,257]
26.	^{16}O $(0^{+},0)$	p^{15}N	$+1/2-1/2=0$	0	[303]
27.	^{16}N $(2^{-},1)$	n^{15}N	$-1/2+-1/2=-1$	1	[266]
28.	^{16}O $(0^{+},0)$	^{4}He^{12}C	$0+0=0$	0	[12,14,136,338]
29.	^{17}O $(5/2^{+},1/2)$	n^{16}O	$-1/2+0=-1/2$	1/2	[277]
30.	^{17}F $(5/2^{+},1/2)$	p^{16}O	$+1/2+0=+1/2$	1/2	[339]

capture form nucleus ^{6}Li in the ground state and the extra energy is released in the form of y – quantum. Because, in such reactions there is no rearrangement, we can consider the potentials of the same nuclear system of particles, i.e., ^{2}H^{4}He in continuous and discrete spectra. In the latter case, it is believed that with high probability the ground bound state of ^{6}Li is caused by the two-body cluster ^{2}H^{4}He configuration, which is confirmed by numerous studies [11].

Such approach leads to the good results at the description of total cross sections or astrophysical S-factors of all 30 capture reactions considered here and in books [14, 332, 334]. Of course, when the spektrofactor value of S_f defining the probability

of the two-body channel for certain cluster channel, for example, $^{2}H^{4}He$, is close to unit, the use of the MPCM and its results do not raise the doubts. But this situation not always exists and the S_f value not always close to unit, although it has wide data interval. In such cases as it was clear, the MPCM leads to the AC of the BSs nuclei, which will be coordinated with the available results for the ANC and S_f in the considered cluster channels and by that considers the probabilities of these channels.

In certain cases, which have also been considered above, the value of spektrofactor can just be accepted equal to 1. It is possible then to explain the successful application of the simple two-body MPCM, if to consider the temporary picture of the capture process. Usually the used values of the S_f for each two-body channel define the probability of this channel in the nucleus, which is in the stable state. But after flowing the capture reaction lot of time has to pass rather that the nucleus has come to such state. It is quite possible to assume that in the first time points, i.e., right after passing of the reaction, the nucleus with bigger degree of probability ($S_f \sim 1$) is in the channel consisting of the initial particles. In these time points the experimental measurement of the characteristics of such reaction, which are compared then to the results of theoretical calculations, for example, within the MPCM is taken.

This situation is clearly seen on the example of ^{8}Be, which, apparently, does not consist of the $p^{7}Li$ cluster system, and is defined, most likely, the $^{4}He^{4}He$ configuration, disintegrating in this channel [14, 334]. However, it is possible to assume that after the proton radiative capture on ^{7}Li reaction, nucleus ^{8}Be will be, for some time, to be in the bound $p^{7}Li$ channel and only then will pass into the state defined generally by the $^{4}He^{4}He$ configuration. Such assumption will allow to consider ^{8}Be, at least, at the initial stage of its formation in the $p + {}^{7}Li \rightarrow {}^{8}Be + y$ reaction as the cluster $p^{7}Li$ system, to apply for it all MPCM methods and to obtain quite reasonable results at description of the main characteristics of this and other reactions considered here and in books [14, 334].

Perhaps, this can explain the good description of the main characteristics of the similar processes on the basis of the MPCM with $S_f = 1$, the FS containing in the certain cases, the existence of which is defined on the basis of classification of such states according to Young tableaux. And methods of the construction of the potentials of such MPCM taking into account the known FSs and ASs have been in detail described in Chapter 1. As a result, these methods allow one to obtain potentials, which do not contain the ambiguities and allow one to describe the total cross sections of the capture radiative processes for 30 reactions correctly. We will consider this as a first variant of interpretation the successful use of the MPCM for consideration of 30 cluster systems and radiative capture reactions with them.

However, also other explanation, which was used by us in the previous edition of this book [332] is possible. Previously it was thought that, apparently, all effects present in the reaction, including the possibility of the cluster configuration, are taken into account in the construction of the interaction potentials. It is possible

because the potentials are constructed taking into account the structure of FSs and on the basis of the description of observed, i.e., experimental characteristics of the interacting clusters in the initial channel and some nucleus formed in a final state at the description its cluster structure consisting of initial particles. Thereby, the presence of S_f is already implicitly considered in the BS wave functions of clusters defined on the basis of such potentials at the solution of the Schrödinger equation [332]. This is the second possible interpretation of successes of the MPCM.

The problem consist in that in the present time spectrofactor errors and ANC, and also AC, are very large. It does not do unambiguous conclusions about two formulated above assumption. Consequently, both of them appear quite believable.

Afterword

In quantum mechanics, the two-point particle system needs to have a unified Hamiltonian. The potentials of continuous and discrete spectra of such a system should be identical. However, some general criteria ought to be satisfied by the general potential of nuclear interaction. In this book, the condition wherein two-body partial potentials depend on the moments of J, L, S and parity P as well as its Young tableaux $\{f\}$ has been considered. Therefore, potentials for different moments and Young tableaux $\{f\}$ can vary (see §1.7 Chapter 1). Young tableau $\{f\}$ is used as an additional quantum number for characterizing the state of the two-body system [11, 20, 21].

As seen in Table C.2 below, when transitions during radiative capture occur between the states in different partial waves, i.e., with different J, L, S, P and $\{f\}$ values, such states have different potentials. In particular, when $M1$ transitions occur between the states with different values of J, L, S, P, for example for n^7Li (transition number 3 in Table C.2) and n^{10}B (transition numbers 6, 8, and 9 in Table C.2) capture, the potentials corresponding to these partial waves are different.

When the two-body system has different Young tableaux $\{f\}$ for identical states, i.e., with identical J, L, S, P, discrete spectrum, and scattering, potentials are expected to vary [11, 20, 21]. For example, such a condition is observed for neutron capture on ^{2}H (transition number 2 in Table C.2) or ^{10}B (transition number 7 in Table C.2).

At $M1$ transitions between identical partial waves with identical quantum numbers J, L, S, P, $\{f\}$, in all cases except one, it is possible to consider that such transitions lead to zero or tend toward zero capture cross-sections, and hence, can be neglected. Such a condition is seen in n^{11}B (transition numbers 8 and 9 in Table C.2) and in p^{14}C (see [14,334]). Among all 30 capture processes considered here and in [14], only in one case $M1$ transition was seen with identical J, L, S, P, which cannot be neglected – process number 4 (highlighted in bold) during the neutron capture by ^{16}O. This defines the shape of total cross-sections at thermal energies.

To explain such a scenario within the MPCM framework, it is possible that, for particle systems with A > 8, there are no complete product tables of Young tableaux, which were used earlier for particles with smaller masses [134]. As a result, the n^{16}O system can be mixed according to Young tableaux in the scattering states, as observed for neutron capture on ^{2}H (see §2.1) with similar $M1$ transition, which also played a major role at thermal energies.

In conclusion, once again we remind that this book is the revised and updated edition of the previous book by the author titles "Primary Nucleosynthesis of the Universe," published by LAP publishing house in 2014 [332]. In this book, phase-shift analysis and three-body model were excluded. These were separately published in "The Phase Shift Analysis in Nuclear Astrophysics" published by LAP publishing house in 2015 [13].

https://doi.org/10.1515/9783110619607-006

Table C.2: Cluster systems wherein the reactions of radiative capture and *EJ* list or *M*1 transitions for each system have been considered.

No.	System	Transitions from the scattering states $^{(2S+1)}L_J$ to the ground (GS) or excited (ES) state of the final nucleus	
		Chapter 2	
1.	n^2H	E1	1. $^2P_{3/2} + {}^2P_{1/2} \to {}^2S_{1/2}$
		M1	2. $^2S_{1/2} \to {}^2S_{1/2}$
2.	n^6Li	E1	1. $^2S_{1/2} \to {}^2P^{g.s.}_{3/2}$ 2. $^2S_{1/2} \to {}^2P^{e.s.}_{1/2}$
3.	n^7Li	E1	1. $^3S_1 \to {}^3P^{g.s.}_2 + {}^5S_2 \to {}^5P^{g.s.}_2$ 2. $^3S_1 \to {}^3P^{e.s.}_1 + {}^5S_2 \to {}^5P^{e.s.}_1$
		M1	3. $^5P_3 \to {}^5P^{g.s.}_2$
4.	n^9Be	E1	1. $^3S_1 \to {}^3P^1_0 + {}^3P^2_0$ 2. $^3S_1 \to {}^3P^1_2 + {}^3P^2_2$ 3. $^3D_3 \to {}^3P^1_2 + {}^3P^2_2$ 4. $^3P_0 + {}^3P_1 + {}^3P_2 \to {}^3S^{e.s.}_1$
5.	n^{12}C	E1	1. $^2S_{1/2} + {}^2D_{3/2} \to {}^2P^{g.s.}_{1/2}$ 2. $^2P_{1/2} + {}^2P_{3/2} \to {}^2S^{e.s.}_{1/2}$ 3. $^2S_{1/2} \to {}^2P^{e.s.}_{3/2}$ 4. $^2P_{3/2} \to {}^2D^{e.s.}_{5/2}$
6.	n^{13}C	E1	1. $^3S_1 + {}^3D_1 \to {}^3P^{g.s.}_0$ 2. $^3P_2 \to {}^3S^{e.s.}_1$
7.	n^{14}C	E1	1. $^2P_{1/2} + {}^2P_{3/2} \to {}^2S^{g.s.}_{1/2}$
8.	n^{14}N	E1	2. $^2S_{1/2} \to {}^2P^{g.s.}_{1/2} + {}^4S_{3/2} \to {}^4P^{g.s.}_{1/2}$ 3. $^2S_{1/2} \to {}^2P^{e.s.}_{1/2} + {}^4S_{3/2} \to {}^4P^{e.s.}_{1/2}$ 4. $^2P_{1/2} + {}^2P_{3/2} \to {}^2S^{e.s.}_{1/2}$
9.	n^{15}N	E1	1. $^3P_2 \to {}^3D^{g.s.}_2$ 2. $^3P_1 \to {}^3D^{g.s.}_2 + {}^1P_1 \to {}^1D^{g.s.}_2$ 3. $^3P_0 \to {}^3S^{e.s.}_1 + {}^3P_2 \to {}^3S^{e.s.}_1 + {}^3P_1 \to {}^3S^{e.s.}_1 + + {}^1P_1 \to {}^1S^{e.s.}_0 + {}^3P_2 \to {}^3D^{e.s.}_3$
10.	n^{16}O	E1	1. $^2P_{3/2} \to {}^2D^{g.s.}_{5/2}$ 2. $^2P_{1/2} + {}^2P_{3/2} \to {}^2S^{e.s.}_{1/2}$
		M1	3. $^2D_{3/2} \to {}^2D^{g.s.}_{5/2}$ 4. $^2S_{1/2} \to {}^2S^{e.s.}_{1/2} \neq 0$

Table C.2 (continued)

No.	System	Transitions from the scattering states $^{(2S+1)}L_J$ to the ground (GS) or excited (ES) state of the final nucleus	
		Chapter 3	
11.	n^8Li	E1	1. $^4S_{3/2}\to{}^4P_{3/2}$
			2. $^4S_{3/2}\to{}^4P_{1/2}$
		M1	3. $^4P_{5/2}\to{}^4P_{3/2}$
12.	n^{10}Be	E1	1. $^2P_{1/2}\to{}^2S_{1/2}+{}^2P_{3/2}\to{}^2S_{1/2}$
			2. $^2S_{1/2}\to{}^2P_{1/2}+{}^2D_{3/2}\to{}^2P_{1/2}$
13.	n^{10}B	E1	1. $^6S_{5/2}\to{}^6P^{e.s.}_{3/2}$
			2. $^6S_{5/2}\to{}^6P^{e.s.}_{5/2}+{}^8S_{7/2}\to{}^8P^{e.s.}_{5/2}$
			3. $^6S_{5/2}\to{}^6P^{e.s.}_{3/2}$
			4. $^6S_{5/2}\to{}^6P^{e.s.}_{7/2}+{}^8S_{7/2}\to{}^8P^{e.s.}_{7/2}$
			5. $^6S_{5/2}\to{}^6P^{e.s.}_{5/2}+{}^8S_{7/2}\to{}^8P^{e.s.}_{5/2}$
		M1	6. $^6P_{5/2}\to{}^6P^{g.s.}_{3/2}$
			7. $^6P_{5/2}\to{}^6P^{e.s.}_{5/2}+{}^8P_{5/2}\to{}^8P^{e.s.}_{5/2}$
			8. $^6P_{5/2}\to{}^6P^{e.s.}_{3/2}$
			9. $^6P_{5/2}\to{}^6P^{e.s.}_{7/2}+{}^8P_{5/2}\to{}^8P^{e.s.}_{7/2}$
14.	n^{11}B	E1	1. $^3S_1\to{}^3P^{g.s.}_1$
			2. $^3D_3\to{}^3P^{e.s.}_2$
			3. $^3P_2\to{}^3S^{e.s.}_1$
			4. $^3S_1\to{}^3P^{e.s.}_2$
			5. $^3S_1\to{}^3P^{e.s.}_0$
			6. $^3P_2\to{}^3D^{e.s.}_2$
		M1	7. $^3P_2\to{}^3P^{g.s.}_1$
			8. $^3P_2\to{}^3P^{e.s.}_2\to 0$
			9. $^3S_1\to{}^3S^{e.s.}_1\to 0$
			10. $^3D_3\to{}^3D^{e.s.}_2$
15.	p^{16}O	E1	1. $^2P_{3/2}\to{}^2D_{5/2}$

All proton reactions presented in the previous book [332] are discussed in the book "Thermonuclear Processes in Stars and the Universe" published by Palmarium Academic Publishing in 2015 [14]. However, in this book, in comparison with [332], new results of five neutron capture reactions of some light nuclei and proton capture by ^{16}O are added, which were not discussed in the earlier versions of the book.

Acknowledgments

The author expresses his great appreciation to the prof. Strakovsky I.I. (G. Washington's University, Washington, DC, USA), to the prof. Mukhamedzhanov A.M. (Texas A&M University, Texas, USA), to the prof. Blokhintsev L.D., to the prof. Ishkhanov B. S. and prof. Neudacthin V.G. (SINP of the Lomonosov Moscow State University, Moscow, Russian Federation), to the prof. Bagrov V.G. (TGU, Tomsk, Russian Federation), to the prof. Chechin L.M. (APFI, Almaty, RK), to the prof. Duysebayev A.D. and prof. Burtebayev N.T. (INP, Almaty, RK), to the prof. Danayev N.T. (al-Farabi Kazakh National University, Almaty, RK) and to the prof. Yarmukhamedov R. (INP, Tashkent, Uzbekistan) for valuable discussions of the single questions considered in this book.

It should be noted especially invaluable assistance to this work from scientific consultants: academician NAS RK, prof. Boos E.G. (FTI, Almaty, RK), academician NAS RK, prof. Omarov T.B. (APFI, Almaty, RK).

The implementation of this work was partially supported by grants of the Ministry of Education and Science of RK through the Fesenkov Astrophysical Institute (APFI) of the National Center of Space Researches and Technologies (NCSRT) RK. In this regard, I express sincere gratitude to the ex-president of NCSRT, the correspondent member NAS RK, prof. Zhantayev Zh.Sh. and to the present president of NCSRT PhD Omarov Ch.T. for the continued cooperation and support of all subject on Nuclear astrophysics.

https://doi.org/10.1515/9783110619607-007

Author information

Dubovichenko Sergey Borisovich – laureate of the al-Farabi State Prize of the Republic of Kazakhstan (RK) in the field of science and technology;

doctor of physical and mathematical sciences on specialties 01.04.16 – physics of an atomic nucleus and elementary particles and 05.13.18 – mathematical modeling, numerical methods and complexes of programs in the RK and the Russian Federation (RF), professor;

honorary Scientist of Europe, vice president and academician of the European Academy of Natural Sciences (EU), academician of the Peter's Academy of Sciences and Arts (RF), academician of the Russian Academy of Natural History (RF), academician of the International Academy of Informatization (RK), academician of the New York Academy of Sciences (US);

member of the International Astronomical Union (IAU); member of the American Physical Society (US), member of the European Physical Society (EU);

laureate of the European Gold Medal, Gauss Medal and Honorary Cross "Merit";

laureate of the State Scientific Stipend of RK, laureate of the International Soros Grant, laureate of the Komsomol Prize of Kaz.SSR (in former USSR);

head of the laboratory "Nuclear astrophysics" at Fesenkov Astrophysical Institute of the National Center of Space Researches and Technologies of Aerospace Agency of Defense Ministry and Space Industry of RK.

E-mail: dubovichenko@mail.ru, dubovichenko@gmail.com

Web-site: www.dubovichenko.ru

Fesenkov Astrophysical Institute – Observatory 23, Kamenskoe plato, 050020, Almaty, Republic of Kazakhstan, www.aphi.kz

https://doi.org/10.1515/9783110619607-008

Appendix

A1 Proton radiative capture on ^{16}O

In conclusion, we consider the $^{16}O(p,\gamma)^{17}F$ capture process, which participates in the CNO cycle [12,14,136] and represents the additional interest as the reaction on the last nucleus of $1p$ shell with the formation of ^{17}F going beyond its limit. As reported in previous studies [12,14,136], we assume that the bound state of ^{17}F is caused by the cluster channel of initial particles participating in the reaction.

Classification of the states

For the analysis of the total cross-sections of proton capture on ^{16}O, we first consider the classification of orbital states of the p^{16}O system according to Young tableaux. The orbital Young tableau {4444} corresponds to the ground bound state of ^{16}O; therefore, for the p^{16}O system, similar to n^{16}O, we have {1} × {4444} → {5444} + {44441} [28,134]. The first of the obtained tableaux is compatible with the orbital moment of $L = 0$ and is forbidden as there cannot be five nucleons in the s shell; and the second tableau is allowed and compatible with the orbital moment of $L = 1$ [28].

Thus, for the potential of the $^2S_{1/2}$ wave, which corresponds to the first excited state of ^{17}F at energies of 0.4953 MeV with moment $J^\pi = 1/2^+$, relative to the ground state, or −0.1052 MeV, relative to the threshold of the p^{16}O channel and scattering states of these particles, there exists a forbidden bound state. The ^2P scattering waves do not contain the forbidden bound state, and the allowed state with {44441} can be show a continuous spectrum. The ground state of ^{17}F with J^π, $T = 5/2^+,1/2$ in the p^{16}O channel, which is at an energy of −0.6005 MeV [258] relative to the threshold of the p^{16}O channel, is the $^2D_{5/2}$ wave which does not contain the forbidden bound state.

Based on the ^{17}F spectra data [258], it can be considered that one of the $E1$ captures is possible from the ^2P scattering waves with a potential without the bound forbidden states (FSs) or allowed states (ASs) to the $^2S_{1/2}$ first ES of ^{17}F with the bound FS

1.
$$\begin{matrix} {}^2P_{1/2} \to {}^2S_{1/2} \\ {}^2P_{3/2} \to {}^2S_{1/2} \end{matrix}.$$

For radiative capture to the $^2D_{5/2}$ of the GS of ^{17}F in the p^{16}O channel without the bound FS, the $E1$ transition from the $^2P_{3/2}$ scattering wave with potential without the BS can be considered to be

2.
$$^2P_{3/2} \to {}^2D_{5/2}.$$

The potentials of the GS and the first ES will be further constructed to describe the channel binding energy and the asymptotic constant of ^{17}F in the p^{16}O channel.

https://doi.org/10.1515/9783110619607-009

Phase-shift analysis

To construct the interaction potentials of clusters or nucleons with the nuclei in the MPCM, the elastic scattering phase shifts of the considered particles are used. One of the first measurements of the differential cross-sections of the elastic p^{16}O scattering with implementation of the phase-shift analysis at energies of 2.0–7.6 MeV have been described previously in [340]. This analysis has been used previously in [341] and [342] as well as some unpublished results [340] in the energy ranges of 2.0–4.26 and 4.25–7.6 MeV, respectively.

Furthermore, in [343], the polarization of the elastic p^{16}O scattering in the range of 2.0–5.0 MeV has been measured, and a new phase-shift analysis without considering resonance at 2.66 MeV was conducted. Furthermore, in [344] and [345], a detailed phase-shift analysis of the elastic p^{16}O scattering at the energies of 1.5–3.0 MeV was conducted, and showed the presence of a narrow resonance at the proton energy of 2.663(7) MeV and the wide of 19(1) keV, which corresponds to the first superthreshold state at 3.104 MeV with $J^{\pi} = 1/2^{-}$ relative to the GS or 2.5035 MeV in the system of the center of masses above the threshold of the p^{16}O channel [258]. Subsequently, the processes of elastic scattering for this system have been discussed in several previous works (see, for example, [258] and [346,347]) in the energy range of 1.0–3.5 MeV. In particular, in [348,349], energy ranges of 0.5–0.6 MeV to 2.0–2.5 MeV were considered; however, phase-shift analysis was not conducted in these ranges.

As discussed later, the radiation capture in the energy range of up to 2.0–2.5 MeV, and the results of the above-mentioned works is sufficient for the implementation of the detailed phase-shift analysis at energies starting from 0.5 MeV. Furthermore, according to these phase shifts, the p^{16}O interaction potentials up to 2.5 MeV, that is, without the first resonance with $J^{\pi} = 1/2^{-}$ can be constructed at 2.663 MeV in the laboratory [258]. Consequently, we have performed the phase-shift analysis of the available data at energy ranging from 0.5 to 2.5 MeV. Meanwhile, it was considered that, in this energy range, all P and D scattering phase shifts are equal or close to zero; results of this analysis have already been published [350]

Therefore, only one $^{2}S_{1/2}$ scattering phase shift participates in our phase-shift analysis and because in this wave within the considered energy range there are no resonances, the curve has a smooth falling-down shape, as shown in Fig. A1.1. The experimental data on excitation functions are taken from previous works [349,351–353]. Our results are well-coordinated with previously obtained phase shifts [340,344], as shown in Fig. A1.1 by open squares and rhombs at energies higher than 1.5 MeV. This is also well described in Fig. A1.1.

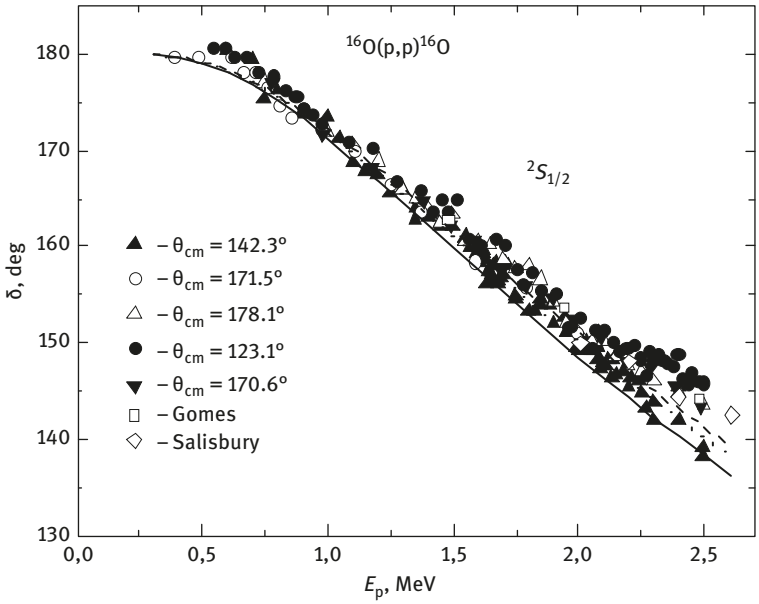

Fig. A1.1: The scattering p^{16}O phase shift obtained in this work on the basis of excitation functions at angles higher than 120°. Experimental data are from previous works [349,351–353]. Open rhombs and squares are the results of the analysis at energies ranging from 1.5 MeV to 2.5 MeV obtained from previous works [340,344].

Asymptotic constants

Data on asymptotic normalizing coefficients (A_{NC}) have been already published [354]. Here, we will use the known ratios (1.7.1) and (1.7.2), and the dimension-less value C_w is defined by the expression (1.2.5). The dimensional AC C from (1.7.2), measured in fm$^{-1/2}$, and the dimensionless AC C_w from (1.2.5) are related as $C_w = C/\sqrt{2k_0}$.

For further calculations, the ^{16}O radius in the GS is equal to 2.710(15) fm [258] or 2.6991(52) was used [214]. For the GS and FES of ^{17}F, the radii data are absent [214]; they also differ, though not strongly, from the relevant data for ^{16}O. The charge radius of proton and its mass radius were considered to be 0.8775(51) fm [126]. In all our calculations for the mass of both the nucleus and proton, exact values were used: $m(^{16}\text{O}) = 15.994915$ amu [306]; the mass of the proton is specified in section 1.6.

Furthermore, we consider the proton radiative capture on ^{16}O to the GS of ^{17}F, which as described earlier, is the $^2D_{5/2}$ level. Its potential also needs to describe the AC correctly. To obtain this constant from the available experimental data, we will consider spectroscopic factors (S_f) and A_{NC}. The A_{NC} results obtained by us are presented in Table A1.1.

Moreover, considerable data was obtained for the spectroscopic factors of the p^{16}O channel of ^{17}F, therefore, we present their values separately in Table A1.2. As seen from Table A1.2. the average values of spectrofactor are close to unity, therefore, for

Table A1.1: Data on the A_{NC} of ^{17}F in the p^{16}O channel and astrophysical S-factors of proton capture on ^{16}O.

The A_{NC} value in the GS, fm$^{-1/2}$	The A_{NC} value in the first ES, fm$^{-1/2}$	S(0) for the GS, keV b	S(0) for the first ES, keV b	S(0) TotalkeV b	References
1.59	98.2	—	—	10.37	[354]
1.04(5)	75.5(1.5)	0.40(4)	9.07(36)	9.45(40)	[355]
1.04(5)	80.6(4.2)	0.40(4)	9.8(1.0)	10.2(1.04)	[356]
1.04(5)	—	0.317(25)	8.552(43)	8.869(44)	[352,357]
1.10(1)	—	—	—	—	[351,357]
1.19(2)	81.0(9)	—	—	7.1–8.2	[357]
1.13(1)	82.3(3)	—	—	7.1–8.2	[357]
0.97–1.09	86.4–91.1	—	—	10.2–11.0	[358]
0.97–1.59	*74.0–98.2*	*0.29–0.44*	*8.7–10.8*	*7.1–11.06*	*Interval values*
1.28(31)	*86.1(12.1)*	*0.37(7)*	*9.76(1.04)*	*9.08(1.98)*	*Average A_{NC} on an interval*

Table A1.2: Data on the spectroscopic factors (S_f) of ^{17}F in the p^{16}O channel.

S_f for the GS	S_f for the first ES	References
0.878	0.921	[354]
0.90(15)	1.00(14)	[359]
0.88	0.99	[359] with reference to other works
0.94	0.83	[258]
0.75–1.05	*0.83–1.14*	*Interval of values*
0.9(15)	*0.99(15)*	*Average S_f on an interval*

simplicity, we will consider them to be 0.9 and 1. Furthermore, based on the expression (1.7.1), for GS, we find $\overline{A}_{NC}/\sqrt{\bar{S}} = \bar{C} = 1.35(33)$ fm$^{-1/2}$, and as $\bar{C}_w = 0.57$, the dimensionless AC defined as $\bar{C}_w = \bar{C}/\sqrt{2k_0}$ is $\sqrt{2k_0} = 2.37(58)$.

For the first ES, at $\sqrt{2k_0} = 0.37$ we can similarly determine $\bar{C}_w = 232.7(32.7)$. To use an error interval of spectrofactor for the GS, C_w can be obtained in the interval of 1.66–3.21. If to use the results of latest work [355] for the ANC, namely 1.04(5) fm$^{-1/2}$ and 75.5(1.5) fm$^{-1/2}$ from Table A1.1, then for an average spectrofactor value of 0.9 in the GS, $\bar{C}_w = 1.92(9)$, and for first ES, $\bar{C}_w = 204.0(4.1)$.

Interaction potentials

For the calculations of radiative capture within the MPCM framework, we need to know the potentials of the p^{16}O elastic scattering in the ^2P waves, as well as the interactions of the $^2D_{5/2}$ ground and $^2S_{1/2}$ first excited but bound state in the p^{16}O

channel of ^{17}F. For the transition to these BS, experimental data regarding the total cross-sections of radiative capture have been described in previous works [351,360]. However, only the $E1$ transition to GS will be considered further. In addition to this, the potential for the first ES of ^{17}F will be specified in the p^{16}O channel.

For the $^2S_{1/2}$ wave, the value of the scattering phase shift is well-known at energy ranging from 0.5 to 2.5 MeV (Fig. A.1.1), which also allows to construct its potential. For example, for this description, $^2S_{1/2}$ phase shift obtained as a result of our phase-shift analysis, it is possible to use simple Gaussian potential (1.2.2) with Coulomb point-like term, that is, the FS and the associated parameters:

$$V_S = -75.02097\,\text{MeV}, \quad \gamma_S = 0.125\,\text{fm}^{-2} \tag{A1.1}$$

The energy dependence of the $^2S_{1/2}$ phase shift of potential (A1.1) is shown in Fig. A1.1 denoted by the solid curve, which starts from 180° because of the presence of FS [11]. Such potential describes the behavior of the ^2S scattering phase shift obtained in our analysis, and is consistent with earlier descriptions of phase shift [340,344]. At the same time, the potential (A1.1) gives the binding energy of the first ES as –0.105200 MeV with an FDM accuracy of 10^{-6} MeV [24] used here, the charge radius of 3.10 fm, the mass radius of 2.93 fm, and the AC at an interval of 5–20 fm was equal to C_w = 215(2). This is consistent with the results given above using the A_{NC} and the spextrofactor S_f, being in the range of the above-mentioned interval is consistent with $\bar{C}_w$= 204.0(4.1) work [355].

For the $^2D_{5/2}$ potential of the GS of ^{17}F in the p^{16}O channel without the FS, the parameters can be obtained as

$$V_D = -85.632465\,\text{MeV}, \quad \gamma_D = 0.12\,\text{fm}^{-2}, \tag{A1.2}$$

which allow to obtain the binding energy of –0.600500 MeV at an FDM accuracy of 10^{-6} MeV [24], the charge radius of 2.82 fm, the mass radius of 2.77 fm, and the AC on an interval of distances of 7–28 fm, being equal to C_w = 1.68(1), which is on the lower limit of the interval mentioned above for the AC. The scattering phase shift of such potential smoothly falls down from zero and at 2.5 MeV, reaching an approximate value of –2°.

Because in the spectra of ^{17}F at energy lower than 2.5 MeV there are no resonances of negative parity, we will consider that the ^2P scattering potentials have to bring this energy range o zero phase shifts, and as they do not contain the bound FSs, their depth can just be zero.

Astrophysical S-factor of the proton capture on ^{16}O

Furthermore, based on the MPCM and experimental data [351,360], the total cross-sections of proton capture on ^{16}O at energies ranging up to 2.5 MeV have been considered. Our calculations results for the $E1$ to GS transition with potential (A1.2) from the ^2P scattering waves with the potentials of zero depth in comparison with the experimental

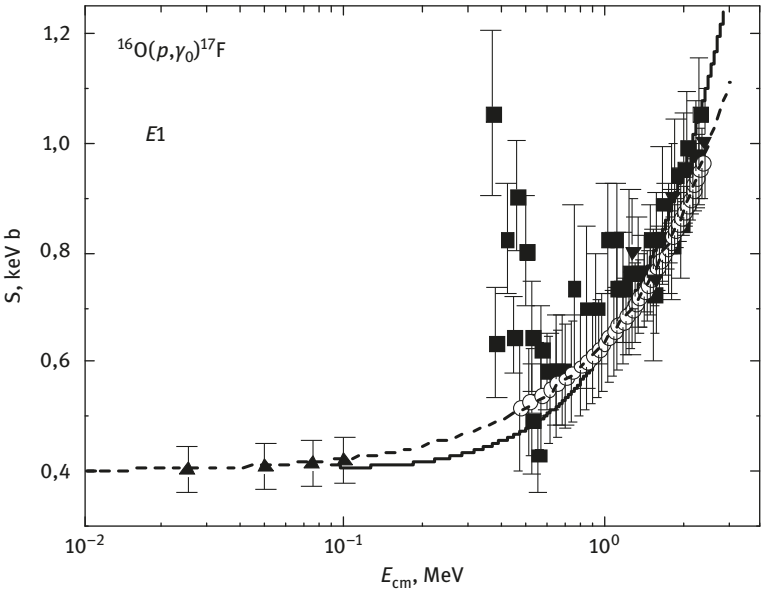

Fig. A1.2: Astrophysical *S*-factor of proton capture on ^{16}O to the GS of ^{17}F. Experimental data: squares – [351] circles – [360], open triangles – [352], and black triangles – [355]. Curves are described in the text.

data are presented in Fig. A1.2, denoted by the solid curve. The black squares show the measurement results of the total cross-sections at energies ranging from 0.4 to 2.5 MeV from work [351]; and the circles show the data [360] at energy range of 0.5–2.5 MeV; open triangles from work [352]. The triangles show the results presented in [355], leading to *S*-factor at zero energy of 0.4 keVb and down triangles show the results presented in [352].

From our calculations, *S*-factor value at energies of 30–330 keV changes from 0.409 to 0.441 keVb, with an average value of 0.425(16) keVb. At energies in the range of 90–150 keV, the *S*-factor has a value of 0.410(1) keVb. The calculation curve at energies of 0.5–2.5 MeV is practically within the limits of the available experimental errors of previously published work [351,360].

The linear data extrapolation [360] for energies lower than 0.5 MeV can be represented as

$$S(E) = 0.237E(\text{MeV}) + 0.40 \tag{A1.3}$$

is shown in Fig. A1.2 by the dashed curve and leads to the results at zero energy of 0.40 keV b. This curve well-describes the data [360] presented in Fig. A1.2 by the circles at energies ranging from 0.5 to 2.5 MeV, and are consistent with the results of [355] at zero energy.

Therefore, from Fig. A1.2, it is clear that the calculations of the *E*1 transition well describe the results of the experimental measurements of the astrophysical *S*-factor

from works [351,360] to the GS of ^{17}F, which is practically within the range of experimental errors. Moreover, the ^2P potentials of the scattering waves, which do not contain the FSs, were constructed based on simple assumptions of the coherence of such potentials with the scattering phase shifts, which are zero in this case. The $^2D_{5/2}$ potential of the ground state of ^{17}F in the p^{16}O channel has been previously coordinated with the main characteristics of this nucleus, namely, the binding energy and AC in the p^{16}O channel.

Please note that in our previous calculations [361] of the *S*-factor for capture up to the GS, all matrix elements (ME) of transitions were calculated only up to 30 fm. Therefore, slightly different results for total cross-sections have been reported. In this case, the ME of *S*-factors for GS were calculated up to distances of 200 fm, and for the first ES up to distances of 300 fm. Meanwhile, the scattering phase shift was obtained from the numerical WF at 30 fm, and at large distances was equated to its asymptotics. This allows one to obtain stable numerical results for *S*-factors at all considered energies.

Furthermore, *S*-factor for capture to the first excited state has been shown by the solid line in Fig. A1.3. The potential (A.1.1) and zero potentials for *P* waves were used. *S*-factor has a value of 11.1 keVb at energies 30 keV, while at higher energies it agrees well with the results of other experimental studies [359–363]. For example, in the RGM for zero energy, a value of 10–11 keVb was obtained [358].

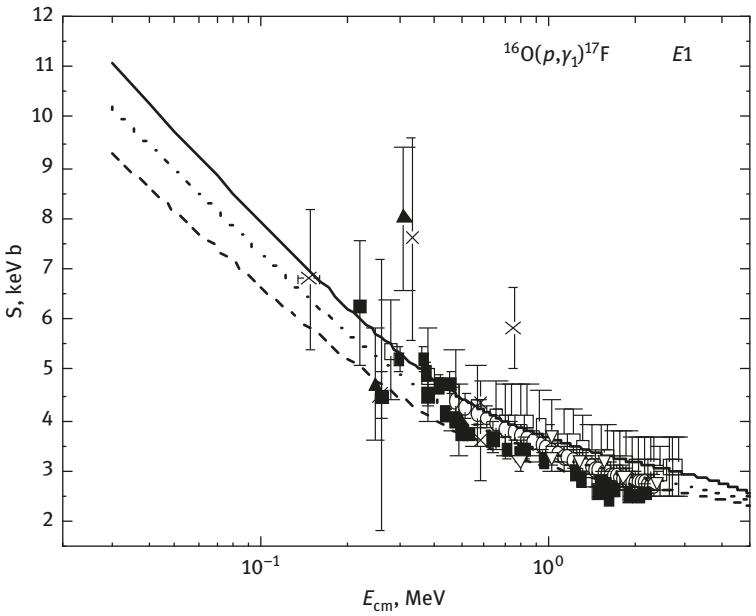

Fig. A1.3: Astrophysical *S*-factor of proton capture on ^{16}O to the first ES of ^{17}F. Experimental data: open squares – [359], black squares – [351], crosses – [362], black triangles – [363], circles – [360], and open triangles – [352]. Lines are described in the text.

The comparison of calculation results of S-factor for the capture to the first ES with data of [351], as done in [355], is shown in Fig. A1.3 by the dashed line, which at 30 keV has a value of 9.3 keVb, and in [355] were obtained 9.07(36) keVb. For the potential parameters next values were used

$$V_S = -87.855325\,\text{MeV}, \quad \gamma_S = 0.15\,\text{fm}^{-2}, \tag{A1.4}$$

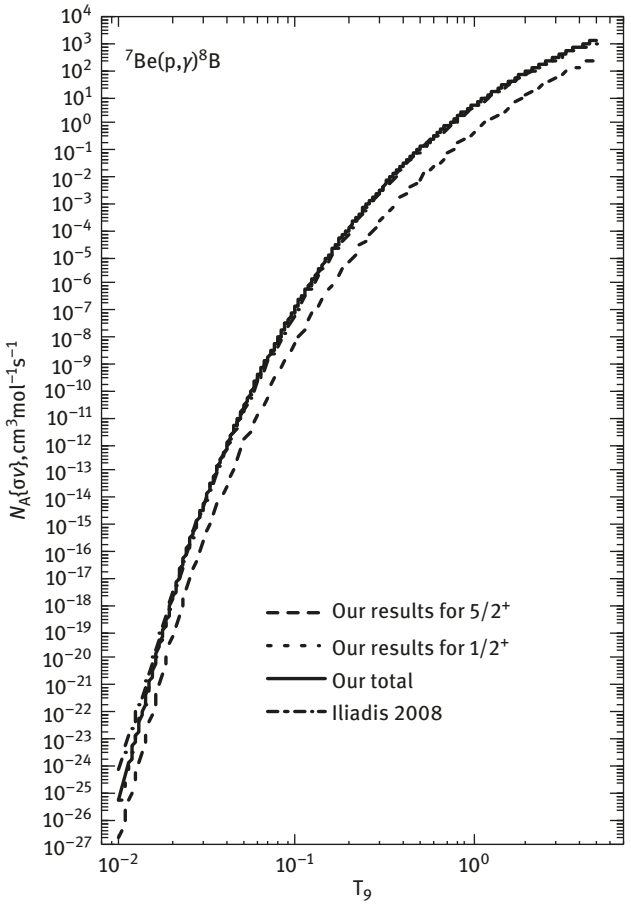

Fig. A1.4: Reaction rates of the proton capture on ^{16}O. Dashed line is from [357].

Energy dependency of the $^2S_{1/2}$ phase shift is shown in Fig. A1.1 by the dashed line. Potential allows one to obtain binding energy equal to −0.105200 MeV with the accuracy of finite-difference method of 10^{-6} MeV, charge radius of 3.05 fm, mass radius of 2.90 fm of ^{17}F, and AC of p^{16}O channel at a distance 5–20 fm of C_W = 197(2). This value remains at the low limit of the above-mentioned interval for AC.

It is possible to consider another variant of calculations, whose results are shown in Fig. A1.3 by the dotted line. The *S*-factor has a value of 10.2 keV b at 30 keV, and the next values were used for potential parameters as

$$V_S = -82.74659\,\text{MeV}, \quad \gamma_S = 0.14\,\text{fm}^{-2}. \tag{A1.5}$$

Energy dependency of the $^2S_{1/2}$ phase shift is shown in Fig. A1.1 by the dotted line. Potential allows one to obtain binding energy equals to −0.105200 MeV with the accuracy of finite-difference method of 10^{-6} MeV, charge radius of 3.07 fm, mass radius of 2.91 fm of ^{17}F, and AC at a distance of 6–18 fm is equal to $C_W = 204(2)$. These results better agree with the data published in [360] and RGM results for zero energy published in [358]. The AC value for this potential is consistent with the data published in [355].

Reaction rates of the proton capture on ^{16}O are presented in Fig. A1.4. Potentials (A1.1) and (A1.2) were used for calculating these rates, and astrophysical *S*-factors were calculated at energies ranging from 30 keV to 5 MeV without taking into account resonances above 2.5 MeV. The calculation results of the reaction rate from [357], which practically coincides with our results, are shown in Fig. A1.4 by the dotted-dashed line. Small differences exist only at temperatures lower than 0.02–0.03 T_9.

Therefore, the above-mentioned methods of construction of interaction potentials of clusters allow one to correctly reproduce experimental data for astrophysical *S*-factor of the radiative capture at energies ranging from 0.03 MeV to 2.5 MeV. The potential of the $^2D_{5/2}$ scattering wave was obtained without FS with the approximately zero phase shift, which is used for the GS and describes its basic characteristics. The potential for the $^2S_{1/2}$ wave with FS correctly reproduces the form of the scattering phase shift obtained in our phase-shift analysis, and agrees with the fundamental characteristics of the first ES.

A2 The variation two-body program

Here, we briefly describe the variation method and the computer program, as the results obtained by this method [261] were discussed above. The wave functions in the matrix elements for the ground and resonance states can be expressed in the form of expansion on nonorthogonal Gaussian as

$$\Phi_L(r) = \frac{\chi_L(r)}{r} = N_0 r^L \sum_i C_i \exp(-\alpha_i r^2),$$

and are determined by the variation method for the bound states or by the approximation of Gaussian functions of the numerical wave functions at resonance levels [261,364].

For determining the spectrum of eigenvalues of energy and wave functions in the standard variation method at the expansion of the WF on the orthogonal basis the matrix problem on eigenvalues is solved as [261,365]

$$\sum_i (H_{ij} - EI_{ij})C_i = 0,$$

where H is the symmetric matrix of the Hamiltonian, I is the identity matrix, E are eigenvalues, and C are eigenvectors of the problem.

In this case, at the nonorthogonal basis of the Gaussian functions, we come to the generalized matrix problem described in Chapter 1 along with other previously published studies [261,366]. On using the WF given above, it is possible to easily determine the expressions for all two-body matrix elements [261,366]

$$H_{ij} = T_{ij} + V_{ij} + \left\langle i\left|\frac{Z_1Z_2}{r}\right|j\right\rangle + \left\langle i\left|\frac{\hbar^2L(L+1)}{2\mu r^2}\right|j\right\rangle,$$

$$N_0 = \left[\sum C_iC_jL_{ij}\right]^{-1/2},$$

$$T_{ij} = -\frac{\hbar^2}{2\mu}\frac{\sqrt{\pi}(2L-1)!!}{2^{L+1}\alpha_{ij}^{L+1/2}}\left\{L(2L+1) - L^2 - \frac{\alpha_i\alpha_j(2L+1)(2L+3)}{\alpha_{ij}^2}\right\},$$

$$V_{ij} = \int V(r)r^{2L+2}\exp(-\alpha_{ij}r^2)dr,$$

$$L_{ij} = \frac{\sqrt{\pi}(2L+1)!!}{2^{L+2}\alpha_{ij}^{L+3/2}}, \qquad \alpha_{ij} = \alpha_i + \alpha_j.$$

$$\left\langle i\left|\frac{Z_1Z_2}{r}\right|j\right\rangle = \frac{Z_1Z_2L!}{2\alpha_{ij}^{L+1}},$$

$$\left\langle i\left|\frac{\hbar^2L(L+1)}{2\mu r^2}\right|j\right\rangle = \frac{\sqrt{\pi}(2L-1)!!}{2^{L+1}\alpha_{ij}^{L+1/2}}\frac{L(L+1)\hbar^2}{2\mu},$$

In case of Gaussian potential of intercluster interaction of the form (1.2.2), the matrix element of the potential V_{ij} is defined in analytical form as

$$V_{ij} = V_0\frac{\sqrt{\pi}(2L+1)!!}{2^{L+2}(\alpha_{ij}+\gamma)^{L+3/2}},$$

where y is the potential depth parameter.

Below, we provide the text of the computer program used for this method with an independent variation of parameters in Fortran-90 language. The description of a majority of key parameters and potentials is provided in the program text.

```
PROGRAM AL_3H_SOB
! THE VARIATION PROGRAM FOR SEARCH OF THE !BINDING ENERGY
USE MSIMSL
IMPLICIT REAL(8) (A-Z)
INTEGER I,J,K,LO,NV,NI,NP,NF,LK
DIMENSION XP(0:100)
!,XPN(0:100)
```

```
!DIMENSION E2(0:100)
!DIMENSION FU(0:10240000)
DIMENSION C0(0:100),CW0(0:100),CW(0:100)
!,ALA(0:100)
COMMON                                                  /A/
B44,B23,B11,B33,A11,PM,B55,S22,S44,C22,LO,S11,LK, RC,
PI,C11,C33,B22
COMMON                                                  /B/
T(0:100,0:100),VC(0:100,0:100),VN(0:100,0:100),
VK(0:100,0:100),RN,RN1,F1(0:10240000)
COMMON /C/ EP,PNC,PVC,HC,EPP
COMMON /D/ AA(0:100,0:100)
COMMON                                                  /F/
AL1(0:100,0:100),C(0:100,0:100),B(0:100,0:100),
AD(0:100,0:100),AL(0:100,0:100),Y(0:100),AN(0:100),D(0:100),
X(0:100),SV(0:100),H(0:100,0:100)
COMMON /G/ FF(0:10240000)
! ********* INITIAL VALUES *****************
Z1=2.0D-000       ;! Masses and charges of the clusters
Z2=1.0D-000
Z=Z1+Z2
AM1=4.001506179127D-000; ! AL
AM2=3.0155007134D-000; ! 3H
!AM2=3.0149322473D-000; ! 3HE
R01=1.67D-000   ;! Radii of clusters
R02=1.73D-000
RK11=1.67D-000   ;! Radii of clusters
RK22=1.73D-000
AM=AM1+AM2   ; ! Input constants
PM=AM1*AM2/AM
GK=3.44476D-002*Z1*Z2*PM
A11=20.7343D-000
A22=1.4399750D-000*Z1*Z2
P1=4.0D-000*ATAN(1.0D-000)
NF=1000  ; ! The number of steps of the calculation function
R00=25.0D-000
HFF=R00/NF   ; ! The step of the calculation function
NFF=NF/100
NP=10         ;! Dimension of the basis
NI=1        ; ! The number of iterations
NV=0  ;!  = 0 - without the minimization, = 1 - with the minimization by the energy!
EP=1.0D-015    ;! The accuracy of energy
EPP=1.0D-015   ;! Search of zero determinant
HC=0.001230D-000      ;! The step of search of zero determinant
PNC=-2.7D-000      ;! The lower value of energy for the search of zero determinant !
PVC=-0.0001D-000  ; ! The top value of energy for the search of zero determinant !
PHN=0.000123450D-000    ;! The step of change of the alpha parameters!
! ******** THE POTENTIAL PARAMETERS **************
V0=-83.616808D-000;! RCU=3.095 R0=0.15747 E=-2.467000 -!CW=3.92(2) RCH=2.46
```

```
(1.67,1.73) RMAS=2.50
RN=0.15747D-000
LO=1
RC=3.095D-000
V1=0.0D-000
RN1=1.0D-000
! ******* THE INITIAL ALPHA  PARAMETERS*********
NPP=NP
OPEN (1,FILE='ALFA.DAT')
DO I=1,NPP
READ(1,*) I,XP(I)
PRINT *,I,XP(I)
ENDDO
CLOSE(1)
PRINT *
! ********* THE INITIAL CONSTANTS ***************
C11=LO+1.50D-000
C22=LO+0.50D-000
PI=DSQRT(P1)
C33=LO+1.0D-000
N11=2*LO+3
S44=1.0D-000
DO K=1,N11,2
S44=S44*K
ENDDO
LK=LO*LO
S11=S44/(2.0D-000*LO+3.0D-000)
S22=S11/(2.0D-000*LO+1.0D-000)
R1=1.0D-000
DO K=1,LO
R1=R1*K
ENDDO
B11=PI*S11/(2.0D-000**(LO+2.0D-000))
B22=B11*V0
B23=B11*V1
B33=1.0D-000*LO*(LO+1.0D-000)*PI*S22/(2.0D-000**(LO+1.0D-000))
B44=A22*R1/2.0D-000
B55=PI/(2.0D-000**(LO+1.0D-000))
! SEARCH OF THE WF PARAMETERS AND THE BINDING ENERGY
CALL VARMIN(PHN,NP,NI,XP,EP,BIND,NV)
! ******** NUCLEAR CHARACTERISTICS *************
PRINT *,'------- ENERGIES ----------'
PRINT *,'                            E = ',BIND
PRINT *,'- - - - - - - - - - - - - - - - -  ALPHA  - - - - - - - - - - - - - - -'
DO I=1,NP
PRINT *,I,XP(I)
ENDDO
! *********** EIGENVECTORS ***********
CALL SVV(BIND,NP,XP)
```

```
! ************* NORMALIZATION OF VECTORS *********
A111: DO I=1,NP
DO J=1,NP
AL(I,J)=PI*S11/(2.0D-000**(LO+2)*(XP(I)+XP(J))**C11)
ENDDO
ENDDO A111
S=0.0D-000
B111: DO I=1,NP
DO J=1,NP
S=S+SV(I)*SV(J)*AL(I,J)
ENDDO
ENDDO B111
ANOR=1.0D-000/SQRT(S)
PRINT *,'                                    VECTORS          '
DO I=1,NP
SV(I)=ANOR*SV(I)
PRINT *,I,SV(I)
ENDDO
! ************* CALCULATION OF THE WF **************
FFFF=0.0D-000
DO I=0,NF
R=HFF*I
S=0.0D-000
DO J=1,NP
RRR=R**2.0D-000*XP(J)
IF (RRR>50) GOTO 9182
S=S+SV(J)*EXP(-RRR)
9182  ENDDO
FF(I)=R**(LO+1)*S
ENDDO
IF (FFFF==0.0D-000) GOTO 246
PRINT ' R                F(R)'
DO I=0,NF,NFF
R=I*HFF
PRINT *,R
PRINT *,FF(I)
ENDDO
246 CONTINUE
! **** CHECK OF THE NORMALIZATION *********************
DO I=0,NF
R=I*HFF
F1(I)=FF(I)**2
ENDDO
CALL SIM(F1,NF,HFF,SII)
PRINT *,'                              NOR = ',SII
! ******** ASYMPTOTIC CONSTANTS ********
SKS=(ABS(BIND)*PM/A11)
SS=SQRT(ABS(SKS))
SQQ=SQRT(2.*SS)
```

```
GGG=GK/SS
M1=NF/4
M3=NF/20
M2=NF
PRINT *,'         R       C0        CW0       CW'
K=0
DO I=M1,M2,M3
K=K+1
R=I*HFF
CALL ASIMP(R,SKS,GK,LO,I,C01,CW01,CW1)
C0(K)=C01
CW0(K)=CW01
CW(K)=CW1
WRITE(*,1) R,C01,CW01,CW1
ENDDO
1 FORMAT(3X,4(F10.5))
! ************* RADIUS OF THE NUCLEUS ********************
SS=0.0D-000
DO I=1,NP
DO J=1,NP
SS=SS+SV(I)*SV(J)/(XP(I)+XP(J))**(LO+2.5)
ENDDO
ENDDO
RR=PI*S44*SS/2.0D-000**(LO+3)
RRR=SQRT(RR)
RCH=AM1*R01**2.0D-000/AM+AM2*R02**2.0D-000/AM+AM1*AM2*RR/AM**2
RZ=Z1/Z*RK11**2 + Z2/Z*RK22**2 + (((Z1*AM2**2+Z2*AM1**2)/AM**2)/Z)*RR
PRINT *,'        RM =,  RZ = ‘,SQRT(RCH),SQRT(RZ)
PRINT *,'------- ENERGIES ----------’
PRINT *,'                            E = ‘,BIND
! *************** SAVE TO FILE *********************
PRINT *,‘SAVE???’
READ *
OPEN (1,FILE=‘ALFA.DAT’)
DO I=1,NP
WRITE(1,*) I,XP(I)
ENDDO
CLOSE(1)
OPEN (1,FILE=‘SV.DAT’)
DO I=1,NP
WRITE(1,*) I,SV(I)
ENDDO
WRITE(1,*)
WRITE(1,*) ‘E = ‘,BIND
CLOSE(1)
END

SUBROUTINE VARMIN(PHN,NP,NI,XP,EP,AMIN,NV)
IMPLICIT REAL(8) (A-Z)
```

```
INTEGER I,NV,NI,NP,NN
DIMENSION XPN(0:100),XP(0:100)
! ************** SEARCH OF THE MINIMUM ***********
DO I=1,NP
XPN(I)=XP(I)
ENDDO
NN=1
PH=PHN
CALL DETNUL(XPN,NP,ALAA)
BB=ALAA
IF (NV==0) GOTO 3012
A111: DO IIN=1,NI
NN=0
GOTO 1119
1159 XPN(NN)=XPN(NN)-PH*XP(NN)
1119 NN=NN+1
IN=0
2229 A=BB
XPN(NN)=XPN(NN)+PH*XP(NN)
IF (XP(NN)<0.0D-000) GOTO 1159
IN=IN+1
CALL DETNUL(XPN,NP,ALAA)
BB=ALAA
PRINT *,NN,XPN(NN),ALAA
IF (BB<A) GOTO 2229
C=A
XPN(NN)=XPN(NN)-PH*XP(NN)
IF (IN>1) GOTO 3339
PH=-PH
GOTO 5559
3339 IF (ABS(C-BB)<EP) GOTO 4449
PH=PH*0.50D-000
5559 BB=C
GOTO 2229
4449 PH=PHN
IF (NN<NP) GOTO 1119
PH=PHN*1.0D-000
AMIN=BB
ENDDO A111
3012 AMIN=BB
DO I=1,NP
XP(I)=XPN(I)
ENDDO
END

SUBROUTINE MAT(XP,NP)
IMPLICIT REAL(8) (A-Z)
INTEGER I,NP,NFF,LO,LK
DIMENSION XP(0:100)
```

```
COMMON                                                                  /A/
B44,B23,B11,B33,A11,PM,B55,S22,S44,C22,LO,S11,LK,RCC,
PI,C11,C33,B22
COMMON                                                                  /B/
T(0:100,0:100),VC(0:100,0:100),VN(0:100,
0:100),VK(0:100,0:100),RN,RN1,F1(0:10240000)
COMMON                                                                  /F/
AL1(0:100,0:100),C(0:100,0:100),B(0:100,0:100),AD(0:100,0:100),
AL(0:100,0:100),Y(0:100),AN(0:100),D(0:100),X(0:100),SV(0:100),H(0:100,0:100)
! ************ CALCULATION OF THE MATRICES *************
A111: DO KK=1,NP
B111: DO JJ=1,NP
ALL=XP(KK)+XP(JJ)
T(KK,JJ)=-B55*(LO*S11-LK*S22-XP(KK)*XP(JJ)*S44/ALL**2)/ALL**C22
SF=1.0D-000
SS1=1.0D-000
IF (RCC==0.0D-000) GOTO 7654
PF=RCC*DSQRT(ALL)
NFF=200
HF=PF/NFF
IF (PF>3.0D-000) GOTO 9765
DO I=0,NFF
XX=HF*I
F1(I)=DEXP(-XX**2)
ENDDO
CALL SIM(F1,NFF,HF,SI)
SF=SI*2.0D-000/PI
9765 ALR=DSQRT(ALL)*RCC
ALR2=ALR**2
EX=DEXP(-ALR2)
SS=PI*(9.0D-000*ALR-15.0D-000/(2.0D-000*ALR))*SF
SS1=(15.0D-000*EX+SS)/(8.0D-000*ALR2)
7654  VK(KK,JJ)=B44/ALL**C33*SS1
VN(KK,JJ)=B22/(ALL+RN)**C11
VN(KK,JJ)=VN(KK,JJ)+B23/(ALL+RN1)**C11
VC(KK,JJ)=B33/ALL**C22
H(KK,JJ)=(A11/PM)*(T(KK,JJ)+VC(KK,JJ))+VN(KK,JJ)+VK(KK,JJ)
AL1(KK,JJ)=B11/ALL**C11
H(JJ,KK)=H(KK,JJ)
AL1(JJ,KK)=AL1(KK,JJ)
ENDDO B111
ENDDO A111
END

SUBROUTINE DETNUL(XP,NP,ALA)
IMPLICIT REAL(8) (A-Z)
INTEGER NP
COMMON /C/ EP,PNC,PVC,HC,EPP
DIMENSION XP(0:100)
```

```
! ***** SEARCH OF ZERO OF THE DETERMINANT *************
! ----- FORMATION OF THE MATRIX -------
CALL MAT(XP,NP)
! ----SEARCH OF ZERO OF THE DETERMINANT
A2=PNC
B2=PNC+HC
CALL DETER(A2,D12,NP)
51 CALL DETER(B2,D11,NP)
IF (D12*D11>0.0D-000) GOTO 4
44 A3=A2
B3=B2
11 C3=(A3+B3)/2.0D-000
IF (ABS(A3-B3)<EPP) GOTO 151
CALL DETER(C3,F2,NP)
IF (D12*F2>0.0D-000) GOTO 14
B3=C3
D11=F2
GOTO 15
14 A3=C3
D12=F2
15 IF (ABS(F2)>EPP) GOTO 11
151 ALA=C3
GOTO 7
4 IF (ABS(D11*D12)<EPP) GOTO 44
A2=A2+HC
B2=B2+HC
D12=D11
IF (B2-PVC<0.010D-000) GOTO 51
7 END

SUBROUTINE DETER(ALL,DET,NP)
IMPLICIT REAL(8) (A-Z)
INTEGER NP,I,J
COMMON       /F/      AL1(0:100,0:100),      C(0:100,0:100),
B(0:100,0:100),AD(0:100,0:100),AL(0:100,0:100),Y(0:100),
AN(0:100),D(0:100),X(0:100),SV(0:100),H(0:100,0:100)
! ****** CALCULATION OF THE DETERMINANT OF THE MATRIX
DO I=1,NP
DO J=1,NP
AL(I,J)=(H(I,J)-ALL*AL1(I,J))
B(I,J)=0.0D-000
C(I,J)=0.0D-000
ENDDO
ENDDO
CALL TRIAN(AL,B,C,DET,NP)
END

SUBROUTINE SVV(ALL,NP,XP)
IMPLICIT REAL(8) (A-Z)
```

```
INTEGER NP,I,J,K
COMMON                /F/
AL1(0:100,0:100),C(0:100,0:100),B(0:100,0:100),AD(0:100,0:
100),AL(0:100,0:100),Y(0:100),AN(0:100),D(0:100),X(0:100),SV(0:100),H(0:100,0:100)
DIMENSION XP(0:100)
! ********* EIGENVECTORS ****************
! -----FORMATION OF THE MATRIX -------
CALL MAT(XP,NP)
! ---- PREPARATION OF THE MATRIX ----------
DO I=1, NP
DO J=1, NP
AL(I,J)=(H(I,J)-ALL*AL1(I,J))
B(I,J)=0.0D-000
C(I,J)=0.0D-000
ENDDO
ENDDO
DO I=1, NP-1
DO J=1, NP-1
AD(I,J)=AL(I,J)
ENDDO
ENDDO
DO I=1,NP-1
D(I)=-AL(I,NP)
ENDDO
NP=NP-1
CALL TRIAN(AD,B,C,DET,NP)
! ------- THE CALCULATION OF VECTORS ------------
Y(1)=D(1)/B(1,1)
DO I=2, NP
S=0.0D-000
DO K=1, I-1
S=S+B(I,K)*Y(K)
ENDDO
Y(I)=(D(I)-S)/B(I,I)
ENDDO
X(NP)=Y(NP)
DO I=NP-1,1,-1
S=0.0D-000
DO K=I+1,NP
S=S+C(I,K)*X(K)
ENDDO
X(I)=Y(I)-S
ENDDO
DO I=1, NP
SV(I)=X(I)
ENDDO
NP=NP+1
SV(NP)=1
S=0.0D-000
```

```
DO I=1, NP
S=S+SV(I)**2
ENDDO
DO I=1, NP
SV(I)=SV(I)/SQRT(S)
ENDDO
! ---- CALCULATION OF RESIDUALS ----------
DO I=1, NP
S=0.0D-000
SS=0.0D-000
DO J=1, NP
S=S+H(I,J)*SV(J)
SS=SS+ALL*AL1(I,J)*SV(J)
ENDDO
AN(I)=S-SS
ENDDO
PRINT *,'                                H*SV-LA*L*SV=0'
DO I=1, NP
PRINT *,I,AN(I)
ENDDO
END

SUBROUTINE TRIAN(AD,B,C,DET,NP)
IMPLICIT REAL(8) (A-Z)
INTEGER NP,I,J
COMMON /D/ AA(0:100,0:100)
DIMENSION B(0:100,0:100),C(0:100,0:100),AD(0:100,0:100)
! EXPANSION OF THE MATRIX ON TRIANGULAR AD=B*C
DO I=1,NP
C(I,I)=1.0D-000
B(I,1)=AD(I,1)
C(1,I)=AD(1,I)/B(1,1)
ENDDO
DO I=2, NP
DO J=2, NP
S=0.0D-000
IF (J>I) GOTO 551
DO K=1,I-1
S=S+B(I,K)*C(K,J)
ENDDO
B(I,J)=AD(I,J)-S
GOTO 552
551 S=0.0D-000
DO K=1, I-1
S=S+B(I,K)*C(K,J)
ENDDO
C(I,J)=(AD(I,J)-S)/B(I,I)
552 ENDDO
ENDDO
```

```
S=1.0D-000
DO K=1, NP
S=S*B(K,K)
ENDDO
DET=S
! ---- CALCULATION OF THE RESIDUALS --------
GOTO 578
SS=0.0D-000
DO I=1, NP
DO J=1, NP
S=0.0D-000
DO K=1, NP
S=S+B(I,K)*C(K,J)
ENDDO
AA(I,J)=S-AD(I,J)
SS=SS+AA(I,J)
ENDDO
ENDDO
PRINT *,'                                    N = AD - B*C = 0'
DO I=1, NP
DO J=1, NP
PRINT *,AD(I,J),AA(I,J)
ENDDO
ENDDO
578  END

SUBROUTINE WW(SK,L,GK,R,WH)
IMPLICIT REAL(8) (A-Z)
INTEGER I,L,NN
DIMENSION F(0:1000000)
! ************ THE WHITTAKER'S FUNCTION ***************
SS=DSQRT(ABS(SK))
AA=GK/SS
BB=L
ZZ=1.0D-000+AA+BB
GAM=DGAMMA(ZZ)
RR=R
CC=2.0D-000*RR*SS
NN=30000
HH=0.001D-000
DO I=0, NN
TT=HH*I
F(I)=TT**(AA+BB)*(1.0D-000+TT/CC)**(BB-AA)*DEXP(-TT)
ENDDO
CALL SIM(F,NN,HH,SI)
WH=SI*DEXP(-CC/2.0D-000)/(CC**AA*GAM)
END
```

```
SUBROUTINE SIM(V,N,H,SI)
IMPLICIT REAL(8) (A-Z)
INTEGER I,J,N
! ******* THE INTEGRAL ACCORDING TO SIMPSON
DIMENSION V(0:10240000)
A=0.0D-000
B=0.0D-000
DO I=1,N-1,2
B=B+V(I)
ENDDO
DO J=2,N-2, 2
A=A+V(J)
ENDDO
SI=H*(V(0)+V(N)+2.0D-000*A+4.0D-000*B)/3.0D-000
END

SUBROUTINE ASIMP(R,SK,GK,L,N,C0,CW0,CW)
IMPLICIT REAL(8) (A-Z)
INTEGER L,N
COMMON /G/ FF(0:10240000)
! ******** THE ASYMPTOTIC CONSTANT *********
SS=SQRT(ABS(SK))
SQ=SQRT(2.0D-000*SS)
GG=GK/SS
CALL WW(SK,L,GK,R,WWW)
CW=FF(N)/WWW/SQ
C0=FF(N)/(EXP(-SS*R)*SQ)
CW0=C0*(R*SS*2.0D-000)**GG
END
```

The control account on this program for the $^{4}He^{3}H$ system is presented below.

ALFA

1 6.567905679421632E−001
2 1.849427298619411E−002
3 1.729324040753008E−001
4 4.173925751998056E−002
5 8.818471551829664E−002
6 4.503350223878621E−001
7 9.210585557350788E−001
8 2.000570770210328
9 2.925234985697186
10 3.981951253509630

H × SV − LA × L × SV = 0

1 1.443289932012704E-015

2 2.842170943040401E-014
3 3.019806626980426E-014
4 4.973799150320701E-014
5 2.486899575160351E-014
6 2.831068712794149E-015
7 1.887379141862766E-015
8 4.718447854656915E-016
9 2.775557561562891E-016
10 3.122793690302217E-012

VECTORS

1 4.270672897023774E−001
2 −6.326508827916876E−004
3 −2.047665503209801E−001
4 −1.032337189382823E−002
5 −6.301223045637849E−002
6 6.962475100484991E−001
7 2.076348108196292E−002
8 1.488689730498523E−003
9 −1.124701190142763E−003
10 3.797299221855067E−004

N = 9.999999999917769E−001

R	C_0	C_{w0}	C_w
6.25000	−3.17695	−5.00114	−3.91393
7.50000	−2.92688	−4.83283	−3.91798
8.75000	−2.73971	−4.71016	−3.92041
10.00000	−2.59384	−4.61811	−3.92311
11.25000	−2.46513	−4.52645	−3.90849
12.50000	−2.36455	−4.46326	−3.90566
13.75000	−2.30063	−4.45237	−3.93964
15.00000	−2.24363	−4.44216	−3.96770
16.25000	−2.14262	−4.33204	−3.90062
17.50000	−1.96194	−4.04448	−3.66720
18.75000	−1.70026	−3.56895	−3.25584
20.00000	−1.38590	−2.95868	−2.71369
21.25000	−1.06010	−2.29936	−2.11909
22.50000	−.76060	−1.67464	−1.54998
23.75000	−.51202	−1.14341	−1.06238
25.00000	−.32355	−.73229	−.68278

RM =, RZ = 2.50, 2.46

ENERGY
E = –2.466997950

All required WF parameters and the binding energy of the GS are determined in this manner.

A.3 Computer program for the calculation of the total radiative capture cross-sections

Here, the text of our computer program written in Fortran-90 which allows the calculation of the total cross-sections of proton radiative capture reaction on ^{16}O is presented. The description of all calculation methods is provided in previous works [261,332].

Explanations of some parameters, given at the beginning of the program, for example, potentials as well as the name of computing blocks, are given below and then again in the program.

```
IFUN=0! If = 0, then FDM; if = 1, then RK.
MINI=0! If = 0, then phase is considered on the border area; if = 1, then a phase in
the set accuracy is searched.
RE=30.0D-000! The distance in fm for the determination of energy and scattering phase
shifts.
RR=300.0D-000! The distance in fm for the determination of the WF and ME.
NV=100! The number of steps by the energy at the calculation of total cross-sections.
EH=1.0D-003! A step by the energy at the calculation of the cross-sections
EN=1.0D-003! The initial energy at the calculation of the cross-sections.
EP=1.0D-015! Th absolute accuracy of the search of the zero determinant and Coulomb
functions.
EP1=1.D-006! The absolute accuracy of the search of the binding energy.
EP2=1.0D-005! The accuracy of the search of an asymptotic constant in relative units.
EP3=1.0D-003! The accuracy of the search of the scattering phases in relative units.

PROGRAM p16O
IMPLICIT REAL(8) (A - Z)
INTEGER
L,N,N3,I,NN,NV,NH,N1,IFUN,N5,MINI,IFAZ,LS,LP,LD,IWFUN,ISEC,M
COMMON /M/ V(0:10240000),U1(0:10240000),U(0:10240000)
COMMON /BB/ A2,R0,AK1,RCU
COMMON /FF/
A32,R32,A321,R321,AP,RP,AP1,RP1,AD,AD1,RD,RD1,LS,LP,LD
COMMON /Z/ RR,RE
COMMON /AA/ SKS,GK,SSS,AKK,GAM,L
COMMON /EE/ PI
```

```
COMMON /CC/ HK,IFUN,MINI,IFAZ,ISEC

! *****************    PARAMETERS OF CALCULATIONS  *****************

IFUN=0; ! = 0 then KRM, = 1 then RK
IFAZ=1; !  = 0 phase shift = 0, = 1 - phase shift is calculated
MINI=0; ! = 0 phase shift is calculated at the border of the region, = 1 phase shift
is calculated according the given accuracy
IWFUN=0
ISEC=1

!   *****************  MASSES AND CHARGES    **************

Z1=1.0D0
Z2=8.0D0
Z=Z1+Z2

AM1=1.00727646677D0; ! P
AM2=15.994915D0; ! 16O
AM=AM1+AM2

RK11=0.877D0; ! P
RM11=0.877D0; ! P
RK22=2.7D0; ! 16O
RM22=2.7D0; ! 16O

PI=4.0D0*DATAN(1.0D0)
PM=AM1*AM2/(AM1+AM2)
A1=41.4686D0
B1=2.0D0*PM/A1
AK1=1.439975D0*Z1*Z2*B1
GK=3.44476D-002*Z1*Z2*PM

! **********    PARAMETERS OF CALCULATIONS    ************

N=2000
N3=N
RE=30.0D0
H=RE/N
H1=H
HK=H*H
RR=300.0D0

SKN=-1.0D0
HC=0.1D0
SKV=1.0D0

SKN=SKN*B1
SKV=SKV*B1
```

```
HC=HC*B1

NN=0
NV=500
NH=1

EH=1.0D-002
EN=3.0D-002

EP=1.0D-015;! THE ACCURACY OF SEARCH OF THE ZERO DETERMINANT AND COULOMB FUNCTIONS
EP1=1.D-006;! ACCURACY OF THE SEARCH OF THE BINDING ENERGY IN ABSOLUTE UNITS
EP2=1.0D-005;! ACCURACY OF THE SEARCH OF THE ASYMPTOTIC CONSTANT IN THE RELATIVE UNITS
EP3=1.0D-003;! ACCURACY OF THE SEARCH OF THE SCATTERING PHASES IN THE RELATIVE UNITS
! ****************** POTENTIALS **********************
!E=-0.6005 5/2
!E=-0.6005+0.4953=-0.1052 1/2

V0=82.74659D0;! P16O FOR RCU=0. R0=0.15 CW=204(2) (6-18 FM)  RM=2.91 RCH=3.07
E=-0.105200 1 - FS
R0=0.14D0; L=0; EP1=1.D-007 ! 1/2 ! 1/2

V01=0.0D0
R01=0.0D0

A2=-V0*B1
A01=V01*B1

V32=0.0D0 ! 0 FS IN 2D3/2-VAWE
R32=1.0D0;
LS=0

V321=0.D0
R321=0.0D0

A32=-V32*B1
A321=V321*B1

VD=0.0D0 ! 0 FS IN 2D5/2-VAWE
RD=0.1D0;
LD=2

VD1=0.D0
RD1=0.0D0

AD=-VD*B1
AD1=VD1*B1

VP=0.0D0 ! 2P1/2 WITH 0 FS
RP=0.1D0;
```

```
LP=1

VP1=0.D0
RP1=0.0D0
AP=-VP*B1
AP1=VP1*B1

RCU=0.0D0

! ********  SEARCH OF THE MINIMUM   ***********

CALL MINN(EP,B1,SKN,SKV,HC,H,N,L,A2,R0,AK1,RCU,GK,ESS,SKS,A01,R01,EP1)
SSS=DSQRT(ABS(SKS))
AKK=GK/SSS

M=8
N=N/M
H=RR/N
HK=H*H

ZZ=1.0D0+AKK+L
GAM=DGAMMA(ZZ)

! ********   CALCULATION OF THE WF  ***********

IF (IFUN==0) THEN
CALL FUNN(U,H,N,A2,R0,A01,R01,L,RCU,AK1,SKS)
ELSE
CALL FUNRK(U,N,H,L,SKS,A2,R0,A01,R01)
END IF

! ***********   WF NORMALIZATION   ************

N5=N; N1=1

CALL ASSIM(U,H,N5,C0,CW0,CW,N1,EP2)

DO I=0,N1
V(I)=U(I)*U(I)
ENDDO

CALL SIMP(V,H,N1,SII)
HN=1.0D0/DSQRT(SII)

DO I=0,N1
X=I*H
U(I)=U(I)*HN
ENDDO
```

```
!   ****** ASYMPTOTIC CONSTANTS  ******

CALL ASSIM(U,H,N1,C0,CW0,CW,N1,EP2)
1 FORMAT(1X,4(E13.6,2X))

!  *********   WF TAIL RENORMALIZATION   *****

SQQ=DSQRT(2.0D0*SSS)
DO I=N1+1,N
R=I*H
CC=2.0D0*R*SSS
CALL WHI(R,WWW)
U(I)=CW*WWW*SQQ
ENDDO
1122 CONTINUE

!  ******   ITERATIVE NORMALIZATION OF THE WF   ***

DO I=1,N
V(I)=U(I)*U(I)
ENDDO
CALL SIMP(V,H,N,SIM)
HN=SIM
HN=1.0D0/(HN)**0.5
DO I=1,N
U(I)=U(I)*HN
ENDDO
!  ******** ASYMPTOTIC CONSTANTS ****
CALL ASSIM(U,H,N,C0,CW0,CW,N,EP2)

! ***********   LISTING OF THE WF   ************

!PRINT *,'N = ',N

IF (IWFUN==0) GOTO 2233
OPEN (24,FILE='FUN.DAT')
WRITE(24,*) '          R               U'
PRINT *,'     R          U'
DO I=0,N
X=H*I
PRINT 2,X,U(I)
WRITE(24,2) X,U(I)
ENDDO
CLOSE(24)
2233 CONTINUE

! ****** ********  RADIUS ****************

OPEN (23,FILE='RAD.DAT')
```

```
WRITE(23,*) '     E        SQRT(RM**2)

SQRT(RZ**2)'
DO I=0,N
X=I*H
V(I)=X*X*U(I)*U(I)
ENDDO

CALL SIMP(V,H,N,RKV)

RM=AM1/AM*RM11**2 + AM2/AM*RM22**2 + ((AM1*AM2)/AM**2)*RKV
RZ=Z1/Z*RK11**2 + Z2/Z*RK22**2 + (((Z1*AM2**2+Z2*AM1**2)/AM**2)/Z)*RKV
PRINT *,'(RM^2)^1/2=',SQRT(RM)
PRINT *,'(RZ^2)^1/2=',SQRT(RZ)
WRITE(23,2) SQRT(RM),SQRT(RZ)
2 FORMAT(1X,2(E16.8,2X))
CLOSE(23)

! *************** CALCULATION OF THE S-FACTOR **********

CALL SFAC(EN,EH,NN,NV,NH,B1,ESS,H,N,RCU,AK1,PI,Z1,Z2,AM1,AM2,PM,GK,EP,EP3)
END

SUBROUTINE ASSIM(U,H,N,C0,CW0,CW,I,EP)
IMPLICIT REAL(8) (A-Z)
INTEGER I,L,N,J,N2
DIMENSION U(0:N)
COMMON /AA/ SKS,GK,SS,GGG,GAM,L
COMMON /XX/ CC

N2=10
OPEN (22,FILE='ASIMPTOT.DAT')
WRITE(22,*) '           R              C0              CW0               CW'
SQQ=DSQRT(2.0D0*SS)

IF (I==N) THEN

PRINT *,'       R              C0            CW0            CW'
DO J=N/16,N,N/16
R=J*H
CC=2.0D0*R*SS
C0=U(J)/DEXP(-SS*R)/SQQ
CW0=C0*CC**GGG
CALL WHI(R,WWW)
CW=U(J)/WWW/SQQ
PRINT 1,R,C0,CW0,CW,I
WRITE(22,1) R,C0,CW0,CW
ENDDO
ELSE
```

```
I=N
R=I*H
CC=2.0D0*R*SS
CALL WHI(R,WWW)
CW1=U(I)/WWW/SQQ
12 I=I-N2

IF (I≤0)  THEN
PRINT *,'NO STABLE ASSIMPTOTIC FW'
STOP
END IF
R=I*H
CC=2.0D0*R*SS
CALL WHI(R,WWW)
CW=U(I)/WWW/SQQ
IF (ABS(CW1-CW)/ABS(CW)>EP .OR. CW==0.0D0) THEN
CW1=CW
GOTO 12
END IF

END IF
CLOSE(22)
1 FORMAT(1X,4(E13.6,2X),3X,I8)
END

SUBROUTINE CULFUN(LM,R,Q,F,G,W,EP)
IMPLICIT REAL(8) (A-Z)
INTEGER L,K,LL,LM
EP=1.0D-15
L=0
F0=1.0D0
GK=Q*Q
GR=Q*R
RK=R*R
B01=(L+1)/R+Q/(L+1)
K=1
BK=(2*L+3)*((L+1)*(L+2)+GR)
AK=-R*((L+1)**2+GK)/(L+1)*(L+2)
DK=1.0D0/BK
DEHK=AK*DK
S=B01+DEHK
15 K=K+1
AK=-RK*((L+K)**2-1.0D0)*((L+K)**2+GK)
BK=(2*L+2*K+1)*((L+K)*(L+K+1)+GR)
DK=1.D0/(DK*AK+BK)
IF (DK>0.0D0) GOTO 35
25 F0=-F0
35 DEHK=(BK*DK-1.0D0)*DEHK
S=S+DEHK
```

```
IF (ABS(DEHK)>EP) GOTO 15
FL=S
K=1
RMG=R-Q
LL=L*(L+1)
CK=-GK-LL
DK=Q
GKK=2.0D0*RMG
HK=2.0D0
AA1=GKK*GKK+HK*HK
PBK=GKK/AA1
RBK=-HK/AA1
AOMEK=CK*PBK-DK*RBK
EPSK=CK*RBK+DK*PBK
PB=RMG+AOMEK
QB=EPSK
52 K=K+1
CK=-GK-LL+K*(K-1.)
DK=Q*(2.0D0*K-1.)
HK=2.0D0*K
FI=CK*PBK-DK*RBK+GKK
PSI=PBK*DK+RBK*CK+HK
AA2=FI*FI+PSI*PSI
PBK=FI/AA2
RBK=-PSI/AA2
VK=GKK*PBK-HK*RBK
WK=GKK*RBK+HK*PBK
OM=AOMEK
EPK=EPSK
AOMEK=VK*OM-WK*EPK-OM
EPSK=VK*EPK+WK*OM-EPK
PB=PB+AOMEK
QB=QB+EPSK
IF (( ABS(AOMEK)+ABS(EPSK) )>EP) GOTO 52
PL=-QB/R
QL=PB/R
G0=(FL-PL)*F0/QL
G0P=(PL*(FL-PL)/QL-QL)*F0
F0P=FL*F0
ALFA=1.0D0/((DSQRT(ABS(F0P*G0-F0*G0P))) )
G=ALFA*G0
GP=ALFA*G0P
F=ALFA*F0
FP=ALFA*F0P
W=1.0D0-FP*G+F*GP

IF (LM==0) GOTO 123
AA=DSQRT((1.0D-000+Q**2))
BB=1.0D0/R+Q
```

```
F1=(BB*F-FP)/AA
G1=(BB*G-GP)/AA
WW1=F*G1-F1*G-1.0D0/DSQRT((Q**2+1.0D0))

IF (LM==1) GOTO 234
DO L=1,LM-1
AA=DSQRT(((L+1)**2+Q**2))
BB=(L+1)**2/R+Q
CC=(2*L+1)*(Q+L*(L+1)/R)
DD=(L+1)*DSQRT((L**2+Q**2))
F2=(CC*F1-DD*F)/L/AA
G2=(CC*G1-DD*G)/L/AA
WW2=F1*G2-F2*G1-(L+1)/DSQRT((Q**2+(L+1)**2))
F=F1; G=G1; F1=F2; G1=G2
ENDDO

234 F=F1; G=G1
123 CONTINUE
END

SUBROUTINE FAZ(N,F1,F2,G1,G2,V,F,I,H2)
IMPLICIT REAL(8) (A-Z)
INTEGER I,J,N,MINI,IFUN,IFAZ
DIMENSION V(0:2048000),F(0:1000)
COMMON /CC/ HK,IFUN,MINI,IFAZ
COMMON /EE/ PI
U1=V(N-4)
U2=V(N)
AF=-(F1-F2*U1/U2)/(G1-G2*U1/U2)
FA=DATAN(AF)
IF (ABS(FA)<1.0D-8) THEN
FA=0.0D-000
ENDIF
IF (FA<0.0D0) THEN
FA=FA+PI
ENDIF
F(I)=FA
H2=(DCOS(FA)*F2+DSIN(FA)*G2)/U2
DO J=0,N
V(J)=V(J)*H2
ENDDO
END

SUBROUTINE FUNRK(V,N,H,L,SK,A22,R00,A1,R1)
IMPLICIT REAL(8) (A-Z)
INTEGER I,N,L
DIMENSION V(0:10240000)
VA1=0.0D-000;
PA1=1.0D-003
```

```
DO I=0,N-1
X=H*I+1.0D-015
CALL RRUN(VB1,PB1,VA1,PA1,H,X,L,SK,A22,R00,A1,R1)
VA1=VB1
PA1=PB1
V(I+1)=VA1
ENDDO
END

SUBROUTINE RRUN(VB1,PB1,VA1,PA1,H,X,L,SK,A,R,A1,R1)
IMPLICIT REAL(8) (A-Z)
INTEGER L
X0=X
Y1=VA1
CALL FA(X0,Y1,FK1,L,SK,A,R,A1,R1)
FK1=FK1*H
FM1=H*PA1
X0=X+H/2.0D-000
Y2=VA1+FM1/2.0D-000
CALL FA(X0,Y2,FK2,L,SK,A,R,A1,R1)
FK2=FK2*H
FM2=H*(PA1+FK1/2.0D-000)
Y3=VA1+FM2/2.0D-000
CALL FA(X0,Y3,FK3,L,SK,A,R,A1,R1)
FK3=FK3*H
FM3=H*(PA1+FK2/2.0D-000)
X0=X+H
Y4=VA1+FM3
CALL FA(X0,Y4,FK4,L,SK,A,R,A1,R1)
FK4=FK4*H
FM4=H*(PA1+FK3)
PB1=PA1+(FK1+2.0D-000*FK2+2.0D-000*FK3+FK4)/6.0D-000
VB1=VA1+(FM1+2.0D-000*FM2+2.0D-000*FM3+FM4)/6.0D-000
END

SUBROUTINE FA(X,Y,FF,L,SK,A,R,A1,R1)
IMPLICIT REAL(8) (A-Z)
INTEGER L
COMMON /BB/ A2,R0,AK,RCU
VC=A*DEXP(-R*X*X)+A1*DEXP(-R1*X*X)
IF (X>RCU) GOTO 1
VK=(3.0D-000-(X/RCU)**2)*AK/(2.0D-000*RCU)
GOTO 2
1 VK=AK/X
2 FF=-(SK-VK-VC-L*(L+1)/(X*X))*Y
END

SUBROUTINE FUNN(U,H,N,A0,R0,A1,R1,L,RC,AK,SK)
! NUMEROV METHOD
```

```
IMPLICIT REAL(8) (A-Z)
INTEGER N,L,I
DIMENSION U(0:N),V(0:N)
! INITIAL VALUES
U(0)=0.0D0; U(1)=0.1D0; Q0=0.0D0; HK=H*H; SHS=SK*HK
LL=1.0D0*L*(L+1); AA=1.0D0/12.0D0; DD=5.0D0/6.0D0
IF(RC>0) THEN; RR=1.0D0/RC; BB=AK/(2.0D0*RC); ENDIF

! CALCULATION OF VALUES FOR POTENTIAL VC(R)
DO I=1,N-1,2
X=I*H; XX=X*X
XP=(I+1)*H; XXP=XP*XP
V(I)=A0*DEXP(-R0*XX)+A1*DEXP(-R1*XX)+LL/XX
V(I+1)=A0*DEXP(-R0*XXP)+A1*DEXP(-R1*XXP)+LL/XXP
IF (X>RC) THEN
V(I)=V(I)+AK/X
V(I+1)=V(I+1)+AK/XP
ELSE
V(I)=V(I)+(3.0D0-(X*RR)**2)*BB
V(I+1)=V(I+1)+(3.0D0-(XP*RR)**2)*BB
ENDIF
ENDDO
! CALCULATION OF VALUES FOR POTENTIAL VC(R)
DO I=1,N-1,1
Q1=SHS-V(I)*HK; Q2=SHS-V(I+1)*HK; CC=1.0D0+AA*Q2
FF=(2.0D0-DD*Q1)*U(I)-(1.0D0+AA*Q0)*U(I-1)
U(I+1)=FF/CC; Q0=Q1
ENDDO
END

SUBROUTINE MINN(EP,B1,SKN,SKV,HC,H,N,L,A2,R0,AK1,RCU,GK,ESS,SKS,A01,R01,EP1)
IMPLICIT REAL(8) (A-Z)
INTEGER III,N,L
DIMENSION EEE(0:1000)
III=1
CALL MINIMUM(EP,B1,SKN,SKV,HC,H,N,L,A2,R0,AK1,RCU,GK,ESS,SKS,A01,R01)
PRINT *,'               E                   N                DEL-E'
EEE(III)=ESS
111 N=2*N
H=H/2.0D0
III=III+1
CALL MINIMUM(EP,B1,SKN,SKV,HC,H,N,L,A2,R0,AK1,RCU,GK,ESS1,SKS,A01,R01)
EEE(III)=ESS1
EEPP=ABS(EEE(III))-ABS(EEE(III-1))
PRINT *,EEE(III),N,EEPP
IF (ABS(EEPP)>EP1) GOTO 111
ESS=ESS1
PRINT *,EEE(III),N,EEPP
12 FORMAT(1X,E19.12,2X,I10,2X,3(E10.3,2X))
```

```
OPEN (25,FILE='E.DAT')
WRITE(25,*) ESS,SKS,N,H,DSQRT(2.0D0*DSQRT(ABS(SKS)))
CLOSE(25)
END

SUBROUTINE MINIMUM(EP,B1,PN,PV,HC,HH,N3,L,A22,R0,AK1,RCU,GK,EN,COR,A33,R1)
IMPLICIT REAL(8) (A-Z)
INTEGER I,N3,L,LL
HK=HH**2
LL=L*(L+1)
IF(PN>PV) THEN
PNN=PV; PV=PN; PN=PNN
ENDIF
H=HC; A=PN ; EP=1.0D-015
1 CONTINUE
CALL DET(A,GK,N3,A22,R0,L,LL,AK1,RCU,HH,HK,D1,A33,R1)
B=A+H
2 CONTINUE
CALL DET(B,GK,N3,A22,R0,L,LL,AK1,RCU,HH,HK,D2,A33,R1)
IF (D1*D2>0.0D-000) THEN
B=B+H; D1=D2
IF (B≤PV .AND. B≥PN) GOTO 2
I=0; RETURN; ELSE
A=B-H; H=H*1.0D-001
IF(ABS(D2)<EP .OR. ABS(H)<EP) GOTO 3
B=A+H; GOTO 1
ENDIF
3 I=1; COR=B; D=D2; EN=COR/B1;
END

SUBROUTINE DET(DK,GK,N,A2,R0,L,LL,AK,RCU,H,HK,DD,A3,R1)
IMPLICIT REAL(8) (A-Z)
INTEGER(4) L,N,II,LL
S1=DSQRT(ABS(DK))
G2=GK/S1
D1=0.0D-000
D=1.0D-000
DO II=1,N
X=II*H
XX=X*X
F=A2*DEXP(-XX*R0)+A3*DEXP(-XX*R1)+LL/XX
IF (X>RCU) GOTO 67
F=F+(AK/(2.0D-000*RCU))*(3.0D-000-(X/RCU)**2)
GOTO 66
67 F=F+AK/X
66 IF (II==N) GOTO 111
D2=D1
D1=D
OM=DK*HK-F*HK-2.0D-000
```

```
D=OM*D1-D2
ENDDO
111 Z=2.0D-000*X*S1
OM=DK*HK-F*HK-2.0D-000
W=-S1-2.0D-000*S1*G2/Z-2.0D-000*S1*(L-G2)/(Z*Z)
OM=OM+2.0D-000*H*W
DD=OM*D-2.0D-000*D1
END

SUBROUTINE SFAC(EN,EH,NN,NV,NH,B1,ES,H,N4,RCU,AK1,PI,Z1,Z2,AM1,AM2,PM,GK,EP,EP2)
IMPLICIT REAL(8) (A-Z)
INTEGER(4) N3,NN,NV,NH,N2,N4,IFUN,MINI,I,IFAZ,LS,LP,LD,M,N,J,ISEC
CHARACTER(30) AAA, BBB
COMMON /M/ V(0:10240000),U1(0:10240000),U(0:10240000)
DIMENSION FA1(0:1000),EG(0:1000),ECM(0:1000),EL(0:1000)
DIMENSION SZP(0:1000),SZ(0:1000)
DIMENSION SF(0:1000)
COMMON /CC/ HK,IFUN,MINI,IFAZ,ISEC
COMMON /FF/ A32,R32,A321,R321,AP,RP,AP1,RP1,AD,AD1,RD,RD1,LS,LP,LD
COMMON /Z/ RR,RE
! * CALCULATION OF THE SCATTERING FUNCTIONS, PHASE SHIFTS AND MATRIX ELEMENTS OF S-
FACTORS *
EP2=EP2
N3=N4
N2=4
IF(ISEC==0) GOTO 1111
M=NINT(RR/RE)
N=N4/M
AAA='SF-P16O-S-87-300.DAT'
BBB='SV-P16O-S-87-300.DAT'
OPEN (1,FILE=AAA)
WRITE (1,*) '      ECM           SF            SZ          FA'
PRINT *, '         ECM           SF            SZ          FA'
A1: DO I=NN,NV,NH
ECM(I)=EN+I*EH
EG(I)=ECM(I)+ABS(ES)
SK=ECM(I)*B1
SS1=SK**0.5
G=GK/SS1

! ***  CALCULATION OF THE CULOMB S1- ***

X1=H*SS1*(N-4)
X2=H*SS1*(N)
CALL CULFUN(LP,X1,G,F1,G1,W0,EP)
CALL CULFUN(LP,X2,G,F2,G2,W0,EP)

!*   SCATTERING FUNCTIONS  *
```

```
IF (IFUN==0) THEN
CALL FUNN(U1,H,N,AP,RP,AP1,RP1,LP,RCU,AK1,SK)
ELSE
CALL FUNRK(U1,N,H,LP,SK,AP,RP,AP1,RP1)
END IF

! *******   CALCULATION OF THE S PHASE SHIFTS   ********

CALL FAZ(N,F1,F2,G1,G2,U1,FA1,I,XH2)
FAP=FA1(I)*180.0/PI

! ****  CALCULATION OF THE MATRIX ELEMENTS E1S  **

DO J=N+1,N4
X=H*SS1*J
CALL CULFUN(LP,X,G,F1,G1,W0,EP)
U1(J)=(DCOS(FA1(I))*F1+DSIN(FA1(I))*G1)
ENDDO

DO J=0,N4
X=H*J
V(J)=U1(J)*X*U(J)
ENDDO
CALL SIMP(V,H,N4,AIP)

!** CALCULATION OF THE TOTAL CROSS SECTIONS

E1,E2,M1 **
AMU1=2.793D0 ! P
AMU2=0. ! 16O
AKP=SS1
AKG=(EG(I))/197.331D0
EL(I)=ECM(I)*AM1/PM
BBBB=344.447D-000*8.0D-000*PI*2.0D-000/2.0D-000/1.0D-000/9.0D-000*PM
!AMP1=0.21184D-000*DSQRT(3.0D-000/2.0D-000)*(AMU1*AM2/(AM1+AM2)-AMU2*AM1/(AM1+AM2))*
DSQRT(3.0D-000)*AKG*AIP  ! M1 - S1/2->S1/2
!AMP2=0.21184D-000*DSQRT(4.0D-000/15.0D-000)*(AMU1*AM2/(AM1+AM2)-AMU2*AM1/(AM1+AM2))*
DSQRT(3.0D-000)*AKG*AIP  ! M1 - P3/2->P1/2 - GS

AMP=6.0D0/DSQRT(5.0D0)*AKG*PM*(Z1/AM1-Z2/AM2)*AIP ! P3/2->D5/2
SZP(I)=BBBB*AKG/AKP**3*AMP**2

IF(ABS(ES)<0.5) THEN
AMP12=DSQRT(2.0D0)*AKG*PM*(Z1/AM1-Z2/AM2)*AIP ! P1/2->S1/2
AMP32=DSQRT(4.0D0)*AKG*PM*(Z1/AM1-Z2/AM2)*AIP ! P3/2->S1/2
SZP(I)=BBBB*AKG/AKP**3*(AMP12**2+AMP32**2)
ENDIF

SZ(I)=SZP(I)
```

```
SSS=DEXP(Z1*Z2*31.335D-000*DSQRT(PM)/DSQRT(ECM(I)*1.0D+003))
SF(I)=SZ(I)*1.0D-006*ECM(I)*1.0D+003*SSS ! KEV B

PRINT 2, ECM(I),SF(I),SZ(I),FAP
WRITE (1,2) ECM(I),SF(I),SZ(I),FAP

ENDDO A1
CLOSE (1)
2 FORMAT(1X,9(E10.5,1X))

!   ************ REACTION RATE  ******************
1111 CALL SVT(AAA,BBB,NN,NV,SZ,ECM,EL,AM1,AM2,PM,ISEC)
END

SUBROUTINE SIMP(V,H,N,S)
! MILNE METHOD
IMPLICIT REAL(8) (A-Z)
INTEGER N,I
DIMENSION V(0:N)
SS=0.0D0
DO I=0,N-4,4
SS=SS+7.0D0*V(I)+32.0D0*V(I+1)+12.0D0*V(I+2)+32.0D0*V(I+3)+7.0D0*V(I+4)
ENDDO
S=SS*2.0D0*H/45.0D0
END

SUBROUTINE SVT(AAA,BBB,NN,NV,SE,ECM,EL,AM1,AM2,PM,ISEC)
IMPLICIT REAL(8) (A-Z)
INTEGER(4) NN,NV,I,J,ISEC
CHARACTER(30) AAA, BBB
DIMENSION ECM(0:1000),EL(0:1000),SE(0:1000),SI(0:1000),T9(0:1000),SV(0:1000),
SFS(0:1000)
DIMENSION SF(0:1000),SFD(0:1000),SFM(0:1000),SFT(0:1000)

IF(ISEC==0) THEN
OPEN (2,FILE=AAA)

DO I=NN,NV
READ(2,*) ECM(I),SFS(I),SFD(I),SF(I),SFM(I),SFT(I),FS,FD,FM, SE(I)
ENDDO
CLOSE (2)
ENDIF
PRINT*, '================================================='

EH=ECM(2)-ECM(1)
OPEN (1,FILE=BBB)
WRITE (1,*) '      T9                SV'
PRINT *, '     T9            SV'
```

```
DO J=1,500
T9(J)=1.0D-2*J
DO I=NN,NV
SI(I)=SE(I)*ECM(I)*DEXP(-11.605D0*ECM(I)/T9(J))
ENDDO

CALL SIMP(SI,EH,NV,SSV) ! X(I+1)-X(I) EQ X(I+2)-X(I+1)
SV(J)=3.7313D4*SSV/DSQRT(PM)/(DSQRT(T9(J)))**3

WRITE (*,2) T9(J),SV(J)
WRITE (1,2) T9(J),SV(J)
ENDDO
CLOSE (1)
2 FORMAT(2(E13.6,2X))
END

SUBROUTINE WHI(R,WH)
IMPLICIT REAL(8) (A-Z)
EXTERNAL F
REAL(8) F
INTEGER ERROR,L
COMMON /AA/ SKS,GK,SS,AAK,GAM,L
COMMON /XX/ CC
CC=2.0D-000*R*SS; Z=CC**AAK
XN=0.0E-00; XV=15.0E-00; H=1.05E-03; EPS=1.0E-03
CALL DF60D(F,XN,XV,H,EPS,RES,SE,ERROR)
WH=RES*DEXP(-CC/2.0D-000)/(Z*GAM)
END

FUNCTION F(X)
IMPLICIT REAL(8) (A-Z)
INTEGER L
COMMON /AA/ SKS,GK,SS,AA,GAM,L
COMMON /XX/ CC
REAL(8) F,X
BB=L
F=X**(AA+BB)*(1.0D-000+X/CC)**(BB-AA)*DEXP(-X)
END

SUBROUTINE DF60D(FUN, X, XOUT, H, EPS, SI, SE, ERROR)
! INTEGRATION OF FUNCTION FUN(X) BY BODE FORLULA
! WITH AUTOMATIC В Ы Б О Р О М CHOICE OF INTEGRATION STEP.
! PROGRAMM AUTHOR: VLADIMIR POTEMKIN, FORTRAN@YANDEX.RU
! ST. PETERSBURG, 2005
INTERFACE
 DOUBLE PRECISION FUNCTION FUN(X)
 DOUBLE PRECISION, INTENT(IN):: X
 END FUNCTION FUN
END INTERFACE
```

```
DOUBLE PRECISION, INTENT(IN):: XOUT
DOUBLE PRECISION, INTENT(INOUT):: X, H, EPS
DOUBLE PRECISION:: SI, SE
INTEGER:: ERROR
DOUBLE PRECISION, PARAMETER:: ARB=0.001, ONEP=1.000001, EEE=128.0
DOUBLE PRECISION, PARAMETER:: C=0.35555555555555556D0, &
 C1=0.21875D0, C2=0.375D0
DOUBLE PRECISION, PARAMETER:: CE=1.0835978835978836D0, &
 CE0=-0.078125D0, CE01=0.42857142857142857D0, CE1=-0.9375D0, &
 CE2=-0.46875D0, CE3=0.0625D0, CE4=-0.66964285714285714D-2
LOGICAL:: HDIV2
INTEGER:: N
DOUBLE PRECISION, SAVE:: HM16, DX, F4
DOUBLE PRECISION:: I, ERR
DOUBLE PRECISION, SAVE:: S1, S2
DOUBLE PRECISION:: F0, F1, F2, F3, F01, F12, F33, F44, E, HMIN, SAVEH, R
!BEGIN
 IF (X==XOUT) THEN
 H=0.0; SI=0.0; SE=0.0; ERROR=1; RETURN
 END IF
 HM16=16.0*EPSILON(1.0)
 IF (ABS(X)>ARB) THEN; HMIN=HM16*ABS(X)
 ELSE; HMIN=HM16*ARB
 END IF
 DX=XOUT-X
 IF (ABS(DX)<2.0*HMIN) THEN
 H=DX
 SI=0.5*H*(FUN(X)+FUN(XOUT)); SE=0.0
 X=XOUT; ERROR=1; RETURN
 END IF
 IF (EPS<EPSILON(1.0)/EEE) THEN
 EPS=EPSILON(1.0)/EEE; SI=0.0; SE=0.0
 ERROR=2; RETURN
 END IF
 IF (ABS(H)<HMIN) H=HMIN
 H=SIGN(H, DX); S1=0.D0; S2=0.D0; F4=FUN(X)
 N=0; HDIV2=.FALSE.
 ERROR=0
DO
 IF (2.0*ABS(H)>ABS(DX)) THEN
 SAVEH=H
 IF (ABS(H)≥ABS(DX)) THEN; H=DX; N=1
 ELSE; H=0.5*DX; N=2
 END IF
 END IF
10 CONTINUE
 F0=F4
 F2=FUN(X+0.5*H); F4=FUN(X+H)
20 CONTINUE
```

```
 F1=FUN(X+0.25*H); F3=FUN(X+0.75*H)
30 CONTINUE
 F01=FUN(X+0.125*H); F12=FUN(X+0.375*H)
 I=C*H*(C1*F0+C1*F4+C2*F2+F1+F3)
ERR=CE*H*(CE4*F4+CE0*F0+CE2*F2+CE1*F1+CE3*F3+CE01*F01+F12)
 IF (SNGL(DABS(I))>ARB) THEN; E=SNGL(DABS(ERR)/DABS(I))
 ELSE; E=SNGL(DABS(ERR)/ARB)
 END IF
 E=E/(EEE*EPS)
 IF (E>1.0) THEN
 IF (ABS(X)>ARB) THEN; HMIN=HM16*ABS(X)
 ELSE; HMIN=HM16*ARB
 END IF
 IF (ABS(H)<HMIN*ONEP) THEN
 SI=SNGL(S1); SE=SNGL(S2); ERROR=65; RETURN
 END IF
 H=0.5*H; N=2*N
 IF (ABS(H)<HMIN) THEN
 H=SIGN(HMIN,H); N=0
 HDIV2=.FALSE.; GOTO 10
 END IF
 F44=F4; F33=F3; F4=F2; F3=F12; F2=F1; F1=F01
 HDIV2=.TRUE.; GOTO 30
 END IF
 X=X+H; S1=S1+I; S2=S2+ERR
 IF (N>0) THEN
 N=N-1
 IF (N==0) THEN
 H=SAVEH; SI=SNGL(S1); SE=SNGL(S2); RETURN
 END IF
 END IF
 IF (HDIV2) THEN
 F0=F4; F2=F33; F4=F44
 HDIV2=.FALSE.; GOTO 20
 END IF
 IF (N>0.AND.N<5) GOTO 10
 IF (E>6.1222E-6) THEN
 R=0.9/(E**(1.0/7.0))
 ELSE
 R=5.0
 END IF
 N=0; H=H*R; DX=XOUT-X
END DO
END
```

The results of the control account of the total cross-sections of proton capture on ^{16}O to the first ES for potential (A1.5) using the above program, which are shown in Fig. A1.3, are presented below. The binding energy is first determined.

E	N	δE
−0.10531600213940004	4000	−3.4735629920001898E−004
−0.10522917364400008	8000	−8.6828495399954297E−005
−0.10520746717920007	16000	−2.1706464800014258E−005
−0.10520204061710001	32000	−5.4265621000637587E−006
−0.10520068395979999	64000	−1.3566573000139970E−006
−0.10520034490069999	128000	−3.3905910000464612E−007
−0.10520025964980005	256000	−8.5250899936606395E−008

This listing output shows the convergence of the binding energy of E for the first ES of the p^{16}O system depending on the current accuracy of δE or DEL-E and the given number of steps of N, which provides the accuracy of the given EP1.

Furthermore, the listing output for the calculation of asymptotic constant C_w (as well as C_0 and C_{w0} [12,14]) depending on the intercluster distance of R is presented below, along with the range of distances at which the constant changes are no more than those on EP2

R	C0	CW0	CW
0.187500E+02	−0.226977E+00	−0.829785E+01	−0.205452E+03
0.375000E+02	−0.517858E−01	−0.257584E+02	−0.205452E+03
0.562500E+02	−0.188247E−01	−0.431145E+02	−0.205452E+03
0.750000E+02	−0.862420E−02	−0.583651E+02	−0.205452E+03
0.937500E+02	−0.455287E−02	−0.713999E+02	−0.205452E+03
0.112500E+03	−0.264773E−02	−0.825078E+02	−0.205452E+03
0.131250E+03	−0.165245E−02	−0.920196E+02	−0.205452E+03
0.150000E+03	−0.108847E−02	−0.100225E+03	−0.205452E+03
0.168750E+03	−0.748220E−03	−0.107359E+03	−0.205452E+03
0.187500E+03	−0.532448E−03	−0.113610E+03	−0.205452E+03
0.206250E+03	−0.389923E−03	−0.119126E+03	−0.205452E+03
0.225000E+03	−0.292532E−03	−0.124028E+03	−0.205452E+03
0.243750E+03	−0.22404E−03	−0.128410E+03	−0.205452E+03
0.262500E+03	−0.174680E−03	−0.132349E+03	−0.205452E+03
0.281250E+03	−0.138332E−03	−0.135909E+03	−0.205452E+03
0.300000E+03	−0.111063E−03	−0.139141E+03	−0.205452E+03

The calculation results of charge $\langle R_z^2\rangle^{1/2}$ and mass $\langle R_m^2\rangle^{1/2}$ for the radii of ^{17}F in p^{16}O channel (in fm) are:

$$(\mathrm{RM}^2)^{1/2} = 2.91$$

$$(\mathrm{RZ}^2)^{1/2} = 3.07$$

In conclusion, the results of the total cross-sections (in μb) at energies starting from 0.03 MeV are presented below.

ECM	SF	SZ	FA
.30000E−01	.10187E+02	.15207E−13	.00000E+00
.40000E−01	.94776E+01	.41495E−11	.00000E+00
.50000E−01	.89372E+01	.18392E−09	.00000E+00
.60000E−01	.84987E+01	.29476E−08	.00000E+00
.70000E−01	.81298E+01	.25012E−07	.00000E+00
.80000E−01	.78120E+01	.13834E−06	.00000E+00
.90000E−01	.75262E+01	.56395E−06	.18000E+03
.10000E+00	.72785E+01	.18375E−05	.18000E+03
.11000E+00	.70564E+01	.50415E−05	.18000E+03
.12000E+00	.68555E+01	.12090E−04	.18000E+03
.13000E+00	.66726E+01	.26028E−04	.18000E+03
.14000E+00	.65050E+01	.51324E−04	.18000E+03
.15000E+00	.63508E+01	.94112E−04	.18000E+03
.16000E+00	.62082E+01	.16238E−03	.18000E+03
.17000E+00	.60758E+01	.26607E−03	.18000E+03
.18000E+00	.59524E+01	.41712E−03	.18000E+03
.19000E+00	.58371E+01	.62947E−03	.18000E+03
.20000E+00	.57291E+01	.91888E−03	.18000E+03
.21000E+00	.56275E+01	.13029E−02	.18000E+03
.22000E+00	.55318E+01	.18005E−02	.18000E+03
.23000E+00	.54414E+01	.24321E−02	.17999E+03
.24000E+00	.53559E+01	.32193E−02	.17999E+03
.25000E+00	.52749E+01	.41843E−02	.17999E+03
.26000E+00	.51979E+01	.53501E−02	.17999E+03
.27000E+00	.51247E+01	.67402E−02	.17998E+03
.28000E+00	.50549E+01	.83781E−02	.17998E+03
.29000E+00	.49884E+01	.10287E−01	.17997E+03
.30000E+00	.49248E+01	.12491E−01	.17997E+03
.31000E+00	.48641E+01	.15013E−01	.17996E+03
.32000E+00	.48059E+01	.17875E−01	.17995E+03
.33000E+00	.47501E+01	.21100E−01	.17994E+03
.34000E+00	.46967E+01	.24708E−01	.17993E+03
.35000E+00	.46454E+01	.28720E−01	.17992E+03
.36000E+00	.45961E+01	.33155E−01	.17991E+03
.37000E+00	.45488E+01	.38032E−01	.17990E+03
.38000E+00	.45033E+01	.43368E−01	.17989E+03
.39000E+00	.44595E+01	.49181E−01	.17987E+03

.40000E+00	.44173E+01	.55486E−01	.17986E+03
.41000E+00	.43767E+01	.62298E−01	.17984E+03
.42000E+00	.43377E+01	.69630E−01	.17982E+03
.43000E+00	.43000E+01	.77495E−01	.17980E+03
.44000E+00	.42637E+01	.85905E−01	.17978E+03
.45000E+00	.42287E+01	.94870E−01	.17976E+03
.46000E+00	.41950E+01	.10440E+00	.17974E+03
.47000E+00	.41624E+01	.11451E+00	.17972E+03
.48000E+00	.41310E+01	.12520E+00	.17970E+03
.49000E+00	.41007E+01	.13648E+00	.17968E+03
.50000E+00	.40715E+01	.14835E+00	.17966E+03
.51000E+00	.40433E+01	.16083E+00	.17963E+03
.52000E+00	.40161E+01	.17392E+00	.17961E+03
.53000E+00	.39898E+01	.18762E+00	.17958E+03
.54000E+00	.39644E+01	.20193E+00	.17956E+03
.55000E+00	.39399E+01	.21687E+00	.17954E+03
.56000E+00	.39162E+01	.23242E+00	.17951E+03
.57000E+00	.38933E+01	.24860E+00	.17949E+03
.58000E+00	.38712E+01	.26541E+00	.17946E+03
.59000E+00	.38499E+01	.28284E+00	.17944E+03
.60000E+00	.38292E+01	.30089E+00	.17942E+03
.61000E+00	.38092E+01	.31958E+00	.17939E+03
.62000E+00	.37899E+01	.33888E+00	.17937E+03
.63000E+00	.37712E+01	.35881E+00	.17935E+03
.64000E+00	.37532E+01	.37937E+00	.17933E+03
.65000E+00	.37357E+01	.40054E+00	.17931E+03
.66000E+00	.37187E+01	.42233E+00	.17929E+03
.67000E+00	.37023E+01	.44473E+00	.17927E+03
.68000E+00	.36864E+01	.46775E+00	.17925E+03
.69000E+00	.36710E+01	.49137E+00	.17923E+03
.70000E+00	.36560E+01	.51559E+00	.17921E+03
.71000E+00	.36415E+01	.54041E+00	.17919E+03
.72000E+00	.36274E+01	.56583E+00	.17917E+03
.73000E+00	.36137E+01	.59183E+00	.17916E+03
.74000E+00	.36004E+01	.61841E+00	.17914E+03
.75000E+00	.35875E+01	.64557E+00	.17913E+03
.76000E+00	.35749E+01	.67330E+00	.17912E+03
.77000E+00	.35626E+01	.70159E+00	.17910E+03
.78000E+00	.35507E+01	.73044E+00	.17909E+03
.79000E+00	.35391E+01	.75984E+00	.17908E+03
.80000E+00	.35277E+01	.78978E+00	.17907E+03

.81000E+00	.35166E+01	.82025E+00	.17906E+03
.82000E+00	.35058E+01	.85125E+00	.17905E+03
.83000E+00	.34953E+01	.88276E+00	.17904E+03
.84000E+00	.34849E+01	.91478E+00	.17904E+03
.85000E+00	.34748E+01	.94731E+00	.17903E+03
.86000E+00	.34649E+01	.98032E+00	.17902E+03
.87000E+00	.34553E+01	.10138E+01	.17902E+03
.88000E+00	.34457E+01	.10478E+01	.17902E+03
.89000E+00	.34364E+01	.10822E+01	.17901E+03
.90000E+00	.34273E+01	.11171E+01	.17901E+03
.91000E+00	.34183E+01	.11525E+01	.17901E+03
.92000E+00	.34095E+01	.11882E+01	.17900E+03
.93000E+00	.34008E+01	.12244E+01	.17900E+03
.94000E+00	.33922E+01	.12610E+01	.17900E+03
.95000E+00	.33838E+01	.12981E+01	.17900E+03
.96000E+00	.33756E+01	.13355E+01	.17900E+03
.97000E+00	.33674E+01	.13733E+01	.17900E+03
.98000E+00	.33594E+01	.14115E+01	.17900E+03
.99000E+00	.33514E+01	.14501E+01	.17901E+03
.10000E+01	.33436E+01	.14890E+01	.17901E+03
.10100E+01	.33359E+01	.15283E+01	.17901E+03
.10200E+01	.33283E+01	.15679E+01	.17901E+03
.10300E+01	.33207E+01	.16078E+01	.17901E+03
.10400E+01	.33133E+01	.16481E+01	.17902E+03
.10500E+01	.33060E+01	.16887E+01	.17902E+03
.10600E+01	.32987E+01	.17296E+01	.17902E+03
.10700E+01	.32915E+01	.17708E+01	.17903E+03
.10800E+01	.32844E+01	.18122E+01	.17903E+03
.10900E+01	.32774E+01	.18540E+01	.17903E+03
.11000E+01	.32704E+01	.18960E+01	.17904E+03
.11100E+01	.32635E+01	.19383E+01	.17904E+03
.11200E+01	.32567E+01	.19809E+01	.17905E+03
.11300E+01	.32500E+01	.20237E+01	.17905E+03
.11400E+01	.32433E+01	.20667E+01	.17905E+03
.11500E+01	.32367E+01	.21100E+01	.17906E+03
.11600E+01	.32302E+01	.21535E+01	.17906E+03
.11700E+01	.32238E+01	.21972E+01	.17907E+03
.11800E+01	.32174E+01	.22412E+01	.17907E+03
.11900E+01	.32110E+01	.22853E+01	.17907E+03
.12000E+01	.32048E+01	.23296E+01	.17908E+03
.12100E+01	.31986E+01	.23742E+01	.17908E+03

.12200E+01	.31924E+01	.24189E+01	.17908E+03
.12300E+01	.31864E+01	.24638E+01	.17909E+03
.12400E+01	.31804E+01	.25089E+01	.17909E+03
.12500E+01	.31744E+01	.25541E+01	.17909E+03
.12600E+01	.31686E+01	.25995E+01	.17909E+03
.12700E+01	.31627E+01	.26451E+01	.17910E+03
.12800E+01	.31570E+01	.26908E+01	.17910E+03
.12900E+01	.31513E+01	.27367E+01	.17910E+03
.13000E+01	.31457E+01	.27827E+01	.17910E+03
.13100E+01	.31401E+01	.28288E+01	.17911E+03
.13200E+01	.31346E+01	.28751E+01	.17911E+03
.13300E+01	.31292E+01	.29215E+01	.17911E+03
.13400E+01	.31238E+01	.29681E+01	.17911E+03
.13500E+01	.31185E+01	.30148E+01	.17911E+03
.13600E+01	.31133E+01	.30615E+01	.17911E+03
.13700E+01	.31081E+01	.31084E+01	.17911E+03
.13800E+01	.31030E+01	.31555E+01	.17912E+03
.13900E+01	.30979E+01	.32026E+01	.17912E+03
.14000E+01	.30929E+01	.32498E+01	.17912E+03
.14100E+01	.30880E+01	.32971E+01	.17912E+03
.14200E+01	.30832E+01	.33445E+01	.17912E+03
.14300E+01	.30784E+01	.33920E+01	.17912E+03
.14400E+01	.30736E+01	.34396E+01	.17912E+03
.14500E+01	.30689E+01	.34873E+01	.17912E+03
.14600E+01	.30643E+01	.35351E+01	.17912E+03
.14700E+01	.30597E+01	.35829E+01	.17912E+03
.14800E+01	.30552E+01	.36309E+01	.17912E+03
.14900E+01	.30508E+01	.36789E+01	.17912E+03
.15000E+01	.30464E+01	.37269E+01	.17911E+03
.15100E+01	.30421E+01	.37751E+01	.17911E+03
.15200E+01	.30378E+01	.38233E+01	.17911E+03
.15300E+01	.30336E+01	.38716E+01	.17911E+03
.15400E+01	.30295E+01	.39199E+01	.17911E+03
.15500E+01	.30254E+01	.39683E+01	.17911E+03
.15600E+01	.30214E+01	.40167E+01	.17911E+03
.15700E+01	.30174E+01	.40652E+01	.17911E+03
.15800E+01	.30135E+01	.41137E+01	.17911E+03
.15900E+01	.30096E+01	.41623E+01	.17911E+03
.16000E+01	.30058E+01	.42109E+01	.17910E+03
.16100E+01	.30020E+01	.42596E+01	.17910E+03
.16200E+01	.29983E+01	.43083E+01	.17910E+03

.16300E+01	.29946E+01	.43570E+01	.17910E+03
.16400E+01	.29910E+01	.44058E+01	.17910E+03
.16500E+01	.29874E+01	.44546E+01	.17910E+03
.16600E+01	.29839E+01	.45034E+01	.17910E+03
.16700E+01	.29804E+01	.45523E+01	.17909E+03
.16800E+01	.29770E+01	.46011E+01	.17909E+03
.16900E+01	.29736E+01	.46500E+01	.17909E+03
.17000E+01	.29703E+01	.46989E+01	.17909E+03
.17100E+01	.29670E+01	.47478E+01	.17909E+03
.17200E+01	.29637E+01	.47967E+01	.17909E+03
.17300E+01	.29605E+01	.48457E+01	.17909E+03
.17400E+01	.29573E+01	.48946E+01	.17909E+03
.17500E+01	.29542E+01	.49435E+01	.17909E+03
.17600E+01	.29511E+01	.49925E+01	.17909E+03
.17700E+01	.29480E+01	.50414E+01	.17908E+03
.17800E+01	.29450E+01	.50903E+01	.17908E+03
.17900E+01	.29420E+01	.51392E+01	.17908E+03
.18000E+01	.29391E+01	.51881E+01	.17908E+03
.18100E+01	.29362E+01	.52370E+01	.17908E+03
.18200E+01	.29333E+01	.52859E+01	.17908E+03
.18300E+01	.29304E+01	.53347E+01	.17908E+03
.18400E+01	.29276E+01	.53835E+01	.17908E+03
.18500E+01	.29248E+01	.54323E+01	.17908E+03
.18600E+01	.29221E+01	.54811E+01	.17908E+03
.18700E+01	.29193E+01	.55298E+01	.17908E+03
.18800E+01	.29166E+01	.55785E+01	.17908E+03
.18900E+01	.29139E+01	.56271E+01	.17908E+03
.19000E+01	.29113E+01	.56758E+01	.17908E+03
.19100E+01	.29087E+01	.57243E+01	.17908E+03
.19200E+01	.29061E+01	.57729E+01	.17908E+03
.19300E+01	.29035E+01	.58213E+01	.17908E+03
.19400E+01	.29009E+01	.58698E+01	.17908E+03
.19500E+01	.28984E+01	.59181E+01	.17908E+03
.19600E+01	.28959E+01	.59665E+01	.17908E+03
.19700E+01	.28934E+01	.60147E+01	.17908E+03
.19800E+01	.28909E+01	.60629E+01	.17908E+03
.19900E+01	.28884E+01	.61111E+01	.17908E+03
.20000E+01	.28860E+01	.61591E+01	.17909E+03
.20100E+01	.28836E+01	.62071E+01	.17909E+03
.20200E+01	.28812E+01	.62551E+01	.17909E+03
.20300E+01	.28788E+01	.63029E+01	.17909E+03

.20400E+01	.28764E+01	.63507E+01	.17909E+03
.20500E+01	.28741E+01	.63984E+01	.17909E+03
.20600E+01	.28717E+01	.64460E+01	.17909E+03
.20700E+01	.28694E+01	.64936E+01	.17909E+03
.20800E+01	.28671E+01	.65411E+01	.17909E+03
.20900E+01	.28648E+01	.65884E+01	.17910E+03
.21000E+01	.28625E+01	.66357E+01	.17910E+03
.21100E+01	.28602E+01	.66829E+01	.17910E+03
.21200E+01	.28579E+01	.67300E+01	.17910E+03
.21300E+01	.28557E+01	.67771E+01	.17910E+03
.21400E+01	.28535E+01	.68240E+01	.17910E+03
.21500E+01	.28512E+01	.68708E+01	.17911E+03
.21600E+01	.28490E+01	.69175E+01	.17911E+03
.21700E+01	.28468E+01	.69641E+01	.17911E+03
.21800E+01	.28446E+01	.70107E+01	.17911E+03
.21900E+01	.28424E+01	.70571E+01	.17911E+03
.22000E+01	.28402E+01	.71034E+01	.17911E+03
.22100E+01	.28381E+01	.71496E+01	.17912E+03
.22200E+01	.28359E+01	.71957E+01	.17912E+03
.22300E+01	.28337E+01	.72417E+01	.17912E+03
.22400E+01	.28316E+01	.72876E+01	.17912E+03
.22500E+01	.28295E+01	.73334E+01	.17912E+03
.22600E+01	.28273E+01	.73790E+01	.17913E+03
.22700E+01	.28252E+01	.74246E+01	.17913E+03
.22800E+01	.28231E+01	.74700E+01	.17913E+03
.22900E+01	.28210E+01	.75153E+01	.17913E+03
.23000E+01	.28189E+01	.75605E+01	.17913E+03
.23100E+01	.28168E+01	.76056E+01	.17913E+03
.23200E+01	.28147E+01	.76506E+01	.17914E+03
.23300E+01	.28127E+01	.76954E+01	.17914E+03
.23400E+01	.28106E+01	.77402E+01	.17914E+03
.23500E+01	.28085E+01	.77848E+01	.17914E+03
.23600E+01	.28065E+01	.78293E+01	.17914E+03
.23700E+01	.28044E+01	.78736E+01	.17914E+03
.23800E+01	.28024E+01	.79179E+01	.17915E+03
.23900E+01	.28004E+01	.79620E+01	.17915E+03
.24000E+01	.27983E+01	.80060E+01	.17915E+03
.24100E+01	.27963E+01	.80499E+01	.17915E+03
.24200E+01	.27943E+01	.80936E+01	.17915E+03
.24300E+01	.27923E+01	.81372E+01	.17915E+03
.24400E+01	.27903E+01	.81807E+01	.17916E+03

.24500E+01	.27883E+01	.82241E+01	.17916E+03
.24600E+01	.27863E+01	.82674E+01	.17916E+03
.24700E+01	.27843E+01	.83105E+01	.17916E+03
.24800E+01	.27824E+01	.83535E+01	.17916E+03
.24900E+01	.27804E+01	.83964E+01	.17916E+03
.25000E+01	.27785E+01	.84391E+01	.17916E+03
.25100E+01	.27765E+01	.84818E+01	.17917E+03
.25200E+01	.27746E+01	.85243E+01	.17917E+03
.25300E+01	.27726E+01	.85666E+01	.17917E+03
.25400E+01	.27707E+01	.86089E+01	.17917E+03
.25500E+01	.27688E+01	.86510E+01	.17917E+03
.25600E+01	.27669E+01	.86930E+01	.17917E+03
.25700E+01	.27650E+01	.87349E+01	.17917E+03
.25800E+01	.27631E+01	.87766E+01	.17917E+03
.25900E+01	.27612E+01	.88182E+01	.17917E+03
.26000E+01	.27593E+01	.88597E+01	.17918E+03
.26100E+01	.27574E+01	.89011E+01	.17918E+03
.26200E+01	.27556E+01	.89423E+01	.17918E+03
.26300E+01	.27537E+01	.89834E+01	.17918E+03
.26400E+01	.27518E+01	.90244E+01	.17918E+03
.26500E+01	.27500E+01	.90653E+01	.17918E+03
.26600E+01	.27482E+01	.91060E+01	.17918E+03
.26700E+01	.27463E+01	.91467E+01	.17918E+03
.26800E+01	.27445E+01	.91871E+01	.17918E+03
.26900E+01	.27427E+01	.92275E+01	.17918E+03
.27000E+01	.27409E+01	.92678E+01	.17918E+03
.27100E+01	.27391E+01	.93079E+01	.17918E+03
.27200E+01	.27373E+01	.93479E+01	.17918E+03
.27300E+01	.27355E+01	.93877E+01	.17918E+03
.27400E+01	.27337E+01	.94275E+01	.17918E+03
.27500E+01	.27320E+01	.94671E+01	.17919E+03
.27600E+01	.27302E+01	.95066E+01	.17919E+03
.27700E+01	.27285E+01	.95460E+01	.17919E+03
.27800E+01	.27267E+01	.95853E+01	.17919E+03
.27900E+01	.27250E+01	.96244E+01	.17919E+03
.28000E+01	.27233E+01	.96634E+01	.17919E+03
.28100E+01	.27215E+01	.97023E+01	.17919E+03
.28200E+01	.27198E+01	.97411E+01	.17919E+03
.28300E+01	.27181E+01	.97797E+01	.17919E+03
.28400E+01	.27164E+01	.98182E+01	.17919E+03
.28500E+01	.27147E+01	.98566E+01	.17919E+03

.28600E+01	.27131E+01	.98949E+01	.17919E+03
.28700E+01	.27114E+01	.99331E+01	.17919E+03
.28800E+01	.27097E+01	.99711E+01	.17919E+03
.28900E+01	.27081E+01	.10009E+02	.17919E+03
.29000E+01	.27064E+01	.10047E+02	.17919E+03
.29100E+01	.27048E+01	.10085E+02	.17919E+03
.29200E+01	.27031E+01	.10122E+02	.17919E+03
.29300E+01	.27015E+01	.10160E+02	.17919E+03
.29400E+01	.26999E+01	.10197E+02	.17919E+03
.29500E+01	.26983E+01	.10234E+02	.17919E+03
.29600E+01	.26967E+01	.10271E+02	.17919E+03
.29700E+01	.26951E+01	.10308E+02	.17919E+03
.29800E+01	.26935E+01	.10345E+02	.17919E+03
.29900E+01	.26919E+01	.10382E+02	.17919E+03
.30000E+01	.26903E+01	.10418E+02	.17919E+03
.30100E+01	.26887E+01	.10455E+02	.17919E+03
.30200E+01	.26872E+01	.10491E+02	.17919E+03
.30300E+01	.26856E+01	.10527E+02	.17919E+03
.30400E+01	.26841E+01	.10563E+02	.17919E+03
.30500E+01	.26825E+01	.10599E+02	.17919E+03
.30600E+01	.26810E+01	.10635E+02	.17919E+03
.30700E+01	.26794E+01	.10671E+02	.17919E+03
.30800E+01	.26779E+01	.10707E+02	.17919E+03
.30900E+01	.26764E+01	.10742E+02	.17919E+03
.31000E+01	.26749E+01	.10777E+02	.17919E+03
.31100E+01	.26734E+01	.10813E+02	.17919E+03
.31200E+01	.26719E+01	.10848E+02	.17919E+03
.31300E+01	.26704E+01	.10883E+02	.17919E+03
.31400E+01	.26689E+01	.10918E+02	.17919E+03
.31500E+01	.26674E+01	.10953E+02	.17919E+03
.31600E+01	.26659E+01	.10987E+02	.17919E+03
.31700E+01	.26644E+01	.11022E+02	.17919E+03
.31800E+01	.26629E+01	.11056E+02	.17919E+03
.31900E+01	.26615E+01	.11090E+02	.17919E+03
.32000E+01	.26600E+01	.11125E+02	.17919E+03
.32100E+01	.26585E+01	.11159E+02	.17919E+03
.32200E+01	.26571E+01	.11193E+02	.17919E+03
.32300E+01	.26556E+01	.11226E+02	.17919E+03
.32400E+01	.26542E+01	.11260E+02	.17919E+03
.32500E+01	.26527E+01	.11294E+02	.17919E+03
.32600E+01	.26513E+01	.11327E+02	.17919E+03

.32700E+01	.26499E+01	.11360E+02	.17919E+03
.32800E+01	.26484E+01	.11393E+02	.17919E+03
.32900E+01	.26470E+01	.11426E+02	.17919E+03
.33000E+01	.26456E+01	.11459E+02	.17919E+03
.33100E+01	.26441E+01	.11492E+02	.17919E+03
.33200E+01	.26427E+01	.11525E+02	.17919E+03
.33300E+01	.26413E+01	.11557E+02	.17919E+03
.33400E+01	.26399E+01	.11590E+02	.17919E+03
.33500E+01	.26385E+01	.11622E+02	.17919E+03
.33600E+01	.26371E+01	.11654E+02	.17919E+03
.33700E+01	.26357E+01	.11686E+02	.17919E+03
.33800E+01	.26343E+01	.11718E+02	.17919E+03
.33900E+01	.26329E+01	.11750E+02	.17919E+03
.34000E+01	.26315E+01	.11782E+02	.17919E+03
.34100E+01	.26301E+01	.11813E+02	.17919E+03
.34200E+01	.26287E+01	.11845E+02	.17920E+03
.34300E+01	.26273E+01	.11876E+02	.17920E+03
.34400E+01	.26259E+01	.11907E+02	.17920E+03
.34500E+01	.26245E+01	.11938E+02	.17920E+03
.34600E+01	.26231E+01	.11969E+02	.17920E+03
.34700E+01	.26217E+01	.12000E+02	.17920E+03
.34800E+01	.26203E+01	.12030E+02	.17920E+03
.34900E+01	.26189E+01	.12061E+02	.17920E+03
.35000E+01	.26175E+01	.12091E+02	.17920E+03
.35100E+01	.26162E+01	.12121E+02	.17920E+03
.35200E+01	.26148E+01	.12151E+02	.17920E+03
.35300E+01	.26134E+01	.12181E+02	.17920E+03
.35400E+01	.26120E+01	.12211E+02	.17920E+03
.35500E+01	.26106E+01	.12241E+02	.17920E+03
.35600E+01	.26092E+01	.12271E+02	.17920E+03
.35700E+01	.26079E+01	.12300E+02	.17921E+03
.35800E+01	.26065E+01	.12329E+02	.17921E+03
.35900E+01	.26051E+01	.12359E+02	.17921E+03
.36000E+01	.26037E+01	.12388E+02	.17921E+03
.36100E+01	.26023E+01	.12417E+02	.17921E+03
.36200E+01	.26010E+01	.12445E+02	.17921E+03
.36300E+01	.25996E+01	.12474E+02	.17921E+03
.36400E+01	.25982E+01	.12503E+02	.17921E+03
.36500E+01	.25968E+01	.12531E+02	.17921E+03
.36600E+01	.25954E+01	.12559E+02	.17921E+03
.36700E+01	.25941E+01	.12587E+02	.17921E+03

.36800E+01	.25927E+01	.12615E+02	.17921E+03
.36900E+01	.25913E+01	.12643E+02	.17922E+03
.37000E+01	.25899E+01	.12671E+02	.17922E+03
.37100E+01	.25885E+01	.12699E+02	.17922E+03
.37200E+01	.25872E+01	.12726E+02	.17922E+03
.37300E+01	.25858E+01	.12754E+02	.17922E+03
.37400E+01	.25844E+01	.12781E+02	.17922E+03
.37500E+01	.25830E+01	.12808E+02	.17922E+03
.37600E+01	.25816E+01	.12835E+02	.17922E+03
.37700E+01	.25803E+01	.12862E+02	.17922E+03
.37800E+01	.25789E+01	.12888E+02	.17922E+03
.37900E+01	.25775E+01	.12915E+02	.17923E+03
.38000E+01	.25761E+01	.12941E+02	.17923E+03
.38100E+01	.25747E+01	.12968E+02	.17923E+03
.38200E+01	.25733E+01	.12994E+02	.17923E+03
.38300E+01	.25719E+01	.13020E+02	.17923E+03
.38400E+01	.25706E+01	.13046E+02	.17923E+03
.38500E+01	.25692E+01	.13072E+02	.17923E+03
.38600E+01	.25678E+01	.13097E+02	.17923E+03
.38700E+01	.25664E+01	.13123E+02	.17923E+03
.38800E+01	.25650E+01	.13148E+02	.17923E+03
.38900E+01	.25636E+01	.13174E+02	.17924E+03
.39000E+01	.25622E+01	.13199E+02	.17924E+03
.39100E+01	.25608E+01	.13224E+02	.17924E+03
.39200E+01	.25594E+01	.13249E+02	.17924E+03
.39300E+01	.25580E+01	.13274E+02	.17924E+03
.39400E+01	.25566E+01	.13298E+02	.17924E+03
.39500E+01	.25552E+01	.13323E+02	.17924E+03
.39600E+01	.25538E+01	.13347E+02	.17924E+03
.39700E+01	.25524E+01	.13372E+02	.17924E+03
.39800E+01	.25510E+01	.13396E+02	.17924E+03
.39900E+01	.25496E+01	.13420E+02	.17924E+03
.40000E+01	.25482E+01	.13444E+02	.17925E+03
.40100E+01	.25468E+01	.13467E+02	.17925E+03
.40200E+01	.25454E+01	.13491E+02	.17925E+03
.40300E+01	.25440E+01	.13515E+02	.17925E+03
.40400E+01	.25426E+01	.13538E+02	.17925E+03
.40500E+01	.25412E+01	.13561E+02	.17925E+03
.40600E+01	.25398E+01	.13584E+02	.17925E+03
.40700E+01	.25384E+01	.13608E+02	.17925E+03
.40800E+01	.25370E+01	.13630E+02	.17925E+03

.40900E+01	.25356E+01	.13653E+02	.17925E+03
.41000E+01	.25342E+01	.13676E+02	.17925E+03
.41100E+01	.25328E+01	.13698E+02	.17925E+03
.41200E+01	.25314E+01	.13721E+02	.17926E+03
.41300E+01	.25300E+01	.13743E+02	.17926E+03
.41400E+01	.25286E+01	.13765E+02	.17926E+03
.41500E+01	.25272E+01	.13787E+02	.17926E+03
.41600E+01	.25258E+01	.13809E+02	.17926E+03
.41700E+01	.25244E+01	.13831E+02	.17926E+03
.41800E+01	.25229E+01	.13853E+02	.17926E+03
.41900E+01	.25215E+01	.13875E+02	.17926E+03
.42000E+01	.25201E+01	.13896E+02	.17926E+03
.42100E+01	.25187E+01	.13917E+02	.17926E+03
.42200E+01	.25173E+01	.13939E+02	.17926E+03
.42300E+01	.25159E+01	.13960E+02	.17926E+03
.42400E+01	.25145E+01	.13981E+02	.17926E+03
.42500E+01	.25131E+01	.14002E+02	.17926E+03
.42600E+01	.25117E+01	.14023E+02	.17927E+03
.42700E+01	.25103E+01	.14043E+02	.17927E+03
.42800E+01	.25088E+01	.14064E+02	.17927E+03
.42900E+01	.25074E+01	.14084E+02	.17927E+03
.43000E+01	.25060E+01	.14105E+02	.17927E+03
.43100E+01	.25046E+01	.14125E+02	.17927E+03
.43200E+01	.25032E+01	.14145E+02	.17927E+03
.43300E+01	.25018E+01	.14165E+02	.17927E+03
.43400E+01	.25004E+01	.14185E+02	.17927E+03
.43500E+01	.24990E+01	.14205E+02	.17927E+03
.43600E+01	.24976E+01	.14224E+02	.17927E+03
.43700E+01	.24962E+01	.14244E+02	.17927E+03
.43800E+01	.24947E+01	.14263E+02	.17927E+03
.43900E+01	.24933E+01	.14283E+02	.17927E+03
.44000E+01	.24919E+01	.14302E+02	.17927E+03
.44100E+01	.24905E+01	.14321E+02	.17927E+03
.44200E+01	.24891E+01	.14340E+02	.17927E+03
.44300E+01	.24877E+01	.14359E+02	.17927E+03
.44400E+01	.24863E+01	.14378E+02	.17927E+03
.44500E+01	.24849E+01	.14397E+02	.17927E+03
.44600E+01	.24835E+01	.14415E+02	.17927E+03
.44700E+01	.24821E+01	.14434E+02	.17927E+03
.44800E+01	.24807E+01	.14452E+02	.17927E+03
.44900E+01	.24793E+01	.14471E+02	.17927E+03

.45000E+01	.24779E+01	.14489E+02	.17928E+03
.45100E+01	.24764E+01	.14507E+02	.17928E+03
.45200E+01	.24750E+01	.14525E+02	.17928E+03
.45300E+01	.24736E+01	.14543E+02	.17928E+03
.45400E+01	.24722E+01	.14561E+02	.17928E+03
.45500E+01	.24708E+01	.14578E+02	.17928E+03
.45600E+01	.24694E+01	.14596E+02	.17928E+03
.45700E+01	.24680E+01	.14613E+02	.17928E+03
.45800E+01	.24666E+01	.14631E+02	.17928E+03
.45900E+01	.24652E+01	.14648E+02	.17928E+03
.46000E+01	.24638E+01	.14665E+02	.17928E+03
.46100E+01	.24624E+01	.14682E+02	.17928E+03
.46200E+01	.24610E+01	.14699E+02	.17928E+03
.46300E+01	.24596E+01	.14716E+02	.17928E+03
.46400E+01	.24582E+01	.14733E+02	.17928E+03
.46500E+01	.24568E+01	.14750E+02	.17928E+03
.46600E+01	.24554E+01	.14766E+02	.17928E+03
.46700E+01	.24540E+01	.14783E+02	.17928E+03
.46800E+01	.24526E+01	.14799E+02	.17928E+03
.46900E+01	.24512E+01	.14815E+02	.17928E+03
.47000E+01	.24498E+01	.14832E+02	.17928E+03
.47100E+01	.24484E+01	.14848E+02	.17928E+03
.47200E+01	.24470E+01	.14864E+02	.17928E+03
.47300E+01	.24456E+01	.14880E+02	.17928E+03
.47400E+01	.24442E+01	.14895E+02	.17928E+03
.47500E+01	.24429E+01	.14911E+02	.17928E+03
.47600E+01	.24415E+01	.14927E+02	.17928E+03
.47700E+01	.24401E+01	.14942E+02	.17928E+03
.47800E+01	.24387E+01	.14958E+02	.17928E+03
.47900E+01	.24373E+01	.14973E+02	.17928E+03
.48000E+01	.24359E+01	.14988E+02	.17928E+03
.48100E+01	.24345E+01	.15003E+02	.17928E+03
.48200E+01	.24331E+01	.15018E+02	.17928E+03
.48300E+01	.24317E+01	.15033E+02	.17928E+03
.48400E+01	.24303E+01	.15048E+02	.17928E+03
.48500E+01	.24289E+01	.15063E+02	.17928E+03
.48600E+01	.24275E+01	.15078E+02	.17928E+03
.48700E+01	.24262E+01	.15092E+02	.17928E+03
.48800E+01	.24248E+01	.15107E+02	.17928E+03
.48900E+01	.24234E+01	.15121E+02	.17928E+03
.49000E+01	.24220E+01	.15136E+02	.17928E+03

.49100E+01	.24206E+01	.15150E+02	.17928E+03
.49200E+01	.24192E+01	.15164E+02	.17928E+03
.49300E+01	.24178E+01	.15178E+02	.17928E+03
.49400E+01	.24164E+01	.15192E+02	.17928E+03
.49500E+01	.24150E+01	.15206E+02	.17928E+03
.49600E+01	.24137E+01	.15220E+02	.17928E+03
.49700E+01	.24123E+01	.15233E+02	.17928E+03
.49800E+01	.24109E+01	.15247E+02	.17928E+03
.49900E+01	.24095E+01	.15260E+02	.17928E+03
.50000E+01	.24081E+01	.15274E+02	.17928E+03
.50100E+01	.24067E+01	.15287E+02	.17928E+03
.50200E+01	.24053E+01	.15300E+02	.17928E+03
.50300E+01	.24040E+01	.15314E+02	.17928E+03

From this listing output it is clear that, at a laboratory energy of 30 keV, the total cross-section value becomes 10.2.

References

[1] Kapitonov I.M., Ishkhanov B.S., Tutyn I.A. Nucleosynthesis in the Universe. M.: Librokom. 2009; http://nuclphys.sinp.msu.ru /nuclsynt/index.html (in Russian).

[2] Kapitonov I.M., Ishkhanov B.S., Orlin V.N. Models of atomic nuclei. M.: Moscow State University. 2009; http://nuclphys.sinp.msu.ru/nucmod/nucmod1.htm (in Russian).

[3] Barnes C.A., Clayton, D.D., Schramm D.N. Essays in Nuclear Astrophysics. Presented to William A. Fowler. UK, Cambridge: Cambridge University Press. 1982. 562p.

[4] Gorbunov D.S., Rubakov V.A. Introduction to theory of early Universe. Theory of hot Big Bang. M.: LKI. 2008. 552p. (in Russian). Gorbunov D.S., Rubakov V.A. Introduction to theory of early Universe. Hot Big Bang Theory. World Scientific. 2011. 488p.

[5] Boyarkin O.M., Boyarkina G.G. Quantum electrodynamics and the standard model M.: Librokom. 2013. 440p.; Boyarkin O.M., Boyarkina G.G. From the electron to the Higgs boson. Quantum theory of free fields. M.: Stereotype. 2014. 296p.; Emelyanov V.M. The standard model and its extensions. M.: Fiz.-Math. Lit. 2007. 584p.; http://www.astronet.ru/db/msg/1199352 /experiments/exper2.html. (in Russian).

[6] Wildermuth K., Tang Y.C. A unified theory of the nucleus. Branschweig: Vieweg. 1977. 498p; http://link.springer.com/book/10.1007%2F978-3-322-85255-7.

[7] Mertelmeir T., Hofmann H.M. Consistent cluster model description of the electromagnetic properties of lithium and beryllium nuclei // Nucl. Phys. 1986. V.A459. P.387–416.

[8] Dohet-Eraly J. Microscopic cluster model of elastic scattering and bremsstrahlung of light nuclei. Université Libre De Bruxelles. 2013. 120p.; http://theses.ulb.ac.be/ETD-db/collection/available/ULBetd-09122013-100019/unrestricted/these_Jeremy_Dohet-Eraly.pdf; Dohet-Eraly J. and Baye D. Microscopic cluster model of α+n, α+p, α+^{3}He, and α+α elastic scattering from a realistic effective nuclear interaction // Phys. Rev. 2011. V.C84. P.014604 (1–13).

[9] Descouvemont P., Dufour M. Microscopic cluster model // In: Clusters in Nuclei. V.2. Editor C. Beck. Berlin-Heidelberg: Springer-Verlag. 2012. 353p.; Descouvemont P. Microscopic cluster models. I. // http://www.nucleartheory.net/Talent_6_Course/TALENT_lectures/pd_microscopic_1.pdf

[10] Nesterov A.V. et al. Three clusters description of light nuclei properties // Phys. Part. Nucl. 2010. V.41. No.5. P.716–765; Nesterov A.V., Vasilevsky V.S., Kovalenko T.P. Spectra of nuclei ^{9}Be and ^{9}B in a three-cluster microscopic model // Ukr. Jour. Phys. 2013. V.58. No.7. P.628–635.

[11] Nemets O.F., Neudatchin V.G., Rudchik A.T., Smirnov Y.F., Tchuvil'sky Yu.M. Nucleon association in atomic nuclei and the nuclear reactions of the many nucleons transfers. Kiev: Naukova dumka. 1988. 488p. (in Russian).

[12] Dubovichenko S.B. Thermonuclear processes of the Universe. Second edition, revised and updated. Series "Kazakhstan space research". V.7. Almaty: A-tri. 2011. 402p.; arXiv:1012.0877 [nucl-th]. (in Russian).

[13] Dubovichenko S.B. Phase shifts analysis in nuclear astrophysics. Germany, Saarbrucken: Lambert Academy Publ. GmbH&Co. KG. 2015. 368c.; https://www.lap-publishing.com/catalog/details/store/pl/book/978-3-659-70629-5/Фазовый-анализ. (in Russian).

[14] Dubovichenko S.B. Thermonuclear processes in Stars and Universe. Third edition, revised and enlarged. Germany, Saarbrucken: Palmarium Academy Publ. GmbH&Co. KG. 2015. 348c.; https://www.palmarium-publishing.ru/catalog/details/store/it/book/978-3-659-60165-1/Термоядерные-процессы-в-Звездах. (in Russian); Dubovichenko S.B. Thermonuclear processes in Stars and Universe. Second English edition. Germany, Saarbrucken: Scholar's

https://doi.org/10.1515/9783110619607-010

Press. 2015. 332p.; https://www.scholars-press.com/catalog/details/store/gb/book/978-3-639-76478-9/Thermonuclear-processes-in-stars.
[15] Angulo C. et al. A compilation of charged-particle induced thermonuclear reaction rates // Nucl. Phys. 1999. V.A656. P.3–183.
[16] Shklovskii I.S. Stars: birth, life and death. M.: Nauka. 1984. 384p. (in Russian).
[17] Zel'dovich Ya.B., Novikov I.D. Relativistic Astrophysics, 2: Structure and Evolution of the Universe. Chicago and London: The University of Chicago press. Gary Steigman (Editor) 1983. 718p.
[18] Costantini H. et al. LUNA: a laboratory for underground nuclear astrophysics // Rep. Prog. Phys. 2009. V.72. P.086301(25p.).
[19] Dubovichenko S.B., Uzikov Yu.N. Astrophysical *S*-factors of reactions with light nuclei // Phys. Part. Nucl. 2011. V.42. P.251–301.
[20] Neudatchin V.G., Sakharuk A.A., Smirnov Yu.F. Generalized potential description of interaction of the lightest cluster scattering and photonuclear reactions // Sov. Jour. Part. Nucl. 1992. V.23. P.210–271; Neudatchin V.G., Struzhko B.G., Lebedev V.M. Supermultiplet potential model of the interaction of light clusters and unified description of various nuclear reactions // Phys. Part. Nucl. 2005. V.36. P.468–519.
[21] Neudatchin V.G. et al. Generalized potential model description of mutual scattering of the lightest p^2H, $^2H^3He$ nuclei and the corresponding photonuclear reactions // Phys. Rev. 1992. V.C45. P.1512–1527.
[22] Dubovichenko S.B. Properties of the light nuclei in potential cluster model. Second edition. Almaty: Daneker. 2004. 247p.; arXiv:1006.4944 [nucl-th]. (in Russian).
[23] Dubovichenko S.B., Dzhazairov-Kakhramanov A.V. Astrophysical *S*-factors of proton radiative capture in thermonuclear reactions in the stars and the universe // The Big Bang: Theory, Assumptions and Problems. New-York: Nova Science Publishers. 2011. P.1–60; https://www.novapublishers.com/catalog/product_info.php?products_id =21109.
[24] Dubovichenko S.B. Calculation method of the nuclear characteristics. Almaty: Complex. 2006. 311p.; arXiv:1006.4947 [nucl-th]. (in Russian).
[25] Blatt J.M., Weisskopf V.F. Theoretical nuclear physics. New-York-London: John Wiley. 1952. 864p.
[26] Breit G. Theory of resonance reactions and allied topics. Berlin-Gottingen-Heidelberg: Springer-Verlag. 1959. 398p.
[27] Preston M.A. Physics of the nucleus. Palo Alto-London: Addison-Wesley Publ. Co. Inc. 1962. 661p.
[28] Neudatchin V.G., Smirnov Yu.F. Nucleon associations in light nuclei. Moscow: Nauka. 1969. 414p. (in Russian).
[29] Bohr A., Mottelson B.R. Nuclear structure Vol.I. Single particle motion. Singapore: World Scientific Publ. Co. Ldt. 1998. 471p.
[30] Neudatchin V.G. et al. A microscopic substantiated optical potential for αt system including nucleon exchange // Lett. Nuovo Cim. 1972. V.5. P.834–838.
[31] Neudatchin V.G. et al. A microscopically substantiated local optical potential for αα scattering // Phys. Lett. 1971. V.B34. P.581–583.
[32] Kurdyumov I.V. et al. The high energy limit for the αd form factors in the ^{6}Li nuclei // Phys. Lett. 1972. V.40B. P.607–610.
[33] Neudachin V.G., Smirnov Yu.F. Forbidden states in systems of two and three composite particles // Modern problems of optics and atomic physics. Kiev: Kiev State University. 1974. P.225–241.
[34] Kukulin V.I, Neudatchin V.G., Smirnov Yu.F. Composite particle interaction relevant to the Pauli principle // Sov. Jour. Part. Nucl. 1979. V.10. P.1236–1255.

[35] Dubovichenko S.B., Kukulin V.I., Sazonov A.A. Structure of the ^{6,7}Li nuclei in cluster model based on potentials with forbidden states // Theory of quantum systems with strong interactions. Kalinin: KSU (former USSR). 1983. P.65–79.
[36] Dubovichenko S.B., Mazhitov M. Variation calculations of the ^{6,7}Li nuclei in cluster models with forbidden states // Bull. Acad. Sci. KazSSR ser. phys.-math. 1987. No.4. P.55–64.
[37] Dubovichenko S.B., Mazhitov M. Non orthogonal variational basis in two-body task // Almaty. KazSU P.1729–1735. Kaz. State NIINTI 1987. №1665.
[38] Dubovichenko S.B., Dzhazairov-Kakhramanov A.V. Potential description of cluster channels of lithium nuclei // Phys. Atom. Nucl. 1993. V.56. P.195–202.
[39] Dubovichenko S.B., Dzhazairov-Kakhramanov A.V. Calculation of coulomb form factors of lithium nuclei in a cluster model based on potentials with forbidden states // Phys Atom. Nucl. 1994. V.57. P.733–740.
[40] Dubovichenko S.B., Dzhazairov-Kakhramanov A.V. Photonuclear processes on ^{7}Li and ^{7}Be in the cluster model for potentials with forbidden states // Phys Atom. Nucl. 1995. V.58. P.579–585.
[41] Dubovichenko S.B., Dzhazairov-Kakhramanov A.V. Description of photonuclear processes on the ^{6}Li nucleus in cluster models based on potentials with forbidden states // Phys. Atom. Nucl. 1995. V.58. P.788–795.
[42] Dubovichenko S.B., Dzhazairov-Kakhramanov A.V. Electromagnetic effects in light nuclei and the cluster potential model // Phys. Part. Nucl. 1997. V.28. No.6. P.615–641.
[43] Iskra V. et al. Interference of various potential scattering amplitudes in mutual lightest clusters // Ukr. Phys. Jour. 1988. V.32. P.1141–1147.
[44] Iskra V. et al. Describe the capabilities of potential mutual scattering lightest clusters // Phys. Atom. Nucl. 1988. V.48. P.1674–1683.
[45] Neudachin V.G., Pomerantsev V.N., Sakharuk A.A. Potential description of photonuclear reactions ^{3}Heγ → p^{2}H and ^{3}He^{2}H → ^{5}Liγ // Phys. Atom. Nucl. 1990. V.52. P.738–744.
[46] Kukulin V.I. et al. A generalized potential description of the lightest clusters scattering on the example of systems p^{2}H and ^{2}H^{3}He // Phys. Atom. Nucl. 1990. V.52. P.402–411.
[47] Dubovichenko S.B. et al. Generalized potential description of the interaction of the lightest nuclei p^{3}H and p^{3}He // Bull. Acad. Sci. SSSR. Ser. Phys. 1990. V.54. P.911–916.
[48] Neudatchin V.G., Sakharuk A.A., Dubovichenko S.B. Photodisintegration of ^{4}He and supermultiplet potential model of cluster-cluster interaction //. Few Body Sys 1995. V.18. P.159–172.
[49] Neudatchin V.G. et al. The generalized potential model description of p^{2}H and ^{2}H^{3}He scattering // Phys. Lett. 1991. V.B255. P.482–486.
[50] Dubovichenko S.B., Dzhazairov-Kakhramanov A.V. Potential description of elastic N^{2}H, ^{2}H^{2}H, N^{4}He, and ^{2}H^{3}H scattering // Sov. Jour. Nucl. Phys. (former USSR) 1990. V.51. P.971–977.
[51] Dubovichenko S.B., Dzhazairov-Kakhramanov A.V. Potential description of elastic N^{3}H and N^{3}He scattering // Phys. Atom. Nucl. 1993. V.56. P.447–454.
[52] Dubovichenko S.B. Analysis of photonuclear processes in the N^{2}H and ^{2}H^{3}He systems on the basis of cluster models for potentials with forbidden states // Phys. Atom. Nucl. 1995. V.58. P.1174–1180.
[53] Dubovichenko S.B. Description of photoprocesses in the dd channel of the ^{4}He nucleus in potential cluster models // Phys. Atom. Nucl. 1995. V.58. P.1866–1872.
[54] Dubovichenko S.B. Photonuclear processes in the channels p^{3}H and n^{3}He of the ^{4}He nucleus in potential cluster models // Phys. Atom. Nucl. 1995. V.58. P.1295–1302.
[55] Dubovichenko S.B., Dzhazairov-Kakhramanov A.V., Sakharuk A.A. Potential description of n^{6}Li and ^{3}H^{4}He elastic-scattering // Phys. Atom. Nucl. 1993. V.56. P.1044–1053.

[56] Dubovichenko S.B., Dzhazairov-Kakhramanov A.V. Potential description of elastic αα, ^{2}H^{6}Li, and N^{7}Li scattering // Sov. Jour. Nucl. Phys. (former USSR) 1992. V.55. P.1632–1636.
[57] Dubovichenko S.B. Photonuclear processes in the ^{4}He^{12}C channel of the ^{16}O nucleus in potential cluster models // Phys. Atom. Nucl. 1996. V.59. P.421–427.
[58] Dubovichenko S.B. Photodisintegration of the ^{7}Li nucleus through the n^{6}Li channel in the potential cluster model involving forbidden states // Phys. Atom. Nucl. 1997. V.60. P.195–199.
[59] Dubovichenko S.B. Channels of the light nuclei in potential cluster models // Bull. KazATSO. Almaty. 2006. No.1. P.75–109.
[60] Frick R. et al. Strong tensor term in the optical potential for 20 MeV // Phys. Rev. Lett. 1980. V.44. P.14–16.
[61] Nishioka H., Tostevin J.A., Johnson R.C. Deformation effects in aligned ^{6}Li scattering // Phys. Lett. 1983. V.124B. P.17–20.
[62] Merchant A.C., Rowley N. Alpha deuteron cluster model of ^{6}Li including tensor forces // Phys. Lett. 1985. V.B150. P.35–40.
[63] Kukulin V.I. et al. Detailed study of the cluster structure of light nuclei in a three body model. I. Ground state of ^{6}Li // Nucl. Phys. 1984. V.A417. P.128–156.
[64] Kukulin V.I. et al. Detailed study of the cluster structure of light nuclei in a three body model. II. The spectrum of low lying of nuclei with A=6 // Nucl. Phys. 1986. V.A453. P.365–388.
[65] Kukulin V.I. et al. Detailed study of the cluster structure of light nuclei in a three body model. III. Electromagnetic structure of ^{6}Li // Nucl. Phys. 1990. V.A517. P.221–263.
[66] Lehman D.R., Parke W.C. Shell structure of the A=6 ground states from three body dynamics // Phys. Rev. 1983. V.C28. P.364–382.
[67] Lehman D.R., Parke W.C. A=6 structure from three body dynamics // Phys. Rev. Lett. 1983. V.50. P.98–101.
[68] Lehman D.R. Excluded bound state in the $S_{1/2}$ N^{4}He interaction and the three body bilding energies of ^{6}He and ^{6}Li // Phys. Rev. 1982. V.C25. P.3146–3154.
[69] Dubovichenko S.B. Tensor ^{2}H^{4}He interactions in the potential cluster model involving forbidden states // Phys. Atom. Nucl. 1998. V.61. P.162–168.
[70] Kukulin V.I., Pomerantsev V.N., Cooper S.G., Dubovichenko S.B. Improved ^{2}H^{4}He potentials by inversion: The tensor force and validity of the double folding model // Phys. Rev. 1998. V.C57. P.2462–2473.
[71] Neudatchin V.G., Obukhovsky I.T., Smirnov Yu.F. A nonrelativistic potential model with forbidden state for the NN interaction at small distances // Phys. Lett. 1973. V.B43. P.13–17.
[72] Neudatchin V.G. et al. Attractive potential with forbidden states for the NN interaction // Phys. Rev. 1975. V.C11. P.128–135.
[73] Dubovichenko S.B., Zhusupov M.A. Description of the NN interactions by potential with forbidden states // Bull. Acad. Sci. KazSSR ser. phys.-math. 1982. No.6. P.34–39.
[74] Kukulin V.I., et al. The NN potential with forbidden state suggested from a six-quark model with one-pion exchange // Phys. Lett. 1984. V.B135. P.20–27.
[75] Dubovichenko S.B. Deep exponential potential of nucleon-nucleon interaction // Phys. Atom. Nucl. 1997. V.60. P.621–622.
[76] Dubovichenko S.B. Deuteron form factors for the Nijmegen potentials // Phys. Atom. Nucl. 2000. V.63. P.734–738; Dubovichenko S.B., Strakovsky I.I. Simple local NN potentials involving forbidden states and polarization in ed scattering // Phys. Atom. Nucl. 2000. V.63. P.582–587.
[77] Strakovsky I.I., Dubovichenko S.B. Electron deuteron elastic scattering in a simple NN potential with excluded spurious states: non-relativistic calculations // Bull. Amer. Phys. Soc. 1999. V.44. P.731.

[78] Dubovichenko S.B. An alternative method for solving generalized matrix eigenvalue problem // Bull. Nat. Acad. Sci. Rep. Kazakhstan. ser. phys.-math. 2007. No.4. P.52–55.
[79] Dubovichenko S.B. The method of discrepancy for the solution of the eigenvalue problem for a system of second order differential equations // Bull. Nat. Acad. Sci. Rep. Kazakhstan. ser. phys.-math. 2007. No.4. P.49–51.
[80] Kamke E. Differentialgleichungen: Losungsmethoden und Losungen. I. Leipzig: Gewohnliche Differentialgleichungen. B.G. Teubner. 1977. 575p.
[81] *Abramowitz I.G.* Supplemental math. library. Mathematical analysis. Differentiation and integration. M.: Fiz.-Math. Lit. 1961. 350p. (in Russian).
[82] Kopchenova I.V., Maron I.A. Computational Mathematics in the examples and tasks. M.: Fiz.-Math. Lit. 1972. 399p. (in Russian).
[83] Madelung E. Die mathematischen hilfsmittel des physikers. Berlin-Heidelberg: Springer-Verlag. 1957. 618p.
[84] Troizkii V.A. Engineering calculations on a computer. L.: Mechanical Engineering. 1979. 287p. (in Russian).
[85] Jeffres H., Swirles B. Methods of mathematical physics. Cambridge: Cambr. Univ. Press. 1966. 350p.
[86] Babich V.M. et al. Supplemental mathematical library. Linear equations of mathematical physics. M.: Nauka. 1964. 367p. (in Russian).
[87] Mathews J. Walker R. Mathematical method of physics. New-York: W.A. Benjamin Inc. 1964. 498p.
[88] Zaguskii V.L. Guide on numerical methods of solution of equations. M.: Fiz.-Mat. Lit. 1960. 215p. (in Russian).
[89] Melent'ev P.V. Approximate calculus. M.: Fiz.-Mat. Lit. 1962. 387p. (in Russian).
[90] Marchuk G.I., Kolesov V.E. Application of Numerical Methods to Neutron Cross-Section Calculations. M.: Atomizdat. 1970. 304p. (in Russian).
[91] Demidovich B.P., Maron I.F. Foundation of calculus mathematics. M.: Nauka. 1966. 664p. (in Russian).
[92] Dubovichenko S.B. A three body model of the ^{11}B nucleus // Jour. Exper. Theor. Phys. 2011. V.113. P.221–226.; Dubovichenko S.B. Three bode model of the ^{7}Li // Bull. Russ. Acad. Sci. Ser. Phys. 2000. V.64. P.2289–2292.
[93] Hodgson P.E. The Optical model of elastic scattering. Oxford: Clarendon Press. 1963. 211p.
[94] Plattner G.R., Viollier R.D. Coupling constants of commonly used nuclear probes // Nucl. Phys. 1981. V.A365. P.8–12.
[95] Mukhamedzhanov A.M., Tribble R. E. Connection between asymptotic normalization coefficients, sub threshold bound states, and resonances // Phys. Rev. 1999. V.C59. P.3418–3424.
[96] Blokhintsev L.D., Borbey I., Dolinsky E.I. Nu6clear vertex constants // Phys. Part. Nucl. 1977. V.8. P.1189–1245.
[97] Bateman H., Erdeyn A. Math. library. Higher transcendental functions. V.2. M.: Nauka. 1968. 295p. (in Russian)
[98] Lebedev N.N. Special functions and their applications. M.: Fiz.-Math. Lit. 1963. 358p. (in Russian)
[99] Dubovichenko S.B. Partial-wave analysis of elastic ^{4}He^{4}He scattering in the energy range 40–50 MeV // Phys. Atom. Nucl. 2008. V.71. P.65–74.
[100] Barnet A. et al. Coulomb wave function for all real η and ρ // Comput. Phys. Comm. 1974. V.8. P.377–395.
[101] Dubovichenko S.B., Chechin L.M. Calculating methods of the Coulomb functions and scattering phase shifts // Bull. KazNPU. ser. phys.-math. Almaty. 2003. No.1(7). P.115–122.
[102] Mott N., Messey H. The theory of atomic collisions. UK: Clarendon Press. 1965. 858p.

[103] Abramowitz M., Stegun I.A. Handbook of mathematical functions. Washington: Nat. bur. Stand. 1964. 1046p.
[104] Luke Yu.L. Mathematical functions and their approximations. New York: Academic Press. 1975. 568p.
[105] Melkanoff M.A. Fortran program for elastic scattering analysis with nuclear optical model. Los Angeles: Univ. California Pres. Berkley. 1961. 116p.
[106] Lutz H.F., Karvelis M.D. Numerical calculation of coulomb wave functions for repulsive coulomb fields // Nucl. Phys. 1963. V.43. P.31–44.
[107] Melkanoff M. Nuclear optical model calculations // In: Meth. Comput. Phys. New-York: Acad. Press. 1966. V.6. P.1–80.
[108] Gody W.J., Hillstrom K.E. Chebyshev approximations for the coulomb phase shifts // Meth. Comput. 1970. V.111. P.671–677.
[109] Smith W.R. Nuclear penetrability and phase shift subroutine // Usics Communs. 1969. V.1. P.106–112.
[110] Froberg C.E. Numerical treatment of Coulomb wave functions // Rev. Mod. Phys. 1955. V.27. P.399–411.
[111] Abramowitz M. Tables of Coulomb wave function. V.1. Washington: N.B.S. 1952. 141p.
[112] Danilov V. L. et al. Reference mathematical library. Mathematical analysis. Functions, limits and continued fractions. M.: Fiz.-Mat. Lit. 1961. 439p. (in Russian).
[113] Kuznetsov D. S. Special functions. M.: Graduate School. 1965. 272p. (in Russian).
[114] Dubovichenko S.B. Some versions of the algorithmic language BASIC. Almaty: UEiR 2001. 166p.
[115] Dubovichenko S.B., Zhusupov M.A. On calculation of the Coulomb wave functions // Interaction of radiation with matter. Alma-Ata. KazSU. 1980. P.99–104.
[116] Dubovichenko S.B., Zhusupov M.A. The computation of Coulomb scattering phase shifts // Bull. Acad. Sci. KazSSR ser. phys.-math. 1981. No 6. P.24–26.
[117] Brown G.E., Jackson A.D. The nucleon-nucleon interaction. Amsterdam: North-Holland Publ. Co.; New-York: American Elsevier Publ. Co. 1976. 242p.
[118] Dubovichenko S.B., Chechin L.M. Methods for solving of the generalized eigenvalue problem // Bull. KazNPU. ser. phys.-math. Almaty. 2003. No.1(7). P.110–115.
[119] Dubovichenko S.B., Takibaev N.Zh., Chechin L.M Physical Processes in the Far and Near Space. Almaty: Daik-Press. 2008. 228p.; arXiv:1012.1705 [nucl-th]. (in Russian).
[120] Skornyakov L.A. Reference mathematical library. General algebra. M.: Nauka. 1990. 591p. (in Russian).
[121] Popov B.A., Tesler G. S. Computer calculation of functions. Kiev: Naukova dumka. 1984. 598p. (in Russian).
[122] Korn G., Korn T. Mathematical Handbook. New-York: McGraw Hill Book Co. 1968. 832p.
[123] Dubovichenko S.B. Some methods for solving problems in nuclear physics at the bound states // Bull. KazNU. ser. phys. Almaty. 2008. No.1. P.49–58.
[124] Dubovichenko S.B., Chechin L.M. Modern methods of programming the actual physical problems // In: Current problems and challenges of informatization in Kazakhstan. KazNTU Almaty. 2004. P.358–390.
[125] Mishina A.P., Proskuryakov I.V. Higher algebra. M.: Fiz.-Math. Lit. 1961. 439p. (in Russian).
[126] http://physics.nist.gov/cgi-bin/cuu/Value?mud|search_for =atomnuc!
[127] Ajzenberg-Selove F. Energy levels of light nuclei A=5-10 // Nucl. Phys. 1979. V.A320. P.1–224.
[128] Esmakhanova K. et al. Dark energy in some integrable and nonintegrable FRW cosmological models // Inter. Jour. Mod. Phys. 2011. V.D20. No.12. P.2419–2446.
[129] Chechin L.M. Antigravitational instability of cosmic substrate in the Newtonian cosmology // Chinese Phys. Lett. 2006. V.23. No.8. P.2344–2347.

[130] Chechin L. M. The cosmic vacuum and the rotation of galaxies // Astronomy Reports 2010. V.54. No.8. P.719–723.
[131] White M., Scott D., Silk J. Anisotropies in the Cosmic Microwave Background // Ann. Rev. Astron. & Astrophys. 1994. V.32. P.319.
[132] Chechin L.M., Myrzakul Sh.R. The development of perturbations in the universe described by the nonstationary equation of state // Rus. Phys. Jour. 2009. V.52. P.286.
[133] Omarov T.B., Chechin L.M. On the dynamics of two oscillating cosmic strings // Gen. Relativ. Grav. 1999. V.31. P.443.
[134] Itzykson C., Nauenberg M. Unitary groups: Representations and decompositions // Rev. Mod. Phys. 1966. V. 38. P. 95–101.
[135] Belanova T.S., Ignatyuk A.V., Pashchenko A.B., Plyaskin V.I. Radiative capture of neutrons. M.: Energoatomizdat, 1986. 248p. (in Russian).
[136] Dubovichenko S.B. Thermonuclear Processes of the Universe. First English edition. New-York: NOVA Sci. Publ. 2012. 194p.; https://www.novapublishers.com/catalog/product_info.php?products_id=31125.
[137] Dubovichenko S.B. Astrophysical *S* factors of radiative ^{3}He^{4}He, ^{3}H^{4}He, and ^{2}H^{4}He capture // Phys. Atom. Nucl. 2010. V.73. P.1517–1522; Dubovichenko S.B. Astrophysical *S*-factor of the p^{7}Li→^{8}Beγ capture at low energies // Rus. Phys. Jour. 2010. V.53. P.1254–1263; Dubovichenko S.B. Astrophysical *S*-factor of the p^{9}Be → ^{10}Bγ radiative capture // Rus. Phys. Jour. 2011. V.54. P.814–821.
[138] Adelberger E.G. *et al*. Solar fusion cross sections. II. The pp chain and CNO cycles // Rev. Mod. Phys. 2011. V.83. P.195–245.
[139] Kukulin V.I., Neudatchin V.G., Obukhovsky I.T. and Smirnov Yu.F. Clusters as subsystems in light nuclei // In: Clustering Phenomena in Nuclei edited by K. Wildermuth and P. Kramer. Branschweig: Vieweg. 1983. V.3. P.1.
[140] Dubovichenko S.B. Radiative neutron capture and primordial nucleosynthesis of the Universe. Fifth Russian Edition, corrected and added. Germany, Saarbrucken: Lambert Academy Publ. GmbH&Co. KG. 2016. 496p.
[141] Dubovichenko S.B. Astrophysical *S*-factor radiative p^{13}C capture // Phys. Atom. Nucl. 2012. V.75. P.173–181.
[142] Heil M. et al. The (n,γ) cross section of ^{7}Li // Astrophys. Jour. 1998. V.507. P.997–1002; Guimaraes V. and Bertulani C.A. Light radioactive nuclei capture reactions with phenomenological potential models // arXiv:0912.0221v1 [nucl-th]; Masayuki Igashira, Toshiro Ohsaki Neutron capture nucleosynthesis in the Universe // Sci. Tech. Adv. Materials 2004. V.5. P.567–573; Nagai Y. et al. Fast neutron capture reactions in nuclear astrophysics // Hyperfine Interactions 1996. V.103. P.43–48; Liu Z.H. et al. Asymptotic normalization coefficients and neutron halo of the excited states in ^{12}B and ^{13}C // Phys. Rev. 2001. V.C64. P.034312(1–5).
[143] Dubovichenko S.B. Contribution of the M1 process to the astrophysical *S*-factor of the p^{2}H radiative capture // Rus. Phys. Jour. 2011. V.54. P.157–164; Dubovichenko S.B. Astrophysical S factors for radiative proton capture by ^{3}H and ^{7}Li nuclei // Phys. Atom. Nucl. 2011. V.74. P.358–370.
[144] Fowler W.A. Experimental and Theoretical Nuclear Astrophysics: the Quest for the Original of the Elements. Nobel Lecture. Stockholm. 8 Dec. 1983.
[145] Dubovichenko S.B., Dzhazairov-Kakhramanov A.V. Phase analysis of elastic p^{6}Li scattering at astrophysical energies // Rus. Phys. Jour. 2010. V.53. P.458–464.
[146] Baktybaev M.K. et al. The scattering of protons from ^{6}Li and ^{7}Li nuclei // The 4th Eurasia Conf. "Nucl. Sci. and its Appl." Baku. Azerbaijan. 2006. P.62; Burtebaev N. et al. The new experimental data on the elastic scattering of protons from ^{6}Li, ^{7}Li, ^{16}O and ^{27}Al nuclei // The 5th Eurasian Conf. "Nucl. Sci. and its Appl.". Ankara. Turkey. 2008. P.40.

[147] Dubovichenko S.B. et al. Astrophysical *S*-factor of radiative p^{6}Li capture at low energies // Rus. Phys. Jour. 2010. V.53. P.743–749; Dubovichenko S.B. Astrophysical *S*-factor radiative p^{6}Li capture // Dokl. Nat. Acad. Sci. Rep. Kazakhstan. 2009. №6. P.41–45.
[148] Switkowski Z.E. et al. Cross section of the reaction ^{6}Li(p,γ)^{7}Be // Nucl. Phys. 1979. V. A331. P.50–60; Bruss R. et al. Astrophysical *S*-factors for the radiative capture reaction ^{6}Li(p,γ)^{7}Be at low energies // Proc. 2nd Intern. Symposium on Nuclear Astrophysics. Nuclei in the Cosmos. Karlsruhe. Germany. 6–10 July. 1992. Kappeler F., Wisshak K., Eds. IOP Publishing Ltd. Bristol. England. 1993. P.169.
[149] Arai K., Baye D., Descouvemont P. Microscopic study of the ^{6}Li(p,γ)^{7}Be and ^{6}Li(p,α)^{3}He reactions // Nucl. Phys. 2002. V. A699. P.963–975.
[150] http://cdfe.sinp.msu.ru/exfor/index.php
[151] http://www-nds.iaea.org/exfor/exfor.htm
[152] Bartholomew G.A. and Campion P.J. Neutron capture gamma rays from lithium, boron, and nitrogen // Can. Jour. Phys. 1975. V.35. P.1347–1360.
[153] Jarczyk L. et al. (n,γ) spectrum for lithium and beryllium // Helv. Phys. Acta 1961. V.34. P.483–484.
[154] Jurney E.T. Thermal capture cross sections for ^{6}Li and ^{7}Li // U.S. Nucl. Data Comm. 1973. No.9. P.109.
[155] Chang Su Park, Gwang Min Sun, Choi H.D. Determination of thermal neutron radiative capture cross section of ^{6}Li // Nucl. Instr. Meth. 2006. V.B245. P.367–370.
[156] Tilley D.R. et al. Energy level of light nuclei A=5,6,7 // Nucl. Phys. 2002. V.A708. P.3–163.
[157] Krauss H. et al. The astrophysical *S*-factor of the reaction ^{7}Be(p,γ)^{8}B in the direct capture model // Ann. der Phys. 1993. V.2. P.258–266.
[158] Trache L. et al. Asymptotic normalization coefficients for ^{8}B → ^{7}Be+p from a study of ^{8}Li → ^{7}Li+n // arXiv: nucl-ex/0304016v1.
[159] Mughabghab S.F., Lone M.A., Robertson B.C. Quantitative test of the Lane-Lynn theory of direct radiative capture of thermal neutrons by ^{12}C and ^{13}C // Phys. Rev. 1982. V.C26. P.2698–2701.
[160] Jurney E.T., Bendt P.J., Browne J.C. Thermal neutron capture cross section of deuterium // Phys. Rev. 1982. V.C25. P.2810–2811.
[161] Kikuchi T. et al. Nonresonant direct p- and d-wave neutron capture by ^{12}C // Phys. Rev. 1998. V. C57. P.2724–2730.
[162] Macklin R.L. Neutron Capture by ^{12}C at stellar temperatures // Astrophys. Jour. 1990. V.357. P.649.
[163] Ohsaki T. et al. New measurement of the ^{12}C(n,γ)^{13}C reaction cross section // Astrophys. Jour. 1994. V.422. P.912.
[164] Nagai Y. et al. Neutron capture cross sections of light nuclei in primordial nucleosynthesis // Nucl. Instr. Meth. 1991. V.B56. P.492–495.
[165] Shima T. et al. Experimental studies of KeV energy neutron - induced reactions relevant to astrophysics and nuclear physics // JAERI-C-97-004. 1996. P.131.
[166] Dubovichenko S.B. Astrophysical *S*-factor radiative p^{13}C capture // Phys. Atom. Nucl. 2012. V.75. P.173–181.
[167] Dubovichenko S.B. Phase analysis of elastic p^{12}C scattering for astrophysical energies // Rus. Phys. Jour. 2008. V.51. P.1136–1143.
[168] Sadeghi H. and Bayegan S. Precision calculation for nucleon capture by deuteron with effective field theory // Nucl. Phys. 2005. V.A753. P.291–304.
[169] ENDF/B online database at the NNDC Online Data Service. http://www.nndc.bnl.gov.
[170] Schmelzbach P. et al. Phase shift analysis of p^{2}H elastic scattering // Nucl. Phys. 1972. V.A197. P.273–289; Arvieux J. Analyse en dephasages des sections efficaces et polarisations dans la diffusion elastique p^{2}H // Nucl. Phys. 1967. V.A102. P.513–528; Chauvin J., Arvieux J. Phase

shift analysis of spin correlation coefficients in p^{2}H scattering // Nucl. Phys. 1975. V.A247. P.347–358; Huttel E. et al. Phase shift analysis of p^{2}H elastic scattering below break-up threshold // Nucl. Phys. 1983. V.A406. P.443–455.

[171] Dubovichenko S.B., Dzhazairov-Kakhramanov A.V. Astrophysical *S*-factors of radiative capture of protons on ^{2}H, ^{3}H, ^{6}Li and ^{12}C nuclei // Int. Jour. Mod. Phys. 2012. V.E21. P.1250039 (1–44).

[172] Griffiths G.M., Larson E.A., Robertson L.P. The capture of proton by deuteron // Can. Jour. Phys. 1962. V.40. P.402–411.

[173] Ma L. et al. Measurements of ^{1}H(d→,γ)^{3}He and ^{2}H(p→,γ)^{3}He at very low energies // Phys. Rev. 1997. V.C55. P.588–596.

[174] Schimd G.J. et al. The ^{2}H(p→,γ)^{3}He and ^{1}H(d→,γ)^{3}He reactions below 80 keV // Phys. Rev. 1997. V.C56. P.2565–2681.

[175] Casella C. et al. First measurement of the d(p,γ)^{3}He cross section down to the solar Gamow peak // Nucl. Phys. 2002. V.A706. P.203–216.

[176] Purcell J.E. et al. Energy levels of light nuclei A=3 // Nucl. Phys. 2010. V.A848. P.1–74;http://www.tunl.duke.edu/nucldata/HTML/A=3/03H_2010.shtml

[177] Tilley D.R., Weller H.R., Hasan H.H. Energy levels of light nuclei A = 3 // Nucl. Phys. 1987. V. A474. P.1–60.

[178] Dubovichenko S.B. Neutron Capture by Light Nuclei at Astrophysical Energies // Phys. Part. Nucl. 2013. V.44. P.803–847; Dubovichenko S.B., Dzhazairov-Kakhramanov A.V., Burkova N. A. Neutron radiative capture by ^{2}H, ^{6}Li, ^{7}Li, ^{12}C and ^{13}C at astrophysical energies // Int. Jour. Mod. Phys. 2013. V.E22. P.1350028 (1–52);Dubovichenko S.B., Dzhazairov-Kakhramanov A. V. Neutron radiative capture by ^{2}H, ^{6}Li, ^{7}Li, ^{12}C, ^{13}C, ^{14}C and ^{14}N at astrophysical energies // The Universe Evolution. Astrophysical and Nuclear Aspects. New-York: NOVA Sci. Publ. 2013. P.49–108.

[179] http://physics.nist.gov/cgi-bin/cuu/Value?rd#mid

[180] Kirzhnits D.A. Does deuteron inside tritium? // Lett. Jour. Exper. Theor. Phys. 1978. V.28. P.479–481.

[181] Faul D.D. et al. Photodisintegration of ^{3}H and ^{3}He // Phys. Rev. 1981. V.C24. P.849–873.

[182] Bosch R. et al. Photodisintegration of H^3// Phys. Lett. 1964. V.8. P.120.

[183] Dubovichenko S.B. Radiative capture n^{2}H at low energies // Rus. Phys. Jour. 2012. V.55. C.138–143.

[184] Firestone R.B., Revay Zs. Thermal neutron radiative cross sections for ^{6,7}Li, ^{9}Be, ^{10,11}B, ^{12,13}C, and ^{14,15}N // Phys. Rev. 2016. V.C93. P.054306.

[185] Nagai Y. et al. Measurement of the ^{2}H(n,γ)^{3}H reaction cross section between 10 and 550 keV // Phys. Rev. 2006. V.C74. P.025804 (1–7).

[186] Mitev G. et al. Radiative neutron capture by deuterium // Phys. Rev. 1986. V.C34. P.389–400.

[187] Trail C.C., Raboy S. Neutron capture by deuterium // BAP 1964. V.9. P.176.

[188] Toshiro Ohsaki et al. Role of multiparticle-multihole states of ^{18,19}O in ^{18}O(n,γ)^{19}O reactions at keV energy // Phys. Rev. 2008. V.C77. P.051303 (1–5).

[189] Toshiro Ohsaki et al. keV-neutron capture cross sections of light nuclei and nucleosynthesis // AIP 2000. V.529 P.458–465.

[190] Toshiro Ohsaki et al. First measurement of neutron capture cross section of ^{6}Li at stellar energy // AIP 2000. V.529. P.678–680.

[191] Su Jun et al. Neutron Spectroscopic Factors of ^{7}Li and Astrophysical ^{6}Li(n,γ)^{7}Li Reaction Rates // Chinese Phys. Lett. 2010. V.27. P.052101-1–052101–4.

[192] Petitjean C., Brown L., Seyler R. Polarization and phase shifts in ^{6}Li(p,p)^{6}Li from 0.5 to 5.6 MeV // Nucl. Phys. 1969. V.A129. P.209–219.

[193] Dubovichenko S.B. et al. Astrophysical S factor for the radiative-capture reaction p^{6}Li → ^{7}Beγ // Phys. Atom. Nucl. 2011. V.74. P.984–1000.

[194] Dubovichenko S.B. Radiative capture of neutrons by ^{6}Li at astrophysical energies // Rus. Phys. Jour. 2012. V.55. P.1314–1323.
[195] Mukhamedzhanov A.M., Timofeyuk N.K. Microscopic calculation of nucleon separation vertex constant for 1p shell nuclei // Jour. Sov. Nucl. Phys. 1990. V.51. P.431–441; Blokhintsev L.D., Mukhamedzhanov A.M., Timofeyuk N.K. The Vertex Constant of Virtual Decay t→d+n and a Nucleon-Nucleon Potential // Ukr. Jour. Phys. 1990. V.35. P.341–345.
[196] Nollett K.M., Wiringa R.B. Asymptotic normalization coefficients from ab initio calculations // Phys. Rev. 2011. V.C83. P.041001(R); arXiv:1102.1787v3 [nucl-th].
[197] Timofeyuk N.K. Spectroscopic factors and asymptotic normalization coefficients for 0p-shell nuclei: Recent updates // Phys. Rev. 2013. V.C88. P.044315.
[198] Burkova N.A. et al. One-nucleon spectroscopy of light nuclei // Phys. Part. Nucl. 2009. V.40. P.162–205.
[199] Karataglidis S. et al. The ^{7}Li(γ,n_0)^{6}Li cross section near threshold // Nucl. Phys. 1989. V.A501. P.108–117.
[200] Bramblett R.L. et al. Photoneutron cross sections for ^{7}Li // Proc. of Intern. Conf. Photonucl. React. Appl. California. 1973. V.1. P.175.
[201] Green L., Donahue D.J. Photoneutron cross sections with monoenergetic neutron-capture gamma rays // Phys. Rev. 1964. V.B135. P.B701–B705.
[202] Tombrello T.A. The capture of protons by ^{7}Be // Nucl. Phys. 1965. V.71. P.459–464; Aurdal A. Proton capture by ^{7}Be // Nucl. Phys. 1970. V.146. P.385–389.
[203] Descouvemont P., Baye D. Microscopic study of the ^{7}Li(n,γ)^{8}Li and ^{7}Be(p,γ)^{8}B reactions in a multiconfiguration three-cluster model // Nucl. Phys. 1994. V.A567. P.341–353.
[204] Fernando L., Higa R. and Rupak G. Leading E1 and M1 contributions to radiative neutron capture on lithium-7 // Eur. Phys. Jour. 2012. V.A48:24(1–13);arXiv:1109.1876v1 [nucl-th].
[205] Tilley D.R. et al. Energy level of light nuclei. A=8,9,10 // Nucl. Phys. 2004. V.A745. P.155–363.
[206] Huang J.T., Bertulani C.A., Guimaraes V. Radiative capture of protons and neutrons at astrophysical energies and potential models // Atom. Data and Nucl. Data Tabl. 2010. V.96. P.824–847.
[207] Dubovichenko S.B. Dzhazairov-Kakhramanov A.V. Astrophysical *S*-factor of the radiative p^{2}H capture // Euro. Phys. Jour. 2009. V.A39. P.139–143; Dubovichenko S.B., Dzhazairov-Kakhramanov A.V. The ^{7}Li(n, γ)^{8}Li radiative capture at astrophysical energies // Ann. der Phys. 2012. V.524. P.850–861.
[208] Imhof W. L. et al. Cross Sections for the Li^{7}(n,γ)Li^{8} Reaction // Phys. Rev. 1959. V.114. P.1037–1039.
[209] Nagai Y. et al. ^{7}Li(n,γ)^{8}Li reaction and the S_{17} factor at $E_{c.m.}$ > 500 keV // Phys. Rev. 2005. V.C71. P.055803 (1–8).
[210] Weischer M., Steininger R., Kaeppeler F. ^{7}Li(n,γ)^{8}Li trigger reaction to a primordial r-process? // Astrophys. Jour. 1989. V.344. P.464.
[211] Blackmon J.C. et al. Measurement of ^{7}Li(n,γ_0)^{8}Li cross sections at E_n = 1.5–1340 eV // Phys. Rev. 1996. V.C54. P.383–388.
[212] Lynn J.E., Jurney E.T., Raman S. Direct and valence neutron capture by ^{7}Li // Phys. Rev. 1991. V.C44. P.764–773.
[213] Dubovichenko S.B., Burkova N.A. Astrophysical n^{9}Be capture // Rus. Phys. Jour. 2013. V.56. P.298–306.
[214] http://cdfe.sinp.msu.ru/cgi-bin/muh/radchartnucl.cgi?zmin=0&zmax=14&tdata=123456
[215] Dolinskii E.I., Mukhamedzhanov A.M., Yarmukhamedov R. Direct nuclear reactions on light nuclei with neutrons emission. Tashkent: FAN 1978. P.7–44. (in Russian).
[216] Boyarkina F.N. Structure of 1p-shell nuclei. M.: MSU 1973. 66p. (in Russian).

[217] Dubovichenko S.B., Dzhazairov-Kakhramanov A.V., Afanasyeva N.V. Neutron radiative capture by ^{9}Be, ^{14}C, ^{14}N, ^{15}N and ^{16}O at astrophysical energies // Int. Jout. Mod. Phys. 2013. V.E22. P.1350075 (1–53).
[218] Conneely C.M., Prestwich W.V., Kennett T.J. The thermal neutron capture cross section of ^{9}Be // Nucl. Inst. Meth. 1986. V.A248. P.416–418.
[219] Wallner A. Nuclear astrophysics and AMS - Probing nucleosynthesis in the lab // Nucl. Instr. Meth. 2010. V.B268. P.1277–1282.
[220] Dubovichenko S.B. Capture of a neutron to excited states of a ^{9}Be nucleus taking into account resonance at 622 keV // Jour. Exper. Theor. Phys. 2013. V.117. P.649–655.
[221] Mengoni A., Otsuka T., Ishigara M. Direct radiative capture of p-wave neutrons // Phys. Rev. 1995. V.C52. P.R2334–R2338.
[222] Lin C.J. et al. Nonresonant capture cross sections of ^{11}B(n,γ) and ^{12}C(n,γ) at stellar energies // Phys. Rev. 2003. V.C68. P.047601 (1–4).
[223] Likar A., Vidmar T. Direct neutron capture in light nuclei // Nucl. Phys. 1997. V.A619. P.49–56.
[224] Kitazawa H. and Go K. Low-energy neutron direct capture by ^{12}C in a dispersive optical potential // Phys. Rev. 1998. V.C57. P.202–209.
[225] Herndl H., Hofinger R., Oberhummer H. The Cross Section of the Neutron Capture Reaction ^{13}C(n,γ)^{14}C // AIP 1998. V.425. P.428.
[226] Shima T. et al. Measurement of the ^{13}C(n,γ)^{14}C cross section at stellar energies // Nucl. Phys. 1997. V.A621. P.231–234.
[227] Dubovichenko S.B., Dzhazairov-Kakhramanov A.V. Astrophysical *S*-factor for p^{12}C → ^{13}Nγ radiative capture // Rus. Phys. Jour. 2009. V.52. P.833–840.
[228] Ajzenberg-Selove F. Energy level of light nuclei A=11,12 // Nucl. Phys. 1990. V.A506. P.1–158.
[229] Ajzenberg-Selove F. Energy level of light nuclei A=13,14,15 // Nucl. Phys. 1991. V.A523. P.1–196.
[230] Dubovichenko S.B. Phase shift analysis of the elastic n^{12}C scattering at low energies // Rus. Phys. Jour. 2012 V.55. P.561–568.
[231] Lane R.O. et al. The Angular Distributions of Neutrons Scattered from Various Nuclei // Ann. Phys. 1961. V.12. P.135.
[232] Mughabghab S.F. Atlas of neutron resonances. National Nuclear Data Center. Brookhaven. National Laboratory. Upton. USA 2006. 1008p.
[233] Dubovichenko S.B. Radiative capture of neutrons on ^{12}C at astrophysical energies // Rus. Phys. Jour. 2013. V.56. P.867–877.
[234] Dubovichenko S.B. Phase shifts analysis of the elastic p^{13}C scattering // Phys. Atom. Nucl. 2012. V.75. P.285–290.
[235] Wallner A. et al. Measurement of the stellar cross sections for the reactions ^{9}Be(n,γ)^{10}Be and ^{13}C(n,γ)^{14}C via AMS // Jour. Phys. 2008. V.G35. P.014018 (1–7).
[236] Allen B.J., Macklin R.L. Neutron Capture Cross Sections of ^{13}C and ^{16}O // Phys. Rev. 1971. V.C3. P.1737–1740.
[237] Hennig G.R. Thermal Neutron Capture Cross Section of Carbon-13 // Phys. Rev. 1954. V.95. P.92–95.
[238] Bao Z.Y. et al. Neutron cross sections for nucleosynthesis studies // Atom. Data and Nucl. Data Tabl. 2000. V.76. P.70–154.
[239] Raman S. et al. Valence capture mechanism in resonance neutron capture by ^{13}C // Phys. Rev. 1990. V.C41. P.458–471.
[240] Wallner et al. Accelerator mass spectroscopy measurements of the ^{13}C(n,γ)^{14}C and ^{14}N(n,p)^{14}C cross sections // Phys. Rev. 2016. V.C93. P.045803(12p.).
[241] Dubovichenko S.B. Astrophysical n^{13}C capture // Rus. Phys. Jour. 2014. V.57. P.16–23.

[242] Lane R.O. et al. States in ^{14}C from σ_T and $\sigma_{el}(\theta)$ for ^{13}C+n: Measurement, R-matrix analysis, and model calculations // Phys. Rev. 1981. V.C23. P.1883–1897.
[243] Dubovichenko S.B. Phase shifts analysis of the differential cross section for elastic p^{12}C scattering at astrophysical energies // Bull. Nat. Acad. Sci. Rep. Kazakhstan. ser. phys.-math. 2007. No.6. P.58–67.
[244] Dubovichenko S.B., Dzhazairov-Kakhramanov A.V., Burkova N.A. Cross Sections for the Astrophysical Neutron Radiative Capture on ^{12}C and ^{13}C Nuclei // Jour. Nucl. Part. Phys. 2013. V.3. No.4. P.108–120; Dubovichenko S.B., Dzhazairov-Kakhramanov A.V., Burkova N.A. Cross Sections for the astrophysical neutron radiative capture on ^{12}C and ^{13}C nuclei // arXiv:1202.1420 [nucl-th].
[245] Summers N. C., F. M. Nunes F. M. Extracting (n,γ) direct capture cross sections from Coulomb dissociation: Application to ^{14}C(n,γ)^{15}C // Phys. Rev. 2008. V.C78. P.011601(R)(1–5).
[246] Mukhamedzhanov A. M. et al. Asymptotic normalization coefficients from the ^{14}C(d,p)^{15}C reaction // Phys. Rev. 2011. V.C84. P.024616 (1–6).
[247] Nakamura T. et al. Neutron capture cross section of ^{14}C of astrophysical interest studied by Coulomb breakup of ^{15}C // Phys. Rev. 2009. V.C79. P.035805 (1–6).
[248] Beer H. et al. A measurement OF the ^{14}C(n,γ)^{15}C cross section at a stellar temperature of KT = 23.3 KeV // Astrophys. Jour. 1992. V.387. P.258.
[249] Reifarth R. et al. Stellar neutron capture rates of ^{14}C // Nucl. Phys. 2005. V.A758. P.787–790.
[250] Reifarth R. et al. The ^{14}C(n,γ) cross section between 10 keV and 1 MeV // Phys. Rev. 2008. V.C77. P.015804 (1–8).
[251] Horvath A. et al. Cross section for the astrophysical ^{14}C(n,γ)^{15}C reaction via the inverse reaction // Astrophys. Jour. 2002. V.570. P.926–934.
[252] Esbensen H. Coulomb dissociation of ^{15}C and radiative neutron capture on ^{14}C // Phys. Rev. 2009. V.C80. P.024608 (1–8).
[253] Dubovichenko S.B. Radiative neutron capture by ^{2}H, ^{7}Li, ^{14}C, and ^{14}N nuclei at astrophysical energies // Phys. Atom. Nucl. 2013. V.76. P.841–861; Afanasyeva N., Dubovichenko S.B., Dzhazairov-Kakhramanov A.V. Radiative neutron capture on ^{14}C and ^{14}N // Jour. Nucl. Energy Science & Power Gener. Technol. 2013. V.2. №3. doi:10.4172/2325-9809.1000112; arXiv:1212.1765 [nucl-th].
[254] Jurney E.T., Motz H. Thermal neutron capture in ^{2}H and ^{16}O // Rep. Argonne Nat. Lab. 1963. No.6797. P.236; Kinsey B. B. et al. Gamma-rays produced by slow neutron capture in beryllium, carbon and nitrogen // Can. Jour. Phys. 1951. V.29. P.1–13; Islam M.A., Kennett T.J., Prestwich W.V. Determination of the thermal radiative capture cross section of ^{14}N // Nucl. Instr. Meth. 1981. V.188. P.243–245; Islam T.J., Kennett W.V., Prestwich W.V. Re-estimation of the Thermal Neutron Capture Cross Section of ^{14}N // Nucl. Instr. Meth. 1990. V.A287. P.460–464; Egorov A. I. et al. Measurement of thermal neutron radiative capture cross-sections of the ^{14}N and ^{19}N by in-beam // Nucl. Instr. Meth. 2005. V.A545. P.296–300.
[255] Jurney E. T. et al. Thermal-neutron capture by ^{14}N // Phys. Rev. 1997. V.C56. P.118–134.
[256] Bostrom N. A. et al. Neutron interactions in lithium, carbon, nitrogen, aluminum, argon, manganese, yttrium, zirconium, radiolead and bismuth // WADC-TN-59-107. 1959.
[257] Dubovichenko S.B. Radiative n^{14}N capture at astrophysical energies // Rus. Phys. Jour. 2013. V.56. P.1–8.
[258] Tilley D. R., Weller H. R., Cheves C. M. Energy levels of light nuclei A=16,17 // Nucl. Phys. 1993. V.A564. P.1–183.
[259] Dubovichenko S.B., Dzhazairov-Kakhramanov A.V., Burkova N.A. Astrophysical *S*-factor for the radiative capture reaction ^{13}C(p,γ)^{14}N // Jour. Nucl. Part. Phys. 2012. V.2. P.6–10.
[260] Burkova N.A. Program for calculation of phase shifts // Private Communication 2012.

[261] Dubovichenko S.B. Calculation method of the nuclear characteristics. Nuclear and thermonuclear processes. Second edition, revised and updated. Germany, Saarbrucken: Lambert Acad. Publ. GmbH&Co. KG. 2012. 425p.; https://www.lap-publishing.com/catalog/details //store/ru/book/978-3-659-21137-9/metody-rascheta-yadernyh-kharacteristic. (in Russian).
[262] http://www.nndc.bnl.gov/exfor/exfor00.htm
[263] http://xxx.lanl.gov/find/nucl-ex
[264] Herndl H. et al. Reaction rates for Neutron Capture Reactions to C-, N- and O-isotopes to the neutron rich side of stability // Phys. Rev. 1999. V.C60. P.064614 (1–12).
[265] Meissner J. et al. Neutron capture cross section of ^{15}N at stellar energies // Phys. Rev. 1996. V. C53. P4.977–981.
[266] Dubovichenko S.B. Radiative n^{15}N capture at low energies // Rus. Phys. Jour. 2013. V.56. P.494–503; Dubovichenko S.B., Afanasyeva N., Burkova N.A. Radiative neutron capture on ^{15}N // Phys. Sci. Inter. Jour. 2014. V.4. P.636–648; Dubovichenko S.B., Afanasyeva N.V. Radiative n^{15}N capture at astrophysical energies // arXiv:1304.1976v1 [nucl-th].
[267] Igashira M. et al. Measurement of the ^{16}O(n,γ)^{17}O reaction cross section at stellar energies and critical role of nonresonant P-wave neutron capture // Astrophys. Jour. 1995. V.441. P.L89–L92; Igashira M., Kitazawa H. and Takaura K. Valence-neutron capture in the 434 keV $P_{3/2}$-wave resonance of ^{16}O // Nucl. Phys. 1992. V.A536. P.285–296.
[268] Hickey G. T. et al. R-matrix and Phase-Shift analyses of neutron polarization measurements from n^{l6}O scattering // Nucl.Phys. 1974. V.A225. P.470–480.
[269] Johnson C. H., Fowler J. L. Scattering of neutrons from ^{16}O in the 2.2- to 4.2-MeV energy range // Phys. Rev. 1967. V.162. P.890–899.
[270] Fowler J.L., Cohn H.O. Oxygen differential neutron scattering and phenomenological nuclear potentials // Phys. Rev. 1958. V.109. P.89–93.
[271] Okazaki A. Scattering of polarized neutrons by heavy nuclei // Phys. Rev. 1955. V.99. P.55–58.
[272] Schouky I. Untersuchung der niveaustruktur von ^{17}O und ^{29}Si im bereich zwischen neutronenbindungsenergie und 12 MeV anregungsenergie // KFK-2503. 7708.
[273] Kitazawa H., Igashira M. and Ohsaki T. Folded-Potential Model Calculation of Low Energy Neutron Direct-Capture Cross Sections // CP529, Capture Gamma-Ray Spectroscopy and Related Topics: 10th Int'l. Symp., edited by S. Wender, 2000, American Institute of Physics 1-56396-952-1/007.
[274] Dufour M., Descouvemont P. Microscopic analysis of the ^{13}C(α,n)^{16}O and ^{16}O(n,γ)^{17}O reactions // Nucl. Phys. 2001. V.A694. P.221–232; Multichannel study of the ^{13}C(α,n)^{16}O and ^{16}O(n,γ)^{17}O reactions // Phys. Rev. 2005. V.C72. P.015801 (1–7).
[275] Yamamoto K. et al. Radiative capture cross section for ^{16}O(n,γ)^{17}O and ^{16}O(p,γ)^{17}F below astrophysical energies // Prog. Theor. Phys. 2009. V.121. P.375–390.
[276] McDonald A. B. et al. Doubly radiative thermal neutron capture in ^{2}H and ^{16}O experiment and theory // Nucl. Phys. 1977. V.A281. P.325–344; Wust N., Seyfarth H. and Aldea L. Two-quantum radiative thermal neutron capture in H1 // Phys. Rev. 1970. V.C19. P.1153–1158.
[277] Dubovichenko S.B. Radiative n^{16}O capture at low energies // Rus. Phys. Jour. 2014. V.57. P.498–508.
[278] Dubovichenko S.B., Dzhazairov-Kakhramanov A.V. Thermonuclear processes for three body system in the potential cluster model // Nucl. Phys. 2015. V.A.941. P.335–363.; arXiv:1504.04899 [nucl-th].
[279] Igashira M. et al. Measurements of keV-neutrons capture gamma rays // Conf. Meas. Calc. and Eval. of Photon Prod. Data. Bologna. 1994. P.269–279.
[280] Kelley J.H. et al. Energy level of light nuclei A = 11 // Nucl. Phys. 2012. V.A880. P.88–195.

[281] Yarmukhamedov R. Determination of ANC for $n^{10}B$ channel in ^{11}B nucleus by $^{10}B(d,p)^{11}B$ reaction at E_d = 12 MeV. // Private Communication 2013.
[282] Avotina M.P., Zolotavin A.V. Moments of the ground and excited states of nuclei. M.: Atomizdat. 1979.
[283] Bartholomew G.A., Campion P.J. Neutron capture gamma rays from lithium, boron and nitrogen // Can. Jour. Phys. 1957. V.35. P.1347–1360.
[284] Dubovichenko S.B. Radiation $n^{10}B$ capture at astrophysical energies // Rus. Phys. Jour. 2014. V.57. P.880–887.
[285] Mooring F.P. et al. $^{11}B(n,\gamma)^{12}B$ cross section at low energies // Argonne National Laboratory 1964. No.6877. P.5.
[286] Imhof W.L. et al. Cross Sections for the $^{11}B(n,\gamma)^{12}B$ Reaction // Phys. Rev. 1962. V.125. P.1334–1336.
[287] Dubovichenko S.B., Burkova N.A. Radiative $n^{11}B$ capture at astrophysical energies // Mod. Phys. Lett. 2014.V.A29. P.1450036(1–14).
[288] Zecher P.D. et al. Measurement of the $^{8}Li(n,\gamma)^{9}Li$ cross section at astrophysical energies by reverse kinematics // Phys. Rev. 1998. V.C57. P.959–966.
[289] Banerjee P., Chatterjee R. and Shyam R. Coulomb dissociation of ^{9}Li and the rate of the $^{8}Li(n,\gamma)^{9}Li$ reaction // Phys. Rev. 2008. V.C78. P.035804.
[290] Bertulani C.A. The astrophysical reaction $^{8}Li(n,\gamma)^{9}Li$ from measurements by reverse kinematics // Jour. Phys. 1999. V.G25. P.1959–1963.
[291] Boyd R.N. et al. Measurement of the $^{8}Li(\alpha,n)^{11}B$ reaction cross section at energies of astrophysical interest // Phys. Rev. Lett. 1992. V.68. P.1283.
[292] Gu X. et al. The $^{8}Li(\alpha,n)^{11}B$ reaction and primordial nucleosynthesis // Phys. Lett. 1995. V.B343. P.31–35.
[293] Malaney R.A. and Fowler W.F. In: Origin and distribution of the elements. // Ed. G.J. Matthews. Singapore: World Scientific. 1988. 780p.
[294] Guimaraes V. et al. Investigation of nucleosynthesis neutron capture reactions using transfer reactions induced by ^{8}Li beam // International Symposium on Nuclear Astrophysics - Nuclei in the Cosmos. IX. June 25–30. CERN. Geneva. Switzerland. 2006. P.108.
[295] Woosley S.E. et al. The r-process and neutrino-heated supernova eject // Astrophys. Jour. 1994. V.433. P.229–246.
[296] Gorres J. et al. Two-neutron capture reactions in supernovae neutrino bubbles // Phys. Rev. 1995. V.C52. P.2231.
[297] Efros V.D. et al. Reaction rate for two-neutron capture by ^{4}He // Z. Phys. 1996. V.A355. P.101–105.
[298] Rauscher T. et al. Production of heavy elements in inhomogeneous cosmologies // Astrophys. Journ. 1994. V.429. P.499–530.
[299] Descouvemont P. The $^{8}Li(n,\gamma)^{9}Li$ and $^{8}B(p,\gamma)^{9}C$ mirror reaction in microscopic cluster model // Astrophys. Journ. 1993. V.405. P.518–521.
[300] Horvath A. et al. Measurements of astrophysical neutron capture cross sections via the inverse reaction // Nucl. Phys. 2003. V.A719. P.9c-12c.
[301] Kobayashi H. et al. Astrophysical reaction rate for the $^{8}Li(n,\gamma)^{9}Li$ reaction // Phys. Rev. 2003. V. C67. P.015806 (1–7).
[302] Guo B. et al. The $^{8}Li(d,p)^{9}Li$ reaction and astrophysical $^{8}B(p,\gamma)^{9}C$ reaction rate // Nucl. Phys. 2005. V.A761. P.162–172.
[303] Dubovichenko S.B., Dzhazairov-Kakhramanov A.V. Neutron radiative capture by ^{10}B, ^{11}B and proton radiative capture by ^{11}B, ^{14}C and ^{15}N at thermal and astrophysical energies // Int. Jour. Mod. Phys. 2014. V.E23. P.1430012 (1–55).
[304] Sanchez R. et al. Nuclear charge radius of ^{11}Li // Hyperfine Interaction 2006. V.171. P.181–188.

[305] Nortershauser W. et al. Measurement oh the nuclear charge radii of ^{8,9}Li // Euro. Phys. Jour. 2005. V.A25. P.199–200.
[306] http://cdfe.sinp.msu.ru/services/ground/NuclChart_release.html
[307] Neugart R. et al. Precision measurement of ^{11}Li moments // Phys. Rev. Lett. 2008. V.101. P.132502.
[308] Kanungo R. et al. Spectroscopic factors for the ^{9}Li ground state and N=6 shell closure // Phys. Lett. 2008. V.B660. P.26–31.
[309] Wuosma A. H. et al. Neutron spectroscopic factors in ^{9}Li from ^{2}H(^{8}Li,p)^{9}Li // Phys. Rev. Lett. 2005. V.94. P.082502.
[310] Li Z.H. et al. The Li^{8}(d,p)Li^{9} reaction and the astrophysical Li^{8}(n,γ)Li^{9} reaction rate // Phys. Rev. 2005. V.C71. P.052801R(1–5).
[311] Guimaraes V. et al. Neutron transfer reactions induced by ^{8}Li on ^{9}Be // Phys. Rev. 2007. V.C75. P.054602 (1–9).
[312] Wiringa R.B. Spectroscopic overlaps // http://www.phy.anl.gov/theory/research/overlap.
[313] Liu Zu-Hua and Zhou Hong-Yu Nuclear halo effect on nucleon capture reaction rate at stellar energies // Chinese Phys. 2005. V.14. P.1544–1548.
[314] Nortershauser W. et al. Nuclear Charge Radii of ^{7,9,10}Be and the One-Neutron Halo Nucleus ^{11}Be // Phys. Rev. Lett. 2009. V.102. P.062503.
[315] Hammer H.W., Phillips D.R. Electric properties of the Beryllium-11 system in Halo EFT // Nucl. Phys. 2011. V.A865. P.17–42.
[316] Belyaeva T. L. et al. Neutron asymptotic normalization coefficients and halo radii of the first excited states of ^{12}C and ^{11}Be // EPJ Web of Conferences 66. 03009. 2014.
[317] Navin A. et al. Direct Evidence for the Breakdown of the *N*=8 Shell Closure in ^{12}Be // Phys. Rev. Lett. 2000. V.85. P.266.
[318] Fukuda N. et al. Coulomb and nuclear breakup of a halo nucleus ^{11}Be // Phys. Rev. 2004. V.C70. P.054606 (1–12).
[319] Palit R. et al. Exclusive measurement of breakup reactions with the one-neutron halo nucleus ^{11}Be // Phys. Rev. 2003. V.C68. P.034318 (1–14).
[320] Pain S.D. et al. Experimental evidence of a $(1d_{5/2})^2$ component to the ^{12}Be ground state // Eur. Phys. Jour. 2005. V.A25. Suppl.1 P.349–351; Pain S.D. et al. Structure of ^{12}Be: Intruder d-Wave Strength at N=8 // Phys. Rev. Lett. 2006. V.96. P.032502.
[321] Auton D.L. Direct reactions on ^{10}Be // Nucl. Phys. 1970. V.A157. P.305–322; Goosman D.R. and Kavanagh R.W. ^{10}Be(d,p)^{11}Be and the ^{10}Be(d,α)^{8}Li Reactions // Phys. Rev. 1970. V.C1. P.1939.
[322] Zwieglinski B. et al. Study of the ^{10}Be(d,p)^{11}Be reaction at 25 MeV // Nucl. Phys. 1979. V.A315. P.124–132.
[323] Quaglioni S.and Navr´atil P. Ab initio many-body calculations of nucleon-nucleus scattering // Phys. Rev. 2009. V.C 79. P.044606 (1–28).
[324] Dubovichenko S.B., Dzhazairov-Kakhramanov A.V. The radiative ^{10}Be(n,γ)^{11}Be capture at thermal and astrophysical energies // J. Phys. 2016. V.G43. No.9. P.095201(14p.).
[325] Mengoni A. et al. Exotic properties of light nuclei and their neutron capture cross sections // 4th International Seminar on Interaction of Neutrons with Nuclei “Neutron Spectroscopy, Nuclear Structure, Related Topics” Dubna (Russia), April 1996; arXiv:nucl-th/9607023[nucl-th].
[326] Nakamura T. et al. Coulomb dissociation of a halo nucleus ^{11}Be at 72 MeV // Phys. Lett. 1994. V. B331. P. 296–301.
[327] Mengoni A. et al. Exotic structure of light nuclei and their neutron capture reaction rates // Nucl. Phys. 1997. V.A621. P.323c-326c.
[328] Caughlan G.R. and Fowler W.A. // Atom. Data Nucl. Data Tab. 1988. V.40. P.283–334.

[329] Dubovichenko S.B. Selected methods of the nuclear astrophysics. First edition. Series "Kazakhstan space research". V.9. Almaty: APHI. 2011. 311p.; http://xxx.lanl.gov/abs/1201.3003. (in Russian).
[330] Dubovichenko S.B. Selected methods of the nuclear astrophysics. Second edition, revised and updated (First Eur. Ed.). Germany, Saarbrucken: Lambert Acad. Publ. GmbH&Co. KG. 2012.; https://www.lap-publishing.com/catalog/details/store/gb/book/978-3-8465-8905-2/izbrannie-metody-yadernoy-astrofiki. (in Russian).
[331] Dubovichenko S.B. Selected methods of the nuclear astrophysics. Third edition, revised and updated (Second European edition). Germany, Saarbrucken: Lambert Acad. Publ. GmbH&Co. KG. 2013 480p.; https://www.lap-publishing.com/catalog/details/store/es/book/978-3-659-34710-8/izbrannie-metody-yadernoy-astrofiki. (in Russian).
[332] Dubovichenko S.B. Primordial nucleosynthesis of the Universe. Third Europe edition of the book "Selected method for nuclear astrophysics", corrected and added. Germany, Saarbrucken: Lambert Academy Publ. GmbH&Co. KG. 2014. 668p.; https://www.lap-publishing.com/catalog/details/store/pl/book/978-3-659-54311-1/Первичный-нуклеосинтез-Вселенной. (in Russian).
[333] Burkova N.A., Dubovichenko S.B. ^{4}He^{3}H^{2}H three-body model of the ^{9}Be nucleus // Rus. Phys. Jour. 2008. V.51. P.99–104.
[334] Dubovichenko S.B. Thermonuclear processes in Stars and Universe. Second English edition, corrected and added. Germany, Saarbrucken: Scholar's Press. 2015. 332p.; https://www.scholars-press.com/catalog/details/store/gb/book/978-3-639-76478-9/thermonuclear-processes-in-stars.
[335] Dubovichenko S.B., Dzhazairov-Kakhramanov A.V., Afanasyeva N.V. New Results for Reaction Rate of the Proton Radiative Capture on ^{3}H // Nucl. Phys. 2017. V.A963. P.52–67.
[336] Dubovichenko S.B., Dzhazairov-Kakhramanov A.V. The reaction ^{8}Li(n,γ)^{9}Li at astrophysical energies and its role in primordial nucleosynthesis // AstroPhys. J. 2016. V.819. 78.
[337] Dubovichenko S.B., Dzhazairov-Kakhramanov A.V., Burtebaev N., Alimov D. Radiative p^{14}C capture at astrophysical energies // Mod. Phys. Lett. 2014. V.A29. P.1450125 (1–16).
[338] Dubovichenko S.B., Dzhazairov-Kakhramanov A.V. Astrophysical *S*-factor of the radiative ^{4}He^{12}C capture reaction at low energies // Bull. Russ. Acad. Sci. Ser. Phys. 2011. V.75. P.1517–1522; Dubovichenko S.B., Dzhazairov-Kakhramanov A.V. Astrophysical *S*-factor of the ^{4}He^{12}C radiative captures at low energies // Uz. Jour. Phys. 2009. V.11. P.239–246; Dubovichenko S.B., Dzhazairov-Kakhramanov A.V. Astrophysical *S*-factor ^{4}He^{12}C radiative capture at low energies // Dokl. Nat. Acad. Sci. Rep. Kazakhstan. 2009. №2. P.9–15.
[339] Dubovichenko S.B. Radiative p^{16}O capture at astrophysical energies // Rus. Phys. Jour. 2016. V.59. P.1145–1152.
[340] Salisbury S.R. and Richards H.T. ^{17}F Level Parameters // Phys. Rev. 1962. V.126. P.2147–2158.
[341] Henry R.R., Phillips G.C., Reich C.W. and Russell J.L. Elastic Scattering of Proton by Oxygen in the Energies Region of 2.5 to 5.6 MeV // Bull. Amer. Phys. Soc. 1956. V.1. P.96.
[342] Salisbury S., Hardie G., Oppliger L., and Bangle R. Proton-Oxygen Differential Scattering Cross Sections // Phys. Rev. 1962. V.126. P.2143–2146.
[343] Blue R.A. and Haeberli W. Polarization of Protons Elastically Scattered by Oxygen // Phys. Rev. 1965. V.137. No.2B. P.B284–B293.
[344] Gomes V., Douglas R.A., Polga T. and Sala O. The E_{p} = 2.66 MeV resonance in ^{16}O(p, p)^{16}O // Nucl. Phys. 1965. V.A68.P.417–425.
[345] Trachslin W. and Brown L. Polarization and phase shifts in ^{12}C(p,p)^{12}C and ^{16}O(p,p)^{16}O from 1.5 and 3 MeV // Nucl. Phys. 1967. V.A101. P.273–287.
[346] Amirikas R., Jamieson D.N. and Dooley S.P. Measurement of (p, p) elastic cross sections for C, O and Si in the energy range 1.0–3.5 MeV // Nucl. Instr. Meth. 1993. V.B77. P.110–116.

[347] Gurbich A.F. Evaluation of non-Rutherford proton elastic scattering for oxygen // Nucl. Instr. Meth. 1997. V.B129. P.311–316.
[348] Braun M., Fried T. Elastic backscattering cross section of proton on Oxygen // Z. Phys. 1983. V. A311. P.173–175.
[349] Ramos A.R. et al. Measurement of (p,p) elastic differential cross-sections for carbon, nitrogen, oxygen, aluminium and silicon in the 500–2500 keV range at 140 and 178 laboratory scattering angles // Nucl. Instr. Meth. 2002. V.B190. P.95–99.
[350] Dubovichenko S.B., Burtebayev N., Dzhazairov-Kakhramanov A.V. et al. New measurements and phase analysis of elastic p^{16}O-scattering at astrophysical energies // Chin. Phys. 2017. V. C41. No.1. P.014001(10p.)
[351] Morlock R. et al. Halo Properties of the First $1/2^+$ State in ^{17}F from the ^{16}O(p,γ)^{17}F Reaction // Phys. Rev.Lett. 1997. V.79. P.3837–3840.
[352] Chow H.C., Griffiths G.M., Hall T.H. The ^{16}O(p,γ)^{17}F Direct Capture Cross Section with an Extrapolation to Astrophysical Energies // Can. Jour. Phys.1975. V.53. P.1672–1687.
[353] Luomajarvi M., Rauhala E. and Hautala M. Oxygen detection by non - Rutherford proton backscattering below 2.5 MeV // Nucl. Instr. Meth. 1985. V.B9. P.255–258.
[354] Barbieri C., Jennings B.K. Study of the ^{16}O(*p*,γ) Reaction at Astrophysical Energies // Nucl. Phys. 2005. V.A758. P.395c-398c.
[355] Artemov S.V. et al. Determination of Nuclear Vertex Constants for the Virtual Decays ^{3}He → d + p and ^{17}F → ^{16}O + p // Bull. Russ. Acad. Sci. Ser. Phys. 2009. V.73. P.165–170.
[356] Gagliardi C.A. et al. Tests of transfer reaction determinations of astrophysical *S*-factors // Phys. Rev. 1999. V.C59. P.1149–1153.
[357] Iliadis C. et al. New reaction rate for ^{16}O(p,γ)^{17}F and its influence on the oxygen isotopic ratios in massive AGB stars // Phys. Rev. 2008. V.C77. P.045802 (1–11).
[358] Baye D., Descouvemont P., and Hesse M. Microscopic analysis of extranuclear capture on the ^{16}O(p,γ)^{17}F reaction // Phys. Rev. 1998. V.C58. P.545–553.
[359] Rolfs C. Spectroscopic factors from radiative capture reactions // Nucl. Phys. 1973. V.A217. P.29–70.
[360] Mohr P., Iliadis C. Recommended cross–section of the ^{16}O(p,γ)^{17}F reaction below 2.5MeV: A potential tool for quantitative analysis and depth profiling of oxygen // Nucl. Instr. Meth. 2012. V.A688. P.62–65.
[361] Dubovichenko S.B., Dzhazairov-Kakhramanov A.V. Study of the Nucleon Radiative Captures ^{8}Li (n,γ), ^{9}Be(p,γ), ^{10}Be(n,γ), ^{10}B(p,γ), and ^{16}O(p,γ) at Thermal and Astrophysical Energies // Int. Jour. Mod. Phys. 2017. V.E26. No.3. P.1630009 (56p.).
[362] Hester R.E., Pixley R. E, and Lamb A. S. Radiative Capture of Protons in Oxygen at 140 to 120 kev // Phys. Rev. 1958. V.111. P.1604–1606.
[363] Tanner N. Direct Radiative Capture of Protons by ^{16}Ond ^{20}Ne// Phys. Rev. 1959. V.114. P.1060–1064.
[364] Kukulin V.I., Neudachin V.G., Smirnov Yu.F., El Khovari R. The role of the Pauli principle in the formation of optical potentials // Bull. Acad. Sci. USSR Ser. Fiz. 1974. V.38. P.2123–2128.
[365] Voevodin V.V., Kuznetsov Y.A. Reference mathematical library. Matrix and calculations. M.: Fiz.-Math. Lit. 1984. 318p. (in Russian).
[366] Dubovichenko S.B., Chechin L.M. Variational methods for solution of the Schrödinger equation // Bull. ASU Fiz.-Math. Ser. 2003. No.2 (8). P.50-58.

Index

allowed state 6, 8, 10, 52, 61, 74, 81, 86, 88, 98, 107, 120, 134, 144, 152, 153, 170, 171, 184, 197, 210, 223
asymptotic constant 6, 12, 16, 30–32, 42, 50, 52, 56, 67, 68, 69, 77, 78, 90, 99, 115, 116, 124, 125, 138, 139, 140, 149, 159, 162, 169, 175, 176, 179, 186, 189, 196, 199, 202, 223, 263

binding energy 6, 10–12, 16, 26, 31, 36, 41–43, 50–52, 54, 56, 62, 67–69, 77–80, 88–91, 94, 96, 98–102, 107–109, 111, 112, 114–117, 119, 120, 124–126, 130, 132, 133, 138–140, 143, 144, 148, 149, 153, 159, 160, 162, 164, 169–171, 175–177, 179, 183, 185, 186, 188, 189, 196, 197, 199, 200, 202, 206, 223, 227, 229, 230, 231, 245, 262, 263
bound state Preface, 5–12, 16, 22, 34, 36, 40, 43, 48, 49, 51, 54, 62–64, 69, 74, 75, 77, 79, 82, 84, 88, 92, 98, 100–102, 105, 112, 120, 123, 125, 126, 128, 130, 134, 135, 139, 142, 147, 153, 158, 168, 170, 171, 174, 176, 180, 197, 209–212, 223, 226, 231

cross section Preface, 1, 2, 6, 9, 10, 12, 14–16, 29–32, 35–41, 43–50, 53–60, 64, 65, 69–74, 79, 81, 83–87, 91–98, 100–106, 109–113, 117–121, 126–136, 141–157, 160, 161, 163–169, 172, 173, 177–185, 191, 193–197, 202–213, 215, 223, 224, 227–229, 245, 262, 264, 276

forbidden state Preface, 5, 35, 37, 38, 40, 48, 50, 59–62, 65, 73, 74, 98, 119, 120, 122, 123, 139, 148, 151–153, 158, 159, 177, 189, 197, 203, 209, 223

neutron capture Preface, 2, 35, 37–40, 44, 45, 54, 55, 58, 61, 74, 83–87, 94, 96, 106, 119, 120, 126–130, 133, 134, 141, 148, 149, 151, 155, 156, 160, 161, 169, 179, 180, 182–184, 193, 194, 196, 202, 203, 206, 215, 217

phase shift Preface, 2, 3, 5, 6, 8–15, 31–34, 36, 39–41, 43, 45–50, 54, 56–58, 62–66, 69, 73, 75, 77, 79–82, 86, 88, 89, 91–93, 96, 98, 99, 101–105, 108, 114, 118–124, 127–129, 133, 135–139, 143–151, 154, 155, 157–160, 168, 171, 173–177, 186, 188–190, 192, 194, 201–203, 208–210, 215, 224, 225, 227, 229–231,
phase-shift analysis Foreword, Preface, 2, 5, 6, 11–13, 15, 16, 35, 36, 38–40, 46, 48, 58, 64, 89, 104, 105, 135–138, 148, 149, 151, 169, 186, 189, 203, 209, 210, 215, 224, 231
potential cluster model Foreword, Preface, 5–7, 9, 10, 29, 35, 37–41, 43, 47, 72, 74, 151, 195, 196, 209, 211

reaction rate 31, 184, 193, 194, 206, 207, 230, 231

S-factor 1, 2, 12, 35, 37, 38, 41, 48, 63, 148, 151, 210, 212, 226, 228–231,

Young tableau Foreword, Preface, 2, 5–10, 12, 31–35, 37, 38, 40, 41, 44, 47–52, 57–63, 66, 74–76, 79, 84, 86, 88, 98, 102, 107, 112, 118–120, 123, 126, 132–134, 143, 147–149, 151–153, 156, 159, 167–171, 181, 184, 185, 188, 196, 197, 201, 203, 208–211, 213, 215, 223

https://doi.org/10.1515/9783110619607-011